Author:
Le, Anthony

Title:
Light driven robots - flare launching autonomous swimming hydrobot (FLASH)

LIGHT DRIVEN ROBOTS - FLARE LAUNCHING AUTONOMOUS SWIMMING HYDROBOT (FLASH)

By

NGUYEN HAO LE

Department of Engineering Mathematics

UNIVERSITY OF BRISTOL

A dissertation submitted to the University of Bristol in accordance with the requirements for award of the degree of Doctor of Philosophy in the Faculty of Engineering.

June 2021.

Word count: Fifty One Thousand One Hundred and Seventy Six

Abstract

Light is a readily available, versatile and compact energy source which could power and remotely control a new generation of light-driven robots. Untethered microrobots are not only capable of navigating through varied natural environments but are also able to perform complex tasks within the human body and inside enclosed systems. Light-driven robots can operate safely in convoluted and delicate physiological environments with significant impact on bioengineering and healthcare. The properties of light (intensity, wavelength, and polarisation) could be tailored towards specific requirements.

This thesis will first discuss recent developments in three main photo-actuation methodologies in micro-robotics namely photocatalysis, photovoltaics and photomechanical/photothermal effects. Then, a road map towards autonomous, smart light-driven robots of the future is introduced. After that, a flare launching autonomous swimming hydro-bot (FLASH) is developed as an early realisation of this new class of intelligent light driven robots. Finally, possible future works aiming at developing micro light-driven swimming/ jump gliding robots are discussed. This includes an early investigation into stimuli-responsive, biodegradable soft hydrogels which could offer a new and novel approach to improve FLASH's performance in areas such as soft body combustion, biocompatibility enhancement (biodegradable materials) and encoded intelligence (stimuli-responsive materials).

This thesis presents a comprehensive investigation into existing and emerging technologies for photo-actuation in microrobots, exploring approaches suitable for *in vivo*, *in vitro* and environmental remediations. It demonstrates that it is beneficial to combine different photo-actuation techniques with novel locomotion mechanisms to create self-sufficient, environmentally friendly light driven microrobots which are capable of performing complex tasks.

YouTube links to supplementary video:

https://youtu.be/IYwyVydDXMw (Movie S1)

https://youtu.be/ZJE129hDXmE (Movie S2)

https://youtu.be/TlK1oaKUIWM (Movie S3 - slow motion)

https://youtu.be/His1QRgdaHM (Movie S3)

https://youtu.be/His1QRgdaHM (Movie S4 - slow motion)

https://youtu.be/kQWu1N5D8l0 (Movie S4)

https://youtu.be/eEykFQOpAB0 (Movie S5)

https://youtu.be/x-TyxVpI5YM (Movie S6)

https://youtu.be/j4MaFPvMFOg (Movie S7)

https://youtu.be/9gUDlimZIbM (Movie S8)

Acknowledgment

I would like to thank Professor Jonathan Rossiter for his valuable guidance, support, encouragement and supervision. The many insightful discussions between us have been useful on both professional and personal level.

I extend my gratitude to all the technicians and support staff at the Bristol Robotics Lab (BRL) who have helped in various ways. Many thanks to Andrew Stinchcombe and Toby Tate-Druiff for making sure that my work proceeded smoothly. A special thanks to Alixander Partridge for encouraging me to stay motivated every day.
Many thanks to colleagues from the SoftLab for the wonderful and lively atmosphere. Special thanks to all those whom I shared a project with. The very efficient staff of UoB/BRL will always be remembered. Thanks to Dr. Jianglong Guo for his suggestions related to the Data Analysis and Graphing Software presented in this work. Thanks also to Dr. Majid Taghavid for his assistance on various issues I encountered during my PhD. I would like to acknowledge the Engineering and Physical Sciences Research Council for their support with my EMAT PhD program.

Finally, I would like express my deepest gratitude for my parents, grandparents and my wife for their continued encouragement and assistance.

Author's Declaration

I declare that the work in this thesis was carried out in accordance with the requirements of the University's *Regulations and Code of Practice for Research Degree Programmes* and that it has not been submitted for any other academic award. Except where indicated by specific reference in the text, the work is the candidate's own work. Work done in collaboration with, or with the assistance of, others, is indicated as such. Any views expressed in the dissertation are those of the author.

SIGN: Nguyen Hao Le DATE: 30/07/2021

Contents

List of Figures

List of Tables

List of Symbols

GaAs	Gallium Arsenide
CdTe	Cadmium Telluride
$CuInSe_2$	Indium Diselenide
TiO_2	Titanium Dioxide
Sp^2	Hybridization States of Carbon Atoms
IE	Input Energy
ER	Energy Release
ECE	Energy Conversion Efficiency
CO_2	Carbon Dioxide gas
C_2H_2	Acetylene gas
NaN_3	Sodium Azide
N_2	Nitrogen gas
O_2 and H_2	Oxyhydrogen gas
H_2O	Water
H_2	Hydrogen gas
O_2	Oxygen gas
Q	Heat
$\dot{m}$	Mass Flow
μ	Velocity
T	Thrust
p_1	Gas Pressure
p_w	Water Density
r	Length of L-shaped tube
$B_4O_7^{2-}$	LF
G′	Tetrahydroxyborate ion
G′′	Storage modulus

Loss modulus	
Maximum load before failure	Healing efficiency
η	Sodium chloride
NaCl	number (related to nonstoichiometry in chemical formulas)
x	

List of Abbreviations

FLASH	Flare Launching Autonomous Swimming Hydrobot
ROS	Reactive Oxidizing Species
NHE	Normal Hydrogen Electrode
MNMs	Micro/Nano Motors
ECE	Energy Conversion Efficiency
USDOE	US Department of Energy
UV	Ultra Violet
VLA	Visible Light Active
JMNPs	Janus Micro/Nanoparticles
TEM	Transmission Electron Microscopy
SEM	Scanning Electron Microscopy
AFM	Atomic Force Microscopy
PV	Photo-voltaic
CIGS	Copper Indium Gallium Selenide
AM	Air Mass
LCPs	Liquid-Crystal Polymers
LCNs	Liquid-Crystal polymer Networks
LCEs	Liquid-Crystal Elastomers
CNT	Carbon Nanotube
ERFs	Electro-Rheological Fluids
MRFs	Magneto-Rhoelogical Fluids
ECFs	Electro-Conjugate Fluids
LPB	Laser Power Beaming
DAQ	Data Acquisition
LiPo	Lithium Polymer

KGM	Konjac GlucoMannan
LVE	Linear ViscoElastic
KGM-Borax	Konjac GlucoMannan Borax-crosslinked

Chapter 1

1 Introduction

In the field of robotics, a microrobot is defined as a miniaturised robotic system manufacture by utilising micro/nanotechnologies. Terms such as micro-mechanisms, micromachines and micro/meso/insect-scale robots are used interchangeable to indicate devices operating at small scales. To date, the majority of small-scale robots are rigid machines and are heavily dependent on pre-programming to carry out tasks. They lack the flexibility and adaptability required in many environmental and biomedical applications such as underwater pollutant degradation, subterranean exploration, targeted drug delivery and cell manipulation. For instance, a soft micro-walker squeezes into confined spaces [1] and a soft mesoscale robotic arm can manipulate fragile objects or act in a "human-friendly" manner [2]. Miniaturisation remains the biggest challenge in conventional robotics. Miniaturisation of traditional electromagnetic actuators, control circuitry, sensors, and power sources is possible down to the centimetre scale. However, it is difficult, to scale these systems to the sub millimetre scale and below [3]. As such, wireless power sources have been proposed as an alternative approach which eliminates the excess electronics (control circuitry) and the power source (battery) from the miniature robot. The energy source driving the robot could be chemical energy, produced from chemical reactions [4] [5] [6], or external stimuli (i.e. magnetic, acoustic, light or electric field) [7] [8] [9] [10] [11] [12] [13] [14] [15] [16] [17] [18] [19] [20]. Table 1.1 summarises differences in key micro-robot designs with respect to their design, energy sources and actuation approaches for locomotion, sensing, environmental and bioengineering. It illustrates the advantages and disadvantages of each energy source and method of actuation.

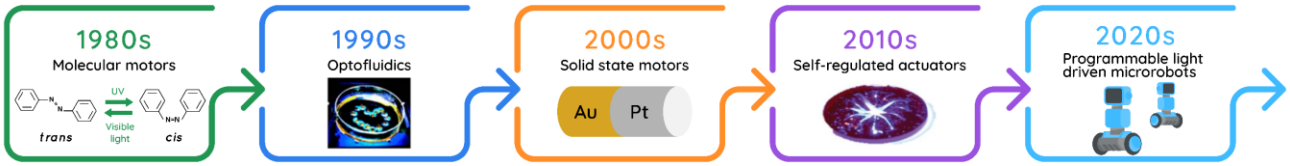

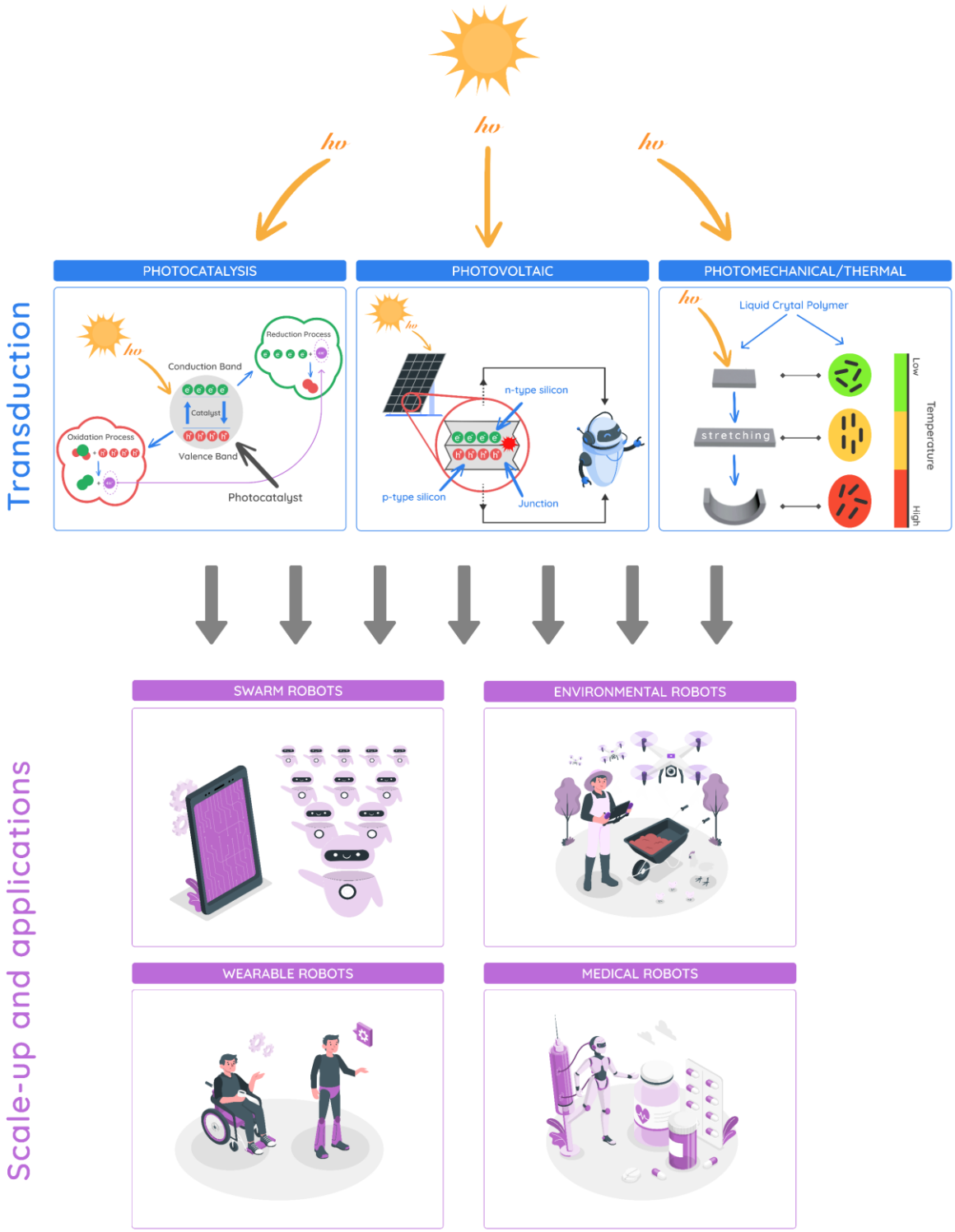

Figure 1.1: a) Milestones in the development of light-powered Micro/Nano motors (MNMs): Molecular motors[21]. Optofluidics[22]. Solid state photonic motors[23]. Self-regulated light-driven actuators[24]. Programmable light driven Microrobots [25] [26]. b) Concept figure from light energy to different photo-actuation methods in robotic applications

Table 1.1: Evaluation of different microrobots designs concerning their design principles, energy sources and actuation approaches for locomotion, sensing and compatibility in vivo.

Design	**Energy source**	**Actuation approaches**	**Design features for powering**	**Advantages in bioengineering applications**	**Major limitations**	**References**
Off board (externally actuated and control	Magnetic energy	Magnetic fields gradient and rotating magnetic fields	Corkscrew-like locomotion using rigid or flexible helices; traveling wave locomotion using synthetic tails; gradient pulling of magnetic robots.	Wireless power source, actuation and manoeuvrability; biocompatible.	Limited in material selections; complex setup; high set up cost; small workspace.	[27] [28] [29] [30] [31]
	Acoustic energy	Acoustic waves	Bubble-integrated vessels; Compliant tails; micro-cannon; inactive particles.	Biocompatible; allows complex geometries; reliable for in vitro applications	Limited study on microrobot material composition and geometry	[32] [33] [34] [35]
	Light energy	Photocatalysis, Photovoltaic and Light-induced photothermal and photomechanical effects	Gas bubble generation by photocatalytic activity. Electrical energy to drive motor by solar cell. Light induced shapes changes in photomechanical materials.	Microscale resolution; offer multiple ways to transfer energy (e.g., thermal, electrical, chemical); highly controllable; Biocompatible; wireless power source	Low energy conversion efficiency; workspace size dependent on illuminated area.	[36] [37]
On board (autonomous)	Chemical energy	Mechanical movement produces from chemical reactions	Gas bubble generation by catalytic activity. Exothermic chemical reaction in a confined reactor produces high pressure.	Can produce high energy density; fast locomotion.	Toxic fuel source (hydrogen peroxide); need toxic catalysts to get high power output	[38]
		Chemical gradients formed around the microrobot.	Electrophoresis e.g., Janus colloids.	Biocompatible catalysts; Capable of operating autonomously - by using chemical components in the environment as fuel.	Movement highly dependent on the ionic strength; difficult to get long distance directiona movement due Brownian effect.	[39] [37]
		Bio-synthetic hybrid cell-based actuators	Combination of live bacteria or sperms with synthetically bodies.	Offer sensing and mobility capability; inherently biocompatible; high energy conversion efficiency	Live cells function only in delicate conditions (37°C, 5% CO_2 nutrients etc.) to survive.	[40] [41]

1. Motivation

Among these power sources, light is the most versatile, as it is a renewable energy, highly controllable and has high power density. The solar energy falling on the earth's surface is around 100-150 mW/cm² [42] and as such, it is important for light-driven micro-robots to be able to operate under this energy range for practical applications. Furthermore, photonic properties (intensity, wavelength, and polarisation) could be tailored towards specific requirements. A complex control over light distribution could be accomplished using specialised laboratory apparatus, such as digital micromirrors and mirror scanners. This is also the case for commercial devices including projectors which can deliver high power output with different wavelengths, and are capable of altering the light patterns at high frequencies (>30 Hz). Owing to these unique properties, light is a suitable power source to drive micro-robots. The locomotion of light-powered micro-robots can be controlled precisely at high resolutions. Light-driven micro-robots operate by converting photonic energy into mechanical energy. In the past decades, many attempts have been made to drive micro-robots using different light-powered strategies. The major breakthroughs leading to light-powered actuation for micro devices are summarised in Figure 1.1a. Azobenzene synthetic molecular motors were first introduced in the 1980s. They are actuated by the photoisomerization of chemical structures of azobenzene, and were the first demonstrations of light-driven nano/micro devices. Taking inspiration from Kinesin's molecular walking, scientists have successfully created synthetic walkers from DNA, where the molecules walks forward based on molecular cleavage and ligation. Light energy enables DNA walkers to copy the function of biological motors in cargo transport and biosynthesis [43] [44] [45] [46]. Subsequently, various light driven molecular motors have been developed. In the 1990s, scientists established that photon energy can actuate liquid droplets. This gave birth to optofluidics, in which the movement of a fluid is propelled by photo-induced capillary forces, optical forces, or a combination of optical and electrical effect [21] [22]. Au-Pt nanomotor was developed by Sen and Mallouk [23] in 2004 using inspiration from the self-propelling plates developed by Whitesides et al. in 2002 [47], and which instigated a new research theme in solid-state motors. Solid-state motors exploit asymmetrical gradient fields which are initiated by light. In these gradient fields, a force is needed to stabilise the field and to keep its stable state within a liquid. This force drives the movement of the motor. In 2017, Zeng [24] reported a first ever tuneable artificial iris made from liquid crystal elastomer that can perform automatic shape-adjustment by reacting to the incident light power density. This breakthrough in light-responsive material design presents a new approach to automatic, self-adjusting systems based on soft smart materials. Owing to these past achievements, in the early 2020s, scientists have successfully created programmable light driven micro/nanorobots with advanced properties and functions. For instance, in 2020, Li [25] reported a 3D printed micro-rocket which can reach a max moving speed of 2.8mm/s (62 body lengths per

second) in blood-like solution. In 2021, a review paper written by Wang [26] highlighted recent breakthroughs in the development of solid-state motors to programmable swarm of light-driven micro/nanorobots.

The objective of chapter 1 and 2 is to provide the reader with a comprehensive investigation of the established and emerging photo-actuation techniques for micro-robots, including photocatalysis, photovoltaic and photomechanical/photothermal effects. By focusing on the designs and applications of photomicrorobots, these chapters present the development of light-powered micro-robots and examines the challenges in each photo-actuation category. Finally, a new design pathway for light-powered micro robots is proposed which could open up opportunities for a new generation of fully autonomous, smart micro machines. Figure 1.1b highlights promising areas of future applications for light driven microrobots utilising these three emerging photoactuation approaches.

2. Research questions

The aim of this thesis is to identify a new design pathway for light-powered insect-scale robots which could open up opportunities for a new generation of fully autonomous, smart machines, and present an early realization of this new concept through development of a flare launching autonomous swimming hydrobot (FLASH). By focusing on the designs and applications of small-scale robots, this thesis presents the development of light-powered robots and examines the challenges in each photo-actuation category using the following set of research questions.

1. What are the advantages and disadvantages of each photo-actuation methods in developing light driven microrobots?
2. What is the research trend in the field of light driven microrobots?
3. What are the benefits of using photovoltaic actuation methods as a baseline to develop intelligent photomicro robots for environmental applications?
4. How can one make light driven microrobots 'green'? i.e. self-sufficient, environmentally friendly (using renewable energy sources to power and materials that produce zero waste).
5. What are the best strategies to create the novel intelligent light-driven microrobots of the future and the potential benefits of combining different photoactuation methods? E.g. Soft-smart, light-responsive materials, biodegradability, combustion in soft bodies, sensing, swarm robots etc.

The work presented here consists of three parts. The first part is a comprehensive review on three emerging photo-actuation methods namely photocatalysis, photovoltaic and photomechanical/photothermal effects. This concludes with an overview about the future development of smart photo-microrobots in terms of a road map. The second part details the development of a novel light driven, swimming/jump gliding robot (FLASH) following the direction pointed out in the road map. The investigation ends with the development of a prototype untethered FLASH. The final part details an early investigation into stimuli-responsive, biodegradable soft hydrogels which could offer a new and novel approach to improve FLASH's performance (soft body combustion), enhance biocompatibility (biodegradable materials) and encoded intelligence (stimuli-responsive materials).

3. Contribution

In addressing the above questions and investigating the mechanism of combustion for water jetting propulsion in a light powered small-scale robot, this thesis makes the following contributions.

6. Comprehensive investigation into existing and emerging technologies for photo-actuation in microrobots, exploring approaches suitable for in vivo, in vitro and environmental remediations (chapter 2).

7. The future of light driven microrobots (chapter 2).

8. The design and characterisation of a novel light driven robots that is autonomous, self-sufficient, and environmentally friendly (chapter 3&4).

9. Untethered Flare Launching Autonomous Swimming Hydrobot - FLASH (chapter 5).

10. Investigation of stimuli responsive biodegradable hydrogel as a potential class of materials for FLASH (chapter 6).

11. The development of a soft smart sensory feedback device using SMAs and soft matter logic (introduced as an alternative way to realise complex control and added functionality as well as adding structural stiffness and stability to the robot in chapter 7 and continued in Appendix C).

4. Publications

The following peer-reviewed works have contributed to this thesis.

Journals

1. M. F. Simons, K. M. Digumarti, **N. H. Le**, H. Chen, S. C. Carreira, N. S. S. Zaghloul, R. S. Diteesawat, M. Garrad, A. T. Conn, C. Kent, J. Rossiter., "B:Ionic Glove: A Soft Smart Wearable Sensory Feedback Device for Upper Limb Robotic Prostheses," in IEEE Robotics and Automation Letters, vol. 6, no. 2, pp. 3311-3316, April 2021, doi: 10.1109/LRA.2021.3064269.

2. **N. Le,** K. M. Digumarti, D. Gosden, J. Rossiter., "Towards stimuli-responsive soft robots with 3D printed self-healing konjac glucomannan gels." in 3D Printing and Additive Manufacturing, accepted on 25 May 2021.

3. **N. Le,** J. Rossiter., "Light Driven Microrobots: A Review," in preparation.

4. **N. Le**, J. Rossiter., "Flare Launching Autonomous Swimming Hydrobot (FLASH)," in preparation.

5. Outline of the thesis

The structure of the thesis is described below (see figure 1.2 for thesis structure diagram).

1. Chapter 2 provides a comprehensive review on emerging photo-actuation methods to drive microrobots. It presents the development of each actuation technique in literature focusing on materials and applications in robotics. It identifies challenges and research gaps in the field and propose a new design pathway which can be used to develop intelligent photomicrorobots of the future.

2. Chapter 3 and 4 show an early realisation of the concept proposed in chapter 2 in terms of a novel autonomous light driven robot. It describes the design and characterization of said robot with a focus on environmental remediation/monitoring applications.

3. Chapter 3 presents the effect of combustion to water jet propulsion by characterising the force generated at different gas volume fraction and nozzle sizes. It also investigates the swimming performance of the robot under water.

4. Chapter 4 investigates the aerial-aquatic locomotion of the robot by charactering the maximum vertical jump height at different gas to water volume fraction and nozzle sizes.

5. Chapter 5 presents an untethered prototype of the novel autonomous light driven robot. It showcases the architecture of the robot and its performance in the environment.

6. Chapter 6 concludes the thesis by summarising the contributions made and presents thoughts on potential avenues for research in the future.

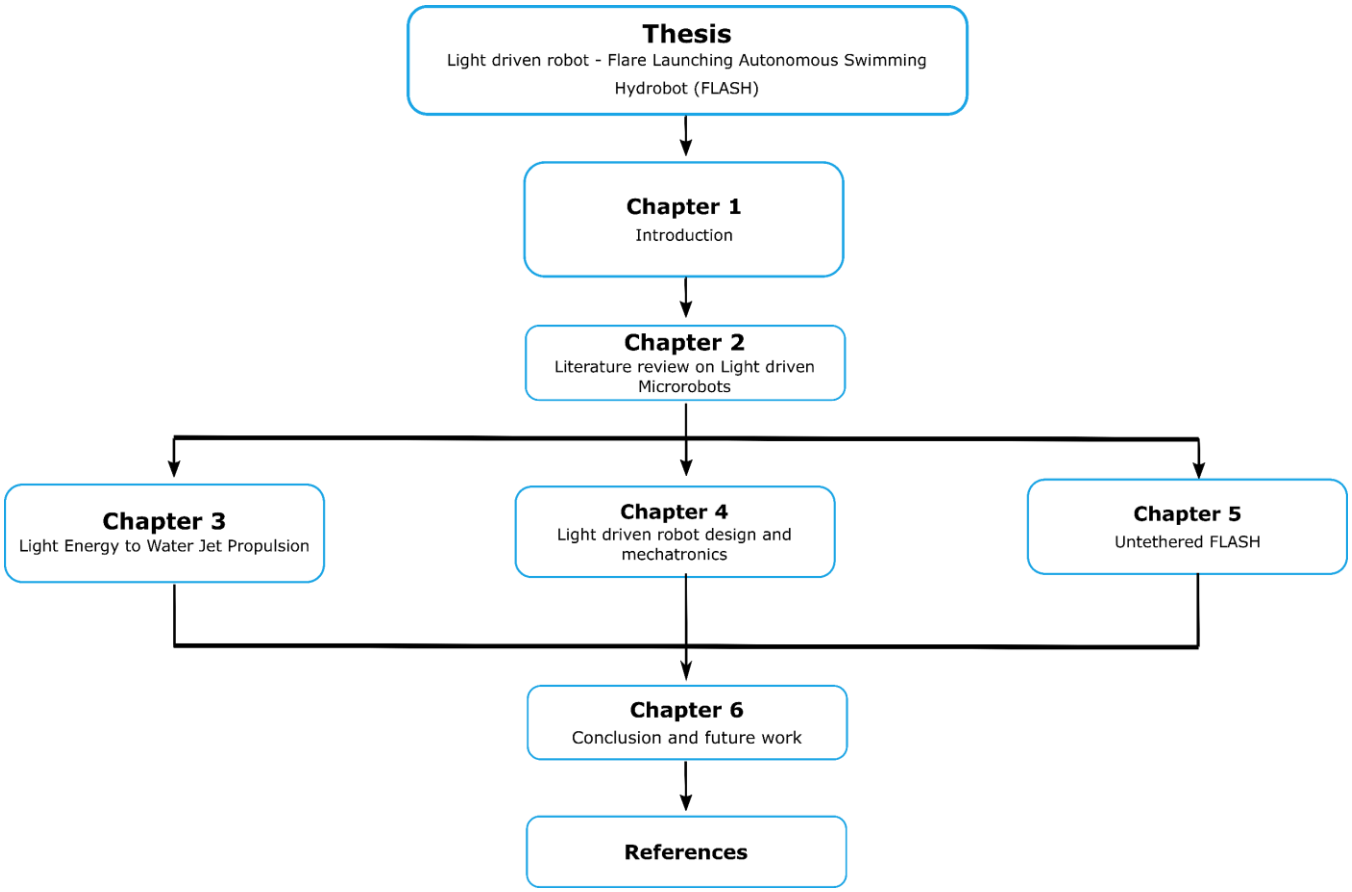

Figure 1.2: Thesis structure diagram.

Chapter 2

2 Light driven microrobots: a review

Sunlight is one of our planet's most abundant and freely available energy resources. The amount of solar energy that reaches the earth's surface in one hour is more than the planet's total energy requirements for a whole year. Solar power falling on earth is about 1.8×10^{11} MW [48]. This is order of magnitude larger than all the current energy consumption rate. The average solar radiation falling on the earth's surface called the solar constant is estimated to be 136 mW/cm^2 [42]. As a result, the ability to harness this abundant energy source is appealing and many efforts have been made to capture and store solar energy for use in robotic systems. This chapter will discuss three photo-actuation strategies commonly adopted in literature to power small-scale robotic systems. The first is photocatalysis, a process which converts light energy into chemical energy which can be used later on to produce mechanical energy. The second is photovoltaic, a process which directly converts light energy into electrical energy to use in mechanical system. The last is photothermal and photomechanical effects, which are inherent characteristics of photoresponsive mechanical materials which change volume upon light irradiation and produce mechanical movements. All these photoactuation strategies are capable of producing mechanical movements from light energy which is an essential requirement in designing any robotic systems. In addition, the ability to convert light energy to different energy forms, either chemical or electrical, for storage is attractive as this enables one to design miniature, self-sustaining robotic systems for various applications.

2.1 Photocatalysis

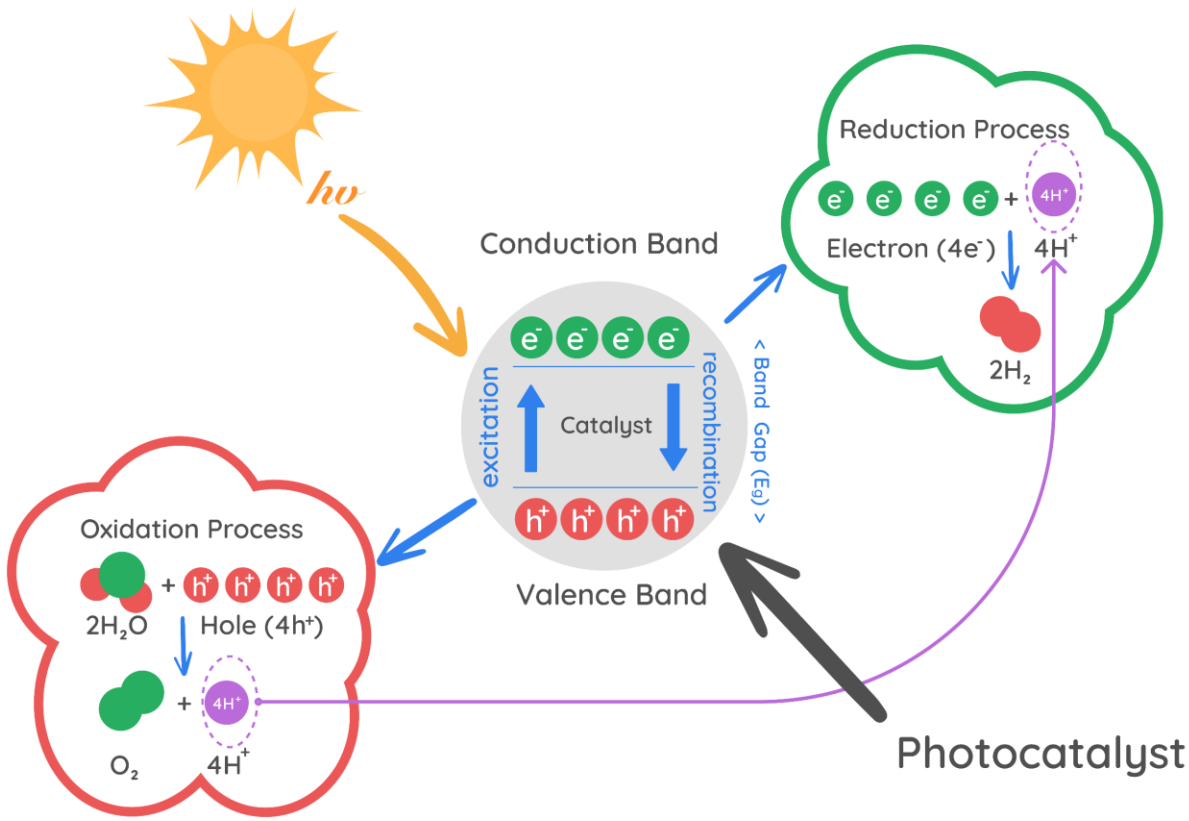

Figure 2.1: Photocatalytic water splitting process on TiO_2. Reactions occur in three steps: (i) absorption of photons greater than the band gap energy to produce an electron–hole pair; (ii) separation of charges and migration to the surface (e- to conduction band and H^+ to valence band); (iii) redox reactions with adsorbed reactants (i.e. reduction of H^+ to hydrogen gas and oxidation of H_2O to oxygen gas).

Catalysis is a term describing a process in which the rate and/or the outcome of the reaction is influenced by the presence of a substance (the catalyst) that is not consumed during the reaction and that is subsequently removed if it is not to constitute as an impurity in the final product. Photocatalysis is a type of catalysis that results in the modification of the rate of a photoreaction - a chemical reaction that involves the absorption of light by one or more reacting species - by adding substances (catalysts) that participate in the chemical reaction without being consumed. Figure 2.1 shows the photocatalytic water splitting reaction using titanium dioxide (TiO_2) as a nominal catalyst. In this reaction water is broken down into oxygen and hydrogen:

$$2H_2O \rightarrow 2H_2 + O_2$$

Specifically, in photocatalytic water splitting process, photon energy is absorbs by a catalyst and as a result, electrons will move from the catalyst valence band to its conduction band. If the band gap is above the threshold needed for water splitting (1.23 eV), then, excited electrons can reduce hydrogen ions and holes can oxidize oxygen anions generating H_2 and O_2 gas respectively. As such, a semiconductor with band gap greater than 1.23 eV would in principal be a suitable catalyst for one-step excitation water splitting [49].

Hydrogen gas is often regarded as a clean renewable source of energy [50] and an alternative to fossil fuel. Hydrogen gas can be safely stored and converted into different forms of energy. For instance, electricity can be generated by a fuel cell through the combination of hydrogen and oxygen gas. In addition, oxyhydrogen combustion can produce thermal energy and mechanical energy which can be used to drive pistons in automobiles or produce thrust for rockets. The thrust generated from the oxyhydrogen could also be used to propel arial-aquatic robots for various environmental applications.

Photocatalysis has received considerable attention in recent years and has been used within a variety of micro-devices across a wide range of research areas, including environmental and energy-related applications [50] [51] [52] [53] [54]. There are many candidate materials for photocatalysis, particularly in the area of converting solar power to hydrogen, a particularly attractive method of generating non-polluting H_2 gas for chemical processes, including hydrocarbon synthesis, and environmentally friendly internal combustion engines. Although various materials demonstrate high photo-sensitivity [55], these semiconductors are not suitable for practical applications because they are prone to corrosion in aqueous environments. Amongst many different photocatalysts, TiO_2 has been most extensively investigated owing to its high photocatalytic activity, abundance, biocompatibility and excellent chemical and thermal stability [56] [57] [58] [59] [60]. Attractive properties include:

- TiO_{2-x} (x is number related to nonstoichiometry in chemical formulas) is sensitive to light and water [61].
- TiO_{2-x} has strong resistance to corrosion in aquatic environments [62]
- TiO_{2-x} properties can be adjusted via doping.
- TiO_{2-x} is significantly cheaper than other photo-responsive materials.

Fabrication techniques for TiO_{2-x} production are less complex compared to those required for valence semiconductors.

2.1.1 TiO_2 Structures and Properties

Titanium dioxide has three polymorphs, anatase, rutile and brookite. Among these three major phases, anatase is reported to be a better photocatalytically active phase [63] [64]. The most abundant and stable form of TiO_2 is rutile. TiO_2 is an n-type semiconductor because of its oxygen deficiency [65]. The band gap is 3.2 eV for anatase, 3.0 eV for rutile, and ~3.2 eV for brookite [66] [67] [68], thus making pure TiO_2 primarily active under UV spectrum. In addition, Anatase and brookite have larger band gap than rutile which increases he oxidation 'power' of electrons and facilitates electron transfer from the TiO_2 to adsorbed molecules [69]. Furthermore, Anatase has a longer electron-hole pair life than rutile which contributes to its enhanced photocatalytic activity [70].

2.1.1.1 Electronic Processes in TiO_2 Photocatalysis

Two photochemical reactions proceed on a TiO_2 surface when irradiated with ultraviolet light: photo-induced redox reactions of adsorbed substances; and the photo-induced hydrophilic conversion of the TiO_2 itself. This was explored in [53]; when the surface of the rutile TiO_2 electrode was irradiated with light of wavelength shorter than its band gap, about 415nm (3.0eV), photocurrent flowed from the platinum counter electrode to the TiO_2 electrode through the external circuit. The direction of the current revealed that the oxidation reaction (oxygen evolution) occurs at the TiO_2 electrode and the reduction reaction (hydrogen evolution) at the Pt electrode. This important observation shows that water can be decomposed, using UV light, into oxygen and hydrogen, without the application of an external voltage, according to the following scheme.

$$\mathbf{TiO_2 + \mathit{hv} \rightarrow e^- + h^+} \qquad \mathbf{(1)}$$

(at the TiO_2 electrode)

$$\mathbf{2H_2O + 4h^+ \rightarrow O_2 + H^+} \qquad \mathbf{(2)}$$

(at the Pt electrode)

The overall reaction is

$$\mathbf{2H_2O + 4\mathit{hv} \rightarrow O_2 + 2H_2} \qquad \mathbf{(3)}$$

The discovery that photocatalysis can be used to generate "free" hydrogen and oxygen from water is a major advance in microrobotics. Appropriately structured from suitable catalytic materials, a photocatalytic microrobot could potentially operate indefinitely in an environment where light and water are available. This is because the

gases produced from the reaction can propel microrobots forward. This breakthrough open ups many potential applications of photocatalysis in microrobotics. However, photocatalysis is not without its challenges and is still very much as emerging field.

2.1.1.2 Recombination

Electrons-holes recombination is the major challenge in semiconductor photocatalysis because it reduces the overall quantum efficiency [56]. When recombination happens, excited electrons flow back to the valence band and combines with the holes without reacting with adsorbed species, dissipating the energy as light or heat. Recombination might happen either on the surface or in the bulk material and generally facilitated by impurities, defects, or other factors which cause bulk or surface imperfections in the crystal [56].

2.1.1.3 Strategies for Improving TiO_2 Photoactivity

Early investigators on solar-hydrogen photocatalysis include Fujishima and Honda, 1972,[71]. They first introduced photocatalytic water splitting using rutile (TiO_{2-x}) as the anode of a photo-electrochemical cell. An important feature of rutile titanium dioxide is that, unlike other photo-responsive semiconductors (Si, GaAs, etc.), it is resistant to corrosion in aqueous medium.

However, the lack of breakthroughs in improving the energy conversion efficiency (ECE) of TiO_{2-x} above ~1% over the last three decades has cast doubt on the feasibility to increase the ECE above ~10%, which is the benchmark for commercialisation set by the US Department of Energy (USDOE) [72]. Despite this, significant breakthroughs have been made in the past decades with respect to increasing the ECE. UV light only constitutes around 3% of solar light and one of the main reasons titanium dioxide has such low ECE is because it is not reactive under visible spectrum. Thus by increasing the absorption spectrum of titanium dioxide to the visible spectrum one can effectively increase the ECE (as summarised in Figure 2.2).

As seen from figure 2.2, a variety of methods have been investigated to improve the photocatalytic efficiency of TiO_2. They are classed as either morphological modifications, for example increasing surface area and porosity [73], or chemical modifications, by tine corporation of additional components in the TiO_2 structure [74]. The graph shows that much progress has been made in the past two decades to make titanium dioxide active under the visible spectrum [75] [76] [77] [78] [79] [80] [81]. This is a significant break-through as compare to early works in 1970s which only show titanium dioxide active under UV spectrum [71] [82] [73] [74]. Although visible light active (VLA) TiO_2 photocatalysts require further modifications, their overall efficiencies have been significantly enhanced by controlling the semiconductor morphology. For instance, Mao reported a significant improvement of

photocatalytic activity of the chitin-modified TiO_2 under visible light irradiation. Compared to the pure TiO_2/carbon fibre, the TiO_2/carbon fibre with 0.6 wt% of chitin sample exhibits an enhanced visible light activity of about 2.25 times [81]. In addition, Le reported enhanced photocatalytic response of TiO_2 under visible light by C and N co doped TiO_2 nanoparticles to maximum wavelength of around 650 nm [83]. The most notable work in this area to date is from Wang where the fabricated Ag-TiO_2 nanoparticles exhibit photosensitivity in the visible spectrum up to 800 nm wavelength [84].

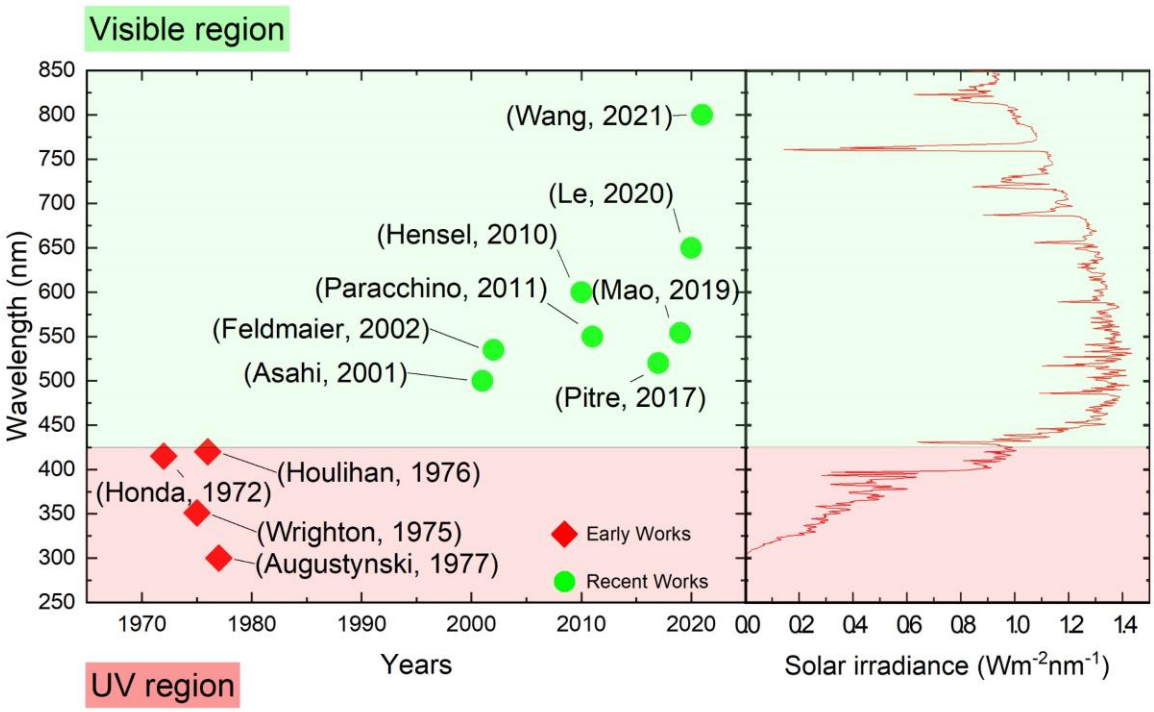

Figure 2.2: Significant developments in Titanium dioxide as a photocatalyst. On The left side, strategies adopted to improve photocatalytic efficiency of TiO_2. On the right side, Solar irradiance energy in the UV and visible spectrum. Note the higher incident energy in the visible spectrum [71], [73], [83], [84], [74]–[78], [80]–[82].

2.1.2 Applications of TiO_2 Photocatalyst-based Micro/Nano robots.

Removal of waterborne pathogens is a critical challenge that requires the developments of microscopic-scale devices for efficient water treatments. Micro/nanorobots, often referred to as micro/nanomotors by chemists, have been developed for degradation of chemical pollutions and recently they have been used for the removal of microbial pathogens [85]. Amongst myriad micro/nano robots, light-powered Micro/Nanorobots have received significant focus due to their remote control by photonic stimulation, cycling stop-and-go movement and simple velocity control via modulation of light intensity [86] [87] [88]. TiO_2 is considered to be well suited for such applications as it is an abundant, large specific surface area, relatively low toxicity, low-cost, highly active catalyst and has been researched over the past few decades due to these unique near semiconductor electronic properties [84]. A niche utilisation of these properties is in environmental remediation, particularly in decomposition of a variety of pollutants in both fluid and gaseous states under ultra violet light illumination [57], [84], [87], [89]–[91]. For instance, light-driven microrobots based on TiO_2 include simple TiO_2 particles, TiO_2 rockets and TiO_2-based Janus particle microrobots. Table 2.1 summarises recent developments in photo-actuated TiO_2-based micro devices used in environmental remediation with respect to material, geometries, medium, velocity, pollutants degraded (if applicable) and the advantages and disadvantages of each devices.

Janus Micro/Nanoparticles (JMNPs) (named after the double-faced Roman god Janus - Figure 2.3a) are monolithic particles made up of two distinct sides with different chemical and/or physical composition. Figure 2.3b illustrates the light-induced self-electrophoresis movement mechanism of a catalytic TiO_2–Au Janus microrobots. When exposed to light, hydrogen ions are generated at the bright side and a flux of electrons is generated inside the Janus microrobot. The hydrogen ions flow from the bright side to the dark side along the particle surface. They then combine with the electrons to produce hydrogen gas. The water at the TiO_2 surface is oxidized to produce oxygen gas. The Janus microrobot moves towards the light source in the opposite direction to that of hydrogen ion flow. These microrobots have been used widely in water purification due to the anisotropic surface characteristics, and tuneable and controllable asymmetric structure which promote multifunctionality. For instance, Guan et al. demonstrated that Pt- TiO_2 Janus microrobots can degrade rhodamine B in water [15]. The locomotion of the Pt-TiO_2 Janus microrobots can be remotely controlled by adjusting the timing, intensity and waveform of incident UV light. Janus particles interact destructively with the fluid within which they are located, and hence the choice of fluid and its solutes (together forming the fuel) are important. The movement of the water-powered Pt-TiO_2 Janus microrobot is governed by light-induced self-electrophoresis mechanism under the

local electrical field. This is generated by the asymmetrical water oxidation and reduction reactions on its surface [92] [23] [93]. Inspired by Guan's work, Wu et al. demonstrated dye-enhanced movement of light-powered TiO_2-Au Janus micromotors in a range of aqueous mediums of methyl blue, cresol red and methyl orange [94]. This confirmed that the photocatalytic degradation of organic compounds improves the motion of TiO_2-based Janus micromotors. Unfortunately, the activity of these photocatalytic micromotors is limited to specific wavelengths of light due to their narrow light absorption spectrum, which limits their effectiveness for applications in biomedicine and environmental remediation. In an effort to overcome this limitation, Jang et al. reported a multiwavelength light-responsive Janus micromotor consisting of a black TiO_2 microsphere asymmetrically coated with a thin Au layer. This Janus microrobot is propelled by light, both in H_2O_2 solutions and in pure H_2O over a broad range of spectrums including ultra violet, blue, cyan, green, and red light [95].

Table 2.1: Photo-actuated TiO_2-based micro devices compared in terms of material, geometries, media, velocity, pollutant degraded, including advantages and disadvantages of each device.

Material	**Geometries**	**Medium**	**Maximum Velocity**	**Pollutant**	**Advantages**	**Disadvantages**	**Reference**
TiO_2/Au	Nanotube – average diameter ≈ 25 nm	Methyl orange solution	No movement is reported	Methyl orange	Confirm the photocatalytic activities of TiO_2 nanotubes are higher than that of nanosized TiO_2; Enhanced photocatalytic activity when TiO_2 nanotube is loaded with Au (orPt); Au loaded TiO_2 nanotube has evident adsorption peak in visible region.	Titanium nanotubes have tubular structure and can be easily damaged when calcined at high temperature (i.e. 500°C - 600°C); no movement of the nanotubes is reported.	[96]
Fe_3O_4@PANI/ TiO_2	Spherical particle ≈ 420 nm	Ethylenediami-netetraacetic acid (EDTA) solution	No movement is reported	Ethylenediami-netetraacetic acid (EDTA)	The photocatalyst exhibited fast interfacial charge migration ability; Superior magnetic separation characteristic; Enhanced visible-light photoactivity and photostability.	The particles do not move.	[97]

TiO_2/Au/Mg	Janus particle ≈ 20µm	NaCl solution	80 µm/s	Bis(4-nitrophenyl) phosphate, Methyl paraoxon, Bacillus globigii spore	A reagent-free operation, generation of reactive oxidizing species (ROS) responsible for the efficient destruction of the cell membranes of the anthrax simulant Bacillus globigii spore.	Low speed (4 body length/s), relatively short lifespan (15 minutes for 30 um sphere), requires off-board power source, stochastic motion.	[98]
TiO_2	Rod shaped, diameter ≈ 6 um	H_2O_2 solution	325 µm/s	No specific pollutants are reported.	The micromotor could be accelerated or decelerated depending on the variation of the light intensity; The light-controlled activation and stop has a short response time 0.2s	The motion of the micromotors highly depend on fuel concentration;	[99]
TiO_2	Thin film ≈ 250nm	Acetone and Benzene gases in a gastight chamber.	Thin film on fixed substrate	Acetone Benzene	Enhanced visible-light photoactivity and photostability; high visible light transmittance.	Increased PVP content decreases TiO_2 crystallite size and thus reduces the photocatalytic activity of TiO_2; The thin film is stationary.	[100]
Au/Pt/ TiO_2	Spherical Particle ≈ 5µm	H_2O_2 solution	130 µm/s	Methylene blue, Rhodamine B, Methyl orange	Using H_2O_2 (fuel) the solar photocatalytic efficiency can be enhanced more than 110 times.	The motion of the micromotors highly depend on fuel concentration or mechanical agitation to work (i.e. magnetic stirring), stochastic motion, Platinum is expensive.	[101]
TiO_2-Au	Janus particle ≈ 1 µm	Water	25 body length/s	No specific pollutant is tested	Requires low intensity UV light energy in pure water; Can be precisely controlled ; The janus micromotors can be easily modified with diverse functional groups towards	Still operates under UV spectrum.	[88]

					complicated tasks; Fuel free.		
TiO_2/Pt	Janus particle ≈ 800 nm	Water	21 µm/s	Rhodamine B	Long-term stability, wirelessly controllable motion, long lifetime, small size, suitable for application in macro- or microenvironment (microchannels and microwells in microchips)	Difficult to scale up, Platinum is expensive.	[15]
TiO_2-Au	Janus particle ≈ 1 µm	Water Methyl blue Cresol red Methyl orange	26 µm/s 43 µm/s 36 µm/s 34 µm/s	Methyl blue, Cresol red, Methyl orange	Reusability, light-induced dye-enhanced motion through self-electrophoretic effects in dye solutions under UV irradiation, high efficiency.	Still operates under UV spectrum.	[94]
Au/B-TiO_2	Janus particle ≈ 3.5 µm	Water H_2O_2 solution	30 µm/s	No specific pollutant is tested	The Au/B-TiO_2 Janus micromotors exhibited directional movement under broad range of light spectrum including UV (360−370 nm), blue (420−440 nm), cyan (460−495 nm), green (540−550 nm), and red (590−650 nm).	Very low speed in pure water ≈ 0.54 µm/s.	[95]

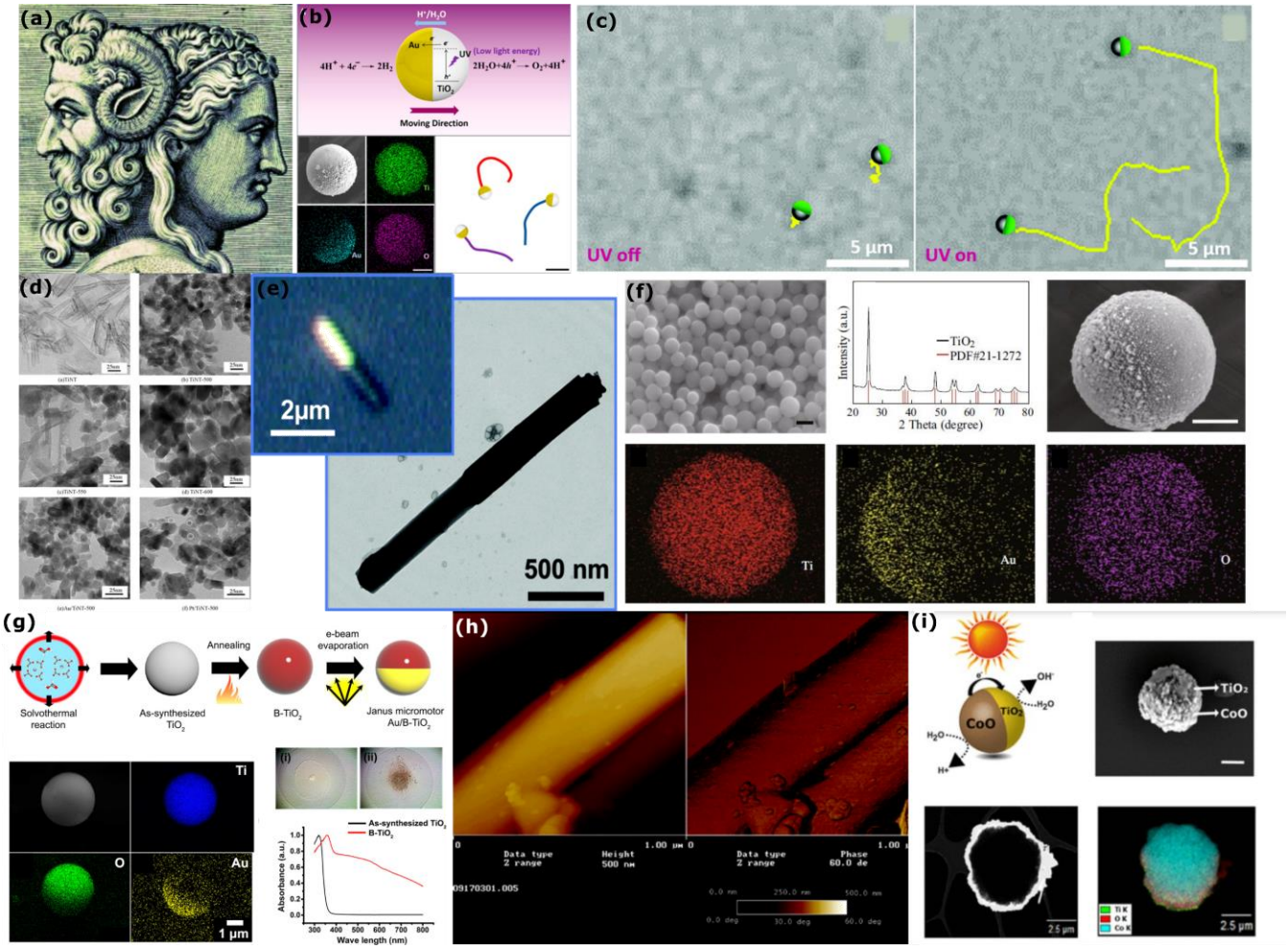

Figure 2.3: Recent development of photo-actuated TiO_2-based microrobots: a) Double-faced Roman god Janus after which the two-sided Janus particle is named. b) Catalytic TiO_2–Au Janus microrobots powered by ultra violet light [88]. c) Movements of two TiO_2-Pt microrobots in water. (left) UV off and (right) UV on for a period of 1 s [15]. d) TEM images of the TiNT samples after calcination at different temperature and Au (or Pt)-loaded, this figure clearly shows that Au and Pt-loaded help retain the tubular structures of the TiNT samples [96]. e) Optical micrograph of a catalase−Ppy−Au nanorod (left) and TEM image of a Ppy−Au nanorod (right) [93]. f) SEM image of the TiO_2 micromotors (scale bar 1 µm) [94]. g) Synthesis and material characterization of Au/B-TiO_2 Janus micromotors [95]. h) Tapping mode AFM topography (left) and phase shift (right) images of Pt/Au nanorods in air [23]. i) Multiwavelength-Steerable Visible-Light-Driven Magnetic CoO–TiO2 Microswimmers [102].

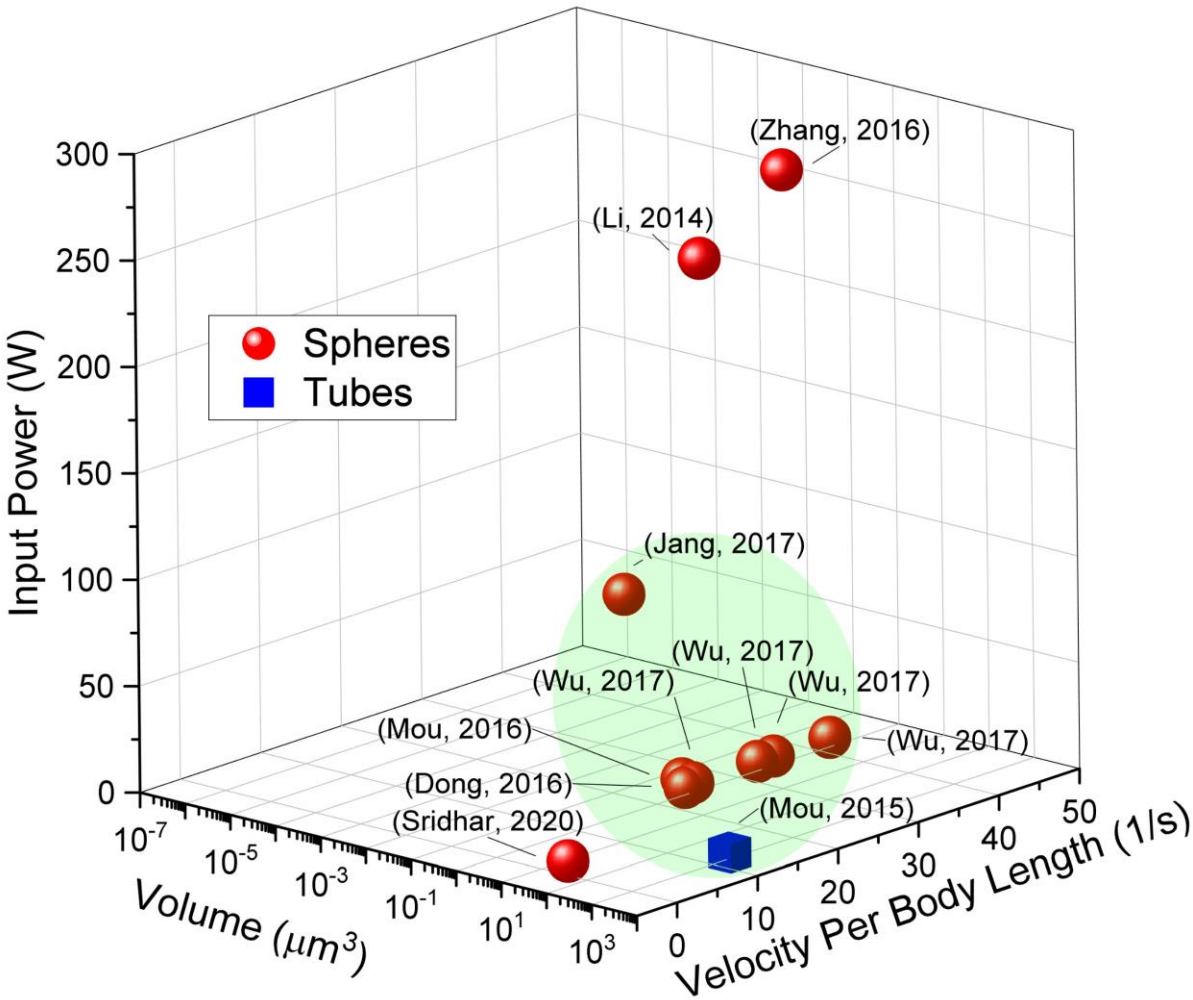

Figure 2.4: Log scale plot of Volume vs Input power vs Velocity of TiO_2 Photocatalyst-based Micro/Nano Devices [15], [88], [95], [98], [99], [101], [102]

It is clear from Table 2.1 that a common drawback reported across the literature is the low speed of photonic micro/nano devices. This has led to the emergence of a research area where the target is to improve the speed of the device whilst keeping the size and input power small (figure 2.4: green region). Based on this metric, the most notable work to date is the light-powered TiO_2-Au Janus microrobot presented by Dong et al. [88]. The fuel free Janus micromotor (diameter 1 µm) can propel in pure water under low UV light intensity 40 x 10^{-3} W/cm^2 with a fast speed of 25 body length/s. This has led to follow up work in which the light driven synthetic microdevices can rapidly detect and degrade organic dye pollutants in aqueous environments [94]. Similar works have also been reported in literature such as autonomous light-activated TiO_2/Au/Mg micro-agents capable of decomposition of biological and chemical warfare agents [98] and a motor plasmonic photocatalyst developed for remediation of polluted anaerobic stagnant waters [101]. In addition, these microrobots exhibit outstanding reusability in the

degradation and detection of pollutants. These results indicate the potential to adjust the propulsion of photocatalytic micro/nanorobots for "on-the-fly" degradation of pollutants in fluidic environments. These light-driven, precisely controllable, and efficient TiO_2-based photocatalytic Janus micromotors hold considerable promise for the design of practical photo-actuated micro/nanomachines towards a wide range of important future robotic applications ranging from nanofabrication [103] to environmental remediation [104] .

2.2 Photovoltaics

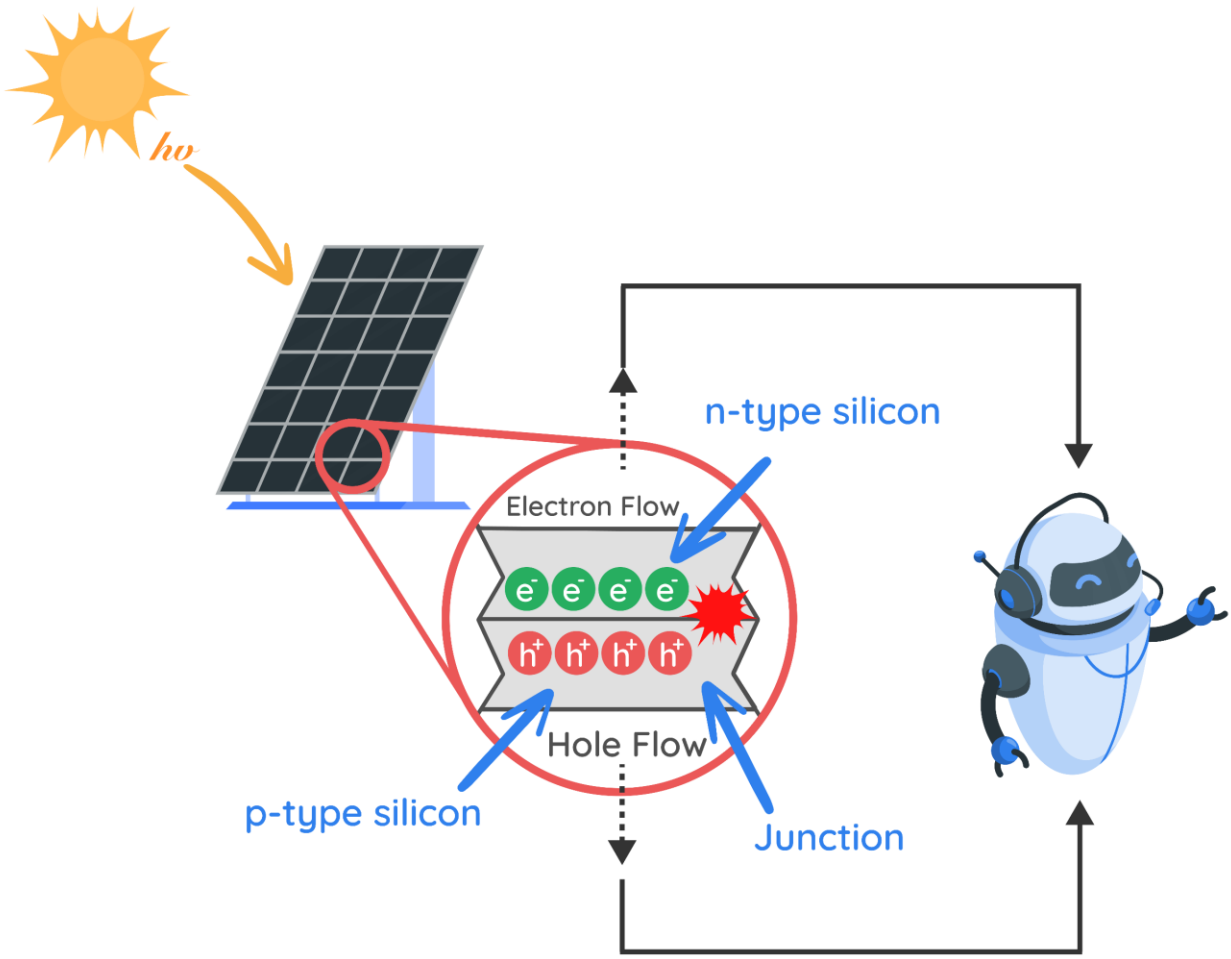

Figure 2.5: Photovoltaic Process, showing conversion of light energy to electrical energy.

It is estimated that, given the solar energy constant of 136mW/cm^2 photovoltaic cells could generate power density up to 100 mW/cm^2 [105]. As such, photovoltaics is one of the most efficient methods to harvest available

solar energy. Photovoltaic energy harvesting uses solar or artificial light and photosensitive semiconductors to generate electricity. This involves three main processes: 1. absorption photon energy from light source; 2. this frees electrons from the semiconductor (separation); and 3. the flow of the electrons (negatively charged) and holes (positively charged) at respective electrodes [106]. This forms an electric current when a load is present (see figure 2.5).

Photovoltaic technology has been the driving force in both the large-scale renewable energy industry and small-scale energy harvesting. It also enable new industrial robotic applications, including an autonomous solar-powered robotic observatory designed to carry out long term marine monitoring [107], the Mars Exploration Rover developed for space exploration [108] and a remotely operated solar-powered metal detector robot for landmine detection [109]. We refer the reader to prior reviews of fundamental solar photovoltaic technologies [48] [110] [111] [112].

In recent years, research and development has focused on the development of organic thin-film photovoltaic cells that are cost effective and require less energy to manufacture than conventional silicon semiconductor photovoltaic cells. Within the last eight years, the initial investment cost of organic thin film solar cell has fallen below silicon-photovoltaics ($2.50/W vs. $3.20/W) [113]. The lower cost of thin-film solar cells not only benefited micro-energy harvesting systems, but also suitable for a wide range of new applications due to their low thickness and flexibility, especially in micro-robotic systems as they often require light weight energy sources which can generate high power density for untethered applications. Here we will give an overview of the development in photovoltaic cell materials which can be used in microrobotic systems and applications of photovoltaic technologies in micro-robotics.

2.2.1 Photovoltaic cell materials in microrobotics

Photovoltaic cells are superior to other power harvesting technologies owing to greater efficiency and energy output. Typical efficiency are 30% for monocrystalline cells, with a power density of 100 $\mu W/cm^2$ to 1000 $\mu W/cm^2$ indoors and 100 mW/cm^2 outdoors [105]. However, in reality this efficiency is lower because these cells are incapable of absorbing photons across the full light spectrum [114]. As a result, many researchers have utilised micro/nanotechnologies in an attempt to modify the surface of such thin film cells, thereby making them more active under different UV wavelengths [115] [116] [117] [118]. If a wider range of wavelengths are absorbed, the efficiency and amount of power harvested will increase. This is similar to the trend reported in photocatalysis where efforts have been made to expand the absorption spectrum of catalysts.

Thin film photovoltaic cells made up of thin layers of semiconductors stacked on to a solid substrate. Thin films significantly reduce the quantity of semiconductor material needed for each cell and thus lower the production cost of photovoltaic cells. Gallium arsenide (GaAs), copper, cadmium telluride (CdTe) indium diselenide ($CuInSe_2$) and titanium dioxide (TiO_2) are materials that commonly used for thin film PV cells. The highest reported conversion efficiencies for solar cells without concentrators are 28.8% for GaAs thin film [119], 25% for bulk single crystal Si [120], 21.7% for CIGS (copper indium gallium selenide) thin films [121], 19.3% for perovskite cells [122], 13.4% for amorphous silicon thin film solar cells [123], 11.9% for dye–sensitized cells [124] and 11.1% for organic solar cells [125] (as summarised in figure 2.6a). Due to the high power conversion efficiency and power density of GaAs thin film solar cells, they have been utilized in cutting edge aerial microrobot such as RoboBee X-wing [126]. However, the size of thin film solar cells remains a challenge for untethered insect-sized aerial robots as these devices often require high power density which can only be achieved with larger size solar cells. As such, there is a strong incentive to fabricate extremely lightweight thin film solar cells which can produce high power density. Thin film organic solar cells show strong potential to meet the strict requirements of micro robotic systems. Even though the efficiencies of organic solar cells remain small compared with other thin film materials such as GaAs or GIGS, they have been continuously improving since 1990 [127]. Organic materials have the advantage of being able to absorb light across the entire solar spectrum due to the presence of π-bonded electrons which are able to move along the delocalized π-orbitals arising from sp^2 - hybridization states of carbon atoms. The charge carrier mobility of these materials is small ($\approx 10^{-5}$ to 1 $cm^2/V\text{-}s$) compared to inorganic semiconductors, but their absorption coefficients in the visible region of the electromagnetic spectrum are high: $\sim 10^{-5}\ cm^{-1}$. This makes them good absorbers for thin-film solar cells with thicknesses of 50–100 nm [128] [129]. Most organic semiconductors are p-type with a relatively large optical bandgap (1.5–3 eV), reducing the production costs and the cell mass, because of the very thin layers involved. Due to the small size and high energy absorption in the visible region, organic thin-film cells could become an alternative power source for micro-robots as they can be easily incorporated into the robot body as an onboard energy source. Many works have been carried out over the last two decades to increase the power conversion efficiency of organic thin film photovoltaic cell. As shown in figure 2.6b, organic thin film cells continually show significant increases in power conversion efficiency reaching 10% in 2013 [130] and recently increase to 15.2% [131]. It is clear in figure 2.6b that the power conversion efficiency of organic thin film cells has increased by fivefold in the last two decades. Meanwhile the power conversion efficiency of GaAs thin-film only increased by 6% in the past 2 decades (from 24%-30%) [132][131]. According to the current trend, it is expected that in ten-year time the power conversion efficiency of organic thin film cells will surpass

that of GaAs thin film. As a result, in the near future, organic thin film solar cells will play an important role in micro robotic systems as a light-weight powerful onboard power source.

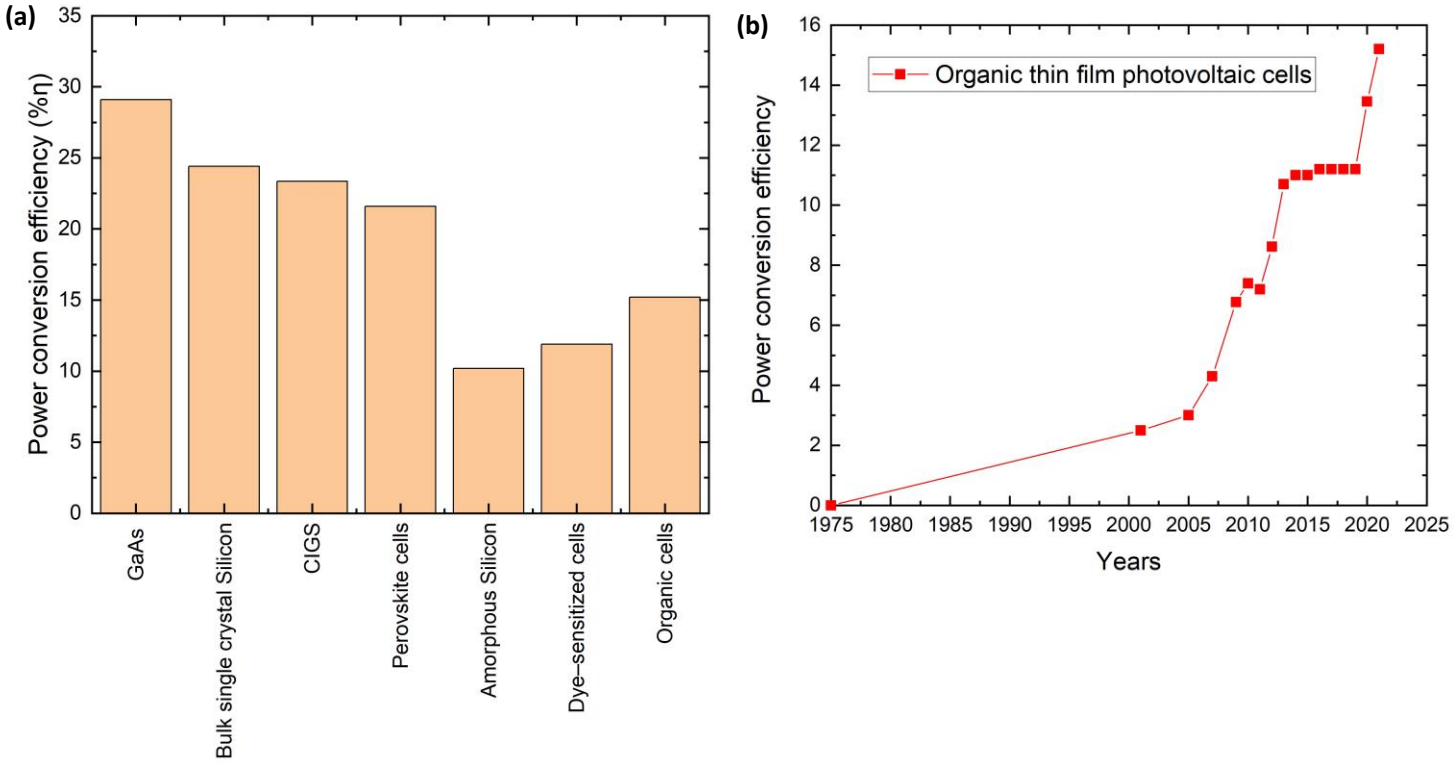

Figure 2.6. Development of thin film solar cells. (a) Power conversion efficiency of thin film solar cells [131]. (b) Power conversion efficiency of organic thin film solar cells development over the last 46 years [130], [131], [133]–[146]

2.2.2 Application of Photovoltaic technologies in micro-robotics

High voltage compact photovoltaic sources can be realised by connecting multiple cells in series. In 2003, Bellew et al. presented a photovoltaic source with groups of up to 200 individual cells, each sized 400 µm by 400 µm, connected in series to obtain open circuit output voltages as high as 88.5 V [147]. The maximum power output of 2.01 mW (62.8 µW/mm) with a solar illumination air mass of 1.71 (the air mass defines the direct optical path length via the Earth's atmosphere, expressed as a ratio relative to the path length vertically upwards) corresponds to an efficiency of 8.3%. This is low compared to efficiency over 20% commonly achieved with larger commercial photovoltaic cells but was sufficient for the intended small scale application. In 2003, Hollar et al. reported what is believed to be the first solar-powered microrobot utilising photovoltaic technology (figure 2.7a) [148]. To create the large voltages needed to drive the robot, 90 solar cells were connected in series to produce an open-circuit voltage above 50 V. With a total effective area of 2 mm^2, the solar cells generated over 100µW of power under solar illumination. The robot used two piezoelectric actuators to move autonomously, and its legs exerted enough force to lift its body above the walking surface. However, the robot has not yet been shown to walk forward and only shows 3 mm of motion shuffling sideways. Subsequently a group of scientists from University of California, Berkeley developed a millimetre-sized, piezoelectric driven, jumping robot capable of 1.2 cm vertical jump (figure 2.7h) [149]. The robot has a mass of 10 mg and is powered by a solar cell similar to that reported in [148]. However, the robot is not robust enough to withstand multiple jumps and the jump direction cannot be controlled. Reid et al. reported a 0.7 mm diameter spherical robot (figure 2.7c) powered by a thin film solar cell capable of rolling using electrostatic actuators [150]. However, this work mainly focused on developing the fabrication process for creating the spherical shells rather than the locomotion, performance or applications of the as-fabricated robot. Edqvist et al. presented a mm-sized autonomous micro robot (figure 2.7e) including communication, locomotion, energy storage and electronics. The total volume of the robot is less than 23 mm^3 and the weight is 65 mg. Energy is provided by a solar cell made of amorphous silicon (a-Si:H) with an efficiency of 23%. The cell is multifunctional since it provides the robot with power, and capabilities for sensing and communication [151]. Maximum power from the cell was 1.28 mW at an illumination of one sun (AM1.5 spectra, 100 mW/cm^2). Similar work has also been reported through the design of photovoltaic cells intended for untethered aqueous micro-robots [152]. Four cells with an estimated efficiency of 12.5% could produce up to 100 µA of photo current to the electronics embedded in each microrobot from an incident source of green light. The microrobot consists of a microcircuit capable of generating small magnetic fields through an embedded conductor network to force the magnetotactic

bacteria that are encapsulated in micro-reservoirs to push in the desired direction. As can be seen from these studies, many attempts have been made to incorporate photovoltaic technologies in microrobots to act as onboard power sources and control systems.

Exploiting recent advances in photovoltaic cells optimised for a single wavelength and high power densities [153], the first wireless lift off of a 190 mg insect-scale aerial robot (RoboFly) was reported in 2018 [154]. The robot is remotely powered using a 976 nm laser and its wings are moved by piezo actuators. In its current form, RoboFly can only take off and land, as other maneuvers place its photovoltaic cell out of alignment with the laser. Once its photovoltaic cell is out of the direct line-of-sight of the laser, the robot runs out of power and lands (figure 2.7g). Recently, a new design has been reported for RoboFly which significantly reduce the weight of the robot to 74 mg. The new version shows steering capability as well as air-water interfacial locomotion (figure 2.7d) [155]. The RoboBee X-wing [126] has demonstrated untethered flight using ultra-lightweight solar cells, powering piezoelectric actuators, via a stripped down circuit board. This robot weights around 90 mg and is powered by the solar cells which are positioned 3 cm above the vehicle to prevent aerodynamic interference with the wings (figure 2.7f). Although this marks an important milestone for flying robots at the insect scale, this technology is in its infancy. One of the limitations of the current system is that the flight lasts less than a second because the robot will quickly use all its energy when it moves out of the irradiation area. Additionally, the light intensity needed for this untethered flight is approximately three suns, which makes it impractical for autonomous outdoor flight (the photovoltaic cells used can provide power densities of about 300 mW/cm^2 at 3 Suns. Recently, Miskin et al [156] showcased a light-driven microscopic walking robot requiring only 10nW to operate (figure 2.7b). Given the low power requirement of the robot, it could be powered by sunlight. The authors argue that a photovoltaic cell on the order of 30 µm and 10% ECE could provide the robot roughly 100 nW, nearly an order of magnitude more power than needed to actuate the robot. Although the functionality of this robot is still limited, this is a step in the right direction. New actuator based on this design could be combined with more complex systems to carry-out more sophisticated tasks ranging from cancer treatments to fighting crop pests.

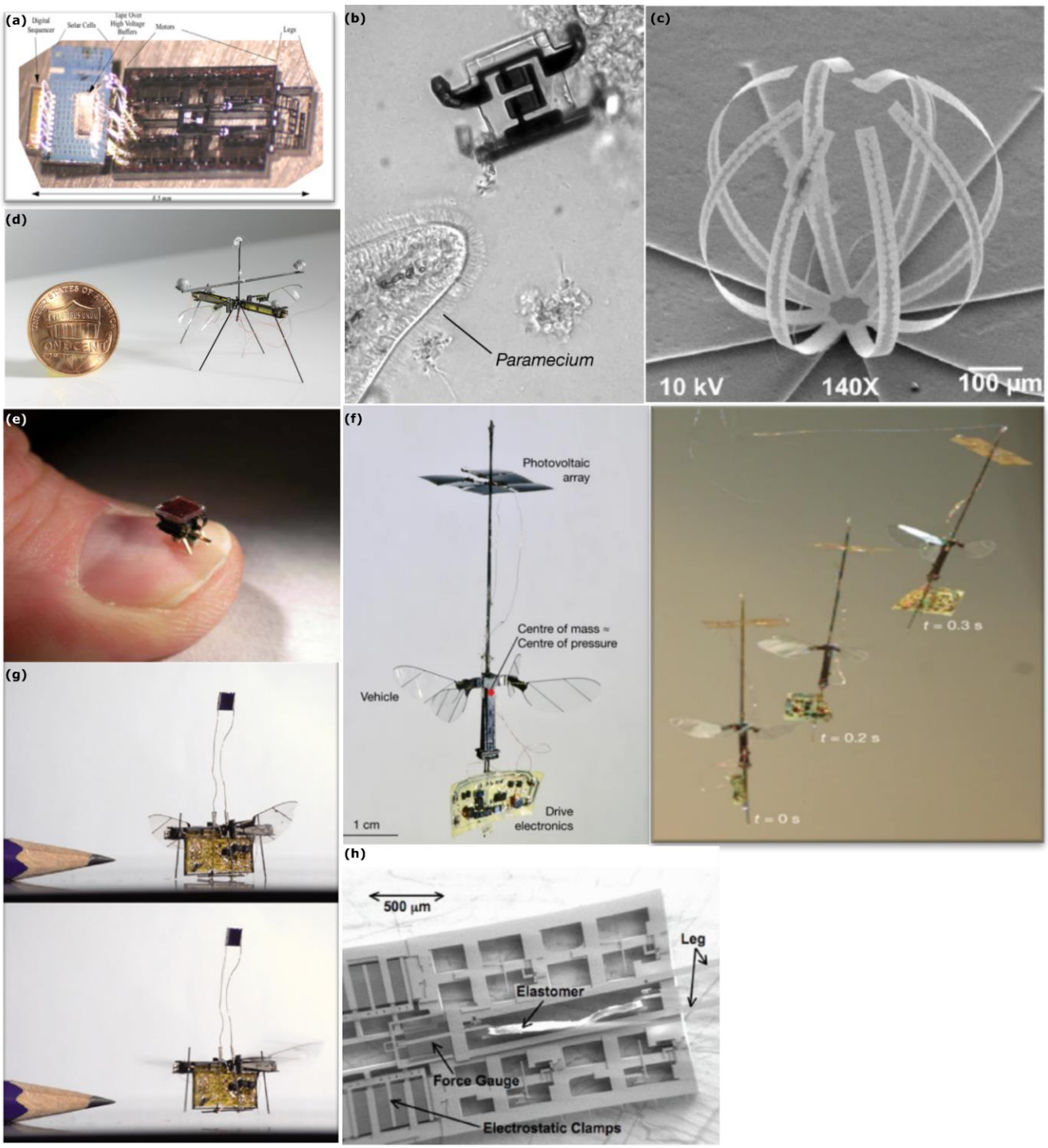

Figure 2.7. Photovoltaic technology utilised in microrobots: a) Three-chip walking robot [148]. b) Light-driven microscopic walking robot [156]. c) Scanning electron micrograph of a spherical mirorobot formed from glass-silicon-glass layers. The robot has diameter between 0.5-0.3 mm [150]. d) RoboFly version 2 [155]. e) I-SWARM autonomous microrobot [151]. f) Insect-sized flapping-wing microscale aerial vehicle [126]. g) RoboFly version 1 [154]. h) An autonomous jumping microrobot [149].

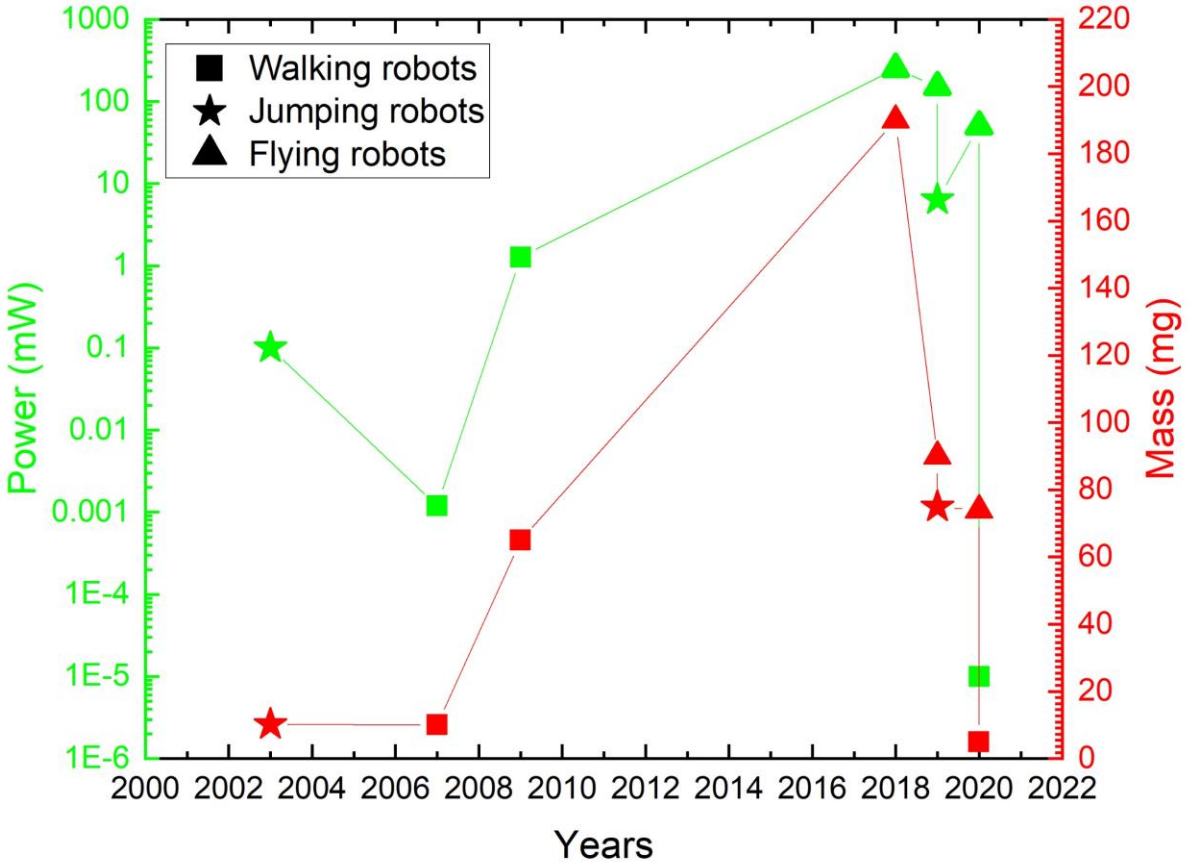

Figure 2.8. Micro-Photovoltaic-cell microrobots progress, showing mass and input power for the robots over the last 20 years.

Figure 2.8 shows a comparison of photovoltaic cell-powered microrobots since the first reported example in 2003. As illustrated, limited work has been done in this area and it is clear from the most recent breakthroughs in insect scale flying robots that most progress has been made through the development of larger robots with more functionalities rather than miniaturised robots. This may be due to a number of factors: it is challenging to scale down the photovoltaic cells to submillimetre scale [157]; the power generated by submillimetre-scale solar cells is not sufficient to drive the microrobots [126]; extra electronics components including voltage converters and capacitors may be needed to boost the voltage provided by the solar cells to power the piezoelectric actuators (as in the case of [126], [148], [149], [154]); and finally, submillimetre solar cells do not capture light properties such as wavelength and polarisation which could be used for control. Nevertheless, the studies reported above have shown significant breakthroughs in the application of photovoltaic technologies in micro-robotic systems and represent a range of high-potential research areas ranging from walking, jumping and flying robots. The challenge now is to produce smaller, more complex robots which require lower power to operate. It is expected that, in the near future, insect-scale photovoltaic robots will be fully autonomous and capable of undertaking complex and

high-value tasks such as swimming for bioremediation, flying for monitoring and jumping for autonomous exploration.

2.3 Photomechanical and photothermal effects

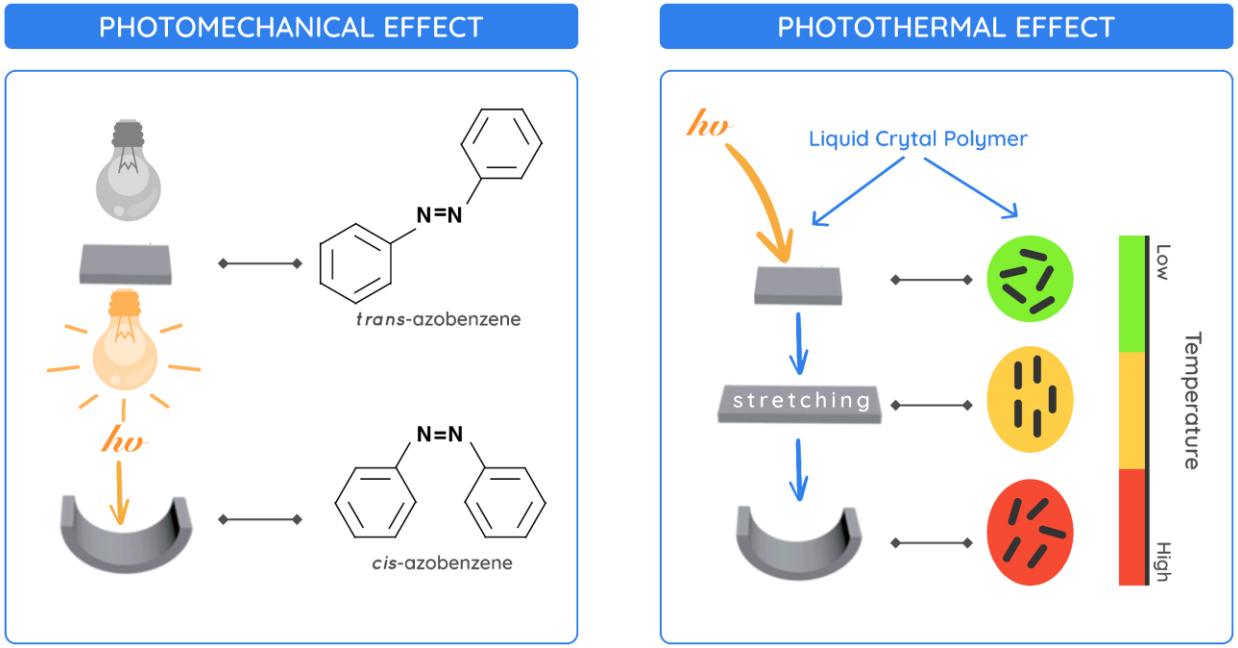

Figure 2.9: Photomechanical and Photothermal Effects. On the left side. The photomechanical effect; this is based on a configurational shape change of part of the molecule (e.g., an azobenzene group) upon light absorption, which disturbs the order of the liquid-crystal network. On the right side. The photothermal effect; this is an intrinsic thermal excitation stage where light is absorbed and a shape change occurs through local heating.

For decades, majority of roboticists mainly focused on rigid systems which enable autonomous operation through sophisticated control with optimal movement accuracy and velocity. Meanwhile, material scientists concentrated on developing polymeric actuators that are miniature, flexible, adaptive, and stimuli-responsive. The fusion of robotics and material science has given rise to soft microrobots which combine key concepts from microrobotics and stimuli-responsive materials research. Soft microrobots offer numerous advantages over their rigid counterparts, exhibiting remote control and power delivery, adaptive manipulation and safe human interaction, with device architecture and locomotion often inspired by nature. Soft photonic microbots, in contrast to magnetic microbots [27]–[29] photocatalytic robots and photovoltaic robots, are driven directly from light. Whilst magnetic microrobots can only operate in constrained environments enclosed by bulky electromagnets, photonic

soft microrobots can be driven by small discrete lasers which can be a large distance from the robot. In the previous sections, we explored photocatalysis which uses light to drive a chemical reaction to evolve the gas that propels the robot, and photovoltaic systems which convert light energy first into electrical energy and then into mechanical movements. In this section, we review a different propulsion mechanism, based on the movement or deformation of body parts, for optically driven microrobotic systems. This is achieved by utilising photo-responsive mechanical materials, typically liquid-crystalline elastomers—crosslinked polymer networks that can deform upon illumination by light. There are two main mechanisms responsible for the deformation in these polymer networks. The first mechanism is based on a configurational shape change of part of the molecule (e.g., an azobenzene group) upon light absorption, which disturbs the order of the liquid-crystal network. We call this the photomechanical effect [158]. The second makes use of an intrinsic thermal excitation stage where light is absorbed and a shape change occurs through local heating. This is defined as the photothermal effect [159].

These optical microrobots can achieve various solid surface, underwater, and air–water interface locomotion modes, such as crawling, rolling, swimming, and jumping, to navigate in diverse environments to achieve their desired tasks. The sections below will investigate the materials and potential applications of optical microrobots made from photo-responsive mechanical materials. Here, we focus on recent advances in soft photo-reponsive mechanical materials and it applications in microrobotics, as the underlying physics and other area of applications have been comprehensively discussed in literature [160] [161].

2.3.1 Photo-reponsive mechanical materials as a source of actuation via photomechanical and photothermal effects.

The fundamental actuation mechanism of photo-responsive mechanical materials governs by two processes namely photomechanical and photothermal effects. The photomechanical effect is the intrinsic shape change of materials under light irradiation. Upon exposing to light, the materials convert photo energy to mechanical movements due to cis-trans isomerism (see figure 2.9 left). This effect was first reported by Alexander Graham Bell in 1880 [162] in experiments which produced the world's first wireless telephone communication. A hundred years after Bell's work, Uchino and Cross reported that a photomechanical material could be used as legs in the fabrication of a small-scale light-driven "walker" [163]. Since then, many attempts have been made to address key challenges in realizing light-driven robots. Liquid-crystal-polymers (LCPs) and hydrogels have received much attention because they can not only undergo large, reversible shape changes upon light illumination but can also respond to changing light intensity [164] [165], wavelength [166] [167], or polarisation [168] [169].

In contrast, the photothermal effect induces volume changes due to thermal expansion and/or small molecular absorption in materials as a result of light-to-heat conversion. To be more specific, these materials function as black objects that can harvest and transform energy from electromagnetic waves into heat. The increased temperature causes deformation due to thermal expansion and/or desorption of small molecules like water [161] [165] (see figure 2.9 right). These dynamics can be found in biological species, including E.coli, blue-green algae and mycoplasma [170] [171] where locomotion is governed by the photothermal shape transformation which interact with surrounding environment. While these species have continuously evolved and optimised through millions of years of evolution, the optimisation of LCPs robots have been limited to laboratory experiments and theoretical study. As such, nature is a valuable source of inspiration for the design and optimisation of photo-responsive mechanical material microrobots.

Table 2.2 shows a collection of soft materials and their actuation stimuli. The 'x' marker shows whether the material is responsive to the specific stimuli and associated works reported in literature. The O marker presents opportunities in which the materials could be stimulated and controlled by light and U marker shows ongoing work to prove that the material is responsive to light. As seen from table 2.2, under the light column, there is a wide range of light-responsive mechanical materials with variable stiffness ranging from carbon to hydrogels. This allows micro-roboticists to pick and choose appropriate materials for specific applications as well as opens up many research routes. For instance, one interesting research route could be to develop soft, environmentally friendly, light-driven microrobots utilising the large shape change of LCEs and biodegradability of hydrogels. This is particularly beneficial in vivo, vitro and environmental applications as the robots can become an integral part of the environments and operate in harmony with other micro-organisms. As soft polymeric materials with smart behaviour have been comprehensively covered in review [172], here, we briefly discussed the two most popular classes of soft photo-responsive materials used in light-controlled microrobots namely hydrogels and liquid crystalline polymers. The bulk of the remaining sections will focus on discussing the development of photo microrobots in this area throughout literature.

Soft smart polymeric materials open up new pathways for the development of photo-microrobots [173] [174] [175]. The intrinsic softness of polymers is highly dependent on the formulation. Young modulus range from tens of kPa for hydrogels [164] to MPa for liquid crystalline networks (LCNs) [176]. Hydrogels are hydrophilic networks able to absorb large amount of water. This is particularly beneficial for microrobots that operate in liquid environments.

Another class of photo-responsive mechanical materials for photo-microrobotics are liquid crystalline elastomers (LCEs) and LCNs [177]–[182]. These polymers are fabricated by grafting liquid crystal (LC) moieties (mesogens) inside a polymeric network. Upon light irradiation, the molecular order is changed resulted in shape deformation. For example, a contraction along the liquid crystalline alignment direction and an expansion in the perpendicular direction are observed [183], [184]. Notable features of this is the deformation is reversible once the stimulus is absented, and the ability to code different deformations modifying the LC alignment [185], [186]. In contrast to hydrogels, LCNs can operate in environments outside water, as deformation can happen in other solutions, and LC alignment engineering can produce bending, torsional, or rotational motion [187].

Table 2.2. A collection of soft materials and their associated stimuli.

	Electric field	Magnetic field	Pressure differential	Heat (electrode-photothermal, etc.)	Light	Chemical (solvent, water, pH, ect.)	References
Carbon	X		X	X	O		
·Carbon nanotube (CNT) sheets, yarn	X		X	X	O		[188] [189] [190]
·CNT aerogel	X						[191]
Fluids	X	X	X	X	X	X	
·Electrorheological fluids (ERFs)	X						[192]
·Magnetorhoelogical fluids (MRFs)		X					[193]
·Ferrofluids		X					[194] [195] [196]
·Dielectric fluids (electroconjugate fluids (ECFs))	X						[197] [198] [199] [200] [201]
·Liquid metals	X	X		X	X	X	[202] [203] [204]
·Liquid marbles	X	X			X	X	[205] [206] [207]
Paper (cellulose)	X	X		X	O		[208] [209] [210]
Polymers and gels	X	X	X	X	X	X	
·Conductive polymers	X						[211] [212] [213] [214] [215]

·Liquid-crystal polymers (LCPs), polymer networks (LCNs), elastomers (LCEs)	X			X	X	X	[177] [178] [179] [180] [181] [182]
·Ionic-polymer–metal composites (IPMCs)	X						[216] [217] [218] [219]
·Dielectric elastomer actuators (DEAs)	X				U		[220] [221] [222] [223]
·Shape-memory polymers				X	X	X	[224] [225] [226] [227]
·Hygromorphic polymers				X	O	X	[228] [229] [230]
·Ferrogels and ferro-elastomers		X					[231] [232] [233]
·Hydrogels	X	X	X	X	X	X	[234] [230] [235]

2.3.2 Applications of Photomechanical and Photothermal effects in microrobots.

Light-powered soft actuation is attractive because it can be controlled remotely and accurately, rapidly modulated, and easily exploited at the nano/microscale [236] [237]. Photochromic molecules play an important role in artificial photoresponsive devices, harvesting photo energy and converting it into useful mechanical energy via strain [227]. This mimics light-driven mechanisms found in nature. For instance, the light-induced isomerisation of retinal molecules triggers a cascade of chemical events, leading to neural signals and the perception of light [238]. These molecules are essential in microscale soft and compliant actuators made of polymers, gels, fluids, and photomechanical materials. In this section, notable progress in microrobotics is highlighted based on the applications of photothermal and photomechanical effects of photoactive materials in micro/nano scale devices such as mechanical oscillators, walkers, and swimmers which could one day lead to aerial microrobots.

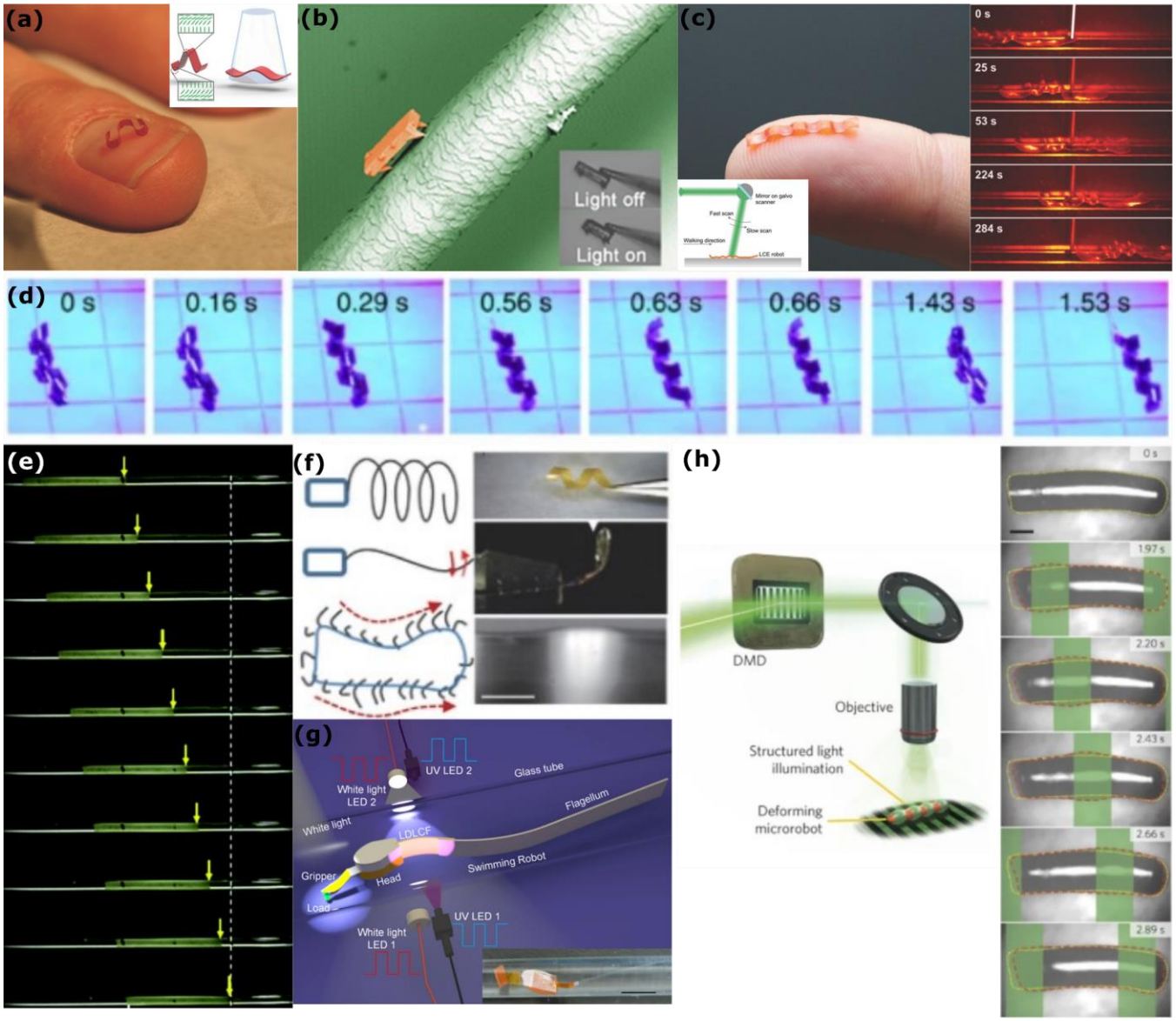

Figure 2.10: Photomicro robots. a) An inch worm robot sit on a human finger. The inset illustrates the operational stages: light on, the robot body heats up and extends; light off, the body contracts and bends. [239] b) A micro walker sits on human hair. The inset shows the actuation stages: light on, the robot body shrinks; light off, the robot body extends. [181] c) Caterpillar microrobot. Left inset: laser light causes deformation of the robot body; right inset: showing the robot squeezes through a 0.9 mm slit.[240] d) A spiral LCPs microrobot rolls under continuous light irradiation. [241] e) An LCPs microrobot crawls inside a capillary. [242] f) Various locomotion strategies for fluidic propulsion: corkscrew,[243] bending, [244] and oscillation. [245] g) A concept diagram of a miniature swimmer. [246] h) A liquid-crystal-polymer robot powered by a dynamic light system (left), the robot swims in a liquid by deforming its body to form a traveling-wave (right). [245].

In early 2018, an inching microrobot made from a liquid crystal elastomer film (Figure 2.10a) was demonstrated [239]. Upon visible-light excitation the millimetre sized caterpillar robot can be observed crawling on different surfaces such as a blazed grating and a paper. However, due to the lack of friction bias and time-symmetric (reciprocal) motion, the walking direction the walkers is dependent on substrate characteristics. The length of the

robot was 8 mm and the speed is 0.25 mm/s (1/32 body length). It is important to note that LCP robots can be made in micrometre scale using laser lithography. Figure 2.10b shows a 60 µm length micro walker sits on a human hair [181]. The locomotion of this robot was very sensitive to friction due to its small mass and the intrinsic (e.g. Van der Waal's) adhesion. Therefore, a straight walking direction is difficult to maintain. The average walking velocity in this case is measured to be around 37 µm/s (half a body length). Directional movement could also be obtained using alternative strategies [247] [248]. Figure 2.10c shows an inch-long caterpillar robot which can move forward by deforming its body into a traveling-wave. The inching locomotion is triggered by shining a laser beam along the robot body. This induces a local bending of the polymer and enables the robot to crawl forward in the scanning direction. This robot also capable of squeezing through a narrow slit (inset of figure 2.10c) [240]. The robot is 14.8 mm long and has a speed of 0.24 mm/s. Recently, a LCP spiral microrobot rolling over large distance under continuous light illumination was demonstrated (Figure 2.10d) [241]. A similar rolling locomotion was also showed in a bilayer LCPs wheel and spring-like motor [249]. Figure 2.10 shows a class of light-driven micro-robots utilising photomechanical and photothermal effects reported in literature to date. These robots are capable of various locomotion ranging from crawling to swimming.

Figure 2.11a reveals that most of the recent soft photomicro devices reported in literature are in the range of a few millimetre in size and require less than 500 mW/cm² of input power. This is because LCP composites have large and rapid response upon irradiation and can be easily fabricated into arbitrary small shapes. This enables them to perform complex tasks such as climbing a slope, squeezing through a slit, and pushing a micro-object. In addition, much research has focused on enabling these micro devices to harvest energy directly from the sun and to operate autonomously. The solar light intensity is between 100-150 mW/cm² and as such, efforts have been made to bring down the energy requirements of light microrobots to below one hundred milliwatts per square centimetre. The blue tetrahedral marker in Figure 2.11a shows the work of Tang et al. [250]. This is the first attempt to construct a light-driven electromechanical generator using the direct photomechanically coupling of azobenzene polymers. The device has fast and strong photoinduced bending and unbending. The bilayer film displayed a high unbending velocity and a fast recovering rate when a longer exposure light was switched off. However, the film's bending motion was hindered by the magnet used and the azobenzene material has very low electricity conversion efficiency (1.4×10^{-3} %), far lower than the conversion efficiencies of conjugated polymer photovoltaic cells. Huang et al. [246] (yellow marker in Figure 2.11a) reported a soft swimming micro robot with a gripper powered by light, which does not carry any electronic devices and batteries. The robot can carry out complex movements such as swimming, grabbing, carrying and transportation. However, the swimming velocity is low (142µm ≈ 1/185 body length/s) and the swim speed reduces as the robot swim away from the centre of

light irradiation. It is interesting to note that both of these robots utilise direct photomechanical effect and not heat-induced motion (photothermal effect).

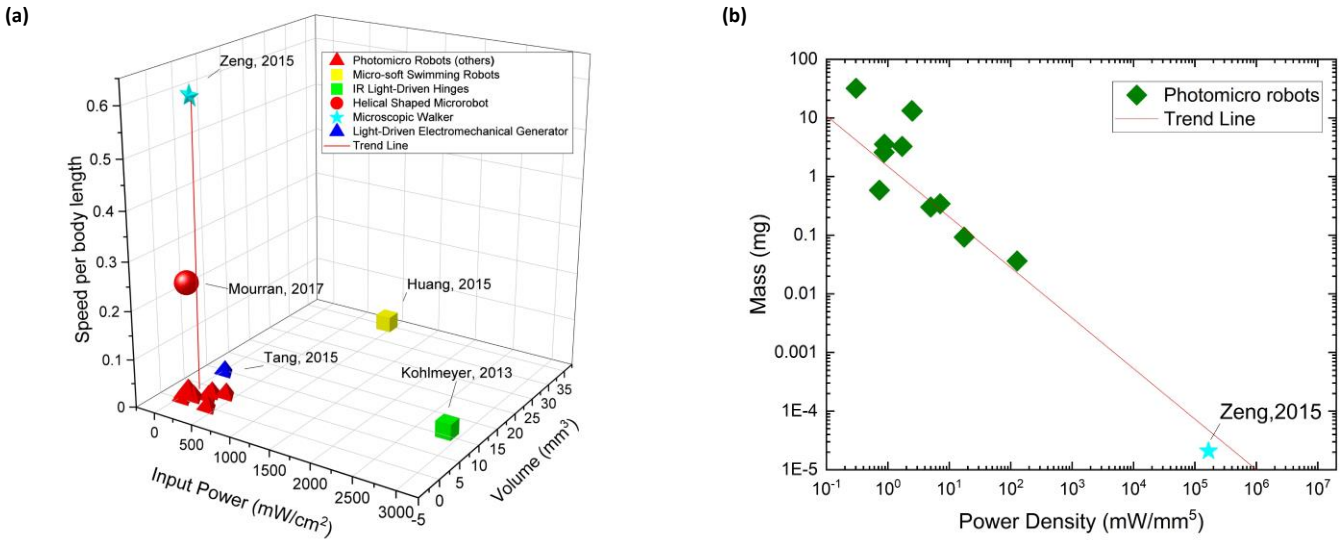

Figure 2.11: Power requirements of photomicro robots: a) Input power of photomicro robots versus their overall size and speed. b) Log scale plot of Power Density of photomicro robots versus their Mass.

Although the majority of photomobile devices operate within UV to visible light spectrum, limited progress has been made to extend the effective wavelength through the visible spectrum towards the infrared. For instance, Kohlmeyer and Chen (green cube in Figure 2.11a) [251] introduced IR light-driven hinges composed of an active LCE composite layer with IR-active fillers and a passive silicone layer. The hinges have fast, reversible bending with a large strain and exhibit IR wavelength selectivity. One drawback of this work is that the temperature of the bilayer film increases very quickly as the IR light intensity increases (T=136 °C at light intensity of 1800 mW/cm^2) which make it unsuitable for certain applications (i.e. biomedical and environmental). Figure 2.11a, shows the potential to make future microrobots devices from photoactive materials which require less input power but have high velocity. The most notable works reported to date are a microscopic walker developed by Zeng et al. (cyan star in Figure 2.11a and 2.11b) [181] and a helical shaped microrobot by Mourran et al. (red sphere) [252] which are powered by light sources of 300 and 170 mW/cm^2 respectively and have speed of 0.62 and 0.25 body lengths/s respectively. The trend line (fitLinear function) in Figure 2.11b suggests that efforts have been made to reduce the size of the robots and its power requirements, and that there we may be able to predict power density for a given robot mass. Although Zeng et al and Mourran et al claim that they can reduce the size of their robots to micrometre scale , their devices are still required very large power density for a given robot volume to operate

(0.167×10^6 mW/mm^5 and 4.25×10^6 mW/mm^5 respectively) [252] [181]. The power density is calculated by diving the input power by the volume of the robots. As a result, more work is needed in order to develop fast and highly efficient light driven microrobots from photoactive materials.

2.4 Light microrobots of the future

Traditional robots are often made up of actuators and sensors operating in synchrony. Feedbacks from sensors (e.g., location, force, and temperature) are sent to actuators to carry out specific actions. As such, to create autonomous, intelligent light microrobots one must integrate all these functions into a miniature system in the order of tens to hundreds of micrometres in size. Recent works on smart LCP actuators can be considered as proof of this concept. Figure 2.12a demonstrates a millimetre-sized flytrap device which can identify different objects based on optical feedback and perform gripping action only when it encounters the right objects [253]. This gripping operation is initiated by reflected or scattered light gathered from the surroundings, realizing simple autonomous recognition of different micro-objects. Figure 2.12b shows the gripper grasps an object which has sufficient reflectance, while it remains open for objects that do not produce sufficient optical feedback. This behaviour resembles the snapping mechanism of the carnivorous Venus flytrap, which allows it to distinguish between living creatures (insects) and non-living environmental elements (dust particles, rain) through different mechanical stimuli, and to snap only when it senses a suitable prey. The second example of self-regulation in photoactivated soft systems is the artificial iris of Zeng et al. as shown in Figure 2.12c. The LCE iris autonomously opens and closes in response to the incident light intensity [24]. The light transmission reduces from 70% (open state) to 30% when the iris closes (Figure 2.12d). This smart device mimics the behaviour of the human iris, which reacts to changes in the environment (light intensity). Wiersma et al developed a microhand with colour recognition capability when different coloured materials gets near the finger [254]. This experiment showed LCNs actuators perform an intelligent behaviour distinguishing between different colours and bends only when specific particles are in their proximity (figure 2.12e). The most notable breakthrough recently in smart light-driven microrobots is the light-controlled rockets developed by Li et al [25]. The 3D printed micro-rockets can achieve a velocity of 2.8mm/s (62 body length/s) and imaged/tracked using photoacoustic tomography in two biological solutions, bovine blood, and an ex vivo mouse blood vessel covered by a mouse ear (figure 2.12f). The examples above have proven that the close interaction of light fields and material response may offer routes to realise microrobotic systems with smart features, such as self-recognition, stabilization, and automatic manipulation.

It is also beneficial to consider alternative light power sources instead of the sun to power and control photomicro robots. Laser power beaming is particularly attractive due to its capability to provide kilowatt power through long

distances. Laser power beaming (LPB) uses electricity from a common source, such as the electrical grid or a portable generator, and converts it into light via a laser. This laser beam is then shaped with a set of optics, and directed via a gimbaled mirror (also known as the beam director) to a remote photovoltaic cell on the robot. This photovoltaic cell, tuned to maximise the absorption at the laser's wavelength, will then convert the laser energy to electricity to be used to power photomicro robots. It has been reported that current laser sources can deliver power in excess of 600 mW/cm^2 (that is almost 4.5 times the amount of power the sun can provide at 136 mW/cm^2) and the range of this laser could reach up to 10km in atmosphere [255]. This could easily solve the high energy requirements of light driven microscale aerial robots. LPB also enables precise control as operators can target a single robot or group of robots specifically to carry out different tasks. This could potentially give rise to complex behaviours and ultimately, swarm intelligence.

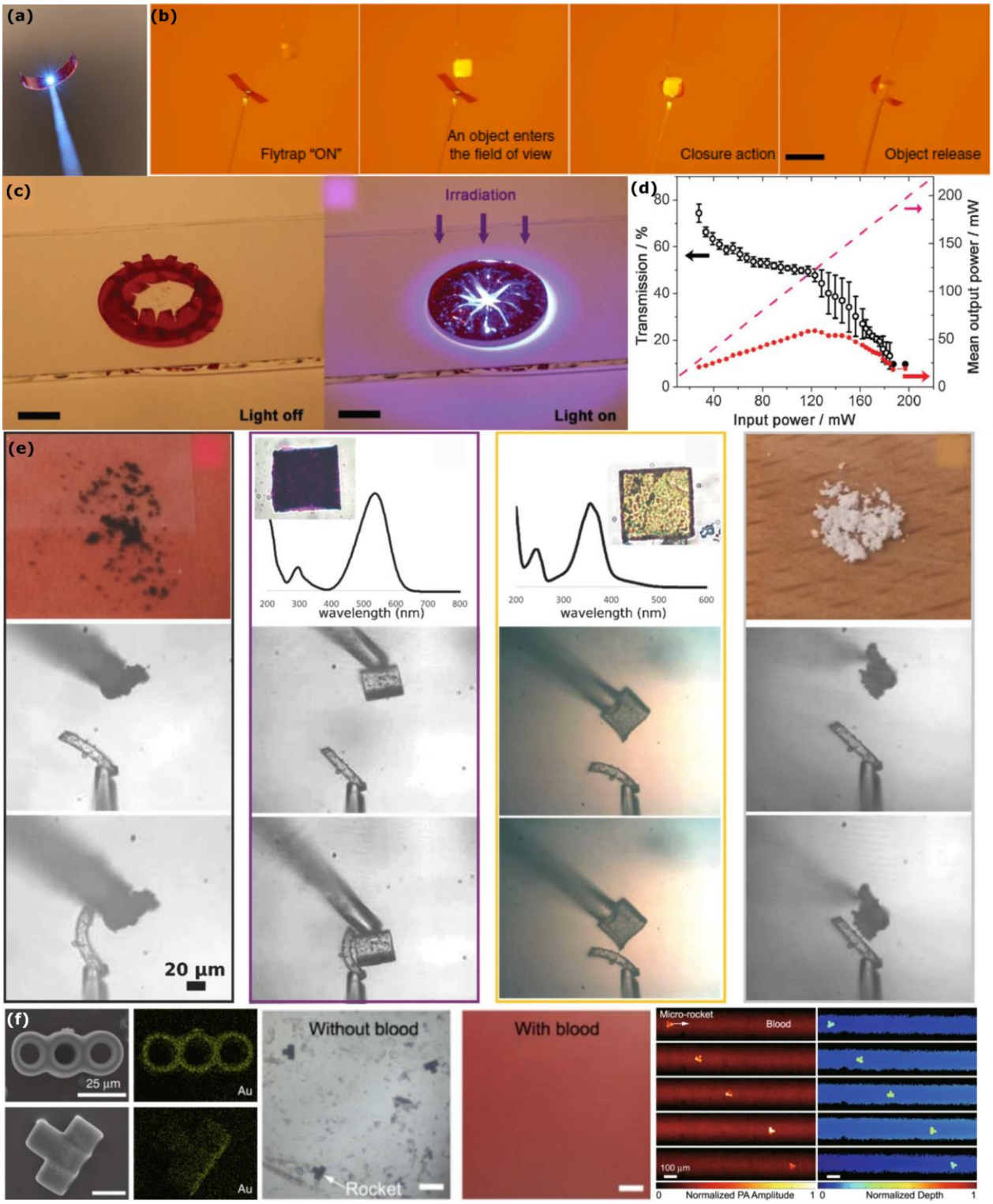

Figure 2.12: Autonomous microrobots. a) A light-driven self-regulating flytrap [253]. b) The flytrap capturing an object [253]. c) An artificial iris opens and closes depending on light intensity [24]. d) Input power of the iris device versus measured light transmission (black dots) and transmitted power (red dots). The dashed line indicates 100% transmission [24]. e) Smart LCN microhand: the top panels show different materials (from left to right, carbon particles, purple and yellow polymeric micro cubes and titanium dioxide particles). The middle panels show an LCN finger does not exhibit any shape change when

irradiated by green light. The bottom panels show LCN response to different particles. In the first two cases (black and purple), the LCN actuator recognizes the objects and bends toward them [254]. f) Micro-rockets (from left to right): left most panels, SEM image (left) and energy dispersive X-ray spectrum (right), middle 2 panels, optical microscopy of the microrockets without and with bovine blood, right most panels, photoacoustic tracking of a microrocket in a microchannel filled with bovine blood: intensity distribution (left) and depth distribution (right) [25].

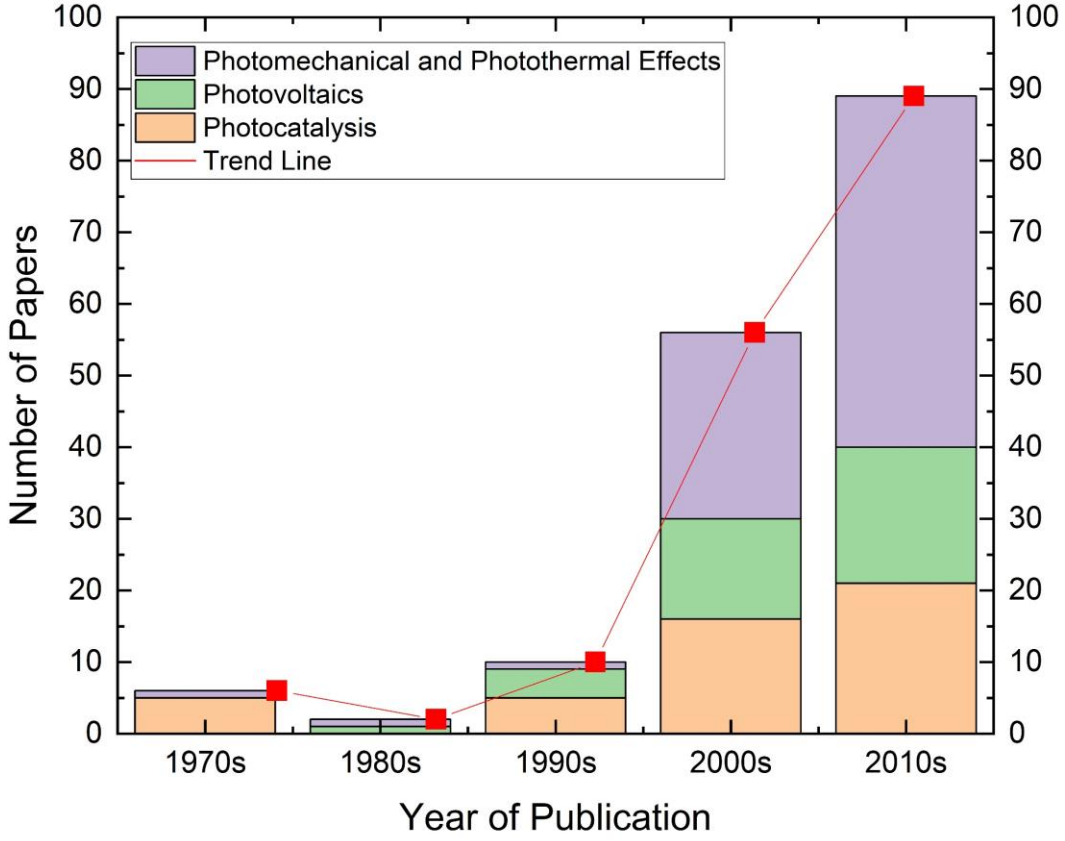

Figure 2.13: Numbers of papers reviewed in this article across three photo-actuation methodologies.

Figure 2.13 compares the number of papers reviewed in this area which represent the major research conducted across the three photo-actuation techniques of photocatalysis (focusing on titanium dioxide photocatalyst), photovoltaics and photomechanical and photothermal effects from the 1970s to the present day. This highlights the trend of rapidly increasing research in photoresponsive microrobots, especially over the last decade. It shows that research in all three photo-actuation areas is very active, with growth especially in photoactive materials. This is attributed to the advancement in micro/nano fabrication techniques, allowing the production of more efficient photocatalysts, photovoltaics cells and photoactive materials. This opens new research routes in which the goal is to produce fully autonomous light-driven micro-robots. Rather than partitioning into the three photo-

actuation technologies, we believe that in order to create the intelligent light-driven robots of the future we should utilise the advantages of all three technologies.

The convergence of all three photoactive technologies is expressed in terms of a road map for intelligent light-driven micro robots, as shown in Figure 2.14. The main capabilities and potential are shown, which will guide future research. Photocatalysis offers great potential for miniaturisation (Nano/micro scale), fast movement and energy storage; photovoltaics offers complex functionalities (e.g. walking, jumping, swimming and flying), low input power requirements (mW) and high energy conversion rate; and photoactive materials offer adaptive motion, human-friendly interactions and intelligent features, such as self-recognition, stabilization, and automatic manipulation through the direct interaction of light fields and material responses. One example of such a future device is an intelligent microrobot capable of harvesting light energy using photovoltaic cells and converting that energy into chemical energy for storage using photocatalysts. The chemical energy then will be used to produce movement (walking, swimming, flying etc.) when photoactive components of the robot are triggered by light with different wavelengths. In addition, by embedding smart photoactive materials into the microrobots, we can create a fully autonomous robot capable of adapting to changing environments. This light driven robot could harvest and store light energy during the day for use the energy at night, seeking light sources for recharging and responding intelligently to different light signals to undertake specific tasks.

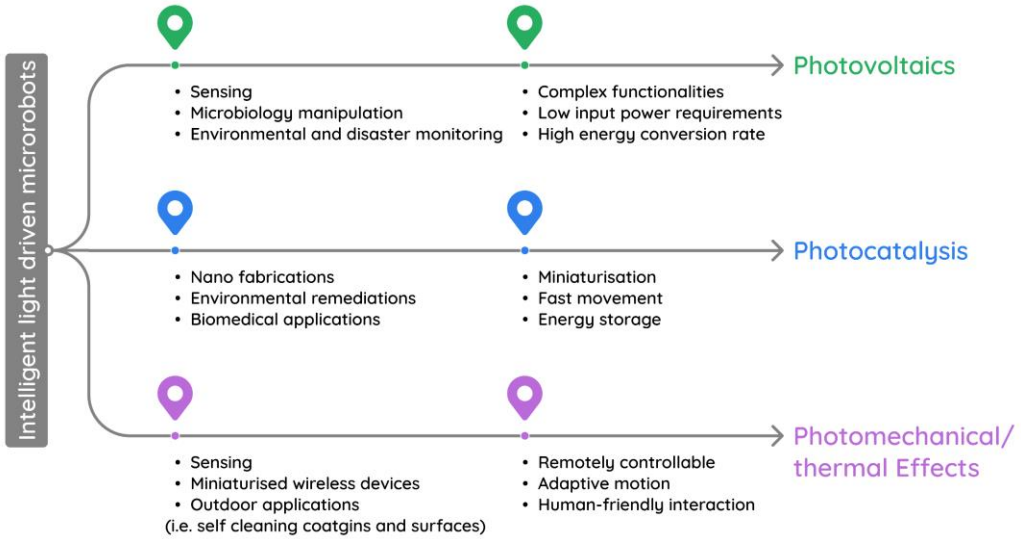

Figure 2.14: A road map showing the unique features and area of applications of the three main photoactuation methods used in the development of light driven microrobots and the goal they are heading towards to create truly intelligent light driven microrobots. Green maker represents the advantages, red marker represents the applications.

2.5 Discussion

This chapter reviewed the three main photo-actuation techniques that have been utilised in the making of light driven microrobots. It identified the unique features offered by each actuation strategy and its drawbacks. It highlighted significant breakthroughs across all three photo-actuation methodologies in the past two decades and proposed that smart light-driven microrobots could be achieved by combining the unique features offered by these methodologies. If this is achieved, one can create autonomous, self-sufficient microrobots which can interact safely with myriad environments and exhibit swarm intelligence in order to execute complex tasks. Through our analysis of leading research and extrapolation of technology trends, we expect significant breakthroughs in the field of light micro-robotics in the future. In this thesis, we focus on photovoltaics acting as a main method to harvest light energy due to its high ECE compared to other photo actuation techniques. Photocatalysis and photomechanical/photothermal effects will be explored in the future as ways to add extra functionalities to the robots and facilitate intelligent behaviours.

As a result, in the next three chapters, a light driven robot was developed with an aim to realise some of the aforementioned features. The robot is specifically geared towards environmental applications as it is considered to be the most practical medium to exploit and showcase these features. The work progresses through major design considerations and lays the foundations to produce a proof of concept prototype towards the creation of a new generation of autonomous photorobots. Chapter three provides the basis of how light energy can be harnessed to produce power intensive actuations, chapter four showcases the design and mechatronics of the robot. Finally, chapter five presents an untethered version of the robot and assesses its behaviour within the wider aqueous environment.

Chapter 3

3 Light Energy to Water Jet propulsion

The previous chapter provided a comprehensive review of different photoactuation strategies for photomicrorobots and discussed the future of the field. The ability to convert light energy to different energy forms, either chemical or electrical energy for storage and actuation using different photoactuation strategies, is an important feature of future light driven robots (see figure 2.14). Across all possible area of applications for light driven robots, environmental monitoring/exploration is the most attractive as it is a more mature area and has many commercial applications. As a result, we develop a novel light driven robot capable of converting photon energy to electrical energy using a photovoltaic cell. The produced electrical energy is converted into chemical energy using an electrolyser with water as fuel. This uses similar physics to water splitting in photocatalysis except the input energy is electrical energy instead of photon energy. This is a more efficient and quicker method to convert input photon energy to chemical energy for storage compared to the direct use of photocatalysis (<1% for titanium dioxide as catalyst - see section 2.1 for more details). In other words, the ECE of a typical photovoltaic cell is 20% and the ECE of the electrolyser is 20%, we would have the overall ECE of 4% which is more than 4 times higher than direct photocatalysis. The generated chemical energy will then be used to generate mechanical energy through an exothermic reaction. This type of reaction typically have ECE of about 20% [256] which gives the overall ECE of the robot of about 0.8%. However, despite the low aggregate ECE, this reaction produces high energy density which is desirable in energy intensive applications such as flying, swimming and continuous jumpgliding. This chapter will lay out the motivation and the basis behind the development of a novel light driven, jet-propelled robot which can swim under water and perform leaps from water when it gets near the surface.

A few animal species [257] [258] [259] [260] [261] demonstrate the remarkable capability of hybrid aerial-aquatic locomotion to search for food sources, chase prey, and evade predators. Hybrid aerial-aquatic robots capable of traversing complex multiphase environments will have a wide range of applications, such as environmental exploration and search and rescue missions [262].

Figure 3.1: Aquatic micro arial vehicle, jumpgliding (aquaMAV). (i) Plunge diving AquaMAV concept sketch [263]. (ii) Arial-aquatic flapping robot [264]. (iii) Aquatic jump-gliding with water-reactive fuel [265]. (iv) An AquaMAV shooting out of water [266]. (v) The EPFL jumpglider (Swiss Federal Institute of Technology (- EPFL), 16.5 g jump-gliding robot that can jump, perform steered gliding flight and move on ground with small jumps. [267]. (vi) CAD rendering of the prototype jumpgliding robot [268]. (vii) Flying Fish Autonomous Seaplane [269].

A few large, 2 to 3 metre wingspan unmanned arial vehicles are employed in real world missions [263], [269] (figure 3.1 (i) and (vii)). Furthermore, preliminary works have demonstrated the capability of an aerial–aquatic flapping propulsor propelled by adaptable wings [264] (figure 3.1 (ii)). Other study has showed the efficacy of jump-gliding in terrestrial robots [267], [268] (figure 3.1 (v) and (vi)). One notable work on fixed-wing aerial-aquatic robot is a water jet-propelled aquatic jumpglider which uses compressed CO_2 gas to produce sufficient thrust to escape from water [266] (figure 3.2 (iv)). However, the size of this robot is still relatively big (552mm in length) and the operating time is short because the compressed gas module of the robot will exhaust which render it unable to carry out continuous operations. As such, a consecutive aquatic jumpglider has been developed to address these drawbacks [265] (figure 3.2 (iii)). The robot uses reactive fuel (calcium carbide powder) to produce C_2H_2 gas and then ignite this combustible gas in a no valve combustion chamber to generate powerful, repeatable combustion for consecutive jump-gliding. The consecutive aquatic jumpglider has demonstrated a longer operating time (22 flights) and is about half the size of its predecessor. However, it still relies on battery power and reactive fuel to generate C_2H_2 gas for combustion. In addition, the exothermic reaction generates waste (i.e. calcium hydroxide and CO_2) which might not be desirable in environmental applications. As such, there is a strong incentive to develop self-sufficient and 'green' robots which can safely operate in natural environments. In this chapter, we will discuss how light energy can be harvested from the environment as an unlimited power source and the physical principles behind water jet propulsion using zero waste oxyhydrogen combustion.

3.1 Light as an energy source

In order for the robot to be self-sufficient and autonomous, it must be able to obtain the energy from the environment to operate. As discussed in chapter 2, solar cells are excellent at converting light energy to electrical energy with ECE as high as 20%. They have the best ECE across all photoactuation strategies reviewed and therefore are the best candidate for light energy harvesting. However, chapter 2 also identified some drawbacks which limit the applications of photovoltaic cells in small-scale robots. For instance, the energy converted by solar cells cannot be stored without additional components which makes it difficult for robots to operate in places where light cannot reach. Size of solar cells is also a problem as smaller solar cells cannot provide enough power to run power hungry locomotion such as swimming or flying. Various strategies have been used to address these problems such as using batteries to store the converted energy or shining a high intensity light beam to solar cells, coupled with electronics to boost the voltage needed for locomotion. These strategies do not offer a complete solution to create autonomous/self-sufficient light driven robots. As such, a solution is urgently needed to realise the potential of light driven robot of the future.

3.1.1 Light to Electrical to chemical energy

This section proposes a multi-phase energy conversion system which first converts light energy into electrical energy for tempory storage. This electrical energy is then converted to chemical energy which in turn is used to produce strong mechanical force though a fast chemical reaction to deliver power intensive locomotion such as swimming and jump-gliding (see figure 3.2). The system uses a flexible solar cell (Powerfilm 0.066W Mini Flexible Solar Panel) which is wrapped around the body of the robot to harvest solar energy. Solar energy is then converted into electrical energy through an ultra-low power solar cell charger (BQ25504, Texas Instruments) to charge a lithium ion battery (3.7V, 270mAh). Subsequently, the electrical energy is turned into chemical energy using an electrolytic module to produce oxyhydrogen gas mixture. Finally, an exothermic reaction is triggered to turn the combustible gas mixture to generate thrust which can be used for swimming or jump-gliding. The entire process is controlled through a microcontroller (ATTiny85). The battery voltage is constantly monitored during charging until the battery reaches sufficient charge, the microcontroller then will trigger the electrolyser to generate oxyhydrogen gas. When the desired amount of gas has been reached, a signal is sent to a spark module to create an electric arc which will create combustion for actuation. After the explosion, the system reverts to charging mode and the cycle repeats. A summary of each stage is shown below.

1. Light energy is harvested by solar cell and converted to electrical energy
2. This electrical energy is then used to charge a LiPo battery through a solar cell charger
3. The LiPo battery runs the microcontroller, the spark module and the electrolyser

4. The electrolyser converts input electrical energy from the battery to chemical energy through water splitting process and produces oxyhydrogen gas mixture.

5. An electric arc is produced by the spark module once sufficient gas has been produced. This creates an explosion which converts the chemical energy (oxyhydrogen gas) to mechanical energy (water jetting).

6. The system repeats step 3-6 until the battery runs low (roughly 20 cycles) then it reverts back to step 1.

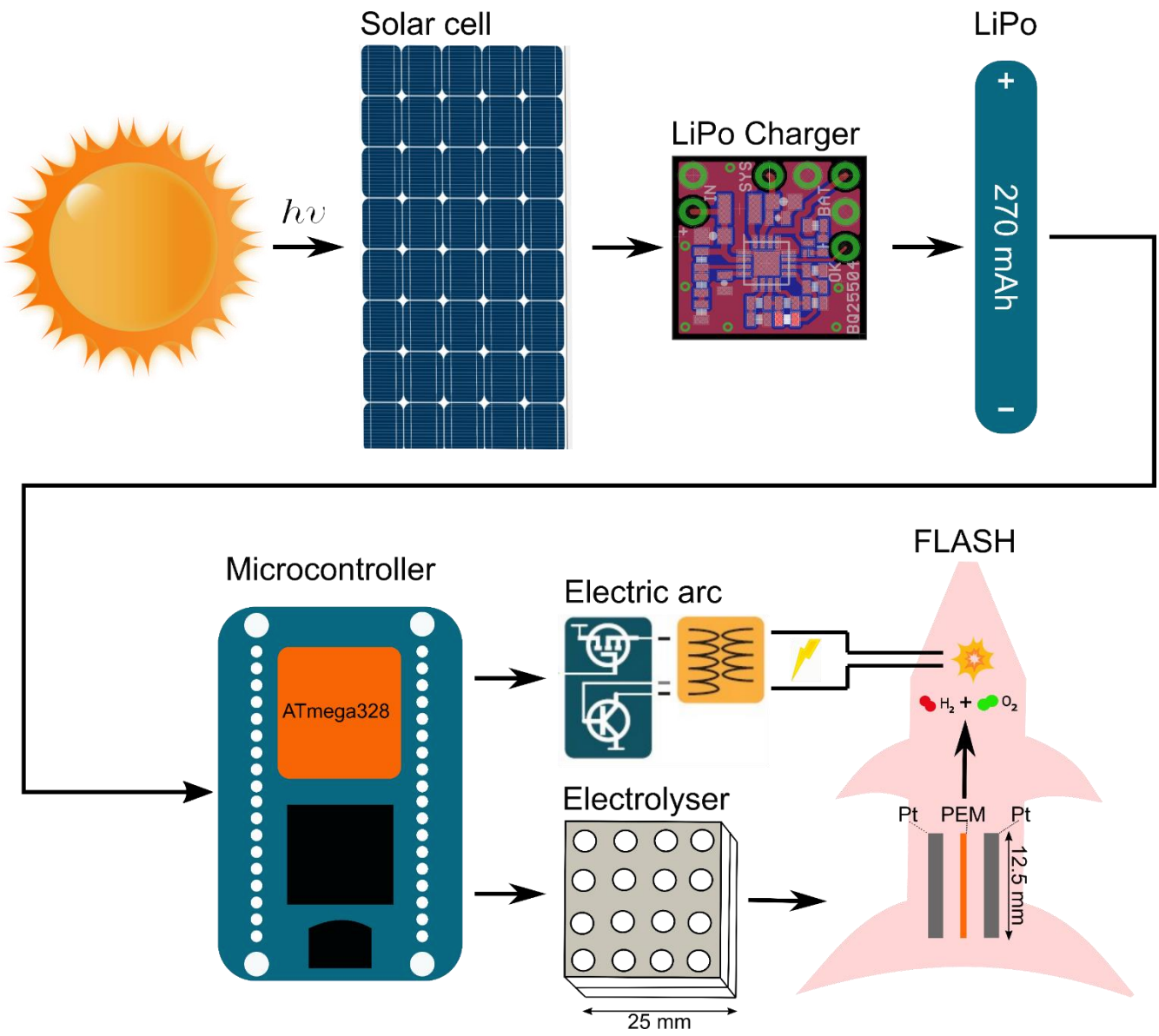

Figure 3.2: System diagram of the onboard electronics. This shows light energy being converted into electrical energy to charge a LiPo battery and this battery is then used to power the microcontroller, produce the combustible oxyhydrogen gas mixture and electric arc for combustion which generates water jetting for locomotion.

As solar energy is a renewable power source, the robot could potentially operate indefinitely as long as there is sunlight. In addition, by storing the solar energy in a battery, FLASH can have ON/OFF modes in which the robot goes into charging mode (OFF mode) during the day and operate (ON mode) at night. These characteristics are ideal for environmental monitoring applications where robots are expected to operate for a significant period of time so as to measure continuous changes in the environment. Owing to the inherent flexibility of solar cell, alternative light sources could be used to power the robot. This allows operation in places sunlight cannot reach. For instance, laser power beaming can be used to power the robot over long distances.

3.1.2 Electrolyser design

Regarding the electrolytic module design, as the electrolyser will be placed inside the combustion chamber, it is important that it is robust enough to withstand consecutive explosions while maintaining consistent electrical functionality and performance. Several designs were tested with different materials as electrodes (stainless steel, titanium, aluminium, copper, and platinum). It was found that platinum is the most desirable material to make electrodes as copper and aluminium degrade quickly during electrolysis. Titanium forms an oxide layer which hinders the electrical connection. Furthermore, a platinum anode does not generate toxic substances like stainless steel in electrode-oxidation process [270]. As a result, the electrolyser is made up of 2 platinum electrodes (12.5x12.5x0.025mm) which are separated by a Nafion membrane (20x20x0.2mm). To protect the electrodes from potential damages caused by the combustion process and ensure that the electrical functionality remains consistent through multiple explosions, 2 laser cut acrylic plates (25x25x2mm) with 1.5mm diameter holes for gas to escape are put on either side of the electrodes and bolted securely using four M2 bolts as illustrated in figure 3.3. This electrolyser has been used in all experiments to ensure consistency in testing results. It was found that this design can withstand many consecutive explosions (around 400 times and counting) without any deterioration in performance. This result is very encouraging as the electrolytic module is essentially the engine of the robot which determines if the robot can be self-sufficient.

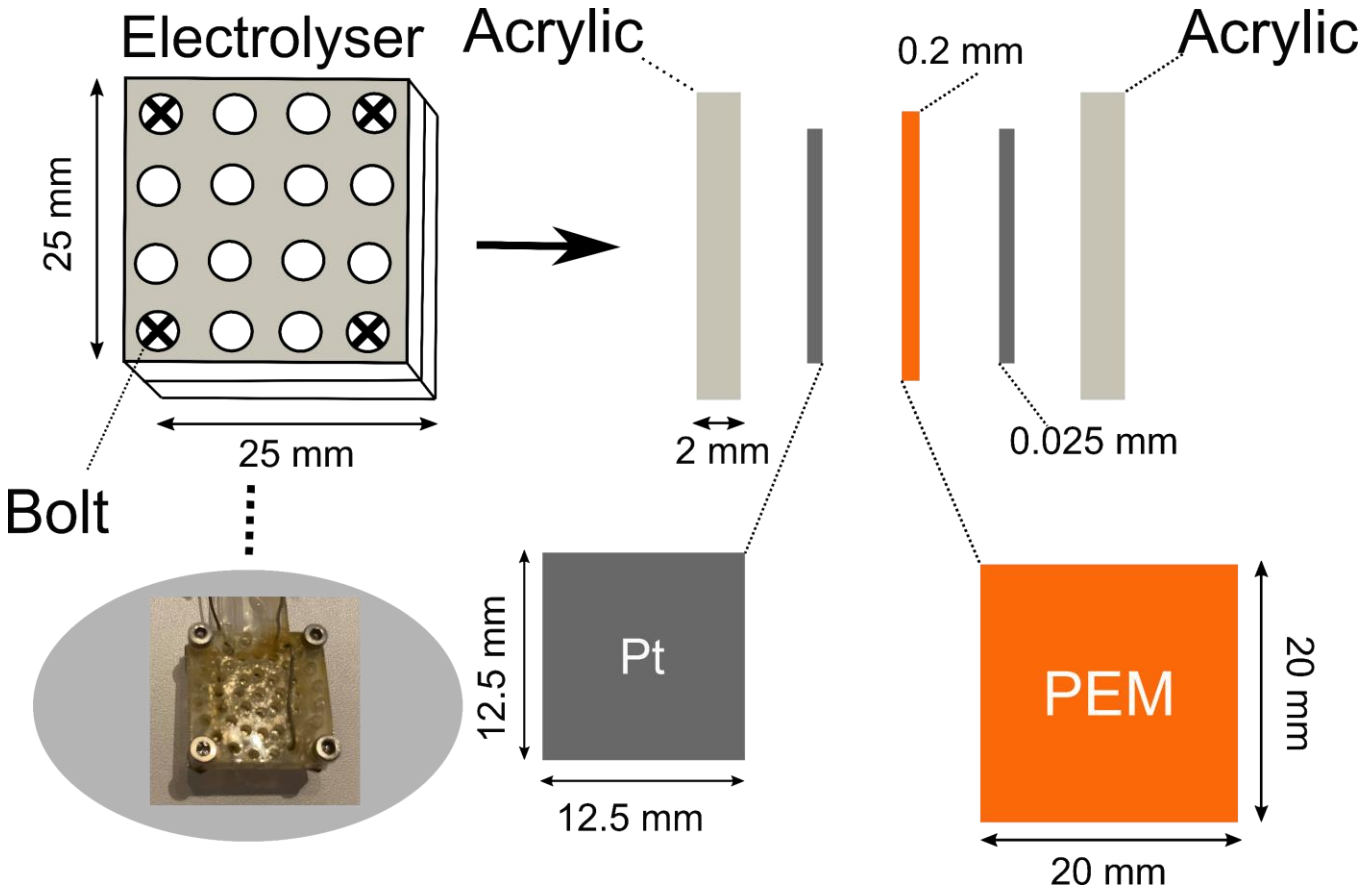

Figure 3.3: Electrolyser design. The electrolyser is made up of two acrylic plates (25x25x2mm), two platinum electrodes (12.5x12.5x0.025mm), a Nafion membrane (20x20x0.2mm). The electrolyser is bolted securely by 4 M2 bolts. Inset: Photo of the electrolyser unit.

3.1.3 Input Energy versus Oxyhydrogen Gas Generation

To quantify the performance of the platinum electrolytic module, it is important to establish the relationship between input energy (IE) versus the amount of oxyhydrogen gas generated. The voltage and current going through the electrolyser are measured by a potentiometer and read into Matlab through a (National Instrument) DAQ for analysis. The amount of oxyhydrogen generated during the experiment is trapped under a measuring beaker. Each experiment takes exactly 70s (see figure 3.4 for the experiment set up) and the process of the experiment is detailed below:

1. The Electrolyser is placed inside a water tank with a measuring beaker sitting upside down above it.
2. The Matlab code is initiated, all the in/output channels of the DAQ are instantiated and ready for data collection. The voltage and current outputs will go through a potentiostat for accurate control of the voltage and current (the potentiostat voltage and current can be monitered by the DAQ).

3. The electrolytic module is turned on for 60s with a voltage specified in the Matlab Script (ranging from 5-10V). The voltage and current are both recorded in real time by a DAQ (USB-6211) capable of reading input and output simultaneously for input energy calculation.

4. After 60s lapsed, all the relevant data is saved.

5. The input energy at different voltages is calculated by taking an average value of the current across the whole experiment and multiply with the voltage and the electrolytic module run time.

$$\mathrm{IE} = \int_0^t (\mathrm{Voltage} \times \mathrm{Current})\, \mathrm{dt}$$

6. The amount of gas generated during the experiment is measured by the beaker.

7. The input energy is varied by changing the voltage in the Matlab script, each voltage associate with different input energy calculated using the formular in step 5 (i.e. 5V≈40J, 6V≈80J, 7V≈140J, 8V≈220J, 9V≈300, 10V≈420J) and repeating step 1-6.

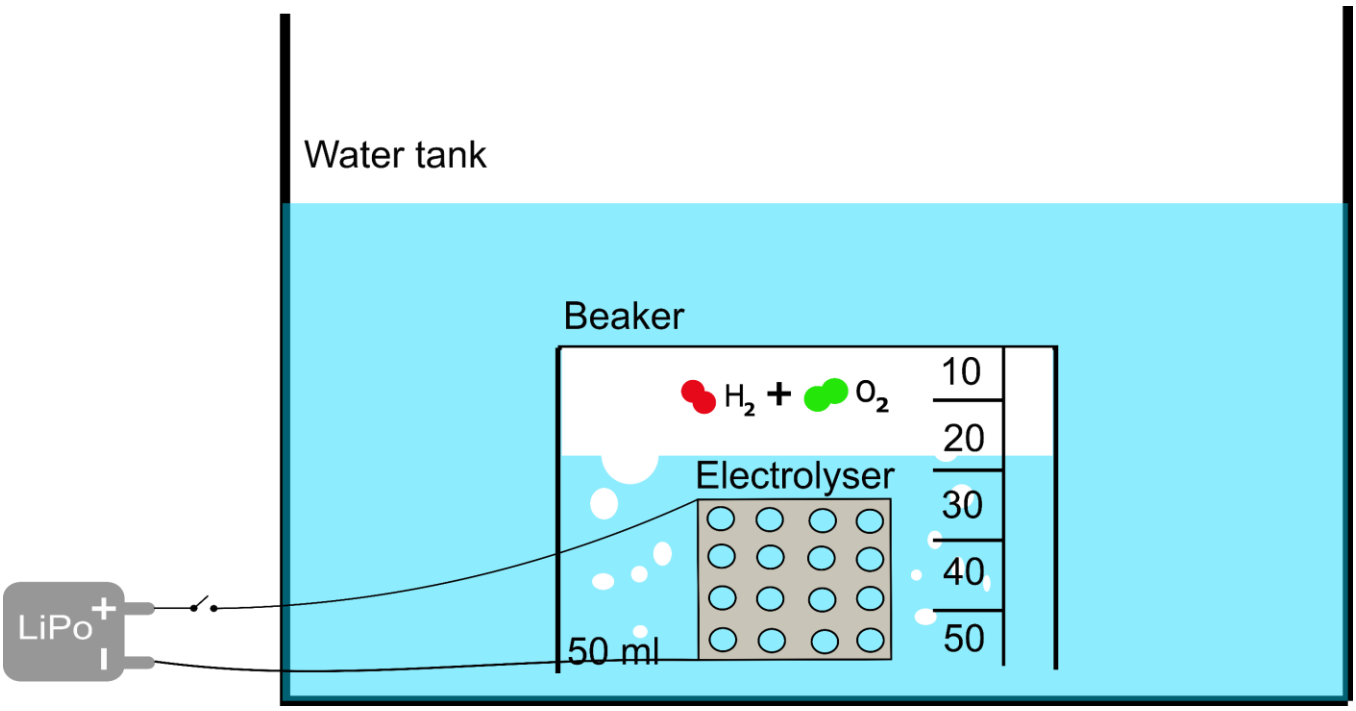

Figure 3.4: Electrolyser experiment set up. A 50 ml beaker is placed upside down in the water tanks to capture the produced oxyhydrogen gas. The gas mixture is generated by an electrolyser using a 3.7V-300mAh LiPo battery.

As expected, there is a relatively linear relationship between input energy and amount of oxyhydrogen produced. This is because higher voltage will allow more current to flow between the electrodes hence speed up the reaction process. Figure 3.5 (red line) shows that there is a tenfold increase in both input energy and oxyhydrogen produced,

40-400J and 0.5-6ml respectively, when the voltage is increase from 5V to 10V. This relationship between input energy and gas generated forms a basis for further design characterisations in chapter 4 in which the impact of orifice size on water jetting was tested at different input energies and the optimal water to gas ratio for consecutive vertical jumps determined.

Assuming the oxyhydrogen gas generated follows the ideal gas law, we can calculate the mole of oxyhydrogen gas within a given volume. After that, the energy converting efficiency (ECE) is calculated by dividing the amount of energy released (ER) when burning the oxyhydrogen gas by the input energy (IE).

$$\text{ER} = \left(\frac{V_{oxyhydrogen}}{22.4\times1000}\right) \times (241.8 \times 1000) \text{ (J)}$$

$$\text{ECE} = \frac{ER}{IE} \times 100 \text{ (\%)}$$

Where 22.4 (L) is the molar volume constant and 241.8 (kJ) is the amount of energy (Lower Heating Value) released for every mole of H_2 burned.

Figure 3.5 (blue line) shows that the highest ECE (20.5%) was achieved at IE = 80J (6V). However, it is interesting to note that after a sharp increase in the ECE between IE=40J and IE=80J, the ECE reduces drastically as the amount of input energy increases (20.5% to 15%). This suggests that the electrolyser is most efficient when operate at 6V and the reduction in ECE maybe due to the overpotential effect. In electrochemistry, “overpotential is the potential difference (voltage) between a half-reaction's thermodynamically determined reduction potential and the potential at which the redox event is experimentally observed” [271]. In an electrochemical system, overpotential indicates the cell needs more energy than thermodynamically expected for a reaction to happen. It is ideal to keep the overpotential low to maximise the efficiency and minimise the heat production. However, in practice, low overpotential slows the reaction, and as such, there is a trade-off between the two. Figure 3.5 clearly shows the effect of overpotential in which the electrolyser is most efficient when IE = 80J (6V) and then reduces as the voltage increases. One possible solution is to make the surface areas between the electrodes and the liquid bigger; this will increase the current flow and keep the overpotential low [272]. Unfortunately, it is not practical to make the electrolyser bigger as it must be small enough to fit inside the robot body. Nevertheless, this provides valuable insight into the performance of this electrolyser design which one can take into consideration in future applications.

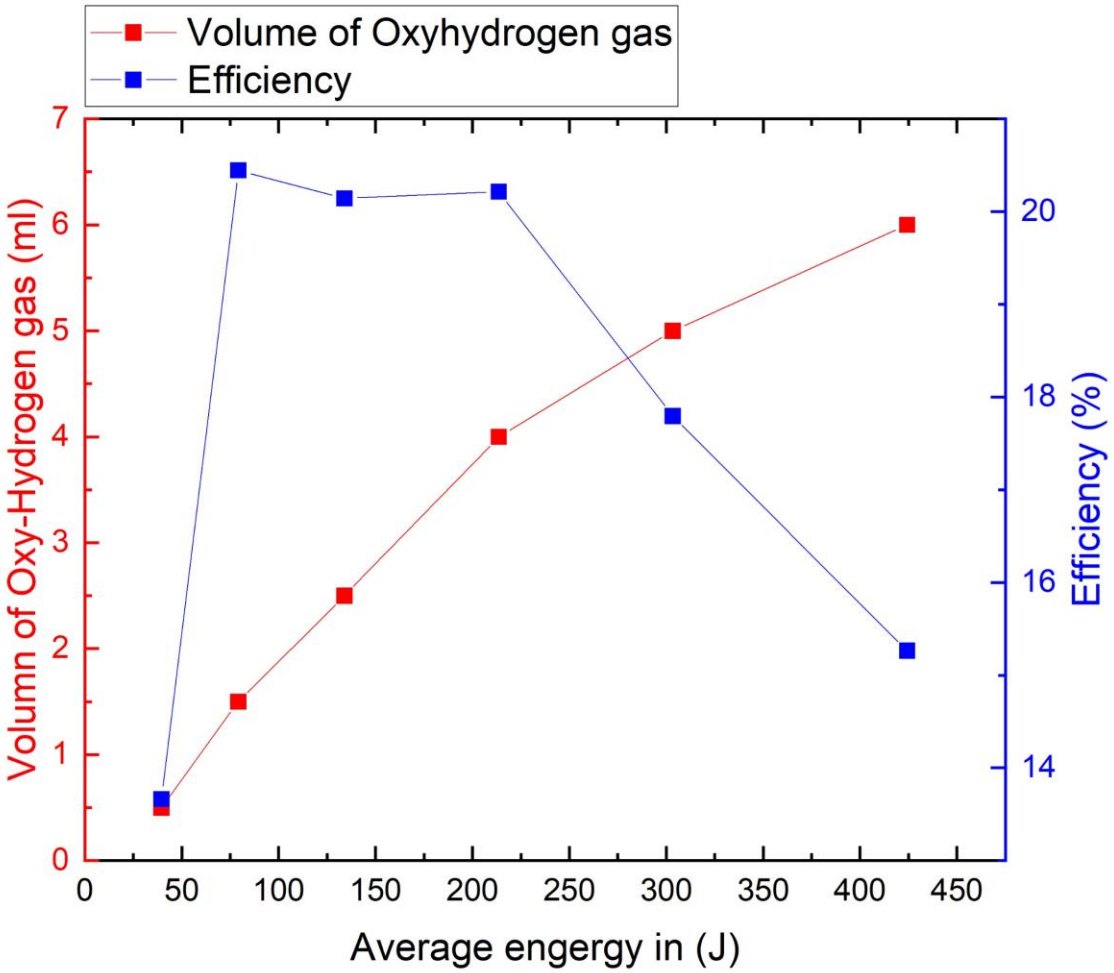

Figure 3.5: Relationship between Input energy and Volume of oxyhydrogen generated and its efficiency.

3.1.4 LiPo battery charging and discharging characterisation

One of the attractive feature of the proposed light driven robot is its potential to operate in the natural environment for an extended period of time autonomously and self-sufficiently. As such, the next step is to characterise the charging performance of the flexible solar cell with the ultra-low power LiPo charger. This characterisation will provide a strong indication regarding the robustness of the system against the claim above.

A charging test was performed to identify the time taken to sufficiently charge the LiPo battery using the solar cell. In this experiment, a 20W halogen desk lamp is used as an alternative to sunlight. This is because the light source is readily available on demand and is consistent. In addition, halogen light can produce light in the region between yellow and red wavelength which is similar to sunlight and best absorbed by the solar cell. Characterisation tests were also carried out to identify the performance of the solar cell with respect to geometry and different light sources (see appendix A). The desk lamp is placed 50mm above a solar cell which lies flat on a desk. The solar cell is connected to the ultra-low power LiPo charger which is connected to a 3.7V-300mAh LiPo battery. The battery

voltage is monitored and recorded through a DAQ (USB-6351) for data analysis. The process of the experiment is details below:

1. 20W halogen desk lamp is turned on.
2. Matlab script is initiated to monitor the LiPo battery voltage and plot in real time.
3. Once the battery voltage reaches a specific value (when it is sufficiently charged, 3.95V), the code terminates, and all the relevant data is saved.
4. 20W halogen desk lamp is turned off.
5. Analyse and plotting the results.

As seen from figure 3.6a, it took around 60 hours for the solar cell to charge the LiPo battery from 5% to 70%, 3.6 - 3.94V respectively. Next, the charged battery was used to run a platinum electrolyser to determine the discharging time. Figure 3.6b shows that it took around 90 minutes to discharge the LiPo battery from 70% to 5%, 3.94 – 3.6V respectively. Note that there is a slight voltage drop between the battery voltage and the electrolyser voltage due to the inherent resistant between the electrodes of the electrolyser. From these results, one can determine that it takes roughly 1 hours to charge the LiPo battery for around 1.5 minutes of electrolysing. It has been determined through testing that 9 minutes of electrolysing can generate around 4ml of oxyhydrogen and this correlates to the optimal gas to water ratio which will be discussed in chapter 4. As such, a charging and discharging cycle test, 6 hours charging and 9 minutes discharging, was carried out to confirm the feasibility of the entire system. Figure 3.6c shows the charging and discharging cycle of the LiPo battery over a period of 160 hours. On average, the battery charge percentage fluctuates between 60% and 80%, 3.87 - 4.02V respectively, across all charging and discharging cycles. The result confirms that the system is capable of running for a prolonged period and provides solid evidence proving the self-sufficiency capability of the robot. By tuning the charging and discharging time of the system to match the input solar energy, the robot can collect sufficient energy from the environments to run the electrolyser, and is capable of operating for a significant period of time (i.e. weeks, perhaps months). Note that the charging time can be significantly reduced using higher wattage solar cells, or a very high intensity light source. However, high wattage solar cells tend to be very large and high intensity light source needs special set up and are not readily available in open environments.

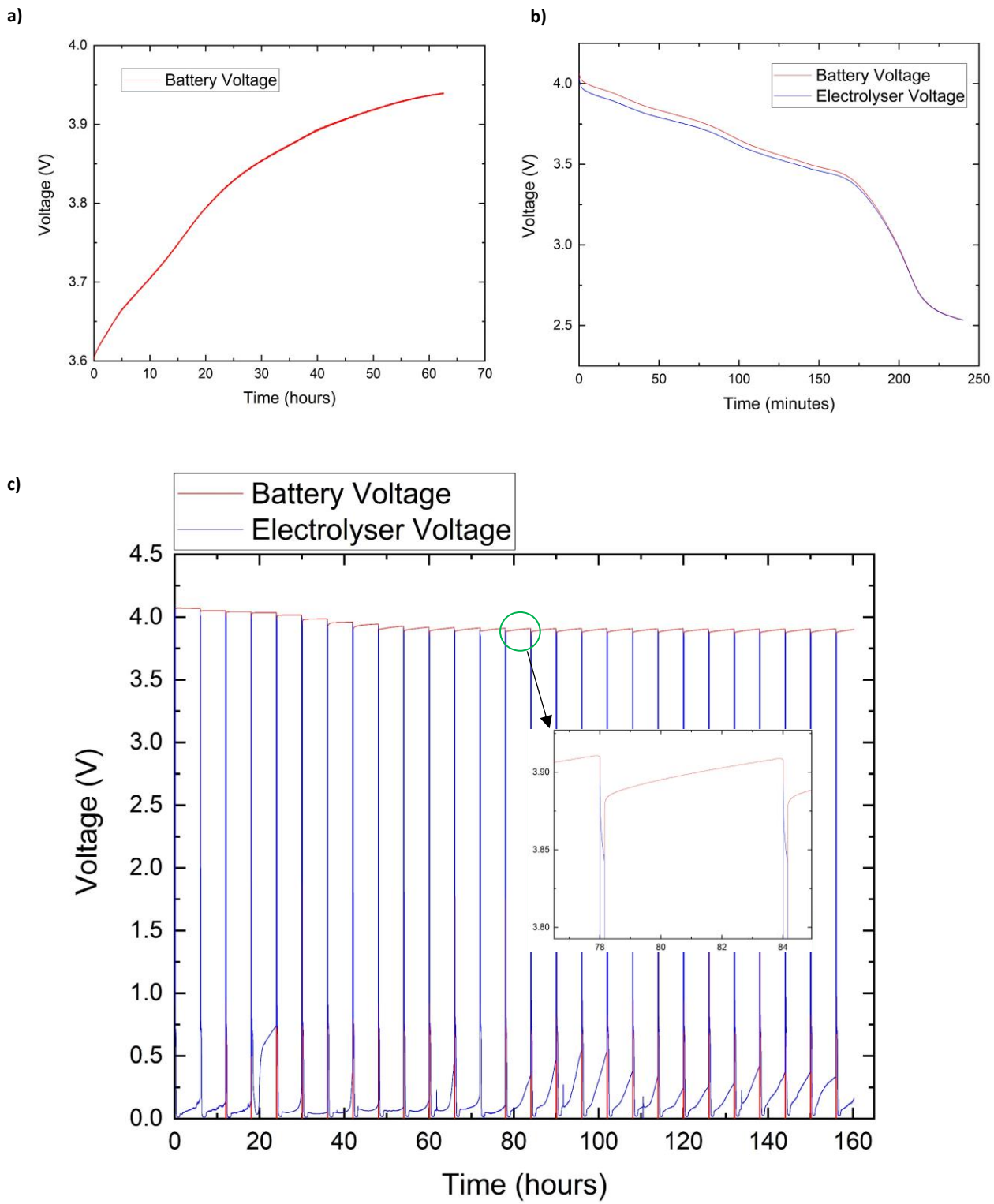

Figure 3.6: LiPo battery charging and discharging results. a) LiPo battery charging via a solar cell. b) LiPo battery running the electrolyser. c) Charging and discharging cycles of LiPo battery. Note that there is a small voltage (<0.5V) generated by the electrolyser when the battery is turn off. This is because a small amount of Hydrogen and Oxygen generated by the electrolyser recombined which creates this voltage. This is similar to the operating principal of a fuel cell. These small voltages does not affect the performance of the overall system and can be consider as noise.

3.2 Electrolysis as a combustion gas source for water jet propulsion

Significant amount of combustible gas can be stored safely in liquid form under large pressure. However, storage and regulating systems able to withstand high pressure are often complex and bulky. In addition, the provision of a pressurized flammable gas container is also a hazard. A solution for this is to produce the required combustible gas on the go via a chemical reaction of two stable substances. This will avoid high pressure and simplify the gas storage and dispensing systems. Combustible gas generation via usage of solid compounds have been employed in many applications. For instance, decomposition of sodium azide (NaN_3) releases nitrogen (N_2) was used in car airbag deployment. Recently, solid alkali metal hydrides have been used in the fuel cell industry for hydrogen generation and storage. Studies carried out by the U.S. Navy [273] [274] indicate different solid reactants (i.e. lithium hydrides) can be used in a torpedo propulsion system or for buoyancy control. Whilst these solid reactants are great candidates for a combustion gas source, they all generate waste. Water electrolysis offers a 'green' alternative because the combustion of O_2 and H_2 (oxyhydrogen) generates zero waste. In addition, using water in the environment as a fuel source would significantly reduce the weight of the robot. This is an attractive feature for miniature aerial-aquatic robot designs. The robot can takeoff from a variety of water bodies, from ponds, rivers to the ocean [275].

3.2.1 Combustion of Oxyhydrogen

Hydrogen is the most abundant and renewable source of energy available and is the most important component of any oxy-fuel application. The burning of hydrogen and oxygen results in only two by-products: energy release in the form of heat and water (H_2O). If water is seperated into H_2 and O_2, then re-combined by burning, the result is water, making it a truly "green" energy source. Oxyhydrogen will ignite when heated up to its autoignition temperature. The stoichiometric mixture, 2:1 (H_2:O_2), at normal atmospheric pressure, will ignite at about 570 °C [276]. The lowest energy needed to combust such a mixture with an electric spark is about 20 µJ [276]. In atmospheric conditions, oxyhydrogen gas mixture can ignite when there is about 4% and 95% hydrogen by volume [276] [277].

During ignition, the oxyhydrogen tranforms to water vapor and releases energy, resulted in a chain reaction: 241.8 kJ of energy (Lower Heating Value) for every mole of H_2 burned. The thermal energy released does not depend on the mode of combustion, but the flame temperature varies [278].

It is known that the most explosive mixture of hydrogen to oxygen is 2:1 [279]. This is the mole ratio from the balance equation. It is most explosive because it allows for the maximum yield of product (water) and the

maximum output of heat. Because the two reactants are present in this optimum ratio, they are both completely consumed; in other words; nothing is wasted.

$$2H_2 + O_2 \rightarrow 2H_2O + Q \text{ (Heat)}$$

It is thought that other ratios of hydrogen to oxygen would allow longer combustion times and reduce flame velocity of the oxyhydrogen explosion. In addition, porous materials such as foams might decrease the flame speed and the phases of the oxyhydrogen combustion. This would amplify the thrust generated from the rapid oxyhydrogen explosion. These will be considered in future works.

3.2.1.1 Ignition strategies

Two methods of ignition were considered, glow pug and spark ignition. The ignition happens when there is a localized rise of heat higher than the flash point of the flammable gas (create by a glow pug or a spark). The glow pug method has been reported in details in [280]. This is a very power-hungry device which operate at approximately 12V and 3A. This requires added electronics, hence more weight and is impractical within the current set up in which the entire system is power by a low wattage solar cell. Despite being a very reliable method of combustion, condensation of water vapour by product on the internals of the chamber and glow pug can occur. This results in the glow plug having to evaporate the water vapour prior to heating the oxyhydrogen gas mixture and producing combustion. Accumulated excess water from multiple combustions could inhibit the combustion from taking place entirely.

Due to the shortcomings of the glow pug method, a spark igniter which exploits arcing due to high voltage potential differences is used. This method is more efficient because the local increase in temperature is caused by an electric arc between anode and cathode. Sparkers are relatively energy efficient and easy to miniaturise, and can even be used when fully and partially submerged.

3.2.1.2 Water jet propulsion

The sections above have provided valuable information regarding the physics behind oxyhydrogen combustion and identified the most efficient ignition strategy for the light driven robot. A powerful water jet can be generated by igniting the oxyhydrogen gas mixture in an open ended chamber. We call this the hydrojetting chamber. This chamber should be robust to withstand consecutive explosions as well as lightweight to offer some swimming advantages.

The chamber is designed after a squid's mantle, which discharges water into a jet for propulsion. It is made of an acrylic tube with length 70mm, outer diameter 30mm and thickness 2mm. The combustion chamber is bolted securely using three long metal bars and two 3D printed end caps. A solid cap holds the electrolyser for water electrolysis and a hollow cap acts as a nozzle for water jet propulsion (figure 3.8c). Subscript 1, 2 and 3 were used to indicate variables corresponding to the oxyhydrogen gas in the robot, the air-water interface and outlet

respectively (see figure 3.7). Equation (1) calculates the thrust produced by a waterjet of mass flow $\dot{m}_3$ and velocity u_3 [266]. Gas' low density makes it an unfavourable propellant because thrust production is low without high exit velocities. As such, to achieve efficient jetting from a limited container, a heavier propellant is preferable. The robot can easily obtained water from the environment with the ignition of oxyhydrogen powering expulsion.

$$T = \dot{m}_3 u_3. \qquad (1)$$

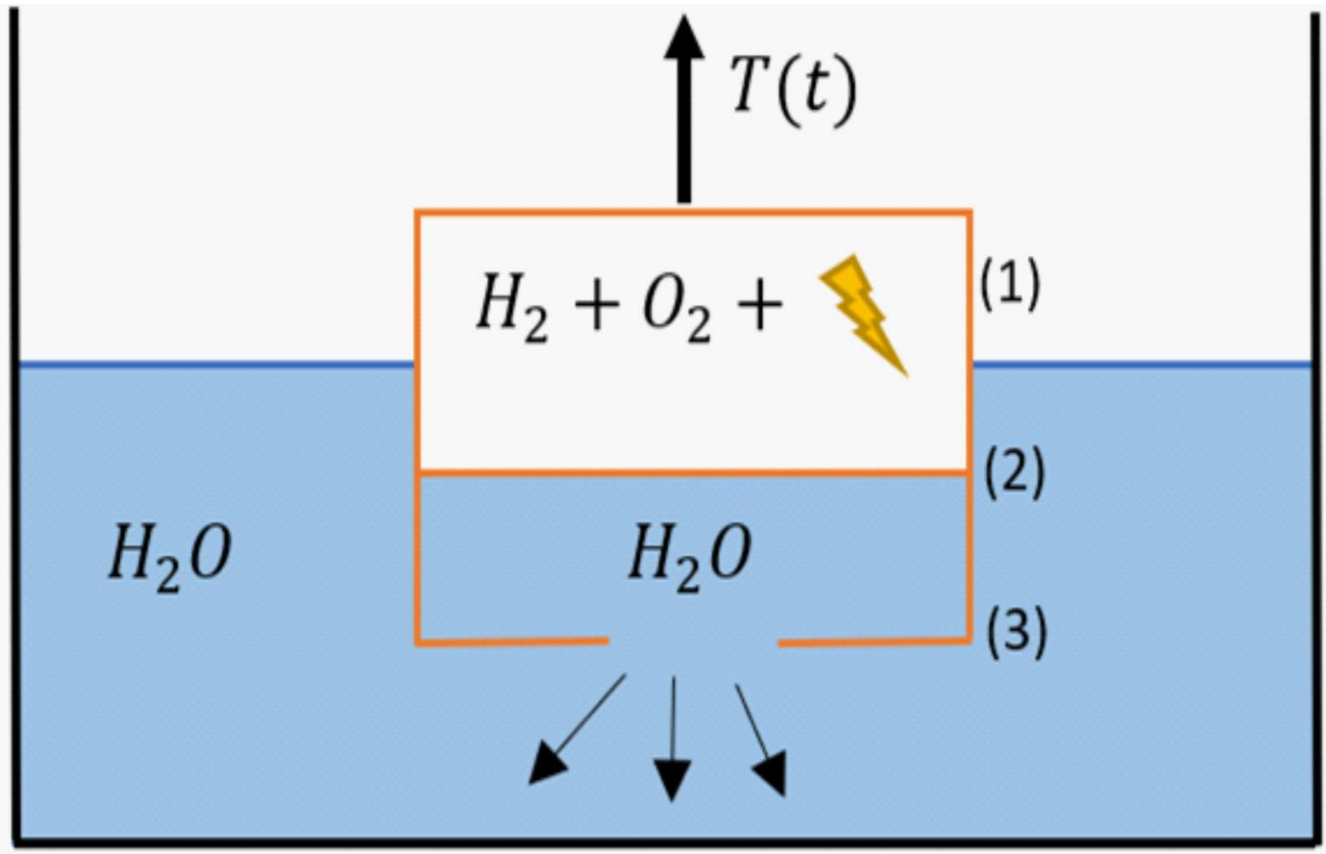

Figure 3.7: Jet propulsion principle: ignition of oxyhydrogen expels water, propelling the vehicle. Bracketed numbers correspond to the locations indicated by equation subscripts.

The thrust is calculated using Euler's flow equation, applied within the hydrojetting chamber from the water-air zone interface (2) to the nozzle. The water flow in the chamber is considered as quasi-one-dimensional, assuming uniform axial flow [281]. According to mass continuity, the local velocity is a function of cross-sectional area, as shown in equation (2). The unsteady Bernoulli equation (3) is used, integrating from the air–water interface to the nozzle exit (ds) (Figure 3.7). The sum of pressure along a flow from 2 to 3 is equal to the immediate gas pressure in the water container [266].

$$A_2(t)u_2(t) = A_3 u_3(t) \qquad (2)$$

$$\int_2^3 \frac{\partial u}{\partial t} ds + \frac{p_1}{\rho_w} + \frac{1}{2}(u_3^2 - u_2^2) = 0 \qquad (3)$$

Where u is the velocity of water, s is the distance from the water-air zone interface (2) to the tail orifice, p_1 the gas pressure and is assumed to follow a dry adiabatic expansion [282], A_n is the jet cross-sectional area, and ρ_w is the water density. The pressure impose on the water is created by the ignition of oxyhydrogen. All these above suggest that the jetting is highly dependent on the geometry of the robot (i.e. body shapes and nozzle sizes). As such, the hydrodynamic properties of oxyhydrogen ignition are investigated by recording the explosion in slow motion using a Photron SAZ high-speed camera. This will provide valuable information with respect to the effect of geometry on water jetting and the dynamic of the combustion under water. The combustion chamber is held securely by 3 steel bars with one end screw tightly to the aluminium frame, the robot is partly submersed under water so that the water jetting hydrodynamic can be fully observed (figure 3.8b). A blast box is placed on top of the whole experiment set up for safety precautions. The entire experiment process is automatically control by Matlab (Simulink R2018a) to ensure accurate and repeatable experimental results. The experimental set up is detailed in figure 3.8a. Each experiment takes exactly 70s and the process of the experiment is detailed below. Note that the same experimental set up is also carried out to analyse the hydrodynamic effect of oxyhydrogen combustion with different orifice sizes in chapter 4. In this test, orifice sizes ranging from 6mm to 26mm (2mm increment) were used and the input energy is 400J at the applied electrolyser voltage of 10V.

1. The Photron SAZ high-speed camera is turned on to adjust the focus and lighting for best video quality.
2. The robot is filled with tap water and screwed tightly onto the frame ready for the experiment. The blast box is place on top of the test rig for safety precaution (figure 3.8a).
3. The matlab code is initiated, all the in/output channels of the DAQ are instantiated and ready for data collection. The Photron SAZ high-speed camera starts recording at 1000 frame/s.
4. The electrolytic module is turned on for 60s with a voltage specified in the Matlab Script. The voltage and current are both recorded in real time by a DAQ (USB-6211).
5. At second 68th an electric spark is generated for exactly 1s causing a combustion of oxyhydrogen gas. This will be captured by the high-speed camera for analysis.
6. After 70s lapsed, all the relevant data is saved. The input energy at different voltages is calculated by taking an average value of the current across the whole experiment and multiply with the voltage and the electrolytic module run time.

$$\mathrm{IE} = \int_0^{\mathrm{t}} (\mathrm{Voltage} \times \mathrm{Current})\, \mathrm{dt}$$

7. The input energy is varied by changing the voltage in the Matlab script and output via a potentiostat. Each voltage associate with different input energy (i.e. 5V≈40J, 6V≈80J, 7V≈140J, 8V≈220J, 9V≈300, 10V≈420J) step 2-6 are repeated.

8. Different orifice samples are tested, repeating step 2-7 for each.

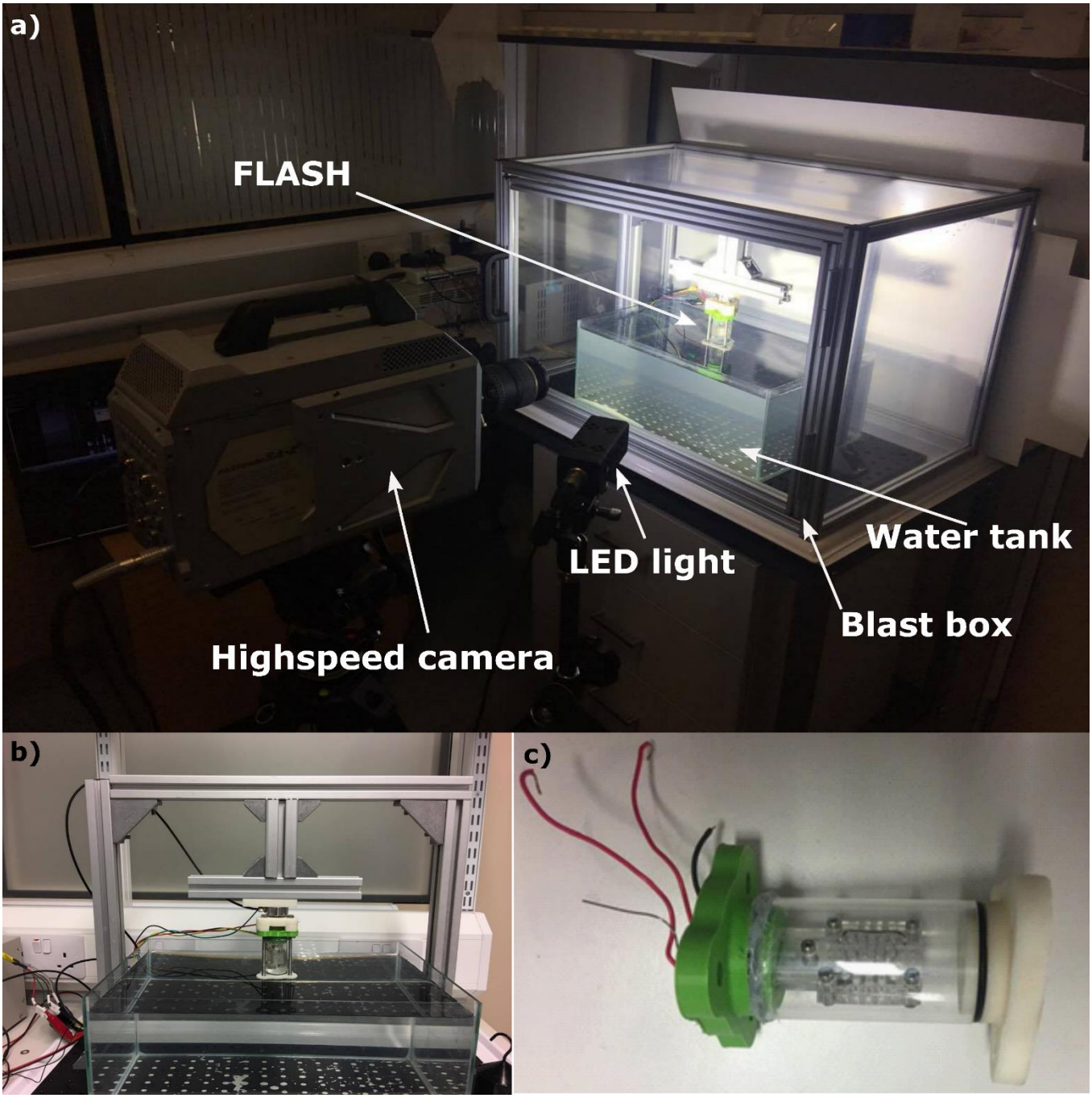

Figure 3.8: Water jet propulsion characterisation experimental setup. a) Highspeed camera configuration. b) Testing frame. c) FLASH combustion chamber and exhaust nozzle (white).

Definitions for each stage of the combustion process have been derived from the highspeed camera footage and the load cell data. These common denominators enable precise and accurate quantification of the combustion time across all geometries and input energies tested. We define the start of the combustion process as when the oxyhydrogen ignites (figure 3.9. A(i), B(i) and C(i)); the thrusting phase happens when the water is pushed out of the combustion chamber (figure 3.9. A(ii), B(ii) and C(ii)); the sucking phase starts when the water is sucked back into the combustions chamber after ignition (figure 3.9. A(iii), B(iii) and C(iii)). The end of the combustion is when there was no swirling of the water in the chamber (figure 3.9. A(iv), B(iv) and C(iv)). This is determined by examining the high-speed camera footage and the force registered by the load cell during the explosion (see appendix B for load cell data). The load cell data suggests that when the force is less than 0.5N there is no or insignificant swirling of the water in the chamber. As such, this has been selected as the end point of the explosion. As can be seen from figure 3.9, the entire four-phase combustion process lasts 295ms, 448ms and 454ms for nozzle size 6mm 18mm and 26mm respectively. During the explosion, a strong thrust was created following by a strong suction. A combustion time of around 70ms was reported in [280] for hydrojetting purposes. The thrusting is caused by a rapid expansion of oxyhydrogen gas when ignited and the subsequent suction is caused by the recombination of H_2 and O_2 gas to form liquid water. As can be seen from the video (supplementary material, movie S1), the thrust generated by the combustion is strong enough to shake the robot which has been bolted tightly to the frame. The next step is to quantify the magnitude of the thrust generated and the effect of geometry. High speed camera footage indicates that the explosion time is dependent on the size of the orifice. The explosion time is shorter at smaller orifice size and increases as the orifice size increases (see supplementary material, movie S1, S2). We recorded a difference of approximately 160ms between the explosion time at smallest (6mm diameter) and largest (26mm diameter) orifice tested. It is thought that longer explosion time would produce more efficient actuation and this result could prove useful in future optimisation of the robot. However, this result is enough to prove that the combustion of oxyhydrogen can be used for water jet propulsion. Further testing to characterise and quantify the thrust generated at different orifice sizes will be detailed in chapter 4. As regard to the phase iii suction, it is thought to be desirable as the combustion chamber will be automatically filled with water after every explosion and the electrolyser will be able to generate oxyhydrogen gas for the next round of electrolysis. This cycle could be repeated indefinitely so long as there is power supplied to the electrolyser. Further tests are needed to determine the effect of the suction on the swimming and jumping performance of the robot and these will be detailed in chapter 4.

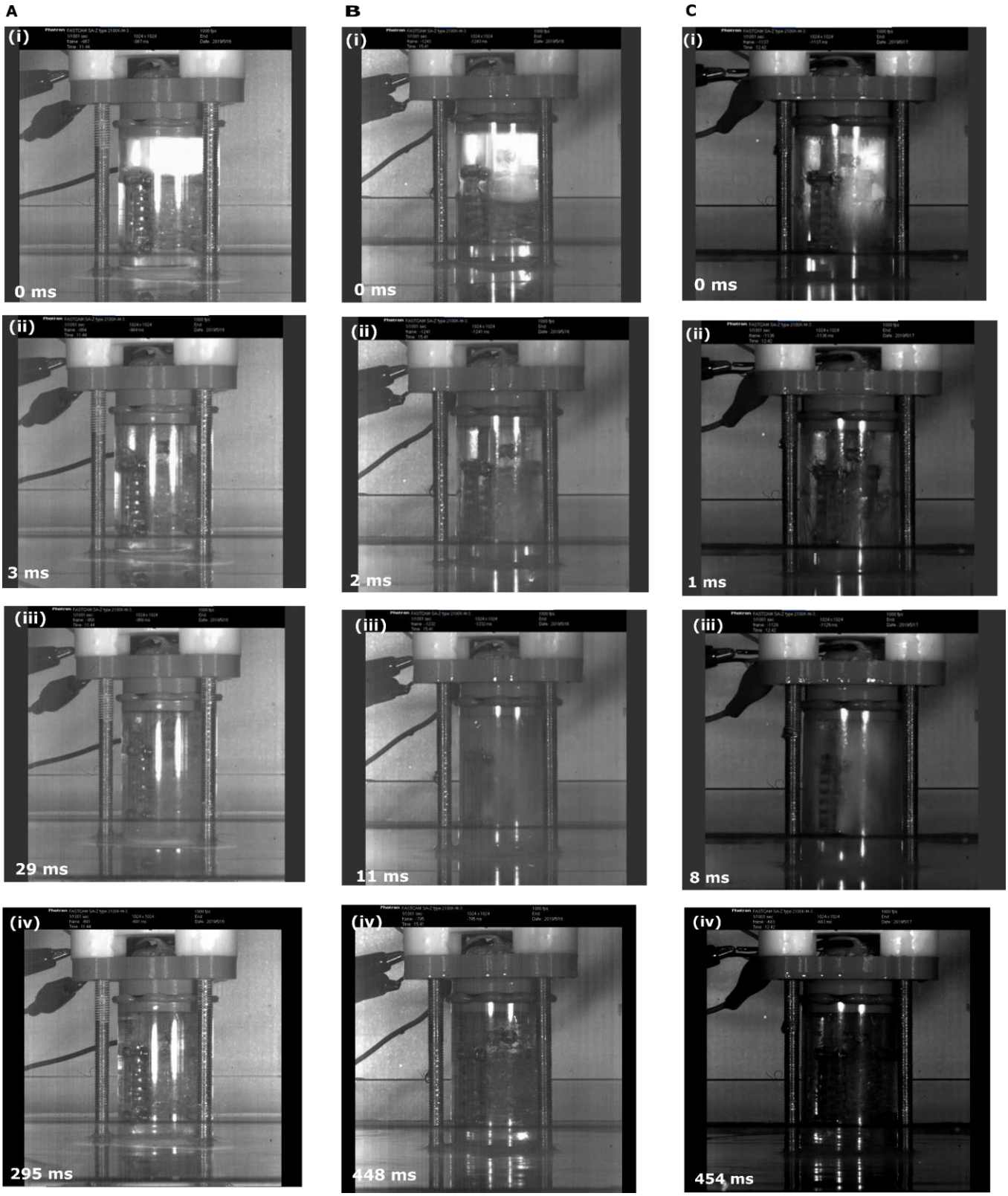

Figure 3.9: High speed camera footage of oxyhydrogen combustion. A) 6mm, 400J (10V). (i) Start of explosion. (ii) Thrusting phase. (iii) Sucking phase. (vi) End of explosion. B) 18mm, 400J (10V) (i) Start of explosion. (ii) Thrusting phase. (iii) Sucking phase. (vi) End of explosion. C) 26mm, 400J (10V) (i) Start of explosion. (ii) Thrusting phase. (iii) Sucking phase. (vi) End of explosion.

3.3 Discussion

This chapter presented a new concept in which light energy can be converted into different forms of energy to store and produce strong mechanical thrust using a multi-phase energy conversion system and combustion. The system allows an autonomous robot to operate independently as long as there is sufficient light energy. It also offers a "green" solution for environmental applications via water electrolysis and zero waste oxyhydrogen combustion. A detailed design process of the electrolytic module, which is the engine of the robot, was presented, and its performance was characterised. Furthermore, a series of characterisation tests for the whole energy conversion system were carried out to confirm the hypothesis regarding the potential for a robot using this mechanism to be self-sufficient.

Finally, the chapter discussed the mechanism of water jetting via oxyhydrogen combustion and different ignition methods. In addition, the hydrodynamic property of the thrust generating mechanism is investigated under a high-speed camera to better understand the interaction between oxyhydrogen gas and water during ignition with respect to the geometry of the robot. Interesting hydrodynamic behaviour was observed including thrusting and suction. Further characterisation on the effect of orifice sizes on hydrodynamic properties will be explored in chapter 4.

To conclude, this chapter has laid out the basis and core components of a light-powered combustion robot, in preparation for characterisation tests in chapter 4. It also suggests strong possibility that the robot can be self-sufficient and presents a "green" solution for environmental applications using oxyhydrogen combustion mechanism for water jet propulsion.

Chapter 4

4. Light driven robot design and mechatronics

Highlighted in the previous chapter, the ability to continuously monitor aquatic environments and obtaining specimens with aquatic robots would increase the safety and efficiency of environment health monitoring and enable water sample acquisition from hazardous or inaccessible regions. An aquatic-arial small scale robot able to swim/jump out of the water offers an efficient solution for water sample collection applications. However, small-scale arial robots often not capable of transition to flight from water due to insufficient power. One solution for this problem, as presents in chapter 3, is igniting oxyhydrogen gas to obtain thrust large enough to move the robot in water and to shoot the robot out of the water. However, this presents some major challenges needed to be addressed. First, the large pressures produced by explosions on a miniature robot impose stress on its structure. The robot must be robust enough to withstand consecutive explosions without becoming dismantled. This concerns the design of the ignition chamber and electrolytic module. Second, achieving repeatable explosions inside the hydrojetting chamber is not easy due to the interference of water on ignition and combustion. As such, it is essential to deepen understanding on the hydrodynamic properties of the water and the ignition with respect to geometry. In addition, the robot needs to operate both over and underwater which includes floating, jetting, diving and refilling for take-off and electrolysing, swimming and refilling for under water operations (figure 4.1). Each of these operational states has contrasting requirements, posing significant challenges to the design of such robotic platform. It is expected that trade-offs need to be made which might limit the performance that can be achieved in each operational state.

In this chapter, we present a novel jet-propelled robot which is able to swim under water and perform leaps from water when it gets near the surface. We call this robot Flare Launching Autonomous Swimming Hydrobot or FLASH. The robot uses a special design electrolytic module to produce oxyhydrogen from the surrounding water. The gas mixture is then ignited by a high voltage spark which allows the robot to propel under water. By controlling the amount of gas generated inside the robot body, the robot is able to dive into the water or perform aquatic takeoff (figure 4.1).

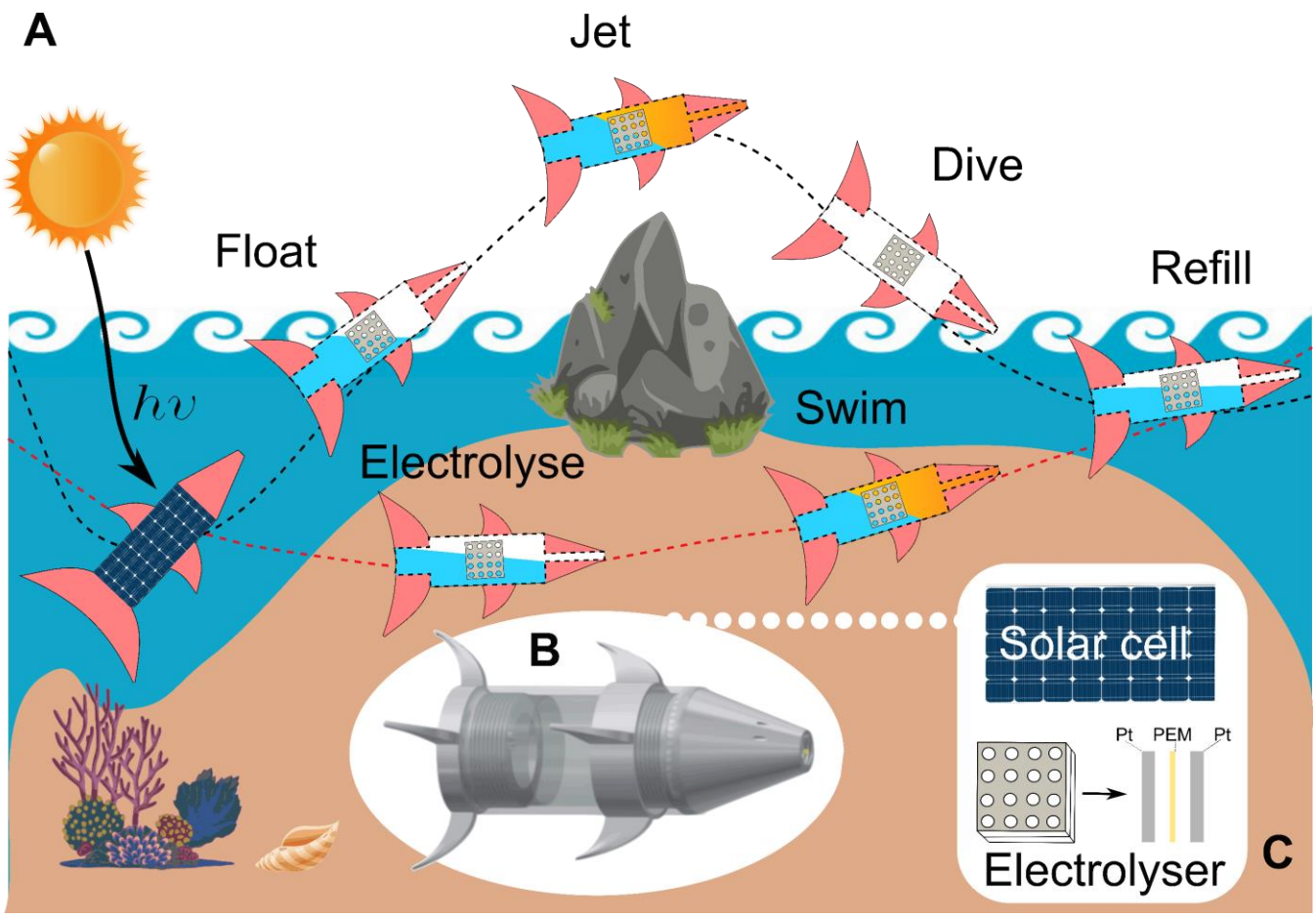

Figure 4.1: FLASH modes of locomotion and design. (A) Proposed locomotion modes: black dashed line shows the transition from a floating state to aquatic-arial jump state, then to jetting/diving state and finally back to floating state. Red dashed line shows the transition from a neutral buoyancy state to hydro jetting (underwater) state and finally back to a neutral buoyancy state. (B) CAD rendering of FLASH. (C) Solar cell and electrolyser, solar cell converts light energy to electrical energy, electrolyser converts electrical energy to chemical energy to generated rapid thrust.

The first part of this chapter explores the relationship between efficiency and geometry and the optimal thrust achievable with a given design. In addition, it also investigates the hydrodynamic properties of oxyhydrogen ignition on each design. The second part of the chapter investigates FLASH's ability to perform aquatic jumpgliding. Finally, swimming performance of FLASH is explored and characterised.

4.1 Optimal geometry to maximum thrust

This section characterises the thrust generated by the ignition of oxyhydrogen with different orifice designs as well as analyses the dynamics of hydrojetting in an aquatic environment. Combustion of oxyhydrogen enables fast propulsion due to the generation of high speed water jets. This could be used for specimen collection, for example by using a beak at the tip of FLASH. The aim of this experiment is to introduce a novel actuation mechanism which utilises the thrust released from the ignition of H_2 and O_2 gases. We aim to investigate the maximum efficiency of this waterjet propulsion device, the effect of geometry on efficiency and the maximum thrust/velocity achievable for a given design.

Since it is difficult to compute the flow rate out of the orifice to work out the thrust (T) numerically, we have designed an experimental rig to measure the input energy to the robot and the force output of a waterjet propulsion mechanism (see section 3.2.2). The combustion chamber is made of a clear acrylic tube (30mm diameter, 50mm length, 2mm wall thickness) with two 3D printed end caps. This enable the ignition to be recorded using a high-speed camera and thereby the hydrodynamics of the water jetting can be observed. The future objective is to run the whole system untethered and miniaturise the robot.

4.1.1 Thrust characterisation experiment setup

The experiment was designed to monitor the input energy to the chamber and the thrust caused by the high speed waterjet. The energy input is measured via the input voltage and current. The electrolyser described in 3.1.1 were used to produce the H_2 and O_2 gases for these tests. The input electrical energy to the electrolytic module was indirectly measured through voltage and current via a potentiostat and DAQ (NI USB-6211). A submersible load cell (Tedea Huntleigh Compression Load Cell 20kg, 15V dc, IP67) is used to measure the thrust generated by the combustion. Finally, a highspeed camera records the hydrodynamics of the water jetting process which shows the volumetric expansion rate of oxyhydrogen gas, combustion time, water jet displacement and effect of thrusting and suction on different geometry. The combustion chamber was held secured by 3 long steel threaded rods with one end screwed tightly to a load cell (figure 4.2). The load cell is fixed tightly to the frame to ensure accurate measurement. The robot is partially submersed under water in the same manner as described in section 3.3.2; however, the free end is now replaceable to test different orifice design. A set of experiments were carried with different orifice sizes and energy inputs to measure the force output. The sample sizes range from 6mm to 26mm with 2mm interval in diameter. Each sample is subjected to different energy inputs to determine the most efficient energy against force output. The entire experiment process is automatically control by Matlab (R2018a) to ensure accurate and repeatable experimental results. Each experiment takes exactly 70s (see figure 4.2 for the set up and experiment timeline).

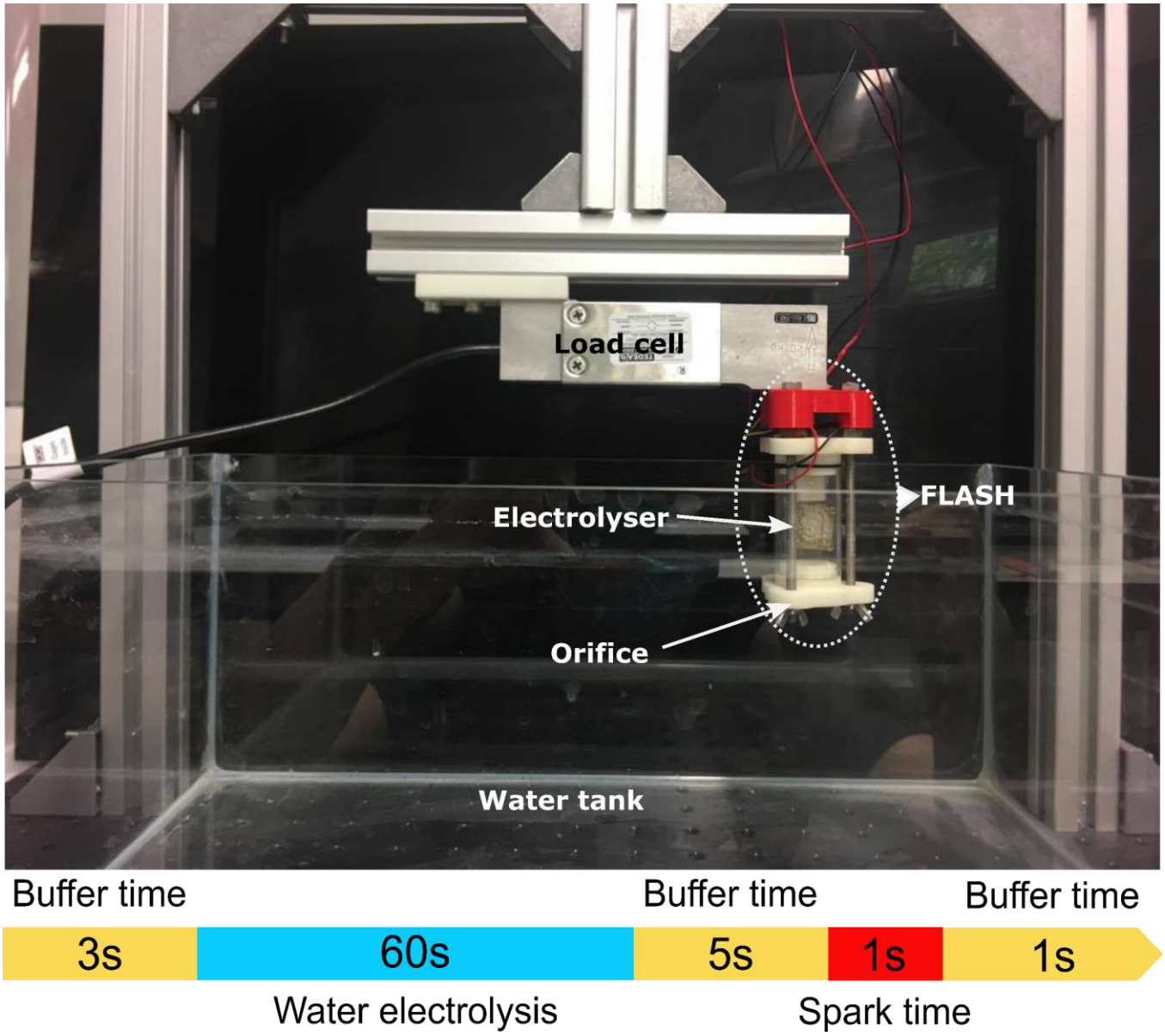

Figure 4.2: Magnitude of thrust generated under different geometry experimental set up and the experimental timeline.

The highspeed camera set up has already been described in section 3.3.2, the procedure for measuring the thrust produced by the waterjet and input energy is detailed bellow:

1. The robot is filled with tap water and screwed tightly onto the inline load cell ready for the experiment. The blast box is place on top of the test rig for safety precaution.

2. The Matlab code is initiated, all the in/output channels of the DAQ are instantiated and ready for data collection.

3. The electrolytic module is turned on for 60s with a voltage specified in the Matlab Script (ranging from 5-10V). The voltage and current are both recorded in real time by a DAQ (USB-6211) capable of reading input and output simultaneously for input energy calculation.

4. At second 68, the spark is turned on for exactly 1s causing a combustion of oxyhydrogen gas

5. The load cell data of the explosion is amplified by a loadcell amplifier and recorded simultaneously.

6. After 70s lapsed, all the relevant data is saved.

7. The energy input is varied by changing the Matlab script and repeating step 2-6.

8. Different orifice samples are tested by replacing the orifice and repeating step 1-7.

4.1.2 Experiment results and discussion

It is interesting to note that the mean force output and the energy input does not strictly follow a linear pattern (see figure 4.3a). This is expected because of the size of the orifice which restricts the outflow of the water jet when the ignition happens. This causes internal choking and swirling of water inside the robot body which hinders the force output. To confirm this hypothesis, highspeed camera footage of oxyhydrogen combustion under different orifice sizes was examined, and it was found that with smaller orifice sizes, there is significant choking and swirling of water and gas mixture within the combustion chamber which reduces the force output (see supplementary material, movie S2). This behaviour is less significant as the orifice size increases which explains the rise in the force output in steps of approximately 5N. In addition, the increase in orifice size allows faster water escape hence the overall combustion time is reduced (see supplementary material, movie S1). For instance, there is a reduction in combustion time of around 50ms when comparing the highspeed camera footages of orifice size 6mm and 26mm (see supplementary material, movie S1, S2). As can be seen from the graph, there is a linear trend between the thrust generated and orifice size of 6mm to 16mm. However, this linear trend breaks down and the curve flatten as orifice size increases. The maximum thrust (40N) was achieved by a largest orifice size of 26mm and largest input energy of 421J. This is expected as larger orifice will allow the water and gas to escape more easily due to less choking and swirling (see supplementary materials, movie S1 and appendix B, table B.1). In addition, larger input energy will produce more oxyhydrogen gas hence bigger explosion and bigger force. These are key findings as with this results, one can optimise the robot design to maximise efficiency and thrust. The time-domain plots of force for different orifice sizes can be found in appendix B.

a)

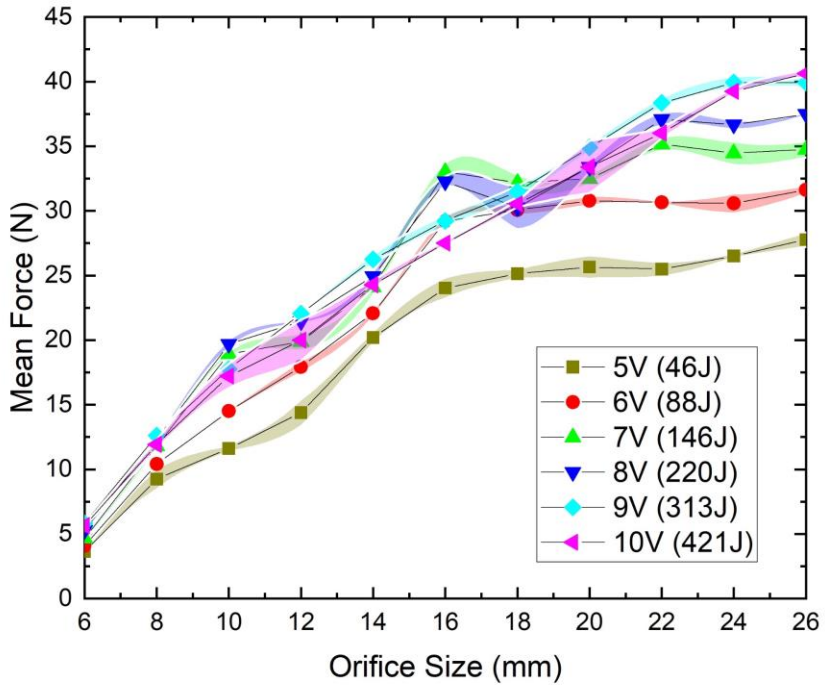
Mean Force (N)
Orifice Size (mm)
5V (46J)
6V (88J)
7V (146J)
8V (220J)
9V (313J)
10V (421J)

b)

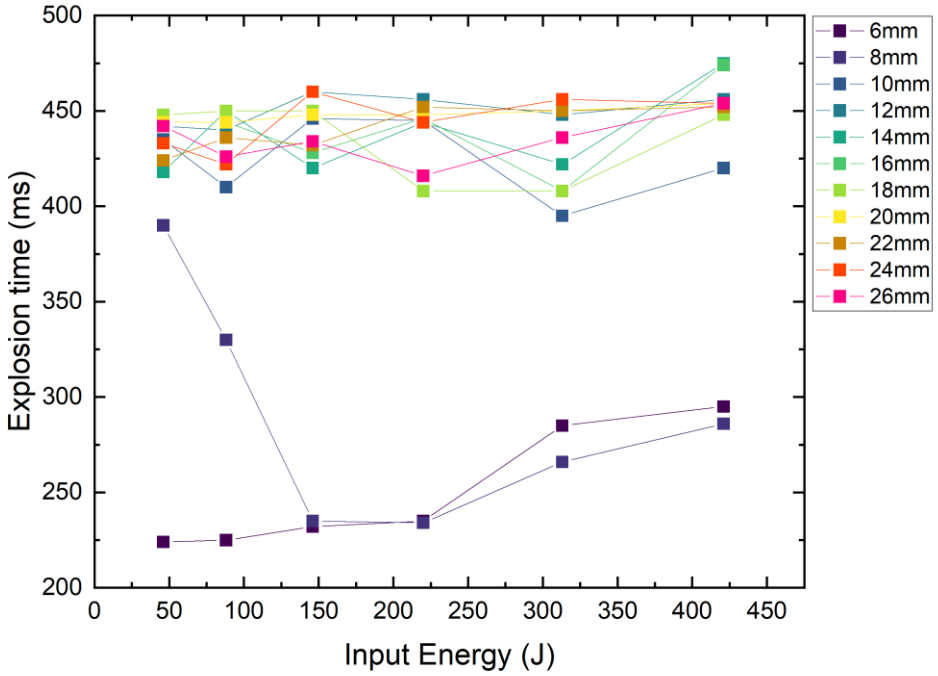
Explosion time (ms)
Input Energy (J)
6mm
8mm
10mm
12mm
14mm
16mm
18mm
20mm
22mm
24mm
26mm

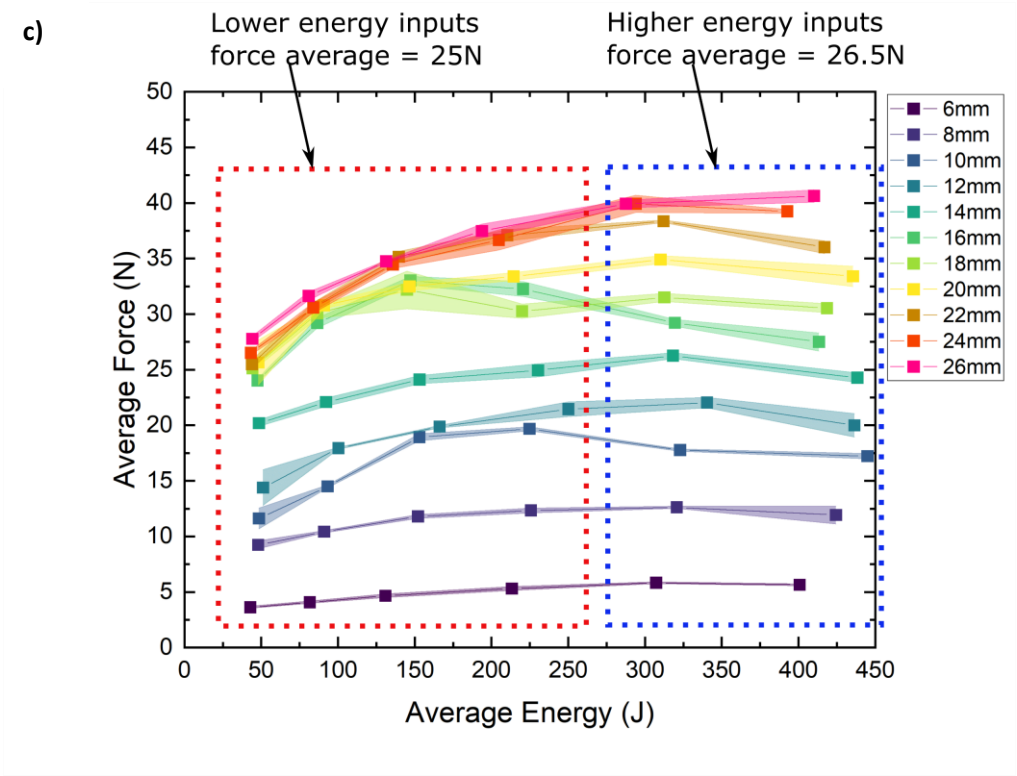

Figure 4.3: Oxyhydrogen combustion characterisation: a) Force outputs vs energy inputs under different orifice sizes. The coloured ribbons are standard deviation of 3 tests. b) Oxyhydrogen combustion time with different geometry. c) Average energy inputs versus average force outputs for each orifice size. The coloured ribbons are standard deviation of 3 tests.

Regarding the efficiency of FLASH, figure 4.3c and table B.1 show that the average force response at lower energy input (25N) is approximately the same as higher energy input (26.5N). This trend is repeated across all tested samples and there are a few possible explanations for this. The first one being the ratio of gas and water mixture in the robot body, as explained at the beginning of section 3.3.2, where the thrust is produced by the mass of water/air and its velocity. More energy input will produce more gas which leads to bigger explosion, hence more force. However, the low density of the gas and the constraints of the orifice means thrust production is negligible without very high exit velocity. As such, it is more efficient to use a heavier propellant, such as water. Unfortunately, due to the size of the robot, more energy input means more gas and as such less water available to propel. When more gas is ignited, even though it creates a more powerful explosion, the thrust produced has been inhibited by lack of sufficient water. For the case of less gas, even though the explosion is not as powerful, more water is available to be ejected and as such, more force is produced. The second explanation is because of the system geometry (i.e. orifice size), it is suspected that a significant proportion of the energy created by the combustion has been consumed internally due to choking and swirling of water and only a certain amount of fluid can escape through a particular orifice. A bigger orifice allows fluid to escape more quickly hence more force. These findings enable us to drive the robot at a more energy efficient mode and open up possibility for miniaturisation as a small onboard power source can be installed onto the robot body. It is important to note that the force response is

lowest at the lowest energy input (≈50J). This is expected as there is not enough gas generated at this energy level to create a large enough explosion to push water out as efficiently as if there were more gas. This also indicates that there is a minimum amount of oxyhydrogen gas needed for efficient locomotion. As such, optimal gas to water ratio for effective locomotion will be investigated in the following vertical jump test. A smaller orifice size will cause more choking and produce less output force, it has been decided that the smallest orifice size needed to obtain an acceptable output force is 6mm diameter.

As mentioned in chapter 3 (section 3.1), the preliminary results suggest that the combustion time may be dependent on orifice size and it is thought that a longer combustion time would be beneficial for the locomotion of the robot. As such, the combustion times at different input energies and various orifice sizes have been characterised. The combustion time is measured by the high-speed camera and the load cell readings described in chapter 3 using the same definition for the start and end of the combustion process. Figure 4.3b shows a significant increase in combustion time as the orifice size increases. The longest explosion time is 475ms at 421J input energy and 14mm orifice size, while the shortest explosion time is 224ms at 46J input energy and 6mm orifice size. This is consistent with the preliminary results and confirms that the explosion time is dependent on geometry of the orifice. The explosion time generally increases as input energy increases for all orifice size (6mm and 26mm). This is expected as higher input energies produce bigger explosions with longer thrusting and sucking phase. However, we observed long combustion times for orifice size 8mm at lower input energies (46J-146J). This unexpected phenomenon could be due to the stochastic nature of the combustion process in which undesirable additional choking and swirling of fluid in the chamber prolong the explosion time. This phenomenon is mitigated at higher input energies of this particular orifice and the explosion time revert back to its expected trend similar to that of the 6mm size orifice. It is thought that bigger explosions produced at higher input energies may mitigate the internal choking and swirling. Bigger orifices let fluid escape readily which produce larger thrust with less internal choking and swirling. This lengthen the explosion time due to longer thrusting and sucking back phases. It is thought that longer explosion time would be beneficial as longer explosion means longer mass transfer rate, hence higher driving force.

Throughout these series of characterisation, it was observed that to optimise the performance and efficiency of FLASH, one needs to maximise the thrust output, keep the input energy low and have long explosion time. However, there are trade-off between these three parameters and as such, it depends on the applications to decide which set of parameters is the most suitable. For instance, for environmental monitoring application, the robot needs to operate for an extended period of time and should be able to traverse different terrains and the ability to consume minimal amount of energy to perform locomotion (swimming, aquatic jumpgliding) is therefore important. In this case, one should look at minimising the input energy and maximising the force output. Long explosion time can be overlooked in this application as aquatic jumps require short bursts of powerful thrust to

break the surface tension of water. Therefore, short explosion time is preferable. Nevertheless, long combustion time is beneficial for efficient swimming locomotion and as such, a right balance is required to ensure the optimal performance of FLASH in any desired application.

In this section, we have quantified and characterised the dependence of thrust generation and orifice geometry. This robot has demonstrated powerful force output (40N) indicating strong swimming and aquatic jumping potential. The geometry and input energy dependence of combustion time have also been characterised. It has been found that there is a relationship between explosion time versus orifice size and input energy. The experiment results suggest several areas for optimisation towards thrust and efficiency maximisation, combustion time, miniaturisation, automation and water sampling and sensing application. Further testing will be carried out to realize the full power of oxyhydrogen combustion to develop a suite of new mesoscale devices that will culminate in a hybrid, aerial-aquatic microrobot.

4.2 Aquatic-aerial transition

As discussed in the previous chapter, combustion offers a way to produce impulsive aquatic escape without the requirement for a pressurised container and a release strategy. Churaman et al. [283] reported the first autonomous jumping microrobot weighing only 314 mg that were capable of performing 8 cm vertical jump using explosive nanoporous energetic silicon, a solid energetic formulation that produces gas when ignited. Recently, roboticists have demonstrated takeoff of 100mg RoboBee using oxyhydrogen combustion for aerial-aquatic transitions [284].

One major limitation of the above robots is they need an offboard power source to operate. As such, bigger, untethered soft terrestrial jumping robots which use explosion to move have been introduced [285] [286] [287] [288]. These robots used pressurised liquid container of combustible gas as fuel (i.e. butane or methane), connected to a silicone combustion chamber by electronic valves and ignited by an electric spark. Nonetheless, the employment of multiple fuel containers and flow regulating equipment led to a big increase in mass and complexity for a small scale arial robot. This integration would be impractical in an aerial-aquatic robot. It is expected that a full design and characterisation of the soft rover will be implemented in the future. In the previous section, we have presented the concept of a novel light driven water thruster for high-power, seamless aquatic-aerial transition. It uses water from the environment to generate actuation pulse through the ignition of oxyhydrogen gas to create propulsion. Capable of providing up to 40N of thrust, this offers a robust means to transition from water surface to flight through the use of one single actuator. This section will characterise the gas to water ratio at various orifice geometry to establish the optimal ratio and geometry for aerial-aquatic takeoff. As input energy directly links to amount of combustible gas generated and the combustion of this gas mixture

directly links to thrust magnitude, in this section, three energy level showcasing the most significant gas to water ratio will be tested (50J, 200J and 400J). To simplify matters, the FLASH robot will jump vertically with a takeoff angle of 90° rather than launching at an angle or follow a particular direction. Figure 4.4 describes the operational stages of the robot in this vertical jump experiment. Finally, it is also important to note that the FLASH design used in this test is a simplified version of the final design for untethered use. This design has several advantages which can be beneficial for aquatic jump-gliding. For instance, a long tube design and pointed head will help FLASH break the water surface tension more easily and facilitate smooth water to air transition and vice versa. In addition, the rocket shape design will simplify future analytic physics model on flight trajectory as it can be modelled as a ballistic projectile. Finally, the screw on head and orifice offer ease of maintenance and design optimisation. It also reduces the weight of the robot while proving to be robust enough to withstand consecutive explosions. To prevent FLASH from getting damaged through multiple explosions and prolong the life span of the robot, the pointed head of the robot is hollowed out and a small duckbill-umbrella combination valve (8.2mm diameter, minivalve.com) was placed inside the head. This serves three purposes. The first is to regulate the jetting direction during combustion, the small valve inside the head will cause the water to escape through the tail orifice rather than through the head for optimal jetting performance. The second is to relieve the high pressure build up in the chamber during the explosion which might damage the robot and the electrolyser. Upon inspecting the slow motion footage of the vertical jump experiment, we notice droplets of water shotting out from the head of FLASH with high velocity immediately after the explosions. This was not the case in the thrust characterisation experiment when the head is not hollow. As such, we believe that the pressure from the explosion might deform the soft valve and force the water droplets out thereby acting as a high pressure safety valve. Excessive high pressure might lead to cracking in the hydrojetting chamber and as a result, reduces the robot operation lifetime. Finally, it prevents sucking through the orifice which might hinder jump performance.

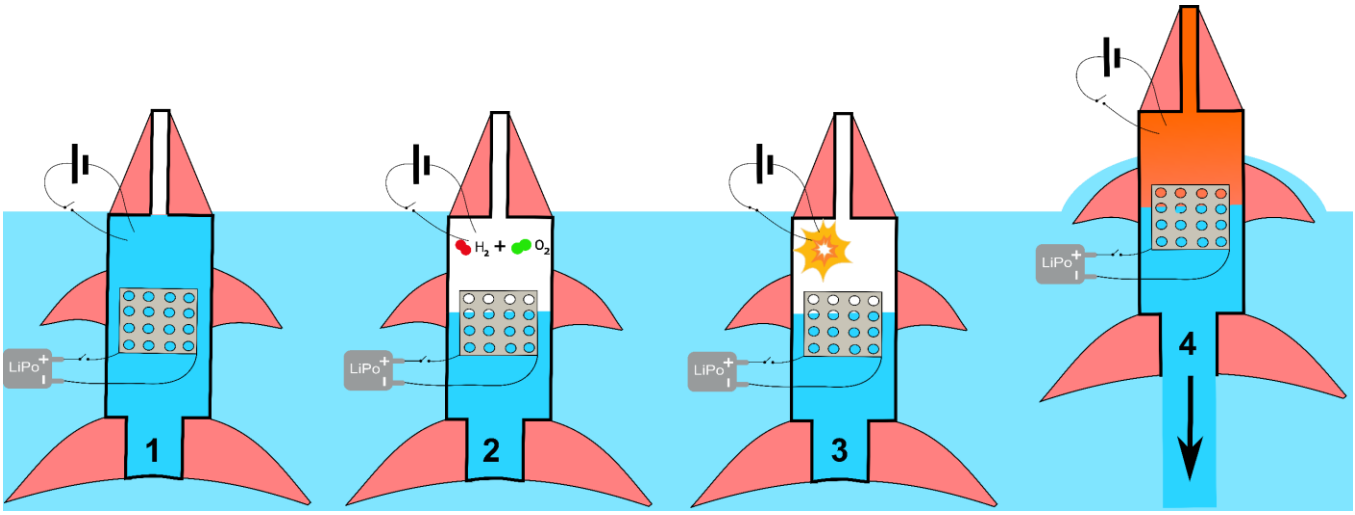

Figure 4.4: Overview of the aerial-aquatic robot operational stages. 1, water intake; 2, electrolysis; 3, ignition; 4, water jetting, showing choke release valve.

4.2.1 Vertical Jump experiment setup

This experiment was designed to characterise the jump height of FLASH at a given energy input (figure 4.5). The energy input is measured through the input voltage and current. The electrolyser described in 3.1.1 were used to produce the oxygen and hydrogen gases. The electrical energy input to the electrolytic module was measured through voltage and current via a potentiostat and DAQ. Finally, a camera is used to capture the vertical jump height of the robot. The robot is suspended by electrical wires inside a clear acrylic tube (80mm diameter, 3mm thickness) which is put inside a glass water tank. The acrylic tube base is raised by 10mm to allow water to escape more easily and simulate takeoff from an open body of water. The robot is partially submersed under water with just the head protruding from the water surface. A soft valve (figure 4.6d) is placed inside the head for flow regulation and pressure relieve (figure 4.6a). The rear end of the robot is replaceable to test different orifice sizes. The orifices size tested ranges from 6mm to 26mm with 2mm interval in diameter. The head (figure 4.6c) and orifice (figure 4.6g) are screwed on to the clear acrylic body (figure 4.5f) using Teflon tape and rubber oring to ensure a water-tight seal. Each design is subjected to different energy inputs to determine the most efficient gas to water ratio. The entire experiment process is automatically control by Matlab (Simulink R2018a) to ensure accurate and repeatable experimental results. Each experiment takes exactly 90s and the experimental process is outlined below:

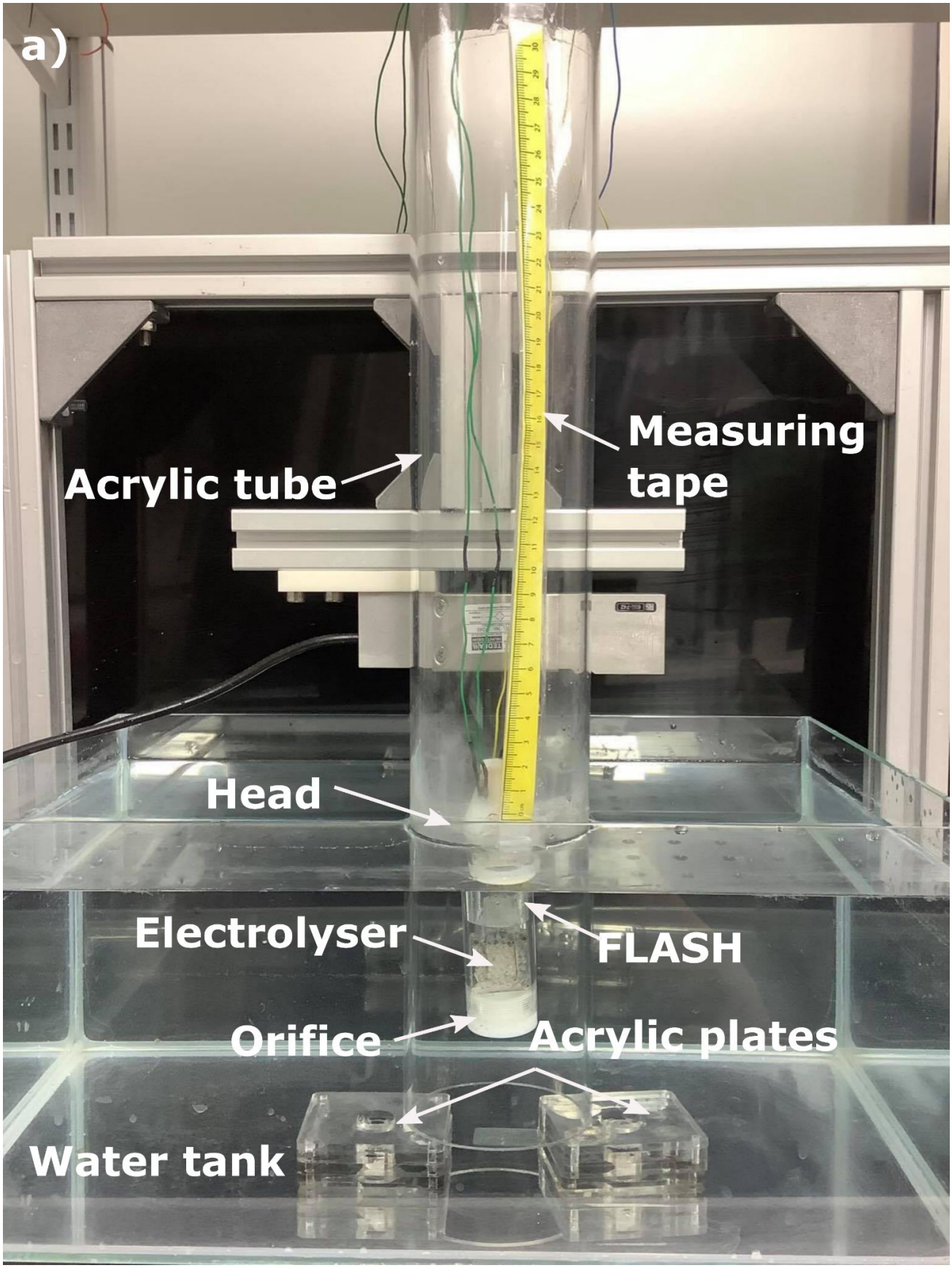

Figure 4.5: Vertical jump experiment. Vertical jump experimental set up. b) Electrolyser. c) Head valve (8.2mm diameter). d)Tail orifice. e) FLASH's Head. f) FLASH's body (hydrojetting chamber). g) FLASH robot.

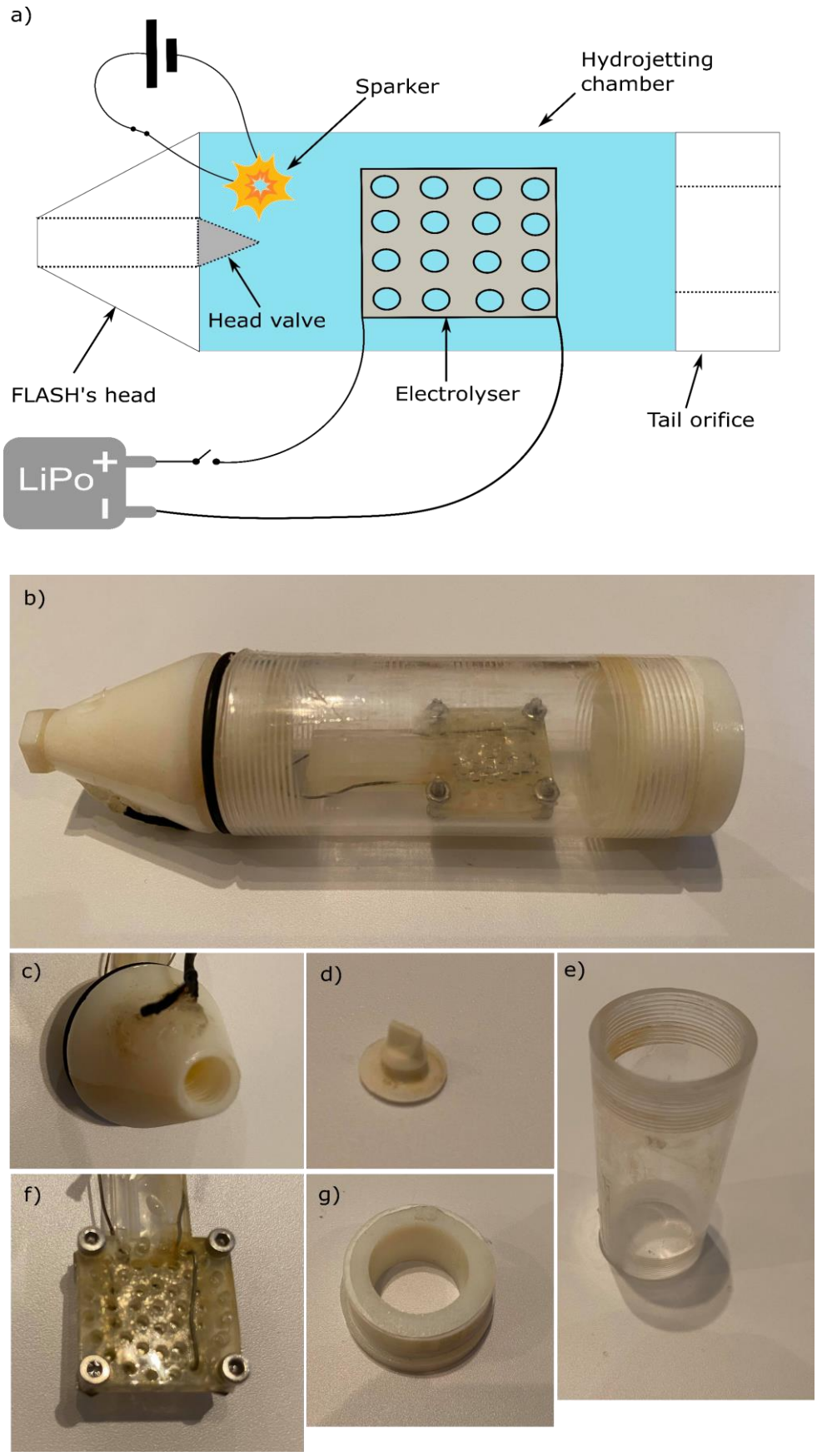

Figure 4.6: FLASH architecture. a) Cross sectional diagram of FLASH. b) FLASH robot. c) FLASH's head. d) Head valve (8.2mm diameter). e) FLASH's body (hydrojetting chamber). f) Electrolyser. g) Tail orifice.

1. The robot (figure 4.6b) is suspended inside the clear acrylic tube and filled with tap water. The tube is placed into a glass tank full of water and the base is raised by 10mm by two clear acrylic sheets.
2. The Matlab code is initiated, all the in/output channels of the DAQ are instantiated and ready for data collection.
3. The electrolytic module (figure 4.6f) is turned on for 80s with a voltage specified in the Matlab Script (ranging from 5-10V). The voltage and current are both recorded in real time by a DAQ (USB-6211) capable of reading input and output simultaneously for input energy calculation.
4. At second 88, the spark is turned on for exactly 1s causing a combustion of oxyhydrogen gas.
5. The jump height created by the oxyhydrogen explosion is recorded by a camera.
6. After 90s lapsed, all the relevant data is saved.
7. The energy input is varied by changing the Matlab script and repeating step 2-6.
8. Different orifice samples are tested by replacing the old orifice and repeating step 1-7.

4.2.2 Experiment results and discussion

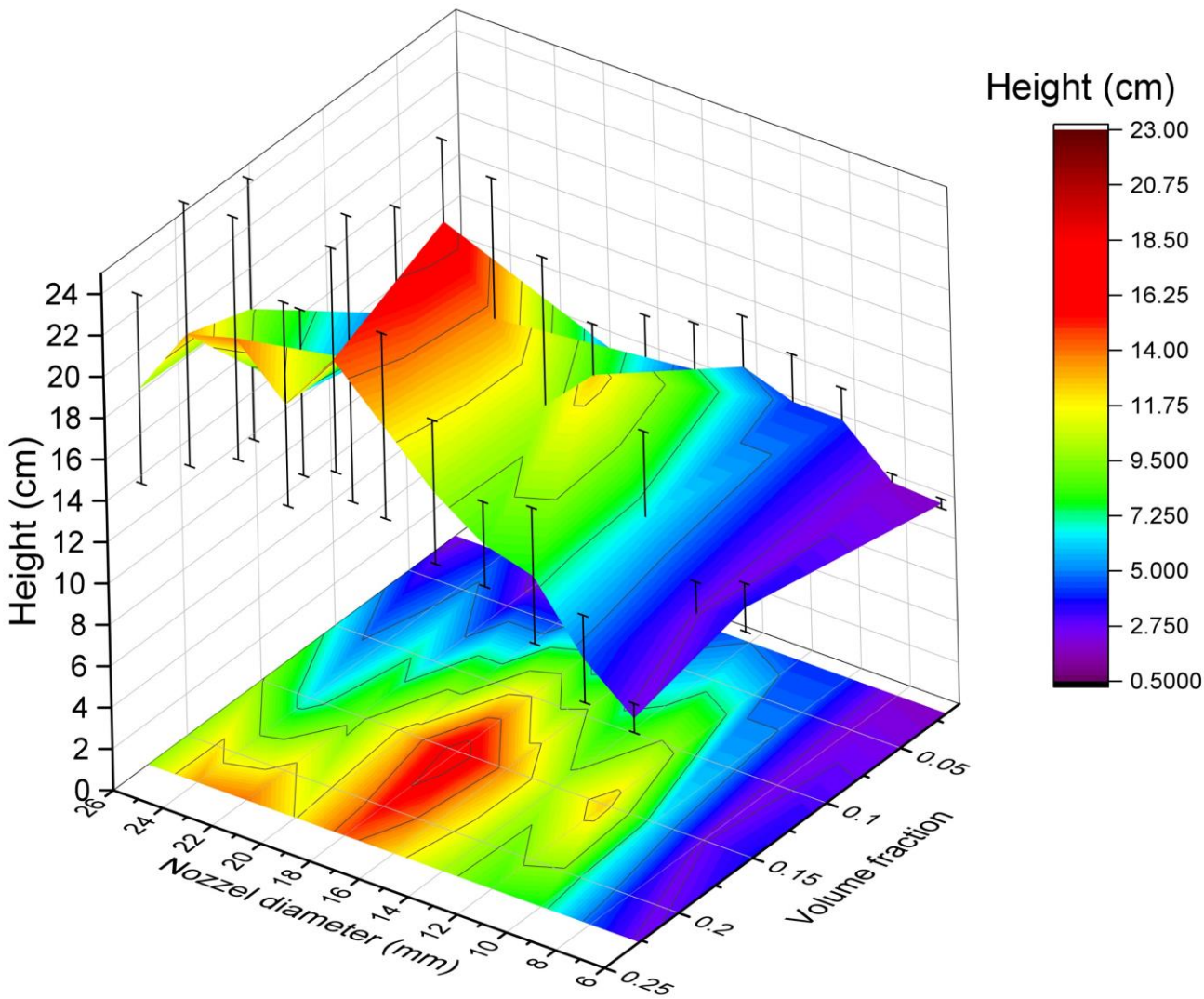

Figure 4.7: Surface plot of vertical jump height vs different nozzle diameter vs oxyhydrogen gas/water volume fraction.

Figure 4.7 shows a 3D surface plot of FLASH vertical jump height with different orifice sizes at different gas to water volume fraction. Through this experiment, it has been determined that there are several parameters which affect the jump height of FLASH. The first one is nozzle size, figures 4.7 shows that the jump height generally increases as the orifice size increases and peaks at 18mm diameter. This is expected as previous experiments show that larger nozzle size will make it easier for water to escape due to less choking and swirling. It is important to note that the jump height drops as the nozzle size increases past 18mm, this is might be due to the gas to water ratio. Previous section has clearly stated that a higher density expellant (i.e. water) is preferable to produce more efficient locomotion and with the right gas to water ratio one can optimize the locomotion performance of FLASH. Figure 4.7 indicates that this optimal ratio is 0.15 (4ml) gas to water ratio; this is equivalent to around 200J of input

energy. Combining these two parameters, it has been determined that the optimal design which produces the maximum jump height of 23 cm is 18mm diameter nozzle and the optimal gas to water ratio is 0.15. Figure 4.8A shows the vertical jump performance of the optimal parameters mentioned above. A strong flame can be seen in figure 4.8A(i) which indicates the start of the explosion. Figure 4.8A(ii) shows FLASH jumping out of water. This followed by a strong jetting phase which can clearly be observed in figure 4.8A(iii). Figure 4.8A(iv) shows the maximum jump height of FLASH at these parameters.

In addition, the combustion of the lowest amount of gas to water ratio, 0.02 (0.5ml, 50J input energy), is not powerful enough for FLASH to completely jump out of the water. Figure 4.8B (i) to (iv) clearly shows that even with the best orifice size (18mm), the robot still unable to jump out of the water. The maximum jump height in this case is about 8cm and for the robot to completely clear the water, the minimum jump height must be 10 cm (yellow and red regions on the graph- figure 4.7). This is consistent with the results observed in previous experiment in which the gas generated at this energy level cannot generate a big enough thrust to propel the robot out of the water. This, however, can be exploited for under water swimming mode in which FLASH can be operated at energy saving mode in the dark, at night or places where light cannot reach. Nevertheless, this minimum vertical jump height threshold has established an important design parameters one should consider to optimise the jump gliding performance of the robot. By examining the experimental footages in which FLASH was unable to completely jump out of the water, this could be due to small orifice size or insufficient gas or the combination of both. We also observed a suction happening immediately after the rapid expansion of gas. Similar hydrodynamic behaviour was also observed in the force response block test (see appendix B for more information). This suction dampens the jump efficiency and as such, it is important to minimise this phenomenon to improve jump performance. To address this, we added a soft one-way cross valve at the end of the nozzle to reduce the unfavourable suction. The valve will minimise the back flow through the orifice which will help the robot perform better jumps. This valve couples with the small valve at the head of the robot to regulate the flow of fluids in (through the top) and out (through the nozzle) of FLASH for optimal performance. To confirm this, we have tested the jump performance of the robot with and without the soft duckbill-umbrella valve - using the best nozzle design (18mm diameter) and running under same input energy (50J). Figure 4.8C clearly show a significant difference in jump performance between the one with valve and no-valve. The one with valve was able to completely jump out of the water (figure 4.8C(iii)) as compared to the one without (figure 4.8B(ii)), with a difference in jump height of 3 cm (figure 4.8B(iv) and figure 4.8C(iv)). This shows a 30% increase in jump height and the robot tested at this orifice size/input energy was able to jump out of the water. Finally, it is important to note that the combustion of oxyhydrogen gas to generate rapid thrusting is a complex and chaotic process which depends on many intrinsic physical and chemical variables such as gas to water ratio, reaction process, launch angle, robot geometry etc. These may explain the rather large standard deviation in figure 4.7.

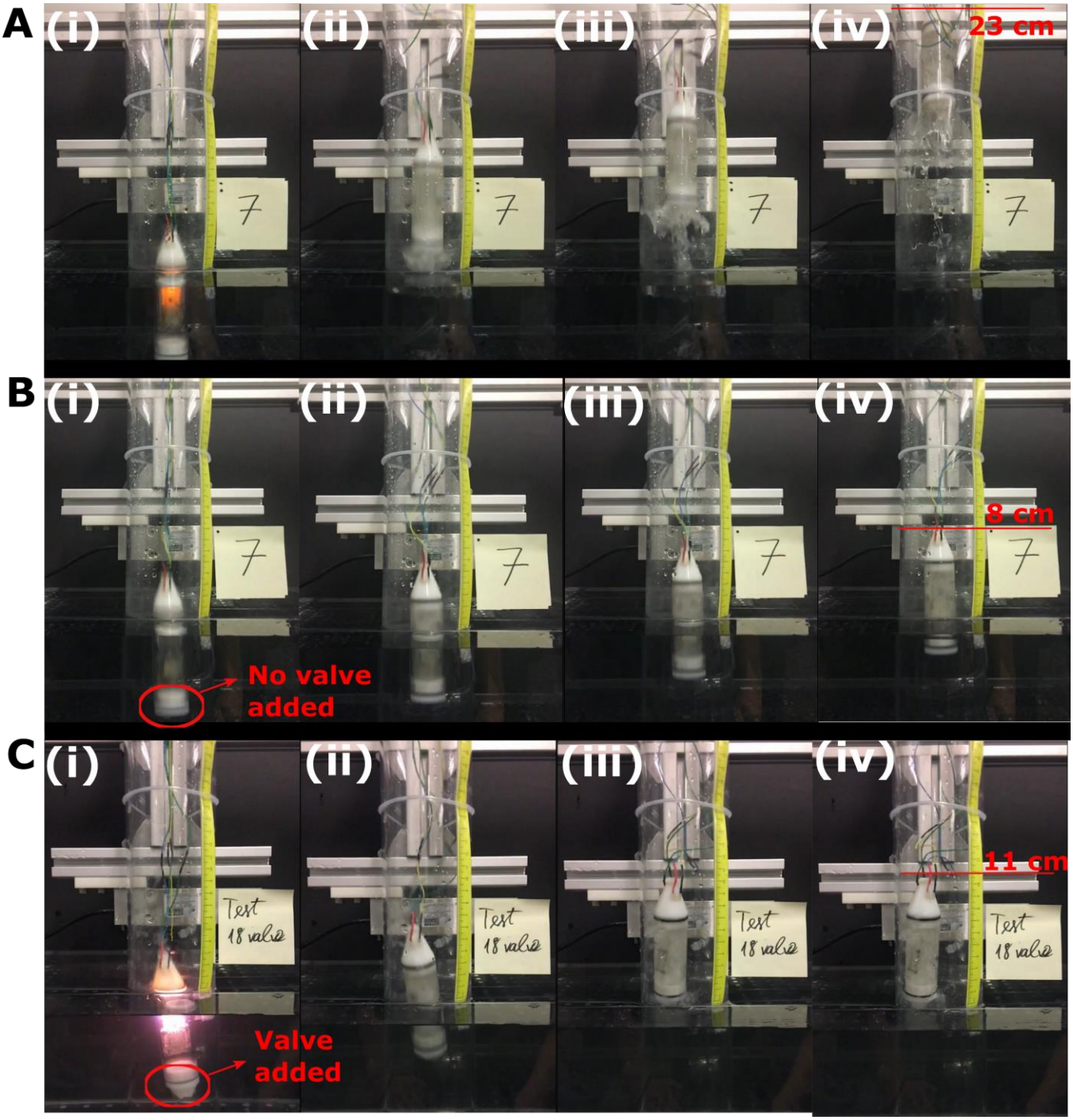

Figure 4.8: Vertical jumps test results from the 18mm orifice size. A) 200J (8V – 0.15 gas to water ratio). (i) Start of Jump (explosion). (ii) Jump out of water. (iii) Jetting phase. (iv) Maximum jump height (23cm). B) 50J (5V – 0.02 gas to water ratio) with no valve added. (i) Start of Jump (explosion). (ii) Fail to jump out of water. (iii) Jetting phase. (iv) Maximum jump height (8cm). C) 50J (5V – 0.02 gas to water ratio) with valve added. (i) Start of Jump (explosion). (ii) Jetting phase. (iii) Jump out of water. (iv) Maximum jump height (11cm).

This section has provided solid evidence regarding FLASH's ability to jump out of water. It has identified the parameters governing the vertical jump performance of the robot and established the optimal geometry and gas to water ratio which produce the maximum jump; 18mm orifice size, 0.15 gas to water ratio and 23cm jump, respectively. The minimum jump threshold for the robot to completely clear the water has been established which

allows different operation modes to be explored. For instance, a low energy mode can be used for swimming at night and the high energy mode can be used for jump-gliding. In the next section, we will visualise the water jetting flow produced by the most optimal design and explore the hydrodynamic properties the hydrojet propulsion by combustion.

4.3 Water jetting flow visualisation

This section introduces a method to capture and visualise the hydrojet produced by FLASH under vertical and horizontal orientation to gain insights into the jumpgliding and swimming performance respectively. Fluorescent dye flow visualization is one of the most well established and efficient technique designed to investigate, quantify flow structures and theorize fluid flow behaviour [289] [290] [291]. Using similar set up as discussed in section 4.1, the robot is suspended in the middle of a tank and fixed at the head. The entire fixing frame was painted black so that it camouflages with the black background and produce high quality flow visualisation. Nozzle size of 18mm and the gas to water volume fraction of 0.15 (≈200J) were used for the vertical orientation test (Figure 4.9A) as these produced the highest vertical jump (23cm) and ensure that a clear jetting phase can be observed and captured in the experiment. This test highlights the hydrojetting phase of FLASH in jumpgliding locomotion mode.

Regarding the horizontal orientation test (Figure 4.9B), nozzle size of 6mm with the same gas to water volume fraction as in the vertical orientation test were used. This nozzle size was selected because it has a longer combustion time as compared to the 18mm nozzle size. It is thought that this will highlight the difference in the hydrojetting phase at various orifice sizes. In addition, this test will verify our hypothesis that longer combustion time may lead to more efficient swimming locomotion. Matlab (2018a) was used to run the electrolyser, control the spark module and recording data. A highspeed camera was used to record the interaction between the combustion and the surrounding fluid.

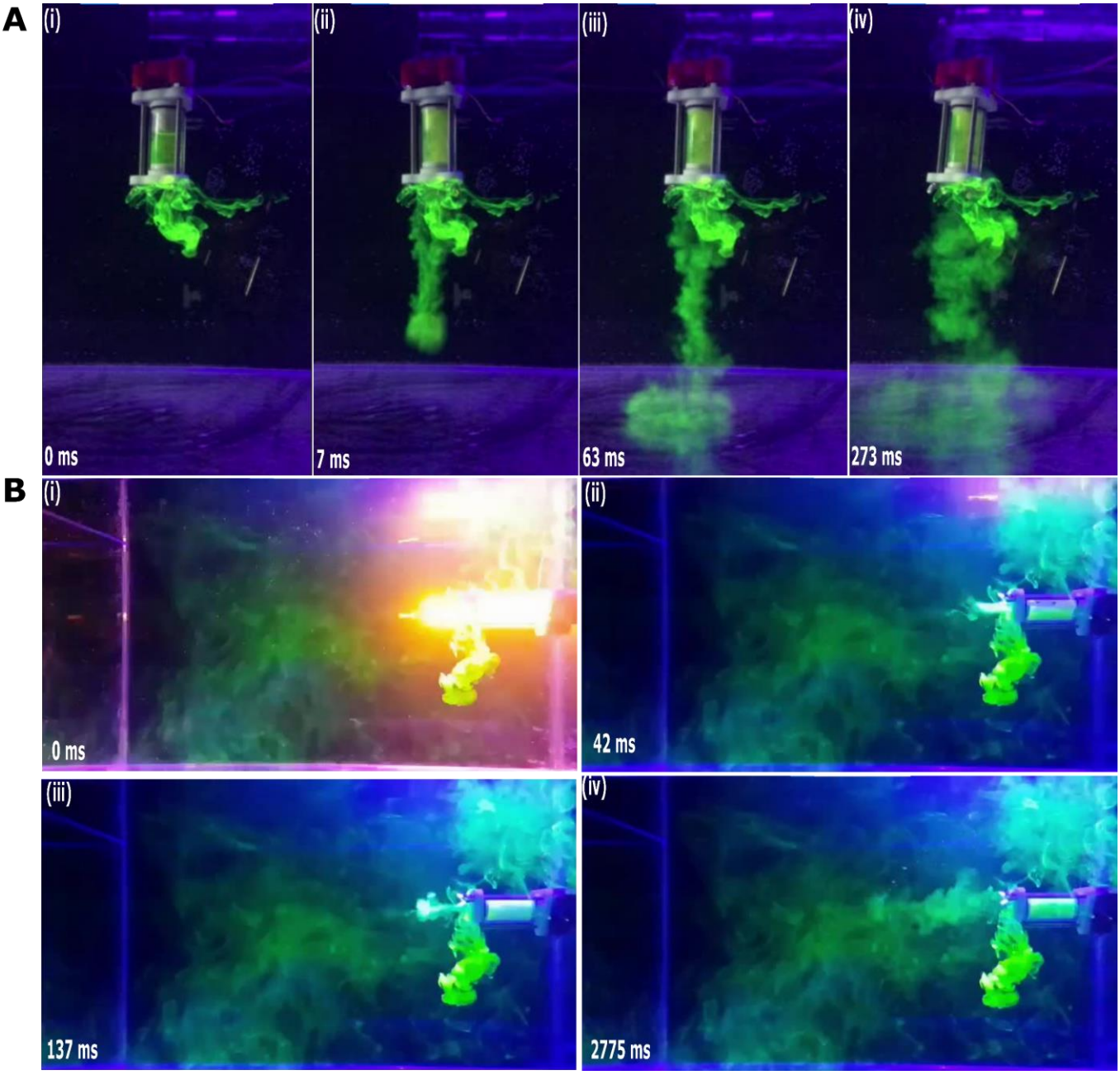

Figure 4.9: Oxyhydrogen combustion fluorescent dye flow visualisation: A) FLASH vertical oxyhydrogen combustion flow visualisation (18mm, input energy 220J (8V). i) FLASH just before the instant when the oxyhydrogen gas is ignited (start of explosion). ii) Combustion started (start of jetting phase). iii) During jetting phase (high speed waterjet form a vortex ring which hits the bottom of the tank). iv) End of jetting phase (Lots of small vortices were created around the highspeed waterjet). B) FLASH horizontal oxyhydrogen combustion flow visualisation (6mm, input energy 220J (8V). i) FLASH at the instant when the oxyhydrogen gas is ignited (start of explosion). ii) FLASH at the instant after the ignition (start of jetting phase). iii) During jetting phase (high speed waterjet form a vortex ring which hit the bottom of the tank). iv) End of jetting phase (Lots of small vortices were created around the highspeed waterjet).

4.3.1 Experimental setup

Experiments were conducted in a 60x40x40 cm glass tank filled with water. The robot was fully submerged so that the combustion hydrodynamics can be observed under water. The behaviour of the fluid during the oxyhydrogen combustion is highlighted by using an optical fluid visualization method: the addition of fluorescent dye in

combination with UV illumination. This simple/low-cost fluid flow visualization technique provides an immediate qualitative measure of how underwater combustion of oxyhydrogen interacts with a fluid by highlighting the flow pattern during the jetting phase right after the explosion. An alternative technique is the particles tracer method (PIV, Particle Image Velocimetry) where particles are added to the flow and illuminated by a laser light in order to trace the fluid pattern. PIV also allows the collection of accurate quantitative data in the form of particles velocity measurements thanks to particle image velocimetry. For our experiments, the dye was created by mixing Monument Fluorescein Drain Dye (MON1260S) with water, in accordance with the manufacturer's recommended dilution rate (250mg per 10ml of water). ≈1ml of the dye solution is added to the robot using a pipet after the desire amount of oxyhydrogen has been generated.

4.3.2 Experiment results and discussion

Figure 4.9 shows that the jetting phase last 272 ms and 2775 ms for vertical and horizontal tests respectively. As can be seen from figure 4.9A(i), B(i), after the dye was added to the robot, there are some diffusion of the dye leak through the nozzle. This is expected and is a common phenomenon. However, to obtain high quality flow visualization, it is important to minimise this effect by either performing the combustion shortly after the dye was added or adding a soft valve at the end of the orifice to limit the diffusion. In this experiment, we chose the first option due to its simplicity. It is also to keep it consistent with the thrust characterisation experimental results. This is because we did not use the soft valve in that experiment and we would like to have comparable results between the thrust characterisation and flow visualisation experiments. The second option will be considered in future work as adding a soft valve at the end of the nozzle has shown to improve the vertical jump performance of the robot (previous chapter). Figure 4.9 A(i), B(i) captures the instant when the oxyhydrogen gas mixture was ignited. It is interesting to note that the flame was clearly seen in 4.9B(i), however, no flame was observed in 4.9A(i). This could be due to several factors. Firstly, the flame is so small it cannot be seen under the lighting condition. Secondly, combustion of all H_2 and O_2 gases after explosion creates a suction effect and sucks the liquid back into the chamber (figure 4.9A(ii)); this hinders visibility. Finally, the propagation speed of the flame maybe too fast to capture with the highspeed camera used (running at 240 fps). Note that the same camera and settings were used for both tests. This results, however, further support the hypothesis that the combustion time is dependent on geometry.

In figures 4.9A (ii) and 4.9B(ii), highspeed jets, highlighted by the fluorescent dye path, can be seen escaping the nozzle causing significant turbulence in the tank. From the timestamps, it can be seen that the 18mm (horizontal) nozzle produce a much faster waterjet than the 6mm (vertical) nozzle (7 ms compared to 42 ms). This suggests that a faster thrust was generated by 18mm diameter nozzle. This is desirable in jumpgliding locomotion where

fast powerful thrust is required to break the surface tension. Moreover, upon investigating the highspeed footage, the waterjet also generates a significant number of counterclockwise vortices (figure 4.9A(iii)).This can also be seen in the supplementary movie S3 where the fluorescent dye dispersed rapidly into the surrounding water. With respect to the 6mm nozzle size, the highspeed jet forms a vortex ring (figure 4.9B(iii)) which propagates through water at a seemingly much lower speed than that of 18mm nozzle (see supplementary movie S4).

The end of the jetting phase is set to be when there are no longer any significant disturbances in the tank (no visible fluorescent vortices can be seen). As can be seen from figures 4.9A(iv) and 4.9B(iv), the jetting phase of the smaller orifice is approximately 10 times longer than that of the larger orifice (273 ms compared to 2775 ms). This observation suggests that a longer combustion time could potentially generate a more efficient swimming locomotion. However, further tests using particle image velocimetry are required to quantify and confirm this hypothesis as the fluorescent dye flow visualisation does not provide a quantifiable solution to support the claim.

The fluorescent dye flow visualization has highlighted (visually) interesting hydrodynamic behaviours of the waterjet produced by the combustion of oxyhydrogen. The highspeed camera footage shows that a strong thrust produced in a short period of time generates many vortices, causing significant turbulence in the surrounding water body. In the next section, underwater locomotion of FLASH will be investigated in detail.

4.4 Underwater locomotion

To ensure the consistency in the robot performance, underwater swimming tests will be carried out with the same combustion chamber using the best nozzle size obtained from the vertical jump test (18mm). The input energy will be kept at 200J which will give 0.15 gas to water ratio. These parameters were used to obtain the best vertical jump experiment. By using the same parameters, it is thought that FLASH would be able to perform both out of water and underwater locomotion without further trade-off between jumping and swimming performance. In this experiment, the same design of FLASH as described in the previous section will be used.

4.4.1 Experimental setup

The swimming test was carried out in a 200 cm (diameter) x 100 cm (height) tank outdoor. A rotating system is placed in the middle of the tank to test the swimming efficiency of FLASH (see figure 4.10). The robot is placed about 15cm underwater and fixed to a rotating rod through a hollow L-shaped aluminium tube. The length of the tube is 40cm, the diameter is 10mm and the thickness is 1mm. Moreover, the L-shaped rod is place just above the water surface to avoid introducing additional drag when the robot is running. All the electrical wires were run inside the hollow supporting tube to avoid water damage and interference. A shaft incremental optical encoder is installed onto the rotating rod to record the displacement of the robot. The rotating rod is fixed at both ends to a

heavy aluminium base and a cross bar via freely rotating ball bearings as seen in figure 4.10 to prevent unexpected movement of the rod during combustion process. The experiment is controlled using a matlab code which records the input energy into the electrolyser and the displacement of the optical encoder. A camera (iPhone 11 pro) is used to record the robot locomotion underwater.

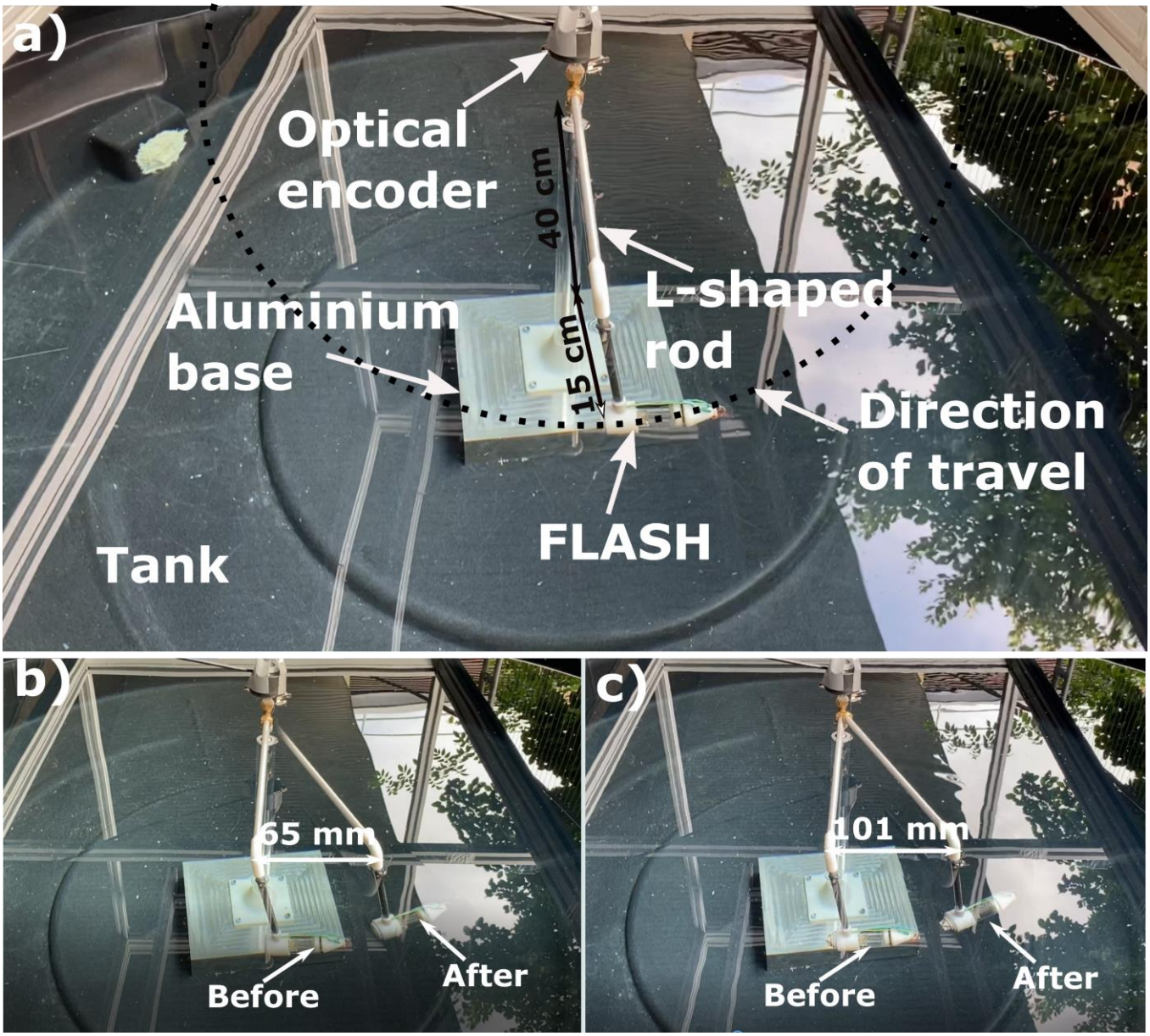

Figure 4.10: FLASH underwater locomotion. a) Experimental set up. b) FLASH no valve swim test. c) FLASH with valve added swim test. The position of FLASH after the explosion finish has been superimposed on the image of FLASH before the explosion in a and b.

4.4.2 Experimental results and discussion

Figure 4.11 show FLASH tethered swim test results. The results indicate that FLASH is capable of swimming underwater with the average swimming distance of 65mm ± 14mm per explosion (figure 4.10b and supplementary materials movie S5). The furthest and shortest distance travelled recoded for this experiment is 77mm and 49mm

respectively. The large standard deviation is due to the highly chaotic and complex nature of the combustion process. The formula used to calculate the distance is described below:

$$\text{Distant travelled} = (\text{encoder reading (deg)} / 360) \times (2\pi r)\ (\text{mm})$$

Where the encoder reading is converted to degree and r is the length of the L-shaped tube (400mm). Further experiments were carried out to optimise the swimming performance of FLASH. Section 4.2 indicates that adding a soft valve at the end of the nozzle would improve the jump height of FLASH by as much as 30%. As such, in these further tests, a similar soft cross valve is attached at the end of the nozzle (figure 4.10c). As expected, the swimming distance increased by 35% to 101mm (figure 4.11 and supplementary materials movie S6). This indicates that the robot overall efficiency can be improved by regulating the water intake during the combustion process.

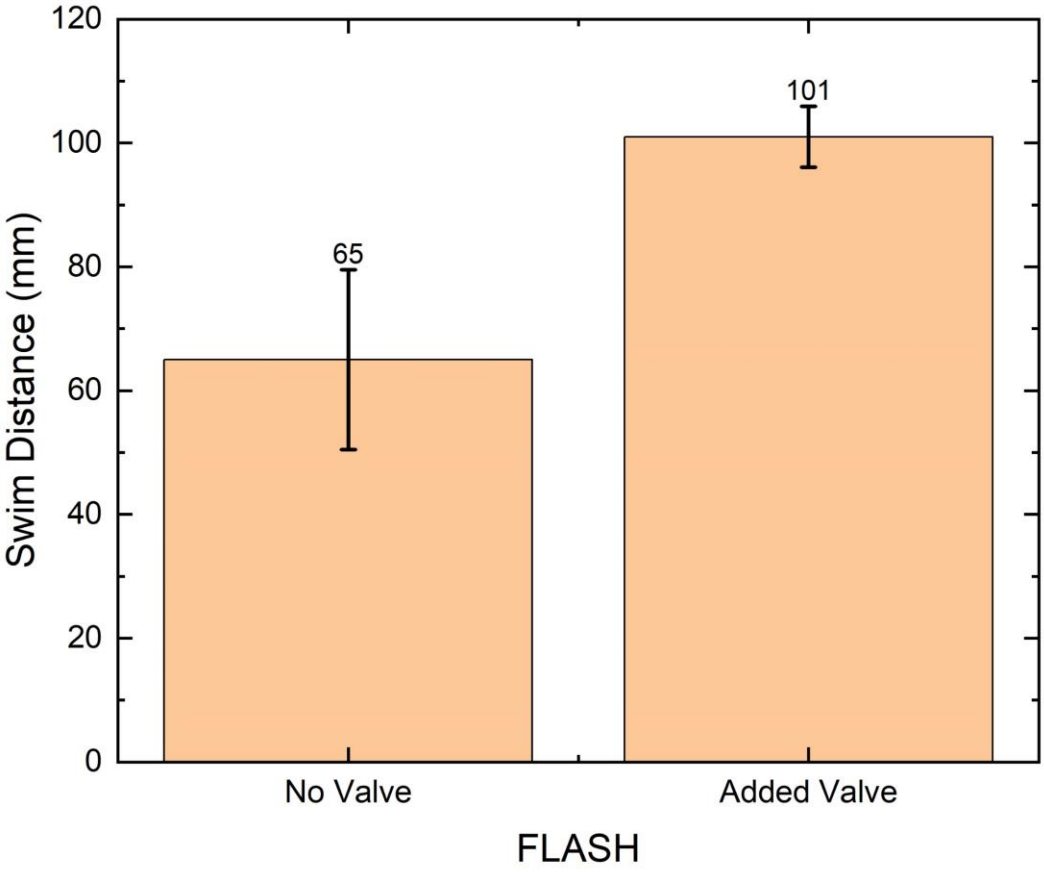

Figure 4.11: FLASH tethered swim test results for the two cases of no tail valve and added tail valve.

To showcase the underwater locomotion of the robot, we have carried out an unconstraint tethered test in which FLASH is allowed to freely swim inside the tank with only thin wires connect to an external power source (figure 4.12a). A small styrofoam (20x20mm) is attached to the head of the robot to ensures that the head of the robot is always higher than the tail of the robot. This prevents the oxyhydrogen gas generated from escaping through the

open end and ensure the spark module, located at the head of the robot, can ignite the combustible gas efficiently (figure 4.12a). It took roughly 80s for the FLASH to float up from the bottom of the tank to the water surface with the head slightly poking out of the water (figure 4.12 a to c). This is expected as 80s is also the time the electrolyser operates. Upon ignition, the robot quickly swims through the water before sinking back to the bottom of the tank. Figure 4.12d shows the start of the explosion, a power thrust was created which allows the robot to surf on the water surface. This can be seen clearly in figure 4.12e where multiples vortexes were left in the travel path of FLASH. This phenomenon is similar to what normally seen in stone skipping in which the rock (in this case FLASH) generated lift by pushing water down as it travels across the water at an angle. This might allow the robot to travel greater distance if the conditions are met. However, it is important to note that this could depend on many factors such as the robot geometry, its floating angle and its weight. As such, this could be explored in future work with an untethered FLASH design. FLASH's underwater locomotion can be described below.

1. Gas generation (sinking underwater)
2. Floating to water surface (buoyancy change)
3. Jump out of water
4. Surfing (jumpgliding)
5. Sink back to underwater (buoyancy change)

This is similar to that of a submarine and has been observed consistently through multiple attempts (supplementary materials movie S7).

This section has demonstrated the ability of FLASH to swim efficiently underwater. The valve system designed to regulate the flow of fluid during combustion has been proven to increase the performance of the robot significantly. It is thought that by manipulating the buoyancy of the robot, different operation modes can be achieved. For example, the gas to water ratio can be controlled to enable the robot to move around underwater or float up to the water surface and jump out of the water (supplementary materials movie S7). This will be explored in the next chapter in which an untethered version of the robot is developed.

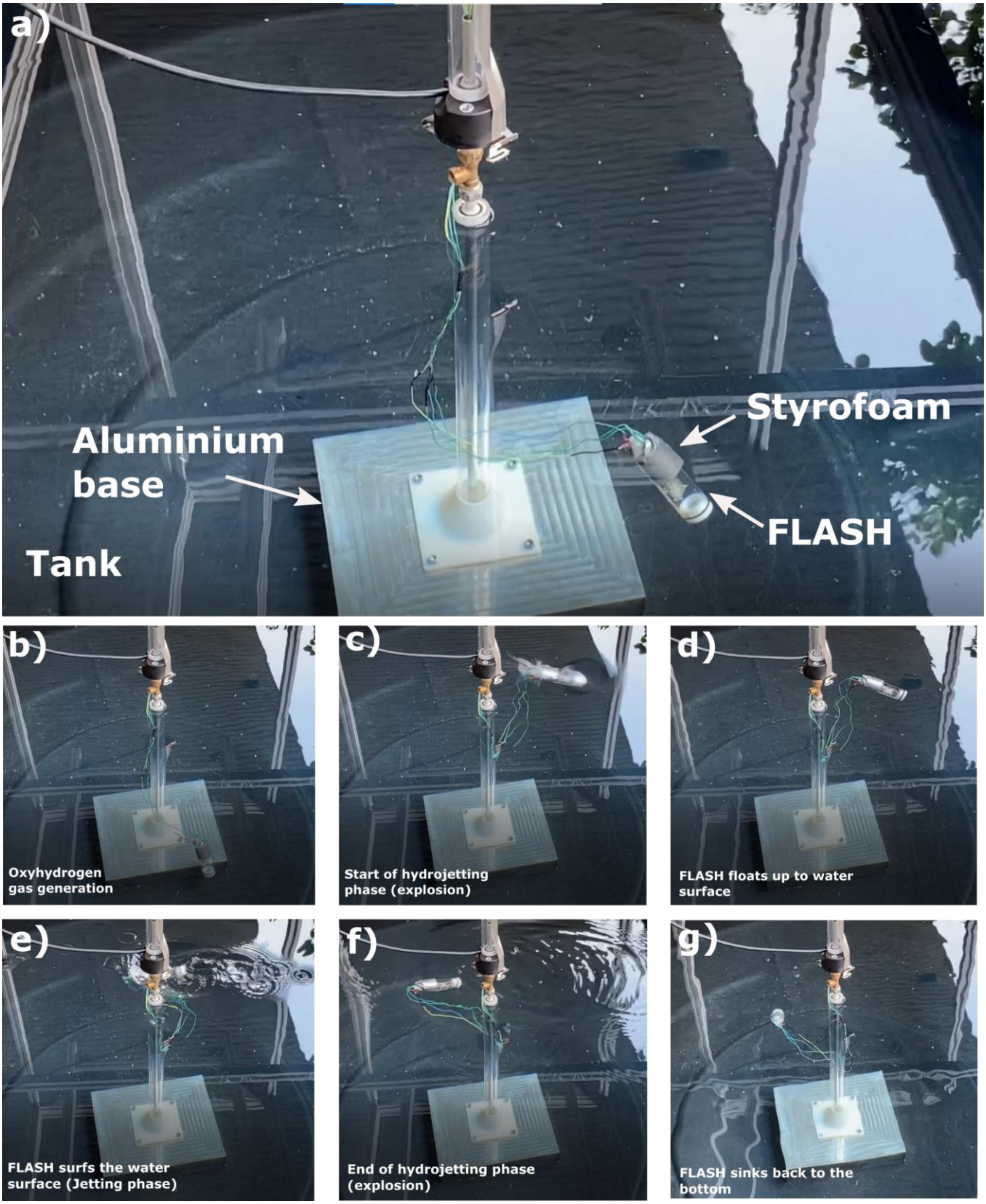

Figure 4.12: FLASH tethered unconstraint swim test. a) experimental set up. b) Electrolyser turned on to generate oxyhydrogen gas. c) FLASH floats up to the water surface due to change in buoyancy, the Styrofoam attached around the head of the robot ensure it float at the right orientation for optimal performance. d) Start of the explosion. e) FLASH can be seen surfing the water due to the hydro-jet produced from the explosion. f) End of the explosion. g) FLASH sinks back to the bottom of the tank due to the change in buoyancy.

Chapter 5

5 Untethered FLASH

Building upon the experimental results from the previous chapters, we now undertake the development of an untethered FLASH robot, including the mechanical system, software, and electronics. The robot is demonstrated operating underwater for an extended period of time without supervision. We also demonstrated the robot's capability to recharge itself when encountering a light source and float up when the battery runs out for data collection and recovery. Such performance is possible due to FLASH's unique propulsion system and reliance on a single actuator, which triggers the reaction and combustion process. This also allows the entire system to be waterproof, increasing its reliability.

5.1 FLASH mechatronics

Figure 5.1 shows the untethered FLASH robot. It is composed of similar components as described in section 4.2.1. With an addition of a soft 20mm diameter cross valve (minivalve) to the rear end to optimise performance and flow regulation. We also added some fins to the screw-in rear end part for aesthetics. The flexible solar cell (Powerfilm - 0.066W Mini Flexible Solar Panel) is wrapped outside the robot body and Styrofoam floats are adhered around the solar cell to increase the buoyancy of the robot and ensure that the solar cell is always facing up for optimal light energy harvesting. The flexible solar cell is waterproofed with a double-layered of clear polythene tubing (38mm width) and heat sealed. A photodiode (Vishay, BPW34 IR + Visible Light Si Photodiode, 65 °, Through Hole) is placed on top of the solar cell to monitor light intensity and instruct the robot to stop for charging when it encounters a light source. To ignite the oxyhydrogen generated by the electrolyser inside the robot, a spark module capable of producing a high-power electric arc, similar to the circuit commonly found in electric lighter, was used. This provides a reliable ignition source for underwater operation as the electric arc can not only provide the spark energy needed to ignite the gas but can also act like a glow plug to burn off excess moisture around the electrodes. This will prevent the sparker tips being fused together when in close proximity, hence, extend the life-time of the sparker. The spark module is waterproof with heat shrink tube and hot glue.

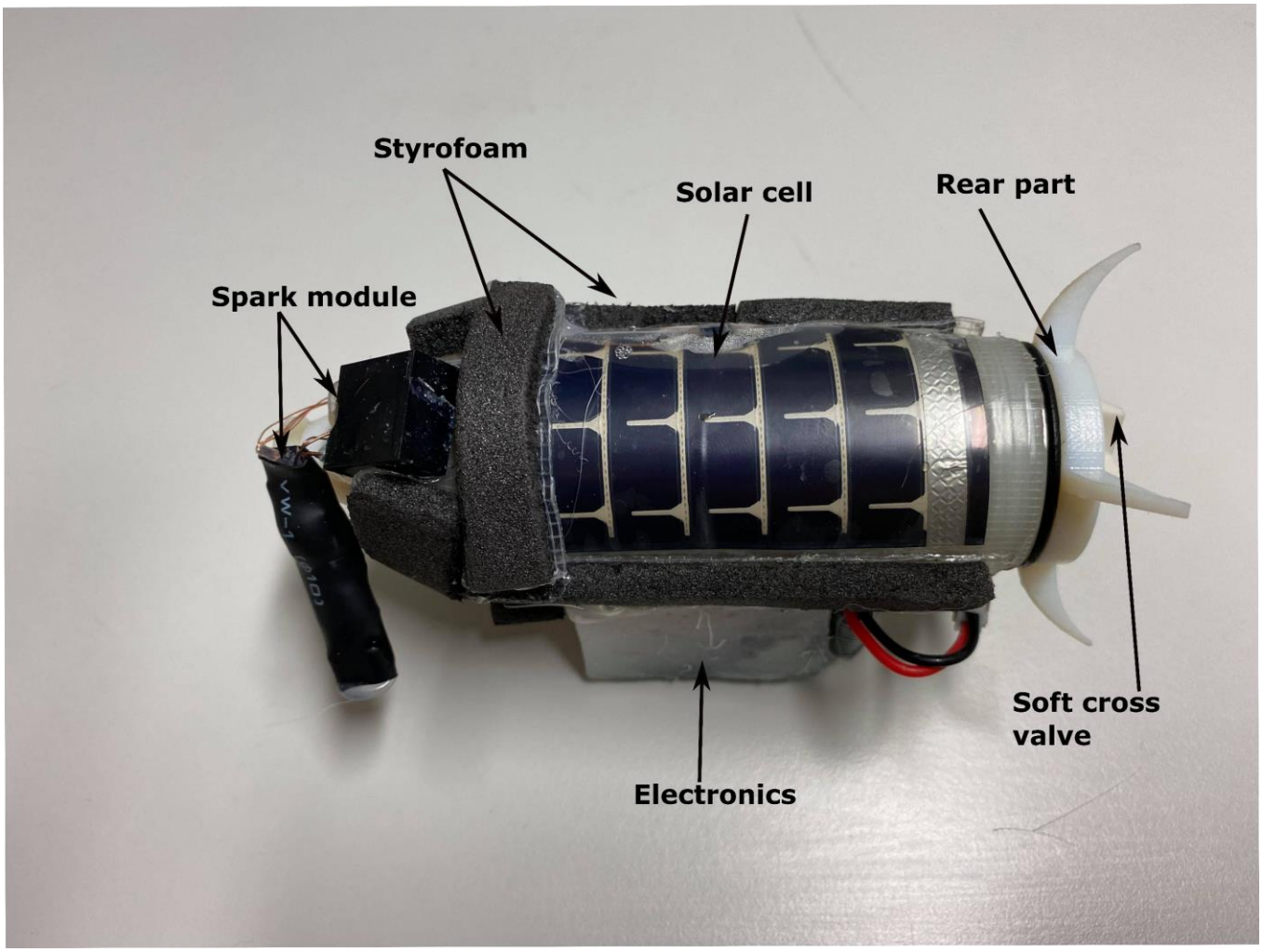

Figure 5.1: Untethered FLASH robot prototype.

The electronics used to control the robot is a miniaturised replication of the system described in section 3.1 with surfaced mount components and a thin PCB board. The Arduino chip is replaced with an ATTiny85 chip which is sufficient to control the robot. Figure 5.2 A-C detail the schematic, board design and soldered board of FLASH's onboard electronics respectively. The board and its associated electronic components are dipped in silicon rubber (Smooth-on Vytaflex 20) for waterproofing.

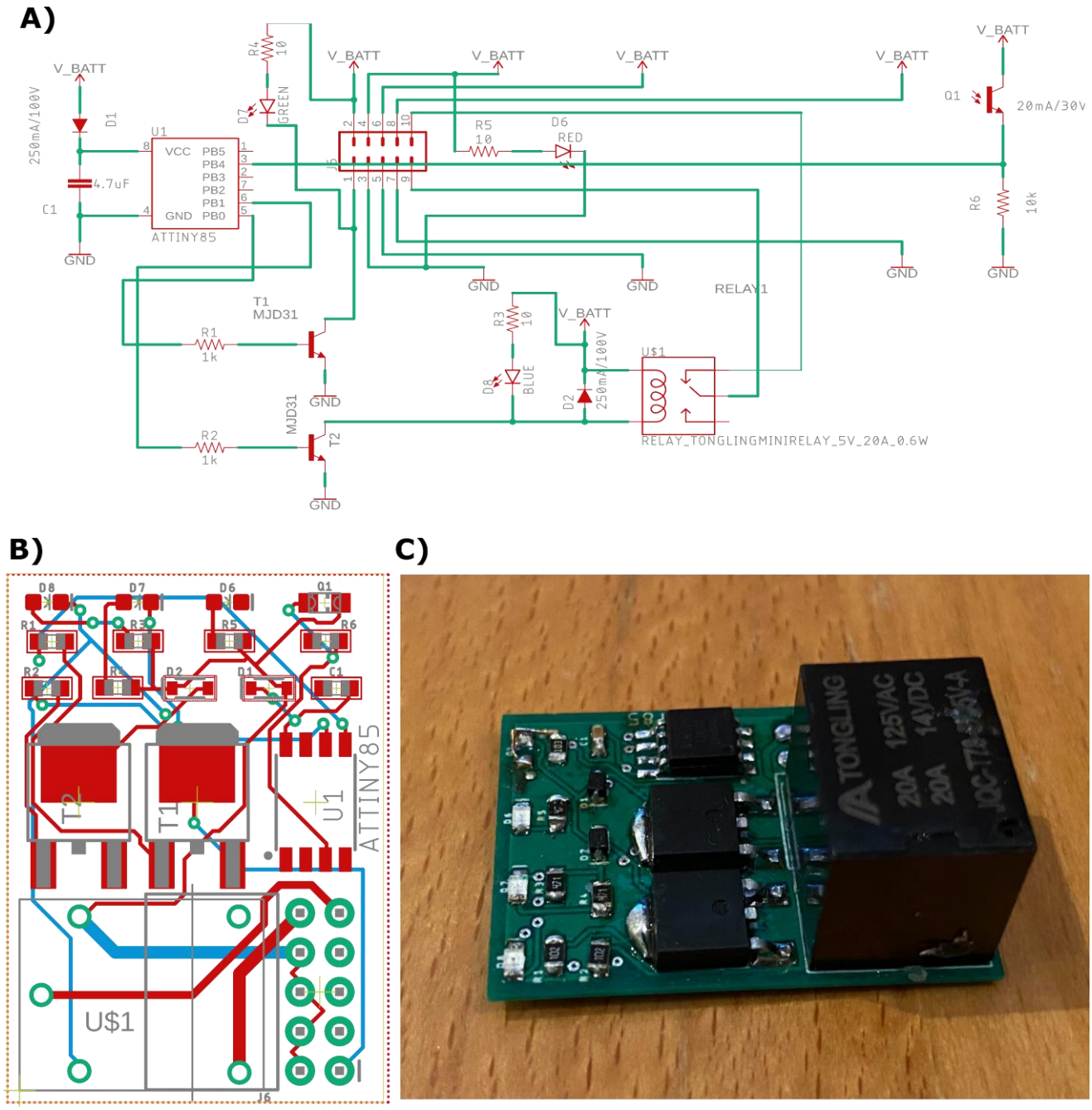

Figure 5.2: FLASH electronics. A) FLASH electronic schematic. B) FLASH board design. C) FLASH electronic board.

As can be seen from figure 5.2 A, the robot is controlled using an ATTiny85 chip. This chip offers a compact yet powerful micro controller which is suitable for this particular application. Moreover, it uses the same programming language as an Arduino which makes the transition to this prototype seamless. Two digital outputs from the Attiny85 chip control two power transistors (MJD31-Mouser) which drive the electrolytic module and the sparker. The electrolyser is turned on for 9 minutes to generate the desired amount of combustible gas mixture. After that, the sparker is turned on for 1 second to ignite the gas mixture. This is done via a signal which is sent to an electromagnetic relay to close the switch of the spark module which produce a high-power electric arc. The whole system is powered by a 3.7V 270mA LiPo battery. The analogue input of the attiny chip is connected to the photodiode which constantly monitors the light intensity of the environment. When the ambient light exceeds a

certain threshold, this signifies the robot has encountered a light source, the chip is put to sleep and the robot stays in the area for a period of time to charge up the LiPo battery. The chip is put to sleep using a watchdog timer function which wakes up every 8 seconds to check if the robot is still within the light source. If this is the case the robot will go back to sleep and wakes up after a further 8 seconds. This cycle keeps repeating until the robot drifted away from the light source, the ambient light falls below the threshold or the robot has been charging for a predetermined amount of time. The robot then fully wakes up and carries on its normal routine. Figure 5.2 B shows the board design layout and figure 5.2 C is the soldered-up board from the design layout.

5.2 Experimental set up

The untethered test was carried out in the outdoor tank, (see 4.4.1). A Grasshopper 3 vision camera (FLIR-USB3 Vision) with a Canon EF 24 lens was used to record a time lapsed video of untethered FLASH underwater swimming performance at a capturing speed of 1 frame per second. The camera was fixed 2 meters above the tank on to an aluminium frame so that it can provide a top view of the entire tank. The camera was set to continuous recording until stop and the entire recoding period was about 24 hours. However, the robot only operated for around 12 hours before the battery ran out completely and floated up. As such, the time lapse video is cut to show only when FLASH is active. The camera is connected to a laptop (Dell latitude 7390) which runs a specialist vision software (Flycapture2) to process the recoded time lapse video. A custom-made halogen spotlight was fixed at the side of the tank to provide a light source to recharge the robot (see figure 5.3). The spotlight was made from a housing and lens of a commercial 3W LED pinspot light (Amazon), the LED light bulb was replaced with a 20W, 12V Halogen bulb to provide higher light intensity. A cooling fan (5V Raspberry Pi fan) was connected in parallel with the light bulb to provide necessary cooling for prolong operation. A adapter/housing for the replacement light bulb and the fan was 3D printed and hot glued to the commercial part.

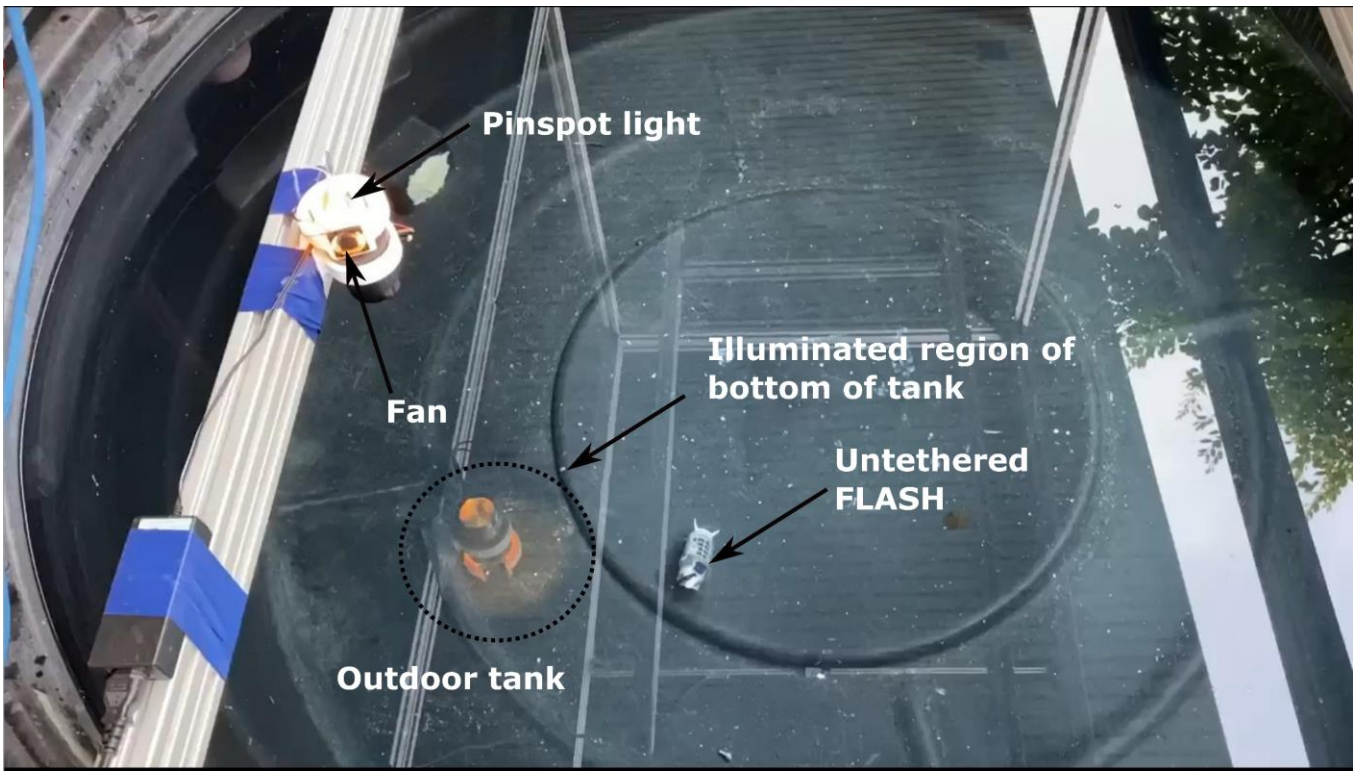

Figure 5.3: Untethered FLASH underwater locomotion experiment setup.

5.3 Experimental results and discussion

The experimental result shows that FLASH is capable of operating underwater for a long time and exhibits interesting behaviours which could be beneficial for environmental applications. As can be seen from the supplementary video S8, the robot can swim well underwater and can cover the whole area of the tank during its operation. It can also operate continuously for 12 hours which is better than similar environmental robots reported in literature [265], [292]. This makes FLASH a good candidate for environmental monitoring and search and rescue tasks where the robots are often required to operate for a long time to collect data and able to cover a large area. Figure 5.4 shows how FLASH compares to similar state-of-the-art robots reported in the literature using six key metrics. The graph clearly shows that FLASH (thick dark purple line) is capable of consecutive thrust generations via combustion of oxyhydrogen gas and is smaller in terms of size and weight compared to other jump/gliding robots. We are aiming to improve the robot flying and/or jumping/gliding performance in future work.

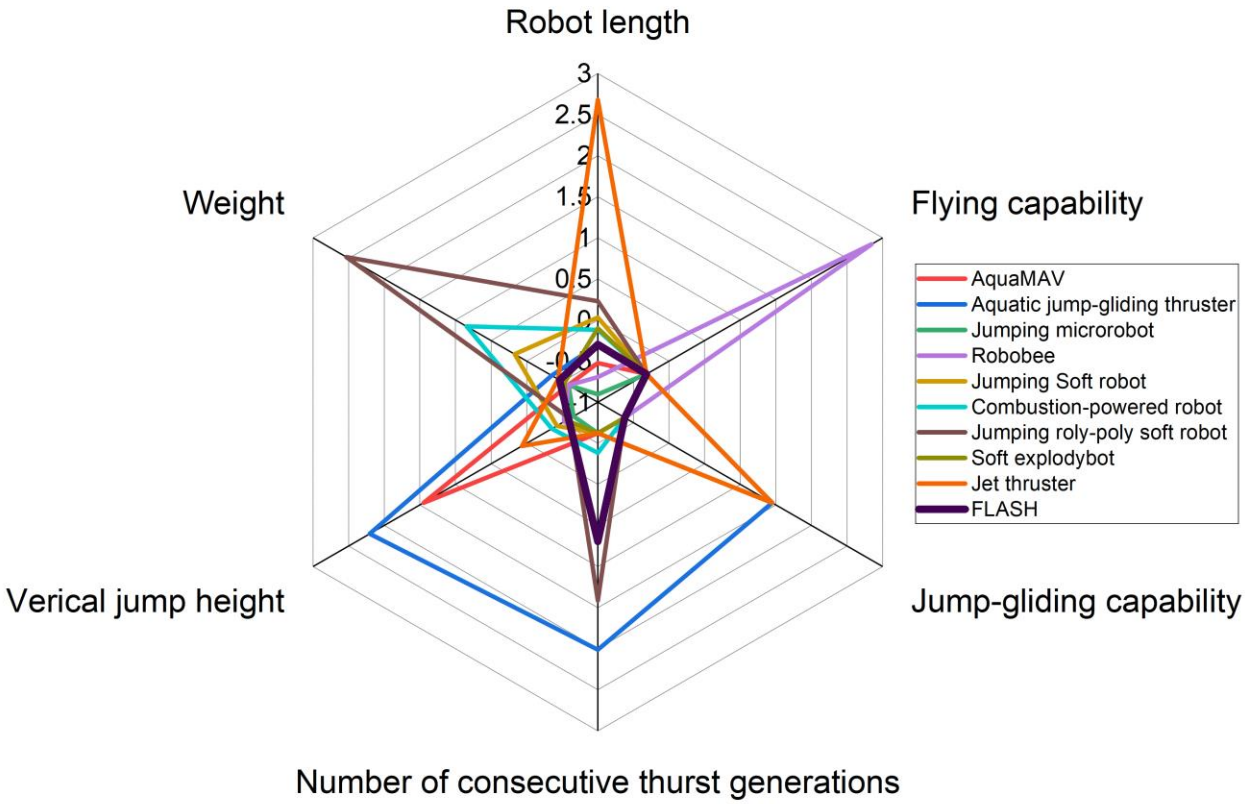

Figure 5.4: FLASH key metrics performance compare to similar state-of-the-art robot in literature [263], [265], [266], [283]–[288].

Figure 5.5 a to d illustrate different operational states of FLASH. The robot starts at the bottom of the tank fully submerged (figure 5.5a). FLASH then will turns on the electrolyser to split the water into oxyhydrogen gas and use it for combustion which produce thrust to propels it forward. This process is repeated multiple times to create locomotion, this is defined as random swim. The green line in figure 5.5b shows the robot travelling path and the red circle indicates the robot position. Figure 5.5c shows that when FLASH encounters a light source, it would stop to charge its battery. After the battery has been sufficiently charge, the robot resuming random swim. Figure 5.5d

clearly illustrates this as the robot propels away (red circle) from the illuminated area. This feature allows the robot to potentially operate indefinitely and fully integrate with the environment to carry out various tasks.

FLASH can also adjust its buoyancy to float up to the surface when the battery runs out by splitting water into hydrogen and oxygen without igniting them. The excess gas adds buoyancy to the robot and causes it to float up for data collection, recovery and/or maintenance. This allows FLASH to have different modes of operation. Figure 5.6 illustrates the operational state diagram of the robot. The first is underwater swimming in which the robot performs a random swim. The second is hibernating in which the robot would come into sleep mode to charge its battery when it encounters a light source. The third is floating when the battery runs out. In addition, it is possible to ignite the excess amount gas generated in the third mode which would propel the robot out of water, as demonstrated in section 4.2. This would be beneficial for traversing different terrains and expand the robot functionality (figure 5.6 black dotted lines). Untethered and unsupervised jumpgliding is a complex process and command significant further investigation. As such, this fourth mode of operation would be explored in future work.

FLASH's takes exactly 9 minutes between combustions and the thrust generated from the explosion propels it forwards. It is thought that the unique propulsion mechanism could also allow the robot to clean the surroundings through producing burst of waterjets every time it moves and clean of the debris along its path. This could be very useful in environmental remediation applications. Moreover, the propulsion mechanism employed is clean and produce no waste where the products of the water electrolysis process is recombined into water via combustion. As such, FLASH will not negatively affect or alter the surrounding environment during deployment which is one of the main criteria when one evaluates the performance of an environmental robot.

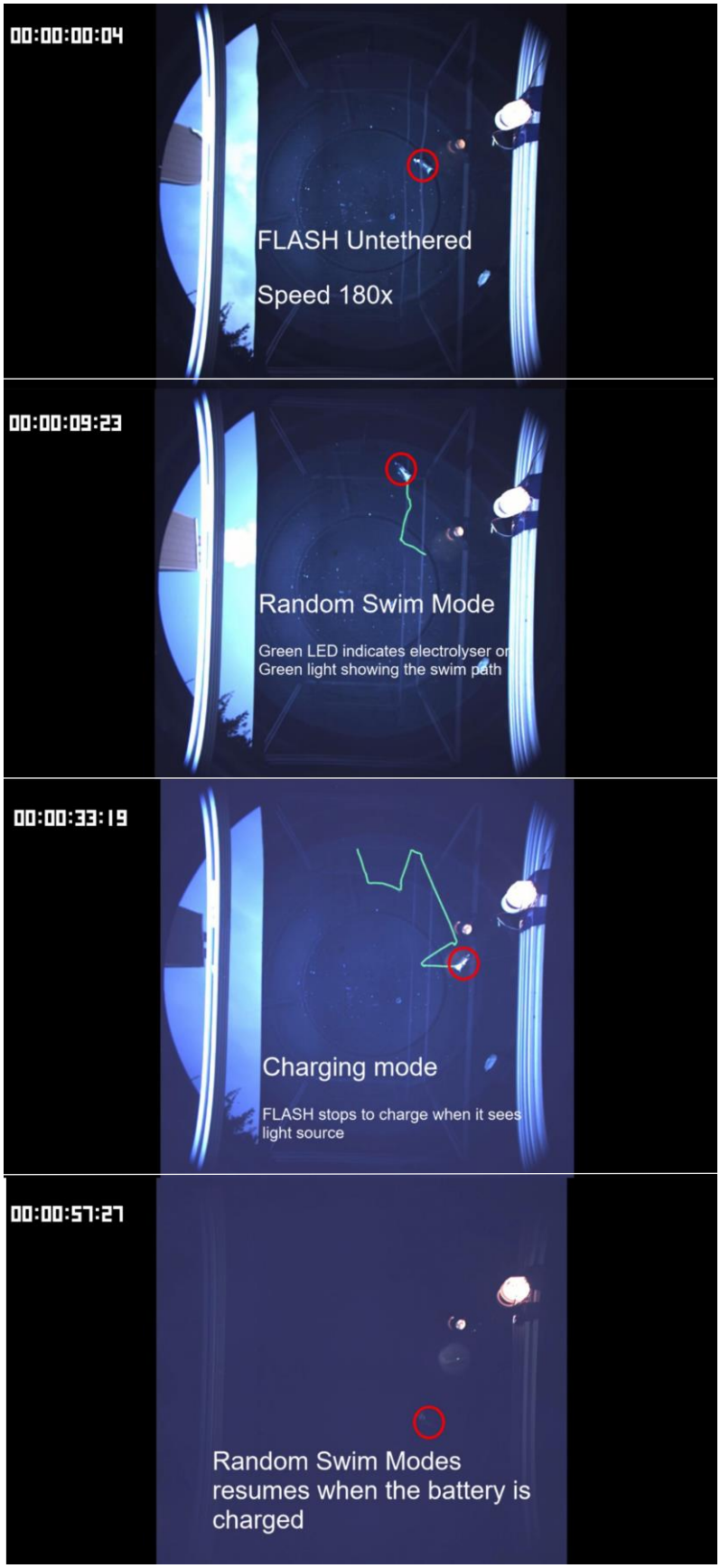

Figure 5.5: Untethered FLASH underwater locomotion. a) FLASH sits at the bottom of a water tank. The video speed is 180x (i.e. 9 mins = 3s in the video). b) FLASH performs random swim. The red circle indicates the position of the robot, the green light indicate its travel path. c) FLASH stops to charge its battery when it sees a light source. d) FLASH resumes random swim after the battery is sufficiently charged.

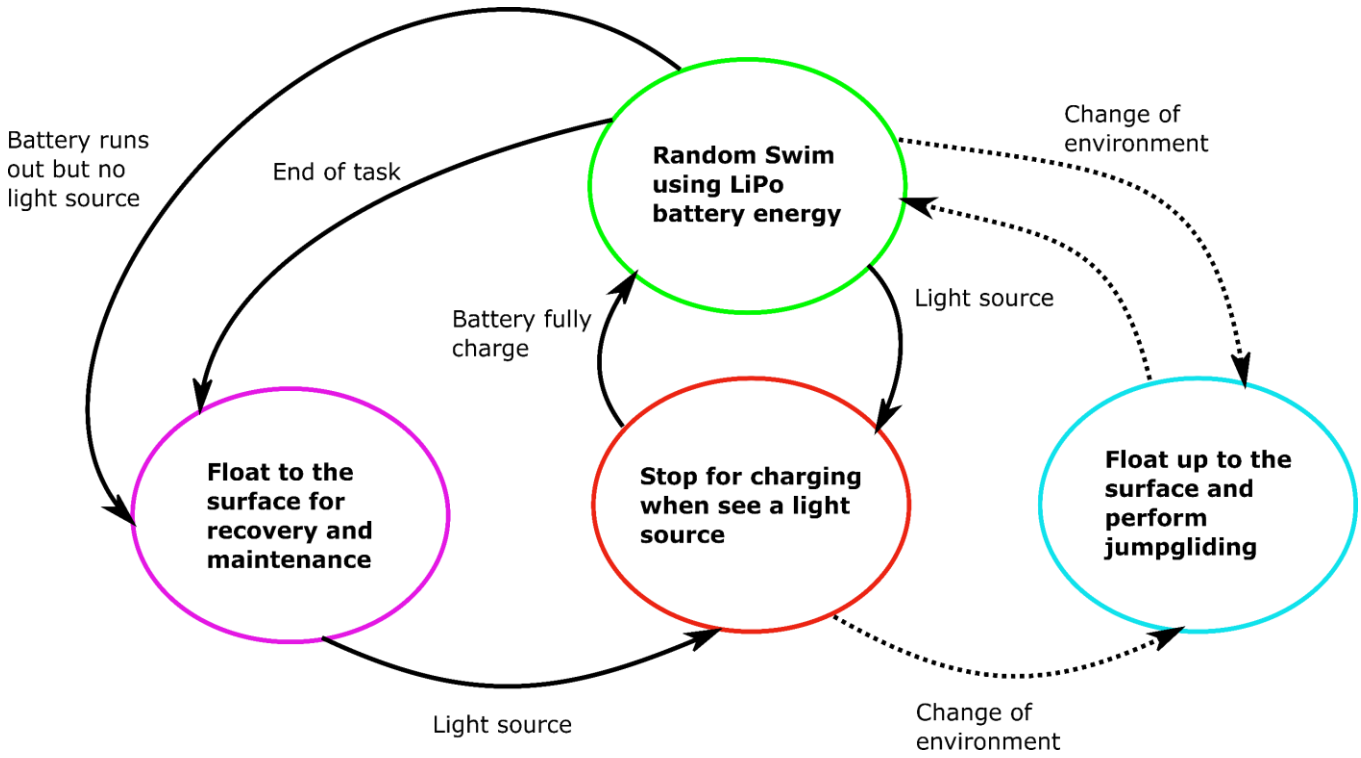

Figure 5.6: Operational state diagram of FLASH. The solid black lines show the robot current capability, the dotted black lines show the robot potential capability.

In summary, this chapter has demonstrated that FLASH is a well-suited robotic platform for environmental applications owing to its attractive features of long operating time, recharging using renewable energy, clean and harmless propulsion system, and ease of maintenance. The prospect of environmental robots capable of fully integrating with the environment presents a green solution to address many urgent environmental problems. FLASH represents a new class of smart light driven environmental robots which open ups many interesting research areas. One of them is combustion within a soft body. It is thought that soft materials would enable more efficient underwater locomotion and provide the compliance the robot needs to interact safely with the environment. This would further enhance the performance and trust worthiness of FLASH as an environmental robot. As such, in the next chapter, we will present my initial investigation into biodegradble soft hydrogel as a potential class of materials for soft body combustion.

Chapter 6

6 Conclusion and future work

This thesis presents a proof of concept light driven swimming robot (FLASH) capable of gathering energy from the environment to perform different modes of locomotion such as swimming underwater and jumping out of water. Following the development of novel light energy to oxyhydrogen combustion actuator, characterisation and design of FLASH, this chapter summaries the main contributions of the work and presents an outlook for future research.

6.1 Conclusions

The aim of this thesis was to design a self-sufficient, environmentally friendly, light-driven robot. This work consists of a review of different photo-actuation techniques employed by light driven microrobots in literature, followed by a detailed characterisation and architecture of the robot. Finally, stimuli-responsive soft materials for future smart light-driven robots are investigated. This resulted in the original contributions as follows.

6.1.1 Review of Photo-actuation techniques used in light driven micro-robots.

Three main photo-actuation approaches have been widely adopted in the design of photo-microrobots namely, photocatalysis, photovoltaic, photothermal/mechanical effects. Chapter 2 discusses the advantages and disadvantages of each actuation method and the area of applications for light driven microrobots. It shows that over the past decade, significant amount of work has been carried out across all three photo actuation strategies. This is due to the improvement in small-scale fabrication techniques and deeper understanding of molecules interactions/behaviour at microscopic scale.

Photocatalytic devices have been widely investigated due to its simple control, small size, abundant, low-cost and high efficiency. However, one common challenge reported throughout literature is the low velocity of photocatalytic microrobots. As such, efforts have been made to enhance the velocity whilst maintaining small size and input power. Notable works including wireless steering and velocity control Janus micromotors [88], swimming microrobots that detect and degrade organic pollutants [94] and autonomous micro-agents capable of decomposing biological and chemical warfare agents [98] . These microrobots exhibit exceptional ability to detect and degrade various pollutants with long service life. Due to these unique qualities, photocatalytic Janus microrobots present great potential in environmental remediation applications.

Despite having advantages over other photo-actuation strategies such as high ECE and energy output, researchers still face significant challenge in the integration of photovoltaic cells in microrobots as an on-board power source due to its big size. Fortunately, recent advances in micro/nano fabrication have made it possible to manufacture small-scale and high-power density photovoltaic cells [153]. This has enabled the development of many state-of-the-art insect scale aerial robots namely RoboFly [155] and RoboBee X-wing [126]. These robots, however, require intense light energy to generate sufficient power to takeoff (at least three times the light intensity of the sun in the case of RoboBee) and unable to sustain continuous fly. Nevertheless, advances in nanofabrication could soon make it possible to manufacture micro scale solar cells, and with the fast-improving capabilities of nanoelectronics and communication technology, these microrobots could be the future solutions to many environmental problems such crop pollination.

Light induced soft actuation due to photomechanical and photothermal effects offer many advantages at the nano/micro scale such as wireless control and fast modulation. However, some challenges still need to be addressed to realise the full potential of this technology. For instance, these photo-robots only response to limited light spectrum and the power density required for a given mass is significant. Nevertheless, progress has been made to extend the responsive wavelength of these devices [251] and initial steps have been taken towards reducing the size and the power requirements of these photo-robots [252] [181]. Looking at the current trend in literature, it is expected that in the near future, photomicrorobots made of photoactive materials would be able to carry out complex tasks such as walking, jumping, swimming, manipulation and transportation.

In conclusion, many research routes can be explored to realised fully autonomous light driven microrobots. The road map (figure 2.13) highlights the benefits of converging all three light actuation strategies to create intelligent photo-microrobots of the future. For instance, a robot capable of harvesting light energy using solar cells and converts that energy to chemical energy for actuation. Furthermore, by embedding photo-responsive materials into the design of the robot, smart behaviour can be programmed into the robot.

6.1.2 Waterjet propulsion via oxyhydrogen combustion

Chapter 3 presents a multi-phase energy conversion system turning photon energy into electrical energy for storage and subsequently chemical energy for actuation. This is realised by a flexible solar cell, an ultra-low power solar cell charger and a custom-made electrolytic module, respectively. Photovoltaic has been chosen as the primary candidate for light energy harvesting due to its relatively high ECE of 20%. Solar energy is a renewable energy source and readily available in the environment. As such a photovoltaically powered robot should be able to operate indefinitely autonomously and safely within the environments if it receives enough sunlight.

A custom design of an electrolyser, the ‘engine’ of the robot, has been demonstrated and characterised. Platinum was found to be the best electrodes for electrolysis out of the whole cohort of metals tested in terms of degradation, performance, and toxicity. A linear relationship has been observed between the input energy and amount of

oxyhydrogen gas produced by the electrolyser. The ECE of the module peaked at 20.5% (80J IE) then reduced to 15% as the IE increases. This is due to overpotential effect which hinder the reaction efficiency. The rugged design has demonstrated impressive resistance through multiples cycle of explosions (400 times plus) without noticeable deterioration in performance. This further supports the self-sufficiency of light-powered autonomous robots.

The viability of the energy conversion system was also investigated through analysing multiple charging (LiPo charger active) and discharging (electrolyser active) cycles of a LiPo battery. Halogen light was used as an alternative to sunlight due to the similarity between the light spectrum produced which are best absorbed by the solar cell. The results show that the electrolyser can run for 1.5 minute for every hour of charging while the LiPo battery is at 5%-70% (3.6-3.94V) charged. It took around 9 minutes to generate enough gas (≈4ml) to meet to the optimal gas to water ratio for actuation. As a result, 6 hours charging, and 9 minutes discharging cycle was carried out over 160 hours to validate potential the self-sufficiency of a light powered robot. It has been found that, after 26 cycles the system is still operating normally and on average, across all cycles, the battery charging percentage varies between 60%-80%, 3.87-4.02V respectively.

Finally, the theory behind combustion of oxyhydrogen and the hydrodynamic relationship between this combustible gas ignition and waterjet propulsion were investigated. Literature stated that the product of water electrolysis produces the most explosive mixture of oxyhydrogen gas because it allows the maximum yield of water and heat. Sparking was chosen as the method of ignition due to its low energy requirement, ease of miniaturisation and effectiveness underwater.

These above laid out the fundamental requirements for the design and testing of the FLASH autonomous light- powered robot in subsequent chapters.

6.1.3 FLASH architectures and characterisation

In chapter 4 and 5, we developed the FLASH, a light driven, jet-propelled robot capable of consecutive aquatic-arial jumps and swimming for an extended period in the environment. The robot presented in this thesis has been demonstrated to perform swimming and consecutive aquatic-arial takeoffs. The dependence of geometry on oxyhydrogen combustion thrust generation and hydrodynamics have been characterised. We have identified the design parameters governing the vertical jump performance of the robot and established the optimal geometry and gas to water ratio which produce the maximum jump, 18mm orifice size, 0.15 gas to water ratio and 23cm jump, respectively. The minimum jump threshold for the robot to completely clear the water has been established which allows different operation modes to be explored. For instance, a low energy mode can be used for swimming at night and the high energy mode can be used for jump-gliding.

The fluorescent dye flow visualization has highlighted the hydrodynamic behaviour of the waterjet produced by the combustion of oxyhydrogen. The highspeed camera footage indicates a strong thrust produced in a brief amount of

time and generated many vortices causing significant turbulence in the surrounding water body. Moreover, it is thought that this turbulent behaviour could be utilise in environmental applications where the robot can produce a strong waterjet to clean up the surrounding area.

We have also showcased the ability of FLASH to swim efficiently underwater. The valve system designed to regulate the flow of fluid during combustion has been proven to increase the performance of the robot significantly. It is thought that by manipulating the buoyancy of the robot, different operation modes can be achieved. For example, the gas to water ratio can be controlled to enable the robot swim around underwater for data collection or float up to the water surface and jump out of the water to traverse different terrains or for environmental samples retrieval.

The untethered FLASH robot has demonstrated the robot's ability to operate for an extended period of time within the environment without supervision (12 hours). The robot also exhibits different mode of operation such as underwater random swim, hibernation (charging) when encounter light source, changing buoyancy to float up when battery runs out. This indicates that FLASH is a suited candidate for environmental applications as well as open up interesting research areas into green environmental robots which can fully integrate with the environments.

6.2 Limitations and Future work

This research introduces a novel light powered, combustion-driven robot for environmental applications. We investigate the influence of the underlying physics and main design parameters on performance of the robots. This includes detailed analysis on the multi-phase energy conversion system, combustion to waterjetting, design parameters as well as operational modes. This leads to the development of an untethered FLASH robot. A comprehensive description of the mechatronics of the device was included. The robot is capable of underwater swimming for an extended period in the environment due to its unique propulsion system and the ability to obtain energy from its surroundings. The reliance on a single actuator to trigger the exothermic reaction and combustion of oxyhydrogen gas offer an environmentally friendly solution for various environmental applications. However, there is scope for improvement in several aspects of FLASH.

6.2.1 Combustion in soft body

It is important to note that all state-of-the-art aerial-aquatic robots reported in literature has a stiff combustion chamber which is beneficial for reliable and repeatable jumpgliding or takeoff and landing. In addition, the stiff body simplifies physical modelling of the robots in terms of flight trajectory calculations and combustion dynamic analysis. It also enables effective design, characterisations and miniaturisation. However, combustion in soft and compliant materials may enable innovative methods for underwater locomotion. For instance, the use of combustion has shown to increase the speed of terrestrial soft actuators [293] [287] [285] and could introduce new ways to increase the displacement speed of underwater actuators. For example, a terrestrial jumping soft robot was able to reach 3.6 m/s velocities using methane combustion [285]. It was found that the combustion causes no damage to the silicon membranes because the

temperature decreases to below 300 °C degradation point of silicon within 10ms after the combustion was initiated [287]. Further work has shown that an untethered soft jumper is capable of withstanding combustion temperatures of greater than 500 °C for multiple cycles (> 30) [286]. Inspired by the motion of the soft bodied cephalopods, a Combustion Powered Hydro-Jet Engine (CPHJE) using methane combustion and expandable silicon bladder for underwater propulsion was developed [292]. The 0.7kg CPHJE can achieve velocities as high as 450mm/s and able to produce consecutive actuation with the same bladder. Nonetheless, the need of multiple liquid fuel containers and flow control equipment has led to a substantial increase in weight and complexity making it not feasible to integrate into miniature aerial-aquatic vehicles. A promising on-going work, currently carried out by researchers at Cornell university, on a soft-robotic rover for Europa exploration capable of harvesting electrodynamic power from the environments for locomotion via oxyhydrogen combustion [280] could be considered to be an attempt to remove the need of off board power source and reduce the amount of components the robots need to operate. However, this work is still at a very early stage, only theoretical concepts and preliminary results were investigated and reported, respectively.

Although there are many benefits in exploring combustion in soft body, one should recognise that there is a trade-off between miniaturisation and softness for combustion powered microrobots. This should be taken into account in future version of FLASH to realise suitable solutions for particular applications.

6.2.2 Improvements to FLASH's current limitations

One of the limitations of the current system is the fast combustion time which hinders the performance of the robot. It is thought that it may be beneficial to change the molar ratio of oxyhydrogen (2:1) to maximise the potential benefits from longer burn times and reduced flame speeds of the oxyhydrogen combustion. In addition, oxyhydrogen combustion within porous materials (i.e. foams) might decrease the flame speed and as a result, increase the amount of power collected. Another limitation is the long charging time of the robot, which is about 6 hours for every 9 minutes of electrolysis. This time could be shortened by utilising a bigger solar cell and/or more efficient LiPo charger. However, this would increase the size/weight of the robot and ultimately affect the performance. We believe that as battery and nanofabrication technologies advance, miniaturisation of the robot could be achieved without performance trade-offs. FLASH currently has no methods to detect whether the hydrojetting chamber is full, or whether a desire amount of gas has been generated before launch. This could be addressed with further sensor integration. The usage of shape memory alloy (SMA) would be advantageous to realise complex control and added functionality such as steering and objects manipulation. Finally, with the integration of functional light sensitive material [253], [254], directional control and swarm intelligence could be achieved. An interesting area that could be explored in the future is phototaxis, where FLASH fins, made from light responsive materials, 'sense' nearby light source and guide the robot towards it. This would enable autonomous behaviour and more complex control and/or information sharing through light intensity and wavelengths.

Bibliography

[1] R. F. Shepherd *et al.*, “Multigait soft robot,” *PNAS*, vol. 108, no. 51, pp. 20400–20403, 2011, doi: 10.1073/pnas.1116564108/-/DCSupplemental.www.pnas.org/cgi/doi/10.1073/pnas.1116564108.

[2] F. Ilievski, A. D. Mazzeo, R. F. Shepherd, X. Chen, and G. M. Whitesides, “Soft robotics for chemists,” *Angew. Chemie - Int. Ed.*, vol. 50, no. 8, pp. 1890–1895, 2011, doi: 10.1002/anie.201006464.

[3] V. Kumar *et al.*, “Structural characterization of new fluorinated mesogens obtained through halogen-bond driven self-assembly,” *J. Fluor. Chem.*, vol. 198, pp. 54–60, 2017, doi: 10.1016/j.jfluchem.2016.12.011.

[4] X. Ma *et al.*, “Enzyme-Powered Hollow Mesoporous Janus Nanomotors,” *Nano Lett.*, vol. 15, no. 10, pp. 7043–7050, 2015, doi: 10.1021/acs.nanolett.5b03100.

[5] M. Uygun, V. V. Singh, K. Kaufmann, D. A. Uygun, S. D. S. De Oliveira, and J. Wang, “Micromotor-Based Biomimetic Carbon Dioxide Sequestration: Towards Mobile Microscrubbers,” *Angew. Chemie - Int. Ed.*, vol. 54, no. 44, pp. 12900–12904, 2015, doi: 10.1002/anie.201505155.

[6] V. V. Singh, F. Soto, K. Kaufmann, and J. Wang, “Micromotor-based energy generation,” *Angew. Chemie - Int. Ed.*, vol. 54, no. 23, pp. 6896–6899, 2015, doi: 10.1002/anie.201501971.

[7] J. Wang and W. Gao, “Nano/microscale motors: Biomedical opportunities and challenges,” *ACS Nano*, vol. 6, no. 7, pp. 5745–5751, 2012, doi: 10.1021/nn3028997.

[8] S. J. Wezenberg, K. Y. Chen, and B. L. Feringa, “Visible-Light-Driven Photoisomerization and Increased Rotation Speed of a Molecular Motor Acting as a Ligand in a Ruthenium(II) Complex,” *Angew. Chemie - Int. Ed.*, vol. 54, no. 39, pp. 11457–11461, 2015, doi: 10.1002/anie.201505781.

[9] R. S. M. Rikken, R. J. M. Nolte, J. C. Maan, J. C. M. Van Hest, D. A. Wilson, and P. C. M. Christianen, “Manipulation of micro- and nanostructure motion with magnetic fields,” *Soft Matter*, vol. 10, no. 9, pp. 1295–1308, 2014, doi: 10.1039/c3sm52294f.

[10] J. Li *et al.*, “Magneto-Acoustic Hybrid Nanomotor,” *Nano Lett.*, vol. 15, no. 7, pp. 4814–4821, 2015, doi: 10.1021/acs.nanolett.5b01945.

[11] S. Tottori, L. Zhang, F. Qiu, K. K. Krawczyk, A. Franco-Obregõn, and B. J. Nelson, “Magnetic helical micromachines: Fabrication, controlled swimming, and cargo transport,” *Adv. Mater.*, vol. 24, no. 6, pp. 811–816, 2012, doi: 10.1002/adma.201103818.

[12] P. Fischer and A. Ghosh, “Magnetically actuated propulsion at low Reynolds numbers: Towards nanoscale control,” *Nanoscale*, vol. 3, no. 2, pp. 557–563, 2011, doi: 10.1039/c0nr00566e.

[13] N. Chaturvedi, Y. Hong, A. Sen, and D. Velegol, “Magnetic enhancement of phototaxing catalytic motors,” *Langmuir*, vol. 26, no. 9, pp. 6308–6313, 2010, doi: 10.1021/la904133a.

[14] S. Campuzano, D. Kagan, J. Orozco, and J. Wang, “Motion-driven sensing and biosensing using electrochemically propelled nanomotors,” *Analyst*, vol. 136, no. 22, pp. 4621–4630, 2011, doi: 10.1039/c1an15599g.

[15] F. Mou, L. Kong, C. Chen, Z. Chen, L. Xu, and J. Guan, “Light-controlled propulsion, aggregation and separation of water-fuelled TiO2/Pt Janus submicromotors and their ‘on-the-fly’ photocatalytic activities,” *Nanoscale*, vol. 8, no. 9. pp. 4976–4983, 2016, doi: 10.1039/c5nr06774j.

[16] T. Xu *et al.*, “Ultrasound-modulated bubble propulsion of chemically powered microengines,” *J. Am. Chem. Soc.*, vol. 136, no. 24, pp. 8552–8555, 2014, doi: 10.1021/ja504150e.

[17] W. Wang, S. Li, L. Mair, S. Ahmed, T. J. Huang, and T. E. Mallouk, “Acoustic propulsion of nanorod motors inside living cells,” *Angew. Chemie - Int. Ed.*, vol. 53, no. 12, pp. 3201–3204, 2014, doi: 10.1002/anie.201309629.

[18] T. Xu *et al.*, “Reversible swarming and separation of self-propelled chemically powered nanomotors under acoustic fields,” *J. Am. Chem. Soc.*, vol. 137, no. 6, pp. 2163–2166, 2015, doi: 10.1021/ja511012v.

[19] S. Ahmed, D. T. Gentekos, C. A. Fink, and T. E. Mallouk, “Self-assembly of nanorod motors into geometrically regular multimers and their propulsion by ultrasound,” *ACS Nano*, vol. 8, no. 11, pp. 11053–11060, 2014, doi: 10.1021/nn5039614.

[20] V. Garcia-Gradilla *et al.*, “Ultrasound-propelled nanoporous gold wire for efficient drug loading and release,” *Small*, vol. 10, no. 20, pp. 4154–4159, 2014, doi: 10.1002/smll.201401013.

[21] D. Baigl, “Photo-actuation of liquids for light-driven microfluidics: State of the art and perspectives,” *Lab Chip*, vol. 12, no. 19, pp. 3637–3653, 2012, doi: 10.1039/c2lc40596b.

[22] A. Diguet *et al.*, “Photomanipulation of a droplet by the chromocapillary effect,” *Angew. Chemie - Int. Ed.*, vol. 48, no. 49, pp. 9281–9284, 2009, doi: 10.1002/anie.200904868.

[23] W. F. Paxton *et al.*, “Catalytic nanomotors: Autonomous movement of striped nanorods,” *J. Am. Chem. Soc.*, vol. 126, no. 41, pp. 13424–13431, 2004, doi: 10.1021/ja047697z.

[24] H. Zeng, O. M. Wani, P. Wasylczyk, R. Kaczmarek, and A. Priimagi, “Self-Regulating Iris Based on Light-Actuated Liquid Crystal Elastomer,” *Adv. Mater.*, vol. 29, no. 30, pp. 1–7, 2017, doi: 10.1002/adma.201701814.

[25] D. Li, C. Liu, Y. Yang, L. Wang, and Y. Shen, “Micro-rocket robot with all-optic actuating and tracking in blood,” *Light Sci. Appl.*, vol. 9, no. 1, 2020, doi: 10.1038/s41377-020-0323-y.

[26] J. Wang, Z. Xiong, and J. Tang, “The Encoding of Light-Driven Micro/Nanorobots: from Single to Swarming Systems,” *Adv. Intell. Syst.*, vol. 2000170, p. 2000170, 2021, doi: 10.1002/aisy.202000170.

[27] H.-G. A. Hwang G, Decanini D, Leroy L, “On-chip multifunctional fluorescent-magnetic Janus helical microswimmers.pdf,” *Rev. Sci. Instrum.*, vol. 87, no. 3, 2016.

[28] M. Hoop *et al.*, “Magnetically Driven Silver-Coated Nanocoils for Efficient Bacterial Contact Killing,” *Advanced Functional Materials*, vol. 26, no. 7. pp. 1063–1069, 2016, doi: 10.1002/adfm.201504463.

[29] P. W. Egolf *et al.*, “Hyperthermia with rotating magnetic nanowires inducing heat into tumor by fluid friction,” *Journal of Applied Physics*, vol. 120, no. 6. 2016, doi: 10.1063/1.4960406.

[30] C. Chen, L. Chen, Y. Yi, C. Chen, L. F. Wu, and T. Song, “Killing of Staphylococcus aureus via magnetic hyperthermia mediated by magnetotactic bacteria,” *Applied and Environmental Microbiology*, vol. 82, no. 7. pp. 2219–2226, 2016, doi: 10.1128/AEM.04103-15.

[31] F. P. Walker D, Käsdorf BT, Jeong HH, Lieleg O, “Enzymatically active biomimetic micropropellers for the penetration of mucin gels.” .

[32] P. Chen, S. Güven, O. B. Usta, M. L. Yarmush, and U. Demirci, “Biotunable Acoustic Node Assembly of Organoids,” *Advanced Healthcare Materials*, vol. 4, no. 13. pp. 1937–1943, 2015, doi: 10.1002/adhm.201500279.

[33] C. Bouyer *et al.*, “A Bio-Acoustic Levitational (BAL) Assembly Method for Engineering of Multilayered, 3D Brain-Like Constructs, Using Human Embryonic Stem Cell Derived Neuro-Progenitors,” *Advanced Materials*, vol. 28, no. 1. pp. 161–167, 2016, doi: 10.1002/adma.201503916.

[34] S. Li *et al.*, “Application of an acoustofluidic perfusion bioreactor for cartilage tissue engineering,” *Lab on a Chip*, vol. 14, no. 23. pp. 4475–4485, 2014, doi: 10.1039/c4lc00956h.

[35] J. Wu, “Acoustical tweezers,” *J. Acoust. Soc. Am.*, vol. 89, no. 5, pp. 2140–2143, 1991, doi: 10.1121/1.400907.

[36] M. J. Villangca, D. Palima, A. R. Bañas, and J. Glückstad, “Light-driven micro-tool equipped with a syringe function,” *Light: Science and Applications*, vol. 5, no. 9. 2016, doi: 10.1038/lsa.2016.148.

[37] V. Du Nguyen *et al.*, “Active tumor-therapeutic liposomal bacteriobot combining a drug (paclitaxel)-encapsulated liposome with targeting bacteria (Salmonella Typhimurium),” *Sensors and Actuators, B: Chemical*, vol. 224. pp. 217–224, 2016, doi: 10.1016/j.snb.2015.09.034.

[38] J. Li, I. Rozen, and J. Wang, “Rocket Science at the Nanoscale,” *ACS Nano*, vol. 10, no. 6, pp. 5619–5634, 2016, doi: 10.1021/acsnano.6b02518.

[39] W. Gao *et al.*, “Artificial micromotors in the mouse’s stomach: A step toward in vivo use of synthetic motors,” *ACS Nano*, vol. 9, no. 1. pp. 117–123, 2015, doi: 10.1021/nn507097k.

[40] D. R. & S. M. Ouajdi Felfoul, Mahmood Mohammadi, Samira Taherkhani, Dominic de Lanauze, Yong Zhong Xu, Dumitru Loghin, Sherief Essa, Sylwia Jancik, Daniel Houle, Michel Lafleur, Louis Gaboury, Maryam Tabrizian, Neila Kaou, Michael Atkin, Té Vuong, Gerald Batist, Nicole, “Magneto-aerotactic bacteria deliver drug-containing nanoliposomes to tumour hypoxic regions,” *Nat. Nanotechnol.*, vol. 11, pp. 941–947, 2016.

[41] M. Medina-Sánchez, L. Schwarz, A. K. Meyer, F. Hebenstreit, and O. G. Schmidt, “Cellular Cargo Delivery: Toward Assisted Fertilization by Sperm-Carrying Micromotors,” *Nano Letters*, vol. 16, no. 1. pp. 555–561, 2016, doi: 10.1021/acs.nanolett.5b04221.

[42] T. V. Ramachandra, G. Krishnadas, and R. Jain, “Solar Potential in the Himalayan Landscape,” *ISRN Renew. Energy*,

vol. 2012, pp. 1–13, 2012, doi: 10.5402/2012/203149.

[43] and W. T. Mingxu You, Fujian Huang, Zhuo Chen, Ruo-Wen Wang, “Building a Nanostructure with Reversible Motions Using Photonic Energy,” *ACS Nano*, vol. 6, no. 9, pp. 7935–7941, 2012, doi: 10.1021/nl061786n.Core-Shell.

[44] J. Cheng *et al.*, “Bipedal nanowalker by pure physical mechanisms,” *Phys. Rev. Lett.*, vol. 109, no. 23, pp. 1–5, 2012, doi: 10.1103/PhysRevLett.109.238104.

[45] I. Y. Loh, J. Cheng, S. R. Tee, A. Efremov, and Z. Wang, “From bistate molecular switches to self-directed track-walking nanomotors,” *ACS Nano*, vol. 8, no. 10, pp. 10293–10304, 2014, doi: 10.1021/nn5034983.

[46] Q. Y. Yeo *et al.*, “A DNA bipedal nanowalker with a piston-like expulsion stroke,” *Nanoscale*, vol. 9, no. 33, pp. 12142–12149, 2017, doi: 10.1039/c7nr03809g.

[47] R. F. Ismagilov, A. Schwartz, N. Bowden, and G. M. Whitesides, “Autonomous movement and self-assembly,” *Angew. Chemie - Int. Ed.*, vol. 41, no. 4, pp. 652–654, 2002, doi: 10.1002/1521-3773(20020215)41:4<652::AID-ANIE652>3.0.CO;2-U.

[48] B. Parida, S. Iniyan, and R. Goic, “A review of solar photovoltaic technologies,” *Renew. Sustain. Energy Rev.*, vol. 15, no. 3, pp. 1625–1636, 2011, doi: 10.1016/j.rser.2010.11.032.

[49] Z. Wang, C. Li, and K. Domen, “Recent developments in heterogeneous photocatalysts for solar-driven overall water splitting,” *Chem. Soc. Rev.*, vol. 48, no. 7, pp. 2109–2125, 2019, doi: 10.1039/c8cs00542g.

[50] A. Fujishima, T. N. Rao, and D. A. Tryk, “Titanium dioxide photocatalysis,” *J. Photochem. Photobiol. C Photochem. Rev.*, vol. 1, no. 1, pp. 1–21, 2000, doi: 10.1016/S1389-5567(00)00002-2.

[51] A. Fujishima, T. N. Rao, and D. A. Tryk, “TiO2 photocatalysts and diamond electrodes,” *Electrochim. Acta*, vol. 45, no. 28, pp. 4683–4690, 2000, doi: 10.1016/S0013-4686(00)00620-4.

[52] A. Fujishima, X. Zhang, and D. A. Tryk, “TiO2photocatalysis and related surface phenomena,” *Surf. Sci. Rep.*, vol. 63, no. 12, pp. 515–582, 2008, doi: 10.1016/j.surfrep.2008.10.001.

[53] H. I. and A. F. Kazuhito Hashimoto, “TiO2 photocatalysis A historical overview and future prospects,” *Jpn. J. Appl. Phys.*, vol. 44, no. 12, pp. 8269–8285, 2005.

[54] S. Fang and Y. H. Hu, “Recent progress in photocatalysts for overall water splitting,” *Int. J. Energy Res.*, vol. 43, no. 3, pp. 1082–1098, 2019, doi: 10.1002/er.4259.

[55] S. Licht, B. Wang, and S. Mukerji, “Efficient solar water splitting, exemplified by RuO2-catalyzed AlGaAs/Si photoelectrolysis,” *J. Phys. Chem. B*, vol. 104. pp. 8920–8924, 2000, doi: 10.1021/jp002083b.

[56] W. Choi, A. Termin, and M. R. Hoffmann, “The role of metal ion dopants in quantum-sized TiO2: Correlation between photoreactivity and charge carrier recombination dynamics,” *Journal of Physical Chemistry*, vol. 98, no. 51. pp. 13669–13679, 1994, doi: 10.1021/j100102a038.

[57] D. W. B. M.R. Hoffmann, S.T. Martin, W. Choi, “Environmental Applications of Semiconductor Photocatalysis,” *Chem. Rev.*, vol. 95, no. 1, pp. 69–96, 1995.

[58] Y. Wang, Y. Huang, W. Ho, L. Zhang, Z. Zou, and S. Lee, “Biomolecule-controlled hydrothermal synthesis of C-N-S-tridoped TiO2 nanocrystalline photocatalysts for NO removal under simulated solar light irradiation,” *Journal of Hazardous Materials*, vol. 169. pp. 77–87, 2009, doi: 10.1016/j.jhazmat.2009.03.071.

[59] C. Su, C. M. Tseng, L. F. Chen, B. H. You, B. C. Hsu, and S. S. Chen, “Sol-hydrothermal preparation and photocatalysis of titanium dioxide,” *Thin Solid Films*, vol. 498, no. 1–2. pp. 259–265, 2006, doi: 10.1016/j.tsf.2005.07.123.

[60] M. K. Patil, S. Shaikh, and I. Ganesh, “Recent Advances on TiO2 Thin Film Based Photocatalytic Applications (A Recent Advances on TiO 2 Thin Film Based Photocatalytic Applications (A Review),” *Curr. Nanosci.*, vol. 11, no. 3, pp. 271–285, 2015, doi: 10.2174/1573413711666150212235054.

[61] B. Kennworte *et al.*, “Nonstoichiometry electrical conductivity and diffusion of binary metal oxides,” 1974.

[62] T. Bak, J. Nowotny, M. Rekas, and C. C. Sorrell, “Photo-electrochemical hydrogen generation from water using solar energy,” *International Journal of Hydrogen Energy*, vol. 27, no. 2002. pp. 991–1022, 2002, doi: http://dx.doi.org/10.1016/S0360-3199(02)00022-8.

[63] N. T. Nolan, M. K. Seery, and S. C. Pillai, “Spectroscopic investigation of the anatase-to-rutile transformation of sol-gel-synthesized TiO2 photocatalysts,” *Journal of Physical Chemistry C*, vol. 113, no. 36. pp. 16151–16157, 2009, doi: 10.1021/jp904358g.

[64] T. Luttrell, S. Halpegamage, J. Tao, A. Kramer, E. Sutter, and M. Batzill, “Why is anatase a better photocatalyst than rutile? - Model studies on epitaxial TiO2 films,” *Sci. Rep.*, vol. 4, pp. 1–8, 2015, doi: 10.1038/srep04043.

[65] A. Wisitsoraat, A. Tuantranont, E. Comini, G. Sberveglieri, and W. Wlodarski, “Characterization of n-type and p-type semiconductor gas sensors based on NiOx doped TiO2 thin films,” *Thin Solid Films*, vol. 517, no. 8. pp. 2775–2780, 2009, doi: 10.1016/j.tsf.2008.10.090.

[66] R. Asahi, Y. Taga, W. Mannstadt, and A. J. Freeman, “Electronic and optical properties of anatase TiO2,” *Phys. Rev. B*, vol. 61, no. 11, pp. 7459–7465, Mar. 2000, doi: 10.1103/PhysRevB.61.7459.

[67] A. Amtout and R. Leonelli, “Optical properties of rutile near its fundamental band gap,” *Physical Review B*, vol. 51, no. 11. pp. 6842–6851, 1995, doi: 10.1103/PhysRevB.51.6842.

[68] M. Koelsch, S. Cassaignon, C. Ta Thanh Minh, J. F. Guillemoles, and J. P. Jolivet, “Electrochemical comparative study of titania (anatase, brookite and rutile) nanoparticles synthesized in aqueous medium,” *Thin Solid Films*, vol. 451–452. pp. 86–92, 2004, doi: 10.1016/j.tsf.2003.11.150.

[69] M. Batzill, “Fundamental aspects of surface engineering of transition metal oxide photocatalysts,” *Energy Environ. Sci.*, vol. 4, no. 9, pp. 3275–3286, 2011, doi: 10.1039/c1ee01577j.

[70] M. Xu *et al.*, “Photocatalytic activity of bulk TiO2 anatase and rutile single crystals using infrared absorption

spectroscopy.," *Phys. Rev. Lett.*, vol. 106, no. 13, p. 138302, Apr. 2011, doi: 10.1103/PhysRevLett.106.138302.

[71] A. F. & K. HONDA, "Electrochemical Photolysis of Water at a Semiconductor Electrode," *Nature*, vol. 238, pp. 37–38, 1972.

[72] S. RF, "Catalyst boosts hopes for hydrogen bonanza," *Science (80-.).*, vol. 297, no. 5590, pp. 2189–2190, 2002.

[73] J. F. Houlihan, D. P. Madacsi, S. V. Campus, and L. N. Mulay, "Improved solar energy conversion efficiencies for the photocatalytic production of hydrogen via TiO2 semiconductor electrodes," *Carbon N. Y.*, vol. ii, 1976.

[74] J. Augustynski, "Novel Semiconducting Electrodes for the Photosensitized Electrolysis of Water," *J. Electrochem. Soc.*, vol. 124, no. 7, p. 1063, 1977, doi: 10.1149/1.2133482.

[75] R. Asahi, T. Morikawa, T. Ohwaki, K. Aoki, and Y. Taga, "Visible-light photocatalysis in nitrogen-doped titanium oxides.," *Science (New York, N.Y.)*, vol. 293, no. 5528. pp. 269–71, 2001, doi: 10.1126/science.1061051.

[76] H. Feldmaier *et al.*, "Efficient Photochemical Water Splitting by a Chemically Modified n-TiO2," vol. 021603, no. 2001. pp. 5–8, 2002.

[77] J. Hensel, G. Wang, Y. Li, and J. Z. Zhang, "Synergistic Effect of CdSe Quantum Dot Sensitization and Nitrogen Doping of TiO2 Nanostructures for Photoelectrochemical Solar Hydrogen Generation," *Nano Letters*, vol. 10, no. 2. pp. 478–483, 2010, doi: 10.1021/nl903217w.

[78] A. Paracchino, V. Laporte, K. Sivula, M. Grätzel, and E. Thimsen, "Highly active oxide photocathode for photoelectrochemical water reduction," *Nat. Mater.*, vol. 10, no. 6, pp. 456–461, 2011, doi: 10.1038/nmat3017.

[79] T. Umebayashi, T. Yamaki, H. Itoh, and K. Asai, "Band gap narrowing of titanium dioxide by sulfur doping Band gap narrowing of titanium dioxide by sulfur doping," *Applied physics letters*, vol. 454, no. 2002. pp. 3–6, 2015, doi: 10.1063/1.1493647.

[80] S. P. Pitre, T. P. Yoon, and J. C. Scaiano, "Titanium dioxide visible light photocatalysis: surface association enables photocatalysis with visible light irradiation," *Chem. Commun.*, vol. 53, no. 31, pp. 4335–4338, 2017, doi: 10.1039/c7cc01952a.

[81] K. Mao, X. Wu, X. Min, Z. Huang, Y. gai Liu, and M. Fang, "New Efficient Visible-Light-Driven Photocatalyst of Chitin-Modified Titanium Dioxide/Carbon Fiber Composites for Wastewater," *Sci. Rep.*, vol. 9, no. 1, pp. 1–9, 2019, doi: 10.1038/s41598-019-52833-y.

[82] M. S. Wrighton, D. S. Ginley, P. T. Wolczanski, A. B. Ellis, D. L. Morse, and A. Linz, "Photoassisted Electrolysis of Water by Irradiation of a Titanium Dioxide Electrode," *Proceedings of the National Academy of Sciences*, vol. 72, no. 4. pp. 1518–1522, 1975, doi: 10.1073/pnas.72.4.1518.

[83] T. T. T. Le and T. D. Tran, "Photocatalytic Degradation of Rhodamine B by C and N Codoped TiO2Nanoparticles under Visible-Light Irradiation," *J. Chem.*, vol. 2020, 2020, doi: 10.1155/2020/4310513.

[84] J. Wang *et al.*, " Enhanced visible-light photodegradation of fluoroquinolone-based antibiotics and E. coli growth

inhibition using Ag–TiO 2 nanoparticles ," *RSC Adv.*, vol. 11, no. 23, pp. 13980–13991, 2021, doi: 10.1039/d0ra10403e.

[85] D. Vilela, M. M. Stanton, J. Parmar, and S. Sánchez, "Microbots Decorated with Silver Nanoparticles Kill Bacteria in Aqueous Media," *ACS Appl. Mater. Interfaces*, vol. 9, no. 27, pp. 22093–22100, 2017, doi: 10.1021/acsami.7b03006.

[86] M. Xuan, Z. Wu, J. Shao, L. Dai, T. Si, and Q. He, "Near Infrared Light-Powered Janus Mesoporous Silica Nanoparticle Motors," *Journal of the American Chemical Society*, vol. 138, no. 20. pp. 6492–6497, 2016, doi: 10.1021/jacs.6b00902.

[87] Q. Zhang, R. Dong, X. Chang, B. Ren, and Z. Tong, "Spiropyran-Decorated SiO2-Pt Janus Micromotor: Preparation and Light-Induced Dynamic Self-Assembly and Disassembly," *ACS Appl. Mater. Interfaces*, vol. 7, no. 44, pp. 24585–24591, 2015, doi: 10.1021/acsami.5b06448.

[88] R. Dong, Q. Zhang, W. Gao, A. Pei, and B. Ren, "Highly efficient light-driven TiO2-Au Janus Micromotors," *ACS Nano*, vol. 10, no. 1, pp. 839–844, 2016, doi: 10.1021/acsnano.5b05940.

[89] A. L. Linsebigler, G. Lu, and J. T. Yates, "Photocatalysis on TiO2Surfaces: Principles, Mechanisms, and Selected Results," *Chem. Rev.*, vol. 95, no. 3, pp. 735–758, 1995, doi: 10.1021/cr00035a013.

[90] K. Kim, O. G. Tsay, D. A. Atwood, and D. G. Churchill, "Destruction and Detection of Chemical Warfare Agents," *Chem. Rev.*, vol. 111, no. 9, pp. 5345–5403, 2011, doi: 10.1021/cr100193y.

[91] M. Dahl, Y. Liu, and Y. Yin, "Composite Titanium Dioxide Nanomaterials," *Chem. Rev.*, vol. 114, no. 19, pp. 9853–9889, 2014, doi: 10.1021/cr400634p.

[92] R. B. Dong R, Zhang Q, Gao W, Pei A, "Highly Efficient Light-Driven TiO2−Au Janus." .

[93] Y. Wang *et al.*, "Bipolar electrochemical mechanism for the propulsion of catalytic nanomotors in hydrogen peroxide solutions," *Langmuir*, vol. 22, no. 25, pp. 10451–10456, 2006, doi: 10.1021/la0615950.

[94] Y. Wu, R. Dong, Q. Zhang, and B. Ren, "Dye-enhanced self-electrophoretic propulsion of light-driven TiO2-Au janus micromotors," *Nano-Micro Lett.*, vol. 9, no. 3, pp. 1–12, 2017, doi: 10.1007/s40820-017-0133-9.

[95] B. Jang *et al.*, "Multiwavelength Light-Responsive Au/B-TiO2 Janus Micromotors," *ACS Nano*, vol. 11, no. 6, pp. 6146–6154, 2017, doi: 10.1021/acsnano.7b02177.

[96] Q. Zhao, M. Li, J. Chu, T. Jiang, and H. Yin, "Preparation, characterization of Au (or Pt)-loaded titania nanotubes and their photocatalytic activities for degradation of methyl orange," *Appl. Surf. Sci.*, vol. 255, no. 6, pp. 3773–3778, 2009, doi: 10.1016/j.apsusc.2008.10.044.

[97] W. Li, B. Zhang, X. Li, H. Zhang, and Q. Zhang, "Preparation and characterization of novel immobilized Fe3O4@SiO2@mSiO2-Pd(0) catalyst with large pore-size mesoporous for Suzuki coupling reaction," *Appl. Catal. A Gen.*, vol. 459, pp. 65–72, 2013, doi: 10.1016/j.apcata.2013.04.010.

[98] J. Li *et al.*, "Water-driven micromotors for rapid photocatalytic degradation of biological and chemical warfare

agents," *ACS Nano*, vol. 8, no. 11. pp. 11118–11125, 2014, doi: 10.1021/nn505029k.

[99] F. Mou *et al.*, "Single-component TiO2tubular microengines with motion controlled by light-induced bubbles," *Small*, vol. 11, no. 21, pp. 2564–2570, 2015, doi: 10.1002/smll.201403372.

[100] H. Xie, B. Liu, and X. Zhao, "Facile process to greatly improve the photocatalytic activity of the TiO2thin film on window glass for the photodegradation of acetone and benzene," *Chem. Eng. J.*, vol. 284, pp. 1156–1164, 2016, doi: 10.1016/j.cej.2015.09.049.

[101] Z. Zhang, A. Zhao, F. Wang, J. Ren, and X. Qu, "Design of a plasmonic micromotor for enhanced photo-remediation of polluted anaerobic stagnant waters," *Chemical Communications*, vol. 52, no. 32. pp. 5550–5553, 2016, doi: 10.1039/c6cc00910g.

[102] V. Sridhar, B. W. Park, S. Guo, P. A. Van Aken, and M. Sitti, "Multiwavelength-Steerable Visible-Light-Driven Magnetic CoO-TiO2 Microswimmers," *ACS Appl. Mater. Interfaces*, vol. 12, no. 21, pp. 24149–24155, 2020, doi: 10.1021/acsami.0c06100.

[103] J. Li, W. Gao, R. Dong, A. Pei, S. Sattayasamitsathit, and J. Wang, "Nanomotor lithography," *Nat. Commun.*, vol. 5, pp. 1–7, 2014, doi: 10.1038/ncomms6026.

[104] J. G. S. Moo and M. Pumera, "Chemical energy powered nano/micro/macromotors and the environment," *Chem. - A Eur. J.*, vol. 21, no. 1, pp. 58–72, 2015, doi: 10.1002/chem.201405011.

[105] M. T. P. ; M. Gasulla, "A Review of Commercial Energy Harvesters for Autonomous Sensors," *IEEE Instrum. Meas. Technol. Conf. IMTC*, pp. 1–5, 2007.

[106] P. Spies, L. Mateu, and M. Pollak, "Handbook of Energy Harvesting Power Supplies and Applications," 2015, doi: 10.1201/b18523.

[107] I. González-Reolid, J. C. Molina-Molina, A. Guerrero-González, F. J. Ortiz, and D. Alonso, "An autonomous solar-powered marine robotic observatory for permanent monitoring of large areas of shallow water," *Sensors (Switzerland)*, vol. 18, no. 10, pp. 1–24, 2018, doi: 10.3390/s18103497.

[108] G. A. Landis, "Exploring Mars with solar-powered rovers," *Conf. Rec. IEEE Photovolt. Spec. Conf.*, pp. 858–861, 2005, doi: 10.1109/pvsc.2005.1488268.

[109] F. Y. C. Albert, C. H. S. Mason, C. K. J. Kiing, K. S. Ee, and K. W. Chan, "Remotely operated solar-powered mobile metal detector robot," *Procedia Comput. Sci.*, vol. 42, no. C, pp. 232–239, 2014, doi: 10.1016/j.procs.2014.11.057.

[110] M. Gul, Y. Kotak, and T. Muneer, *Review on recent trend of solar photovoltaic technology*, vol. 34, no. 4. 2016.

[111] A. Le Donne, A. Scaccabarozzi, S. Tombolato, S. Binetti, M. Acciarri, and A. Abbotto, "Solar Photovoltaics: A Review," *Rev. Adv. Sci. Eng.*, vol. 2, no. 3, pp. 170–178, 2013, doi: 10.1166/rase.2013.1030.

[112] N. Rathore, N. L. Panwar, F. Yettou, and A. Gama, "A comprehensive review of different types of solar photovoltaic cells and their applications," *Int. J. Ambient Energy*, vol. 0, no. 0, pp. 1–18, 2019, doi:

10.1080/01430750.2019.1592774.

[113] V. Lo, C. Landrock, B. Kaminska, and M. Elicia, “Manufacturing cost modeling for flexible organic solar cells,” *2012 Proc. Technol. Manag. Emerg. Technol.*, pp. 2951–2956, 2012, [Online]. Available: http://ieeexplore.ieee.org/xpls/abs_all.jsp?arnumber=6304313.

[114] A. Vakil, “Energy Harvesting Using Graphene Based Antenna for UV Spectrum,” no. Fig 1. 2014.

[115] Y. Zhao, H. Pan, Y. Lou, X. Qiu, J. Zhu, and C. Burda, “Plasmonic Cu 2-x S Nanocrystals : Optical and Structural Properties of Copper-Deficient Copper (I) Sulfides,” *J. Am. Chem. Soc.*, vol. 131, no. I, pp. 4253–4261, 2009.

[116] S.-W. Hsu, W. Bryks, and A. R. Tao, “Effects of Carrier Density and Shape on the Localized Surface Plasmon Resonances of $Cu_{2-x}S$ Nanodisks,” *Chem. Mater.*, vol. 24, no. 19, pp. 3765–3771, 2012, doi: 10.1021/cm302363x.

[117] X. Wang *et al.*, “Cu-Deficient Plasmonic $Cu_{2-x}S$ Nanoplate Electrocatalysts for Oxygen Reduction,” *ACS Catal.*, vol. 5, no. 4, pp. 2534–2540, 2015, doi: 10.1021/acscatal.5b00115.

[118] T. T. Zhuang *et al.*, “Integration of semiconducting sulfides for full-spectrum solar energy absorption and efficient charge separation,” *Angew. Chemie - Int. Ed.*, vol. 55, no. 22, pp. 6396–6400, 2016, doi: 10.1002/anie.201601865.

[119] A. Descoeudres *et al.*, “Silicon Heterojunction Solar Cells: Towards Low-cost High-Efficiency Industrial Devices and Application to Low-concentration PV,” *Energy Procedia*, vol. 77, pp. 508–514, 2015, doi: 10.1016/j.egypro.2015.07.072.

[120] P. Jackson *et al.*, “Properties of Cu(In,Ga)Se2solar cells with new record efficiencies up to 21.7%,” *Phys. Status Solidi - Rapid Res. Lett.*, vol. 9, no. 1, pp. 28–31, 2015, doi: 10.1002/pssr.201409520.

[121] H. S. Jung and N. G. Park, “Perovskite solar cells: From materials to devices,” *Small*, vol. 11, no. 1, pp. 10–25, 2015, doi: 10.1002/smll.201402767.

[122] O. Isabella, A. H. M. Smets, and M. Zeman, “Thin-film silicon-based quadruple junction solar cells approaching 20% conversion efficiency,” *Sol. Energy Mater. Sol. Cells*, vol. 129, pp. 82–89, 2014, doi: 10.1016/j.solmat.2014.03.021.

[123] M. K. Panda, K. Ladomenou, and A. G. Coutsolelos, “Porphyrins in bio-inspired transformations: Light-harvesting to solar cell,” *Coord. Chem. Rev.*, vol. 256, no. 21–22, pp. 2601–2627, 2012, doi: 10.1016/j.ccr.2012.04.041.

[124] O. Adebanjo, P. P. Maharjan, P. Adhikary, M. Wang, S. Yang, and Q. Qiao, “Triple junction polymer solar cells,” *Energy Environ. Sci.*, vol. 6, no. 11, pp. 3150–3170, 2013, doi: 10.1039/c3ee42257g.

[125] and F. W. N. S. Sariciftci, D. Braun, C. Zhang, V. I. Srdanov, A. J. Heeger, G. Stucky, “Semiconducting polymer-buckminsterfullerene heterojunctions: Diodes, photodiodes, and photovoltaic cells,” *Appl. Phys. Lett.*, vol. 62, pp. 585–587, 1998, doi: 10.1063/1.108863.

[126] N. T. Jafferis, E. F. Helbling, M. Karpelson, and R. J. Wood, “Untethered flight of an insect-sized flapping-wing microscale aerial vehicle,” *Nature*, vol. 570, no. 7762, pp. 491–495, 2019, doi: 10.1038/s41586-019-1322-0.

[127] S. Antohe and L. Tugulea, “Electrical and Photovoltaic Properties of a Two-Layer Organic Photovoltaic Cell,” *Phys. status solidi*, vol. 128, no. 1, pp. 253–260, 1991, doi: 10.1002/pssa.2211280128.

[128] S. Antohe, “Electrical and Photovoltaic Properties of Tetrapyrydilporphyrin Sandwich Cells,” *Phys. status solidi*, vol. 136, no. 2, pp. 401–410, 1993, doi: 10.1002/pssa.2211360213.

[129] T. S. and W. Brütting, “Exciton diffusion and optical interference in organic donor–acceptor photovoltaic cells,” *Rev. Mex. Sociol.*, vol. 90, no. 7, pp. 3632–3641, 2001, doi: 10.1063/1.1394920.

[130] M. A. Green, K. Emery, Y. Hishikawa, W. Warta, and E. D. Dunlop, “Solar cell efficiency tables (version 43),” *Prog. Photovoltaics Res. Appl.*, vol. 22, no. 1, pp. 1–9, 2014, doi: 10.1002/pip.2452.

[131] M. Green, E. Dunlop, J. Hohl-Ebinger, M. Yoshita, N. Kopidakis, and X. Hao, “Solar cell efficiency tables (version 57),” *Prog. Photovoltaics Res. Appl.*, vol. 29, no. 1, pp. 3–15, 2021, doi: 10.1002/pip.3371.

[132] M. A. Green, K. Emery, D. L. King, S. Igari, and W. Warta, “Solar cell efficiency tables (version 18),” *Prog. Photovoltaics Res. Appl.*, vol. 9, no. 4, pp. 287–293, 2001, doi: 10.1002/pip.389.

[133] M. A. Green, K. Emery, Y. Hishikawa, W. Warta, and E. D. Dunlop, “Solar cell efficiency tables (Version 45),” *Prog. Photovoltaics Res. Appl.*, vol. 23, no. 1, pp. 1–9, 2015, doi: 10.1002/pip.2573.

[134] M. A. Green, K. Emery, Y. Hishikawa, W. Warta, and E. D. Dunlop, “Solar cell efficiency tables (version 47),” *Prog. Photovoltaics Res. Appl.*, vol. 24, no. 1, pp. 3–11, 2016, doi: 10.1002/pip.2728.

[135] M. A. Green *et al.*, “Solar cell efficiency tables (version 49),” *Prog. Photovoltaics Res. Appl.*, vol. 25, no. 1, pp. 3–13, 2017, doi: 10.1002/pip.2855.

[136] M. A. Green, Y. Hishikawa, E. D. Dunlop, D. H. Levi, J. Hohl-Ebinger, and A. W. Y. Ho-Baillie, “Solar cell efficiency tables (version 51),” *Prog. Photovoltaics Res. Appl.*, vol. 26, no. 1, pp. 3–12, 2018, doi: 10.1002/pip.2978.

[137] M. A. Green *et al.*, “Solar cell efficiency tables (Version 53),” *Prog. Photovoltaics Res. Appl.*, vol. 27, no. 1, pp. 3–12, 2019, doi: 10.1002/pip.3102.

[138] M. A. Green, E. D. Dunlop, J. Hohl-Ebinger, M. Yoshita, N. Kopidakis, and A. W. Y. Ho-Baillie, “Solar cell efficiency tables (Version 55),” *Prog. Photovoltaics Res. Appl.*, vol. 28, no. 1, pp. 3–15, 2020, doi: 10.1002/pip.3228.

[139] C. W. Tang and A. C. Albrecht, “Photovoltaic effects of metal-chlorophyll-a-metal sandwich cells,” *J. Chem. Phys.*, vol. 2139, no. 1975, pp. 2139–2149, 1975, doi: 10.1063/1.430780.

[140] S. E. Shaheen, C. J. Brabec, N. S. Sariciftci, F. Padinger, T. Fromherz, and J. C. Hummelen, “2.5% Efficient Organic Plastic Solar Cells,” *Appl. Phys. Lett.*, vol. 78, no. 6, pp. 841–843, 2001, doi: 10.1063/1.1345834.

[141] Y. Kim, S. A. Choulis, J. Nelson, D. D. C. Bradley, S. Cook, and J. R. Durrant, “Device annealing effect in organic solar cells with blends of regioregular poly(3-hexylthiophene) and soluble fullerene,” *Appl. Phys. Lett.*, vol. 86, no. 6, pp. 1–3, 2005, doi: 10.1063/1.1861123.

[142] W. Wang *et al.*, “High-efficiency polymer photovoltaic devices from regioregular-poly(3- hexylthiophene-2,5-diyl) and [6,6]-phenyl- C61 -butyric acid methyl ester processed with oleic acid surfactant,” *Appl. Phys. Lett.*, vol. 90, no. 18, pp. 67–70, 2007, doi: 10.1063/1.2735937.

[143] H. Y. Chen *et al.*, “Polymer solar cells with enhanced open-circuit voltage and efficiency,” *Nat. Photonics*, vol. 3, no. 11, pp. 649–653, 2009, doi: 10.1038/nphoton.2009.192.

[144] Y. Liang *et al.*, “For the bright future-bulk heterojunction polymer solar cells with power conversion efficiency of 7.4%,” *Adv. Mater.*, vol. 22, no. 20, pp. 135–138, 2010, doi: 10.1002/adma.200903528.

[145] H. Zhou, L. Yang, A. C. Stuart, S. C. Price, S. Liu, and W. You, “Development of fluorinated benzothiadiazole as a structural unit for a polymer solar cell of 7% efficiency,” *Angew. Chemie - Int. Ed.*, vol. 50, no. 13, pp. 2995–2998, 2011, doi: 10.1002/anie.201005451.

[146] J. You *et al.*, “A polymer tandem solar cell with 10.6% power conversion efficiency,” *Nat. Commun.*, vol. 4, 2013, doi: 10.1038/ncomms2411.

[147] C. L. Bellew, S. Hollar, and K. S. J. Pister, “An SOI process for fabrication of solar cells, transistors and electrostatic actuators,” pp. 1075–1079, 2003.

[148] S. Hollar, A. Flynn, C. Bellew, and K. S. J. Pister, “Solar powered 10 mg silicon robot,” *Sixt. Annu. Int. Conf. Micro Electro Mech. Syst. 2003. MEMS-03 Kyoto. IEEE*, pp. 706–711, 2003, doi: 10.1109/MEMSYS.2003.1189847.

[149] S. B. and K. S. J. Pister, “Design of an Autonomous Jumping Microrobot,” *Proc. 2007 IEEE Int. Conf. Robot. Autom.*, pp. 447–453, 2007, doi: 10.1016/0735-1097(89)90399-9.

[150] J. R. Reid, V. Vasilyev, and R. T. Webster, “Building Micro-Robots: A path to sub-mm3 autonomous systems,” *TechConnect Briefs*, vol. 3, pp. 174–177, 2008.

[151] E. Edqvist *et al.*, “Evaluation of building technology for mass producible millimetre-sized robots using flexible printed circuit boards,” *J. Micromechanics Microengineering*, vol. 19, no. 7, 2009, doi: 10.1088/0960-1317/19/7/075011.

[152] W. Andre and S. Martel, “Design of photovoltaic cells to power control electronics embedded in untethered aqueous microrobots propelled by bacteria,” *IEEE Int. Conf. Intell. Robot. Syst.*, pp. 1335–1340, 2006, doi: 10.1109/IROS.2006.281918.

[153] M. Perales *et al.*, “Characterization of high performance silicon-based VMJ PV cells for laser power transmission applications,” 2016, vol. 9733, pp. 97330U-9733–17, [Online]. Available: https://doi.org/10.1117/12.2213886.

[154] J. James, V. Iyer, Y. Chukewad, S. Gollakota, and S. B. Fuller, “Liftoff of a 190 mg Laser-Powered Aerial Vehicle: The Lightest Wireless Robot to Fly,” *2018 IEEE Int. Conf. Robot. Autom.*, pp. 3587–3594, 2018.

[155] Y. Chukewad, S. Member, J. James, S. Member, and A. Singh, “RoboFly : An insect-sized robot with simplified fabrication that is capable of flight , ground , and water surface locomotion,” vol. XX, no. X, pp. 1–15, 2020.

[156] M. Z. Miskin *et al.*, “Electronically integrated, mass-manufactured, microscopic robots,” *Nature*, vol. 584, no. 7822,

pp. 557–561, 2020, doi: 10.1038/s41586-020-2626-9.

[157] C. Domínguez, N. Jost, S. Askins, M. Victoria, and I. Antón, “A review of the promises and challenges of micro-concentrator photovoltaics,” *AIP Conf. Proc.*, vol. 1881, 2017, doi: 10.1063/1.5001441.

[158] X. Pang, J. an Lv, C. Zhu, L. Qin, and Y. Yu, “Photodeformable Azobenzene-Containing Liquid Crystal Polymers and Soft Actuators,” *Adv. Mater.*, vol. 31, no. 52, pp. 1–26, 2019, doi: 10.1002/adma.201904224.

[159] H. K. Bisoyi, A. M. Urbas, and Q. Li, “Soft Materials Driven by Photothermal Effect and Their Applications,” *Adv. Opt. Mater.*, vol. 6, no. 15, pp. 1–21, 2018, doi: 10.1002/adom.201800458.

[160] M. Sitti and D. S. Wiersma, “Pros and Cons: Magnetic versus Optical Microrobots,” *Adv. Mater.*, vol. 32, no. 20, 2020, doi: 10.1002/adma.201906766.

[161] V. H. Nguyen *et al.*, “Stimuli-Responsive MXene-Based Actuators,” *Adv. Funct. Mater.*, vol. 30, no. 47, p. 1909504, 2020, doi: 10.1002/adfm.201909504.

[162] A. G. Bell, “Upon the production and reproduction of sound by light,” *J. Soc. Telegr. Eng.*, vol. 9, no. 34, pp. 404–426, 1880.

[163] K. Uchino and L. E. Cross, “Electrostriction and its interrelation with other anharmonic properties of materials,” *Japanese Journal of Applied Physics*, vol. 19, no. 4. pp. L171–L173, 1980, doi: 10.1143/JJAP.19.L171.

[164] M. Hippler *et al.*, “Controlling the shape of 3D microstructures by temperature and light,” *Nat. Commun.*, vol. 10, no. 1, pp. 1–8, 2019, doi: 10.1038/s41467-018-08175-w.

[165] T. Ikeda, J. I. Mamiya, and Y. Yu, “Photomechanics of liquid-crystalline elastomers and other polymers,” *Angew. Chemie - Int. Ed.*, vol. 46, no. 4, pp. 506–528, 2007, doi: 10.1002/anie.200602372.

[166] K. Kumar *et al.*, “A chaotic self-oscillating sunlight-driven polymer actuator,” *Nat. Commun.*, vol. 7, no. May, pp. 1–8, 2016, doi: 10.1038/ncomms11975.

[167] Z. Cheng, T. Wang, X. Li, Y. Zhang, and H. Yu, “NIR-Vis-UV Light-Responsive Actuator Films of Polymer-Dispersed Liquid Crystal/Graphene Oxide Nanocomposites,” *ACS Appl. Mater. Interfaces*, vol. 7, no. 49, pp. 27494–27501, 2015, doi: 10.1021/acsami.5b09676.

[168] Y. Yu, M. Nakano, and T. Ikeda, “Photomechanics: directed bending of a polymer film by light,” *Nature*, vol. 425, no. 6954, p. 145, 2003, doi: 10.1038/425145a.

[169] N. Tabiryan, S. Serak, X.-M. Dai, and T. Bunning, “Polymer film with optically controlled form and actuation,” *Opt. Express*, vol. 13, no. 19, p. 7442, 2005, doi: 10.1364/OPEX.13.007442.

[170] E. B. Purcell and S. Crosson, “Photoregulation in prokaryotes,” *Curr. Opin. Microbiol.*, vol. 11, no. 2, pp. 168–178, 2008, doi: 10.1016/j.mib.2008.02.014.

[171] D. Schmidt and Y. K. Cho, “Natural photoreceptors and their application to synthetic biology,” *Trends Biotechnol.*,

vol. 33, no. 2, pp. 80–91, 2015, doi: 10.1016/j.tibtech.2014.10.007.

[172] A. Bunea, D. Martella, S. Nocentini, C. Parmeggiani, R. Taboryski, and D. S. Wiersma, “Light-Powered Microrobots: Challenges and Opportunities for Hard and Soft Responsive Microswimmers,” *Adv. Intell. Syst.*, vol. 2000256, p. 2000256, 2021, doi: 10.1002/aisy.202000256.

[173] M. Medina-Sánchez, V. Magdanz, M. Guix, V. M. Fomin, and O. G. Schmidt, “Swimming Microrobots: Soft, Reconfigurable, and Smart,” *Adv. Funct. Mater.*, vol. 28, no. 25, pp. 1–27, 2018, doi: 10.1002/adfm.201707228.

[174] S. Palagi, D. P. Singh, and P. Fischer, “Light-Controlled Micromotors and Soft Microrobots,” *Adv. Opt. Mater.*, vol. 7, no. 16, pp. 1–18, 2019, doi: 10.1002/adom.201900370.

[175] L. Hines, K. Petersen, G. Z. Lum, and M. Sitti, “Soft Actuators for Small-Scale Robotics,” *Adv. Mater.*, vol. 29, no. 13, p. 1603483, 2017, doi: 10.1002/adma.201603483.

[176] R. A. M. Hikmet and D. J. Broer, “Dynamic mechanical properties of anisotropic networks formed by liquid crystalline acrylates,” *Polymer (Guildf).*, vol. 32, no. 9, pp. 1627–1632, 1991.

[177] Y. Fuchigami, T. Takigawa, and K. Urayama, “Electrical actuation of cholesteric liquid crystal gels,” *ACS Macro Lett.*, vol. 3, no. 8, pp. 813–818, 2014, doi: 10.1021/mz5003382.

[178] K. F. Lehmann W, Skupin H, Tolksdorf C, Gebhard E, Zentel R, Krüger P, Lösche M, “Giant lateral electrostriction in ferroelectric liquid-crystalline elastomers,” *Lett. to Nat.*, vol. 410, pp. 447–450, 2001, doi: 10.1038/35068522.

[179] H. Wermter and H. Finkelmann, “Liquid crystalline elastomers as artificial muscles,” *E-Polymers*, vol. 1, no. 1, pp. 1–13, 2001, doi: 10.1515/epoly.2001.1.1.111.

[180] Y. Hong *et al.*, “Micron-sized main-chain liquid crystalline elastomer actuators with ultralarge amplitude contractions,” *J. Am. Chem. Soc.*, vol. 131, no. 41, pp. 15000–15004, 2009, doi: 10.1021/ja905363f.

[181] H. Zeng, P. Wasylczyk, C. Parmeggiani, D. Martella, M. Burresi, and D. S. Wiersma, “Light-Fueled Microscopic Walkers,” *Adv. Mater.*, vol. 27, no. 26, pp. 3883–3887, 2015, doi: 10.1002/adma.201501446.

[182] T. J. White *et al.*, “A high frequency photodriven polymer oscillator,” *Soft Matter*, vol. 4, no. 9, pp. 1796–1798, 2008, doi: 10.1039/b805434g.

[183] C. Ohm, M. Brehmer, and R. Zentel, “Liquid crystalline elastomers as actuators and sensors,” *Adv. Mater.*, vol. 22, no. 31, pp. 3366–3387, 2010, doi: 10.1002/adma.200904059.

[184] T. Qiu, S. Palagi, A. G. Mark, K. Melde, F. Adams, and P. Fischer, “Wireless actuation with functional acoustic surfaces,” *Appl. Phys. Lett.*, vol. 109, no. 19, pp. 1–5, 2016, doi: 10.1063/1.4967194.

[185] T. J. White and D. J. Broer, “Programmable and adaptive mechanics with liquid crystal polymer networks and elastomers,” *Nat. Mater.*, vol. 14, no. 11, pp. 1087–1098, 2015, doi: 10.1038/nmat4433.

[186] N. P. Godman, B. A. Kowalski, A. D. Auguste, H. Koerner, and T. J. White, “Synthesis of Elastomeric Liquid Crystalline

Polymer Networks via Chain Transfer," *ACS Macro Lett.*, vol. 6, no. 11, pp. 1290–1295, 2017, doi: 10.1021/acsmacrolett.7b00822.

[187] L. T. De Haan, A. P. H. J. Schenning, and D. J. Broer, "Programmed morphing of liquid crystal networks," *Polymer (Guildf).*, vol. 55, no. 23, pp. 5885–5896, 2014, doi: 10.1016/j.polymer.2014.08.023.

[188] T. Mirfakhrai *et al.*, "Carbon Nanotube Yarns as High Load Actuators and Sensors," *Adv. Sci. Technol.*, vol. 61, pp. 65–74, 2008, doi: 10.4028/www.scientific.net/AST.61.65.

[189] C. National *et al.*, "Torsional carbon nanotube artificial muscles," vol. 334, no. October, pp. 494–498, 2011.

[190] B. G. M. Spinks *et al.*, "Pneumatic Carbon Nanotube Actuators," no. 23, pp. 1728–1732, 2002, doi: 10.1002/1521-4095(20021203)14:23<1728::AID-ADMA1728>3.0.CO;2-8.

[191] A. E. Aliev *et al.*, "Giant-Stroke, Superelastic Carbon Nanotube Aerogel Muscles - Supporting Online Material," *Carbon N. Y.*, vol. 323, no. March, p. 1575, 2009, [Online]. Available: www.sciencemag.org/cgi/content/full/323/5921/1575/DC1.

[192] W. Wen, X. Huang, S. Yang, K. Lu, and P. Sheng, "The giant electrorheological effect in suspensions of nanoparticles," *Nat. Mater.*, vol. 2, no. 11, pp. 727–730, 2003, doi: 10.1038/nmat993.

[193] S. Genç and P. P. Phulé, "Rheological properties of magnetorheological fluids," *Smart Mater. Struct.*, vol. 11, no. 1, pp. 140–146, 2002, doi: 10.1088/0964-1726/11/1/316.

[194] T. Jamin, C. Py, and E. Falcon, "Instability of the origami of a ferrofluid drop in a magnetic field," *Phys. Rev. Lett.*, vol. 107, no. 20, pp. 1–5, 2011, doi: 10.1103/PhysRevLett.107.204503.

[195] I. O. Timonen JV, Latikka M, Leibler L, Ras RH, "Switchable Static and Dynamic Self-Assembly of Magnetic Droplets on Superhydrophobic Surfaces," *Science (80-.).*, vol. 341, no. July, pp. 253–257, 2013, doi: 10.1126/science.1112699.

[196] A. Beyzavi and N. T. Nguyen, "Programmable two-dimensional actuation of ferrofluid droplet using planar microcoils," *J. Micromechanics Microengineering*, vol. 20, no. 1, 2010, doi: 10.1088/0960-1317/20/1/015018.

[197] K. Takemura, F. Yajima, S. Yokota, and K. Edamura, "Integration of micro artificial muscle cells using electro-conjugate fluid," *Sensors Actuators, A Phys.*, vol. 144, no. 2, pp. 348–353, 2008, doi: 10.1016/j.sna.2008.02.011.

[198] R. Abe, K. Takemura, K. Edamura, and S. Yokota, "Concept of a micro finger using electro-conjugate fluid and fabrication of a large model prototype," *Sensors Actuators, A Phys.*, vol. 136, no. 2, pp. 629–637, 2007, doi: 10.1016/j.sna.2006.10.046.

[199] A. Yamaguchi, K. Takemura, S. Yokota, and K. Edamura, "A robot hand using electro-conjugate fluid: Grasping experiment with balloon actuators inducing a palm motion of robot hand," *Sensors Actuators, A Phys.*, vol. 174, no. 1, pp. 181–188, 2012, doi: 10.1016/j.sna.2011.11.036.

[200] I. Moon and J. Kim, "Using EWOD (electrowetting-on-dielectric) actuation in a micro conveyor system," *Sensors*

Actuators, A Phys., vol. 130–131, no. SPEC. ISS., pp. 537–544, 2006, doi: 10.1016/j.sna.2005.12.016.

[201] N. B. Crane, P. Mishra, and A. A. Volinsky, "Characterization of electrowetting processes through force measurements," *Rev. Sci. Instrum.*, vol. 81, no. 4, 2010, doi: 10.1063/1.3373945.

[202] M. R. Khan, C. B. Eaker, E. F. Bowden, and M. D. Dickey, "Giant and switchable surface activity of liquid metal via surface oxidation," *Proc. Natl. Acad. Sci.*, vol. 111, no. 39, pp. 14047–14051, 2014, doi: 10.1073/pnas.1412227111.

[203] S. Y. Tang *et al.*, "Electrochemically induced actuation of liquid metal marbles," *Nanoscale*, vol. 5, no. 13, pp. 5949–5957, 2013, doi: 10.1039/c3nr00185g.

[204] B. E. Schubert and D. Floreano, "Variable stiffness material based on rigid low-melting-point-alloy microstructures embedded in soft poly(dimethylsiloxane) (PDMS)," *RSC Adv.*, vol. 3, no. 46, pp. 24671–24679, 2013, doi: 10.1039/c3ra44412k.

[205] E. Bormashenko, R. Pogreb, R. Balter, O. Gendelman, and D. Aurbach, "Composite non-stick droplets and their actuation with electric field," *Appl. Phys. Lett.*, vol. 100, no. 15, pp. 1–6, 2012, doi: 10.1063/1.3702568.

[206] Y. Zhao, J. Fang, H. Wang, X. Wang, and T. Lin, "Magnetic liquid marbles: Manipulation of liquid droplets using highly hydrophobic Fe3O4nanoparticles," *Adv. Mater.*, vol. 22, no. 6, pp. 707–710, 2010, doi: 10.1002/adma.200902512.

[207] X. Tang *et al.*, "Photochemically induced motion of liquid metal marbles," *Appl. Phys. Lett.*, vol. 103, no. 17, p. 174104, 2013, doi: 10.1063/1.4826923.

[208] J. Kim, S. Yun, and Z. Ounaies, "Discovery of cellulose as a smart material," *Macromolecules*, vol. 39, no. 12, pp. 4202–4206, 2006, doi: 10.1021/ma060261e.

[209] J. Kim, S. Yun, S. K. Mahadeva, K. Yun, S. Y. Yang, and M. Maniruzzaman, "Paper actuators made with cellulose and hybrid materials," *Sensors*, vol. 10, no. 3, pp. 1473–1485, 2010, doi: 10.3390/s100301473.

[210] M. M. Hamedi *et al.*, "Electrically Activated Paper Actuators," *Adv. Funct. Mater.*, vol. 26, no. 15, pp. 2446–2453, 2016, doi: 10.1002/adfm.201505123.

[211] J. D. W. Madden *et al.*, "Artificial muscle technology: physical principles and naval prospects," vol. 29, no. 3, pp. 706–728, 2004.

[212] I. Must *et al.*, "Ionic and Capacitive Artificial Muscle for Biomimetic Soft Robotics," *Adv. Eng. Mater.*, vol. 17, 2015.

[213] L. Bay, K. West, P. Sommer-Larsen, S. Skaarup, and M. Benslimane, "A Conducting Polymer Artificial Muscle with 12 % Linear Strain," *Adv. Mater.*, vol. 15, pp. 310–313, 2003.

[214] Y. Liu *et al.*, "High Electromechanical Response of Ionic Polymer Actuators with Controlled-Morphology Aligned Carbon Nanotube/Nafion Nanocomposite Electrodes," vol. 20, no. 19, pp. 3266–3271, 2016, doi: 10.1002/adfm.201000570.High.

[215] G. M. Spinks and V. T. Truong, "Work-per-cycle analysis for electromechanical actuators," *Sensors Actuators, A Phys.*,

vol. 119, no. 2, pp. 455–461, 2005, doi: 10.1016/j.sna.2004.10.010.

[216] S. M. Kim and K. J. Kim, “Palladium buffer-layered high performance ionic polymer-metal composites,” *Smart Mater. Struct.*, vol. 17, no. 3, 2008, doi: 10.1088/0964-1726/17/3/035011.

[217] V. Palmre, D. Pugal, K. J. Kim, K. K. Leang, K. Asaka, and A. Aabloo, “Nanothorn electrodes for ionic polymer-metal composite artificial muscles,” *Sci. Rep.*, vol. 4, pp. 1–10, 2014, doi: 10.1038/srep06176.

[218] M. Shahinpoor and K. J. Kim, “Ionic polymer-metal composites: IV. Industrial and medical applications,” *Smart Mater. Struct.*, vol. 14, no. 1, pp. 197–214, 2005, doi: 10.1088/0964-1726/14/1/020.

[219] V. Palmre *et al.*, “Nanoporous carbon-based electrodes for high strain ionomeric bending actuators,” *Smart Mater. Struct.*, vol. 18, no. 9, 2009, doi: 10.1088/0964-1726/18/9/095028.

[220] S. Akbari, “Arrays of dielectric elastomer microactuators for cell mechanotransduction,” vol. 5697, p. 134, 2013.

[221] N. America *et al.*, “High-Speed Electrically Actuated Elastomers with Strain Greater Than 100 %,” vol. 287, pp. 836–840, 2000, doi: 10.1126/science.287.5454.836.

[222] C. Keplinger, T. Li, R. Baumgartner, Z. Suo, and S. Bauer, “Harnessing snap-through instability in soft dielectrics to achieve giant voltage-triggered deformation,” *Soft Matter*, vol. 8, no. 2, pp. 285–288, 2012, doi: 10.1039/c1sm06736b.

[223] C. Gillespie, A. Marzo, F. Scarpa, J. Rossiter, and A. T. Conn, “High- voltage photonic switching of dielectric elastomers with amorphous silicon thin-films,” *Electroact. Polym. Actuators Devices*, vol. 10966, 2019.

[224] S. Guitron *et al.*, “An Untethered Miniature Origami Robot that Self-folds , Walks , Swims , and Degrades The MIT Faculty has made this article openly available . Please share Citation Accessed Citable Link Detailed Terms An Untethered Miniature Origami Robot that Self-folds ,” 2018.

[225] W. Voit *et al.*, “High-strain shape-memory polymers,” *Adv. Funct. Mater.*, vol. 20, no. 1, pp. 162–171, 2010, doi: 10.1002/adfm.200901409.

[226] M. Anthamatten, S. Roddecha, and J. Li, “Energy storage capacity of shape-memory polymers,” *Macromolecules*, vol. 46, no. 10, pp. 4230–4234, 2013, doi: 10.1021/ma400742g.

[227] H. Jiang, S. Kelch, and A. Lendlein, “Polymers move in response to light,” *Adv. Mater.*, vol. 18, no. 11, pp. 1471–1475, 2006, doi: 10.1002/adma.200502266.

[228] E. Wang, M. S. Desai, and S. W. Lee, “Light-controlled graphene-elastin composite hydrogel actuators,” *Nano Lett.*, vol. 13, no. 6, pp. 2826–2830, 2013, doi: 10.1021/nl401088b.

[229] Q. Zhao *et al.*, “An instant multi-responsive porous polymer actuator driven by solvent molecule sorption,” *Nat. Commun.*, vol. 5, pp. 1–8, 2014, doi: 10.1038/ncomms5293.

[230] Y. Ma, Y. Zhang, B. Wu, W. Sun, Z. Li, and J. Sun, “Polyelectrolyte multilayer films for building energetic walking

devices," *Angew. Chemie - Int. Ed.*, vol. 50, no. 28, pp. 6254–6257, 2011, doi: 10.1002/anie.201101054.

[231] E. Diller, J. Zhuang, G. Zhan Lum, M. R. Edwards, and M. Sitti, "Continuously distributed magnetization profile for millimeter-scale elastomeric undulatory swimming," *Appl. Phys. Lett.*, vol. 104, no. 17, 2014, doi: 10.1063/1.4874306.

[232] P. Garstecki, P. Tierno, D. B. Weibel, F. Sagués, and G. M. Whitesides, "Propulsion of flexible polymer structures in a rotating magnetic field," *J. Phys. Condens. Matter*, vol. 21, no. 20, 2009, doi: 10.1088/0953-8984/21/20/204110.

[233] B. Jang *et al.*, "Undulatory Locomotion of Magnetic Multilink Nanoswimmers," *Nano Lett.*, vol. 15, no. 7, pp. 4829–4833, 2015, doi: 10.1021/acs.nanolett.5b01981.

[234] T. Satoh, K. Sumaru, T. Takagi, and T. Kanamori, "Fast-reversible light-driven hydrogels consisting of spirobenzopyran- functionalized poly(N-isopropylacrylamide)," *Soft Matter*, vol. 7, no. 18, pp. 8030–8034, 2011, doi: 10.1039/c1sm05797a.

[235] M. P. M. Dicker *et al.*, "Light-triggered soft artificial muscles: Molecular-level amplification of actuation control signals," *Sci. Rep.*, vol. 7, no. 1, pp. 1–8, 2017, doi: 10.1038/s41598-017-08777-2.

[236] F. Ercole, T. P. Davis, and R. A. Evans, "Photo-responsive systems and biomaterials: Photochromic polymers, light-triggered self-assembly, surface modification, fluorescence modulation and beyond," *Polym. Chem.*, vol. 1, no. 1, pp. 37–54, 2010, doi: 10.1039/b9py00300b.

[237] J. Wei and Y. Yu, "Photodeformable polymer gels and crosslinked liquid-crystalline polymers," *Soft Matter*, vol. 8, no. 31, pp. 8050–8059, 2012, doi: 10.1039/c2sm25474c.

[238] M. Irie, *New Polymer Materials*. Heidelberg: Springer-Verlag, 1990.

[239] H. Zeng, O. M. Wani, P. Wasylczyk, and A. Priimagi, "Light-Driven, Caterpillar-Inspired Miniature Inching Robot," *Macromol. Rapid Commun.*, vol. 39, no. 1, pp. 1–6, 2018, doi: 10.1002/marc.201700224.

[240] M. Rogóż, H. Zeng, C. Xuan, D. S. Wiersma, and P. Wasylczyk, "Light-Driven Soft Robot Mimics Caterpillar Locomotion in Natural Scale," *Adv. Opt. Mater.*, vol. 4, no. 11, pp. 1689–1694, 2016, doi: 10.1002/adom.201600503.

[241] J. J. Wie, M. R. Shankar, and T. J. White, "Photomotility of polymers," *Nat. Commun.*, vol. 7, pp. 1–8, 2016, doi: 10.1038/ncomms13260.

[242] X. Liu, S. K. Kim, and X. Wang, "Thermomechanical liquid crystalline elastomer capillaries with biomimetic peristaltic crawling function," *J. Mater. Chem. B*, vol. 4, no. 45, pp. 7293–7302, 2016, doi: 10.1039/C6TB02372J.

[243] S. Iamsaard *et al.*, "Conversion of light into macroscopic helical motion," *Nat. Chem.*, vol. 6, no. 3, pp. 229–235, 2014, doi: 10.1038/nchem.1859.

[244] C. L. Van Oosten, C. W. M. Bastiaansen, and D. J. Broer, "Printed artificial cilia from liquid-crystal network actuators modularly driven by light," *Nat. Mater.*, vol. 8, no. 8, pp. 677–682, 2009, doi: 10.1038/nmat2487.

[245] S. Palagi *et al.*, “Structured light enables biomimetic swimming and versatile locomotion of photoresponsive soft microrobots,” *Nat. Mater.*, vol. 15, no. 6, pp. 647–653, 2016, doi: 10.1038/nmat4569.

[246] C. Huang, J. A. Lv, X. Tian, Y. Wang, Y. Yu, and J. Liu, “Miniaturized swimming soft robot with complex movement actuated and controlled by remote light signals,” *Sci. Rep.*, vol. 5, no. October, pp. 1–8, 2015, doi: 10.1038/srep17414.

[247] A. DeSimone, P. Gidoni, and G. Noselli, “Liquid crystal elastomer strips as soft crawlers,” *J. Mech. Phys. Solids*, vol. 84, pp. 254–272, 2015, doi: 10.1016/j.jmps.2015.07.017.

[248] A. P. Zakharov and L. M. Pismen, “Nematoelastic crawlers,” *Phys. Rev. E*, vol. 93, no. 2, pp. 1–6, 2016, doi: 10.1103/PhysRevE.93.022703.

[249] X. Lu, S. Guo, X. Tong, H. Xia, and Y. Zhao, “Tunable Photocontrolled Motions Using Stored Strain Energy in Malleable Azobenzene Liquid Crystalline Polymer Actuators,” *Adv. Mater.*, vol. 29, no. 28, pp. 1–7, 2017, doi: 10.1002/adma.201606467.

[250] R. Tang, Z. Liu, D. Xu, J. Liu, L. Yu, and H. Yu, “Optical pendulum generator based on photomechanical liquid-crystalline actuators,” *ACS Appl. Mater. Interfaces*, vol. 7, no. 16, pp. 8393–8397, 2015, doi: 10.1021/acsami.5b01732.

[251] R. R. Kohlmeyer and J. Chen, “Wavelength-selective, IR light-driven hinges based on liquid crystalline elastomer composites,” *Angew. Chemie - Int. Ed.*, vol. 52, no. 35, pp. 9234–9237, 2013, doi: 10.1002/anie.201210232.

[252] A. Mourran, H. Zhang, R. Vinokur, and M. Mïller, “Soft Microrobots Employing Nonequilibrium Actuation via Plasmonic Heating,” *Advanced Materials*, vol. 29, no. 2. 2017, doi: 10.1002/adma.201604825.

[253] O. M. Wani, H. Zeng, and A. Priimagi, “A light-driven artificial flytrap,” *Nat. Commun.*, vol. 8, no. May, pp. 1–7, 2017, doi: 10.1038/ncomms15546.

[254] D. Martella, S. Nocentini, D. Nuzhdin, C. Parmeggiani, and D. S. Wiersma, “Photonic Microhand with Autonomous Action,” *Adv. Mater.*, vol. 29, no. 42, p. 1704047, 2017, doi: 10.1002/adma.201704047.

[255] T. J. Nugent, Jr. and J. T. Kare, “Laser power beaming for defense and security applications,” *Unmanned Syst. Technol. XIII*, vol. 8045, no. May 2011, p. 804514, 2011, doi: 10.1117/12.886169.

[256] A. H. Kazim *et al.*, “Effects of oxyhydrogen gas induction on the performance of a small-capacity diesel engine,” *Sci. Prog.*, vol. 103, no. 2, pp. 1–14, 2020, doi: 10.1177/0036850420921685.

[257] S. SUDO, T. Yano, Y. KAN, Y. YAMADA, and K. TSUYUKI, “Swimming behavior of small diving beetles,” *J. Adv. Sci.*, vol. 18, pp. 46–49, 2006, doi: 10.2978/jsas.18.46.

[258] R. J. Lock, R. Vaidyanathan, S. C. Burgess, and J. H. Loveless, “Development of a biologically inspired multi-modal wing model for aerial-aquatic robotic vehicles through empirical and numerical modelling of the common guillemot, Uria aalge,” *Bioinspiration and Biomimetics*, vol. 5, no. 4, 2010, doi: 10.1088/1748-3182/5/4/046001.

[259] J. Davenport, “How and why do flying fish fly?,” *Rev. Fish Biol. Fish.*, vol. 4, no. 2, pp. 184–214, 1994, doi: 10.1007/BF00044128.

[260] H. Park and H. Choi, “Aerodynamic characteristics of flying fish in gliding flight,” *J. Exp. Biol.*, vol. 213, no. 19, pp. 3269–3279, 2010, doi: 10.1242/jeb.046052.

[261] J. M. V Rayner, “Pleuston: animals which move in water and air,” *Endeavour*, vol. 10, no. 2, pp. 58–64, 1986.

[262] K. P. R. R. Murphy, E. Steimle, C. Griffin, C. Cullins, M. Hall, “Cooperative use of unmanned sea surface and micro aerial vehicles at Hurricane Wilma,” *J. F. Robot.*, vol. 25, no. 3, pp. 164–180, 2008, doi: 10.1002/rob.

[263] R. Siddall and M. Kovač, “Launching the AquaMAV: Bioinspired design for aerial-aquatic robotic platforms,” *Bioinspiration and Biomimetics*, vol. 9, no. 3, 2014, doi: 10.1088/1748-3182/9/3/031001.

[264] J. S. Izraelevitz and M. S. Triantafyllou, “A novel degree of freedom in flapping wings shows promise for a dual aerial/aquatic vehicle propulsor,” *Proc. - IEEE Int. Conf. Robot. Autom.*, vol. 2015-June, no. June, pp. 5830–5837, 2015, doi: 10.1109/ICRA.2015.7140015.

[265] R. Zufferey *et al.*, “Consecutive aquatic jump-gliding with water-reactive fuel,” *Sci. Robot.*, vol. 4, no. 34, 2019, doi: 10.1126/scirobotics.aax7330.

[266] R. Siddall and M. Kovac, “Fast Aquatic Escape with a Jet Thruster,” *IEEE/ASME Transactions on Mechatronics*, vol. 22, no. 1. pp. 217–226, 2017, doi: 10.1109/TMECH.2016.2623278.

[267] A. Vidyasagar, J. C. Zufferey, D. Floreano, and M. Kovač, “Performance analysis of jump-gliding locomotion for miniature robotics,” *Bioinspiration and Biomimetics*, vol. 10, no. 2, pp. 1–12, 2015, doi: 10.1088/1748-3190/10/2/025006.

[268] A. L. Desbiens, M. T. Pope, D. L. Christensen, E. W. Hawkes, and M. R. Cutkosky, “Design principles for efficient, repeated jumpgliding,” *Bioinspiration and Biomimetics*, vol. 9, no. 2, 2014, doi: 10.1088/1748-3182/9/2/025009.

[269] R. Eubank, E. Atkins, and G. Meadows, “Unattended operation of an autonomous seaplane for persistent surface and airborne ocean monitoring,” *MTS/IEEE Seattle, Ocean. 2010*, pp. 1–8, 2010, doi: 10.1109/OCEANS.2010.5664098.

[270] F. A. Soriano Moranchell, J. M. Sandoval Pineda, J. N. Hernández Pérez, U. S. Silva-Rivera, C. A. Cortes Escobedo, and R. de G. González Huerta, “Electrodes modified with Ni electrodeposition decrease hexavalent chromium generation in an alkaline electrolysis process,” *Int. J. Hydrogen Energy*, vol. 45, no. 26, pp. 13683–13692, 2020, doi: 10.1016/j.ijhydene.2020.01.050.

[271] L. R. F. Allen J. Bard, *Electrochemical Methods: Fundamentals and Applications, 2nd Edition*. Wiley, 2001.

[272] E. Zoulias, E. Varkaraki, N. Lymberopoulos, C. N. Christodoulou, and G. N. Karagiorgis, “A review on alkaline water electrolysis,” *Tcjst*, vol. 4, no. 2, pp. 41–71, 2004, [Online]. Available: http://hydrogenoman.com/docs/click on the attached.pdf.

[273] H. L. Newhouse and P. R. Payne, “Underwater Power Source Study,” 1981.

[274] J. Borchsenius and S. Pinder, “Underwater glider propulsion using chemical hydrides,” in *OCEANS’10 IEEE SYDNEY*, May 2010, pp. 1–8, doi: 10.1109/OCEANSSYD.2010.5603515.

[275] R. E. Threlfall, *The Story of 100 Years of Phosphorus Making 1851–1951 (Albright & Wilson, 1951)*. 1951.

[276] K. O’Connor, “NASA Glenn Safety Manual CHAPTER 6 – HYDROGEN,” 2003.

[277] M. P. Moyle, R. B. Morrison, and S. W. Churchill, “Detonation characteristics of hydrogen-oxygen mixtures,” *AIChE J.*, vol. 6, no. 1, pp. 92–96, 1960, doi: 10.1002/aic.690060118.

[278] H. Chisholm, “1911 Encyclopædia Britannica / Oxyhydrogen Flame,” no. September. p. 8838308, 2018.

[279] A. H. WILLBOURN and C. N. HINSHELWOOD, “The mechanism of the hydrogen-oxygen reaction,” *Proc. R. Soc. Lond. A. Math. Phys. Sci.*, vol. 185, no. March 1945, pp. 353–369, 1946, doi: 10.1098/rspa.1946.0023.

[280] M. Peck, “Soft-Robotic Rover with Electrodynamic Power Scavenging,” 2016. [Online]. Available: https://www.nasa.gov/sites/default/files/atoms/files/11-2015_phase_i_mason_peck_soft_robotic_rover_electrodynamic_power_scavenging.pdf.

[281] A. Romanelli, I. Bove, and F. González Madina, “Air expansion in a water rocket,” *Am. J. Phys.*, vol. 81, no. 10, pp. 762–766, 2013, doi: 10.1119/1.4811116.

[282] C. J. Gommes, “A more thorough analysis of water rockets: Moist adiabats, transient flows, and inertial forces in a soda bottle,” *Am. J. Phys.*, vol. 78, no. 3, pp. 236–243, 2010, doi: 10.1119/1.3257702.

[283] W. A. Churaman, L. J. Currano, C. J. Morris, J. E. Rajkowski, and S. Bergbreiter, “The first launch of an autonomous thrust-driven microrobot using nanoporous energetic silicon,” *J. Microelectromechanical Syst.*, vol. 21, no. 1, pp. 198–205, 2012, doi: 10.1109/JMEMS.2011.2174414.

[284] Y. Chen *et al.*, “A biologically inspired , flapping-wing , hybrid aerial-aquatic microrobot,” vol. 5619, no. October, pp. 1–12, 2017, doi: 10.1126/scirobotics.aao5619.

[285] R. F. Shepherd *et al.*, “Using explosions to power a soft robot,” *Angew. Chemie - Int. Ed.*, vol. 52, no. 10, pp. 2892–2896, 2013, doi: 10.1002/anie.201209540.

[286] M. T. Tolley *et al.*, “An untethered jumping soft robot,” *IEEE Int. Conf. Intell. Robot. Syst.*, no. Iros, pp. 561–566, 2014, doi: 10.1109/IROS.2014.6942615.

[287] Nicholas W. Bartlett, Michael T. Tolley, Johannes T. B. Overvelde, James C. Weaver, Bobak Mosadegh, Katia Bertoldi, George M. Whitesides, Robert J. Wood, “A 3D-printed, functionally graded soft robot powered by combustion,” *Science (80-.).*, vol. 349, no. 6244, pp. 161–165, 2015.

[288] M. Loepfe, C. M. Schumacher, U. B. Lustenberger, and W. J. Stark, “An untethered, jumping roly-poly soft robot driven by combustion,” *Soft Robot.*, vol. 2, no. 1, pp. 33–41, 2015, doi: 10.1089/soro.2014.0021.

[289] E. G. Karakolis, B. Nguyen, J. B. You, C. M. Rochman, and D. Sinton, “Fluorescent Dyes for Visualizing Microplastic Particles and Fibers in Laboratory-Based Studies,” *Environ. Sci. Technol. Lett.*, vol. 6, no. 6, pp. 334–340, 2019, doi: 10.1021/acs.estlett.9b00241.

[290] M. Abdellah, A. Bilgili, S. Eilemann, J. Shillcock, H. Markram, and F. Schürmann, “Bio-physically plausible visualization of highly scattering fluorescent neocortical models for in silico experimentation,” *BMC Bioinformatics*, vol. 18, no. Suppl 2, pp. 1–14, 2017, doi: 10.1186/s12859-016-1444-4.

[291] E. Purington, D. Bousfield, and W. M. Gramlich, “Fluorescent dye adsorption in aqueous suspension to produce tagged cellulose nanofibers for visualization on paper,” *Cellulose*, vol. 26, no. 8, pp. 5117–5131, 2019, doi: 10.1007/s10570-019-02439-4.

[292] D. Keithly *et al.*, “A cephalopod-inspired combustion powered hydro-jet engine using soft actuators,” *Extrem. Mech. Lett.*, vol. 20, pp. 1–8, 2018, doi: 10.1016/j.eml.2017.11.007.

[293] M. Loepfe, C. M. Schumacher, and W. J. Stark, “Design, performance and reinforcement of bearing-free soft silicone combustion-driven pumps,” *Ind. Eng. Chem. Res.*, vol. 53, no. 31, pp. 12519–12526, 2014, doi: 10.1021/ie501991d.

[294] H. A. Kazem and M. T. Chaichan, “The Impact of Using Solar Colored Filters to Cover the PV Panel in Its Outcomes,” *Sch. Bull.*, vol. 2, no. 7, pp. 464–469, 2016, doi: 10.21276/sb.2016.2.7.5.

[295] M. Garrad, G. Soter, A. T. Conn, H. Hauser, and J. Rossiter, “A soft matter computer for soft robots,” *Sci. Robot.*, vol. 4, no. 33, 2019, doi: 10.1126/scirobotics.aaw6060.

[296] M. F. Simons, A. C. Haynes, Y. Gao, Y. Zhu, and J. Rossiter, “In contact: Pinching, squeezing and twisting for mediated social touch,” *Conf. Hum. Factors Comput. Syst. - Proc.*, pp. 1–9, 2020, doi: 10.1145/3334480.3382798.

[297] A. B. Watson, “QUEST: A general multidimensional bayesian adaptive psychometric method,” *J. Vis.*, vol. 17, no. 3, pp. 1–27, 2017, doi: 10.1167/17.3.10.

[298] E. Battaglia, J. P. Clark, M. Bianchi, M. G. Catalano, A. Bicchi, and M. K. O’malley, “Skin Stretch Haptic Feedback to Convey Closure Information in Anthropomorphic, Under-Actuated Upper Limb Soft Prostheses,” *IEEE Trans. Haptics*, vol. 12, no. 4, pp. 508–520, 2019, doi: 10.1109/TOH.2019.2915075.

[299] Y. Visell, “Tactile sensory substitution: Models for enaction in HCI,” *Interact. Comput.*, vol. 21, no. 1–2, pp. 38–53, 2009, doi: 10.1016/j.intcom.2008.08.004.

[300] J. R. Alice Haynes, Melanie Simons, Tim Helps, Yuichi Nakamura, “A wearable skin-stretching tactile interface for human-robot and human-human communication,” *IEEE Robot. Autom. Lett.*, vol. 4, no. 2, pp. 1641–1646, 2019.

[301] M. F. Nolan, “Two-Point Discrimination Assessment in the Upper Limb in Young Adult Men and Women,” *Phys. Ther.*, vol. 62, no. 7, pp. 965–969, Jul. 1982, doi: 10.1093/ptj/62.7.965.

[302] S. Kim, C. Laschi, and B. Trimmer, “Soft robotics: a bioinspired evolution in robotics.,” *Trends Biotechnol.*, vol. 31, no. 5, pp. 287–294, May 2013, doi: 10.1016/j.tibtech.2013.03.002.

[303] S. Coyle, C. Majidi, P. LeDuc, and K. J. Hsia, “Bio-inspired soft robotics: Material selection, actuation, and design,” *Extrem. Mech. Lett.*, vol. 22, pp. 51–59, 2018, doi: 10.1016/j.eml.2018.05.003.

[304] Y. Lee, W. J. Song, and J. Y. Sun, “Hydrogel soft robotics,” *Mater. Today Phys.*, vol. 15, p. 100258, 2020, doi: 10.1016/j.mtphys.2020.100258.

[305] E. M. Ahmed, “Hydrogel: Preparation, characterization, and applications: A review,” *J. Adv. Res.*, vol. 6, no. 2, pp. 105–121, 2015, doi: 10.1016/j.jare.2013.07.006.

[306] S. K. Ahn, R. M. Kasi, S. C. Kim, N. Sharma, and Y. Zhou, “Stimuli-responsive polymer gels,” *Soft Matter*, vol. 4, no. 6, pp. 1151–1157, 2008, doi: 10.1039/b714376a.

[307] I. Ieropoulos, L. D. Chambers, J. Winfield, I. Ieropoulos, and J. Rossiter, “Biodegradable and edible gelatine actuators for use as artificial muscles,” *Proc. SPIE*, vol. 9056, p. 90560B, 2014, doi: 10.1117/12.2045104.

[308] J. Shintake, H. Sonar, E. Piskarev, J. Paik, and D. Floreano, “Soft pneumatic gelatin actuator for edible robotics,” *IEEE Int. Conf. Intell. Robot. Syst.*, vol. 2017-Septe, no. September, pp. 6221–6226, 2017, doi: 10.1109/IROS.2017.8206525.

[309] M. Rinaudo, “Main properties and current applications of some polysaccharides as biomaterials,” *Polym Int*, vol. 57, no. March 2008, pp. 397–430, 2008, doi: 10.1002/pi.

[310] S. Dumitriu, *Polysaccharides as Biomaterials in: Polymeric Biomaterials*, 2nd ed. New York: New York, Marcel Dekker, 2001.

[311] J. Jia *et al.*, “Engineering alginate as bioink for bioprinting,” *Acta Biomater.*, vol. 10, no. 10, pp. 4323–4331, 2014, doi: 10.1016/j.actbio.2014.06.034.

[312] X. Wang *et al.*, “Gelatin-based hydrogels for organ 3D bioprinting,” *Polymers (Basel).*, vol. 9, no. 9, 2017, doi: 10.3390/polym9090401.

[313] N. Bhattarai, J. Gunn, and M. Zhang, “Chitosan-based hydrogels for controlled, localized drug delivery,” *Adv. Drug Deliv. Rev.*, vol. 62, no. 1, pp. 83–99, 2010, doi: 10.1016/j.addr.2009.07.019.

[314] F. Ahmadi, Z. Oveisi, S. M. Samani, and Z. Amoozgar, “Chitosan based hydrogels: characteristics and pharmaceutical applications,” *Res. Pharm. Sci.*, vol. 10, no. 1, pp. 1–16, 2015, [Online]. Available: https://pubmed.ncbi.nlm.nih.gov/26430453.

[315] M. Maeda, H. Shimahara, and N. Sugiyama, “Detailed examination of the branched structure of konjac glucomannan,” *Agric. Biol. Chem.*, vol. 44, no. 2, pp. 245–252, 1980, doi: 10.1080/00021369.1980.10863939.

[316] K. Kato and K. Matsuda, “Studies on the Chemical Structure of Konjac Mannan,” *Agric. Biol. Chem.*, vol. 36, no. 4, pp. 639–644, 1972, doi: 10.1080/00021369.1972.10860296.

[317] A. Kurt and T. Kahyaoglu, “Characterization of a new biodegradable edible film made from salep glucomannan,” *Carbohydr. Polym.*, vol. 104, no. 1, pp. 50–58, 2014, doi: 10.1016/j.carbpol.2014.01.003.

[318] K. Maekaji, “The mechanism of gelation of konjac mannan,” *Agric. Biol. Chem.*, vol. 38, no. 2, pp. 315–321, 1974, doi: 10.1080/00021369.1974.10861161.

[319] and K. N. Martin A. K. Williams, Tim J. Foster, Dave R. Martin, Ian T. Norton, Miki Yoshimura, “A molecular description of the gelation mechanism of konjac mannan,” *Biomacromolecules*, vol. 1, no. 3, pp. 440–450, 2000, doi: 10.1016/S0141-8130(01)00187-8.

[320] X. Du, J. Li, J. Chen, and B. Li, “Effect of degree of deacetylation on physicochemical and gelation properties of konjac glucomannan,” *Food Res. Int.*, vol. 46, no. 1, pp. 270–278, 2012, doi: 10.1016/j.foodres.2011.12.015.

[321] S. Gao, J. Guo, and K. Nishinari, “Thermoreversible konjac glucomannan gel crosslinked by borax,” *Carbohydr. Polym.*, vol. 72, no. 2, pp. 315–325, 2008, doi: 10.1016/j.carbpol.2007.08.015.

[322] C. Song, Y. Lv, K. Qian, Y. Chen, and X. Qian, “Preparation of konjac glucomannan–borax hydrogels with good self-healing property and pH-responsive behavior,” *J. Polym. Res.*, vol. 26, no. 2, 2019, doi: 10.1007/s10965-019-1702-z.

[323] K. Yu, A. Xin, and Q. Wang, “Mechanics of self-healing polymer networks crosslinked by dynamic bonds,” *J. Mech. Phys. Solids*, vol. 121, pp. 409–431, 2018, doi: 10.1016/j.jmps.2018.08.007.

[324] J. Dahlke, S. Zechel, M. D. Hager, and U. S. Schubert, “How to Design a Self-Healing Polymer: General Concepts of Dynamic Covalent Bonds and Their Application for Intrinsic Healable Materials,” *Adv. Mater. Interfaces*, vol. 5, no. 17, pp. 1–14, 2018, doi: 10.1002/admi.201800051.

[325] S. Terryn, J. Brancart, D. Lefeber, G. Van Assche, and B. Vanderborght, “Self-healing soft pneumatic robots,” *Sci. Robot.*, vol. 2, no. 9, pp. 1–13, 2017, doi: 10.1126/scirobotics.aan4268.

[326] E. Roels, S. Terryn, J. Brancart, R. Verhelle, G. Van Assche, and B. Vanderborght, “Additive Manufacturing for Self-Healing Soft Robots,” *Soft Robot.*, vol. 7, no. 6, pp. 711–723, 2020, doi: 10.1089/soro.2019.0081.

[327] J. N. I. Balitaan, C. Der Hsiao, J. M. Yeh, and K. S. Santiago, “Innovation inspired by nature: Biocompatible self-healing injectable hydrogels based on modified-β-chitin for wound healing,” *Int. J. Biol. Macromol.*, vol. 162, pp. 723–736, 2020, doi: 10.1016/j.ijbiomac.2020.06.129.

[328] T. Yuan, X. Cui, X. Liu, X. Qu, and J. Sun, “Highly Tough, Stretchable, Self-Healing, and Recyclable Hydrogels Reinforced by in Situ-Formed Polyelectrolyte Complex Nanoparticles,” *Macromolecules*, vol. 52, no. 8, pp. 3141–3149, 2019, doi: 10.1021/acs.macromol.9b00053.

[329] Z. Li, Y. Su, B. Xie, X. Liu, X. Gao, and D. Wang, “A novel biocompatible double network hydrogel consisting of konjac glucomannan with high mechanical strength and ability to be freely shaped,” *J. Mater. Chem. B*, vol. 3, no. 9, pp. 1769–1778, 2015, doi: 10.1039/c4tb01653j.

[330] C. Xu, G. Dai, and Y. Hong, “Recent advances in high-strength and elastic hydrogels for 3D printing in biomedical applications,” *Acta Biomater.*, vol. 95, pp. 50–59, 2019, doi: 10.1016/j.actbio.2019.05.032.

[331] H. Lipson, “Challenges and Opportunities for Design, Simulation, and Fabrication of Soft Robots,” *Soft Robot.*, vol. 1,

no. 1, pp. 21–27, 2014, doi: 10.1089/soro.2013.0007.

[332] T. J. Wallin, J. Pikul, and R. F. Shepherd, “3D printing of soft robotic systems,” *Nat. Rev. Mater.*, vol. 3, no. 6, pp. 84–100, 2018, doi: 10.1038/s41578-018-0002-2.

[333] M. R. D. P Selcan Gungor-Ozkerim, Ilyas Inci, Yu Shrike Zhang, Ali Khademhosseini, “Bioinks for 3D bioprinting: an overview,” *Biomater Sci*, vol. 1, no. 6, pp. 915–946, 2018, doi: 10.1039/c7bm00765e.Bioinks.

[334] Y. Jin, A. Compaan, T. Bhattacharjee, and Y. Huang, “Granular gel support-enabled extrusion of three-dimensional alginate and cellular structures,” *Biofabrication*, vol. 8, no. 2, pp. 1–12, 2016, doi: 10.1088/1758-5090/8/2/025016.

[335] Y. Wang *et al.*, “3D Bioprintability of Konjac Glucomannan Hydrogel,” *Medziagotyra*, vol. 26, no. 1, pp. 109–113, 2020, doi: 10.5755/j01.ms.26.1.20336.

[336] S. Tibbits, “4D Printing Multi-Material Shape Change,” *Archit. Des.*, vol. 84, no. 1, pp. 116–121, 2014, doi: 10.1142/9789811201493_0027.

[337] A. López-Díaz *et al.*, “Autonomous self-healing pneumatic McKibben muscle based on a new hydrogel material,” in *2020 3rd IEEE International Conference on Soft Robotics (RoboSoft)*, 2020, pp. 13–18, doi: 10.1109/RoboSoft48309.2020.9115992.

[338] B. Webb and B. J. Doyle, “Parameter optimization for 3D bioprinting of hydrogels,” *Bioprinting*, vol. 8, no. September, pp. 8–12, 2017, doi: 10.1016/j.bprint.2017.09.001.

[339] B. Lu *et al.*, “One-Pot Assembly of Microfibrillated Cellulose Reinforced PVA-Borax Hydrogels with Self-Healing and pH-Responsive Properties,” *ACS Sustain. Chem. Eng.*, vol. 5, no. 1, pp. 948–956, 2017, doi: 10.1021/acssuschemeng.6b02279.

[340] I. Resano-Goizueta, B. K. Ashokan, T. A. Trezza, and G. W. Padua, “Effect of Nano-Fillers on Tensile Properties of Biopolymer Films,” *J. Polym. Environ.*, vol. 26, no. 9, pp. 3817–3823, 2018, doi: 10.1007/s10924-018-1260-1.

[341] M. Tako, “Synergistic Interaction between Xanthan and Konjac Glucomannan in Aqueous Media,” *Biosci. Biotechnol. Biochem.*, vol. 56, no. 8, pp. 1188–1192, 1992, doi: 10.1271/bbb.56.1188.

[342] T. J. Hinton, A. Hudson, K. Pusch, A. Lee, and A. W. Feinberg, “3D Printing PDMS Elastomer in a Hydrophilic Support Bath via Freeform Reversible Embedding,” *ACS Biomater. Sci. Eng.*, vol. 2, no. 10, pp. 1781–1786, 2016, doi: 10.1021/acsbiomaterials.6b00170.

[343] Q. Zhou, F. Gardea, Z. Sang, S. Lee, M. Pharr, and S. A. Sukhishvili, “A Tailorable Family of Elastomeric-to-Rigid, 3D Printable, Interbonding Polymer Networks,” *Adv. Funct. Mater.*, vol. 30, no. 30, pp. 1–10, 2020, doi: 10.1002/adfm.202002374.

[344] K. Narumi *et al.*, “Self-healing UI: Mechanically and electrically self-healing materials for sensing and actuation interfaces,” *UIST 2019 - Proc. 32nd Annu. ACM Symp. User Interface Softw. Technol.*, pp. 293–306, 2019, doi: 10.1145/3332165.3347901.

[345] V. Davé and S. P. McCarthy, “Review of konjac glucomannan,” *J. Environ. Polym. Degrad.*, vol. 5, no. 4, pp. 237–241, 1997, doi: 10.1007/BF02763667.

Appendix

Appendix A

Characterisation of solar panel performance between curved and flat state and at different light sources.

This section details the characterisation of the energy harvesting system used in FLASH. Several light sources were tested at different distances between curved and flat state of the solar cell (see figure A1 for experimental set up). It was found that halogen light yields the best result as compared to LED because the light produced by halogen bulb mostly fall into yellow to red spectrum which are better absorbed by solar cells [294]. For example, when comparing between the LED and halogen spotlight, blue and cyan lines respectively, at the same shining distance of 320mm, it was found that the halogen light source can produce significantly more voltage to the solar cell than the LED light source, 3.25V as compared to 2.5V. In other words, the LED spotlight is around 23% less effective than the halogen spotlight.

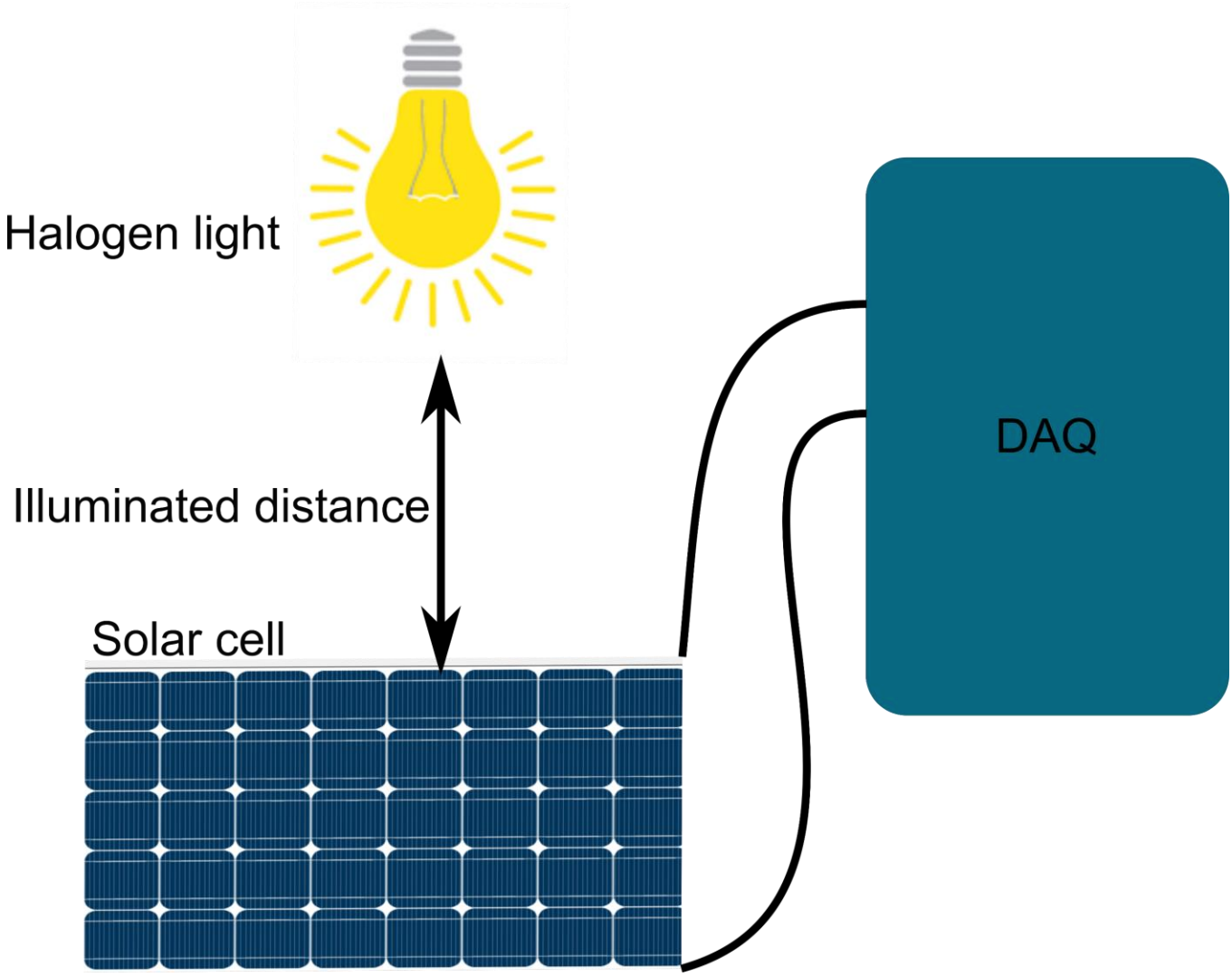

Figure A1: Solar panel performance characterisation experimental set up.

Furthermore, the geometry of the solar cell also affects its performance, as can be seen from figure A2 the curved solar cell perform worse than the flat solar cell. For instance, the curved halogen desk lamp (green line) produced 5% less voltage than the flat halogen desk lamp (red line) at the same shining distance of 50mm. This is because in the curved state, the area of absorption of the solar cell is reduced hence the reduction in voltage.

Figure A2 also shows that the further away the solar cell from the light source, the worse it performs. For instance, there is a significant reduction (25%) in voltage produced by the solar cell between the same halogen light source when it was place at distance 320mm and 50mm apart, red and pink lines respectively. This is expected as the further away the solar cells from the light source, the worse it performs due less photons hitting the semiconductors.

To address this drawback, one can use a series of lenses to focus the light beam so that the light source can be further away from the solar cell whilst maintaining similar voltage. This is particularly beneficial for applications of FLASH in the environment as it allows remote powering and targeted control. As can be seen from figure A2, halogen spotlight can provide similar voltage to the solar cell when compares to a halogen desk lamp at more than 4 times the distance, red and cyan lines, respectively. It is important to note that the same halogen light bulb (20W, 12V) has been used for both the spotlight and the desk lamp and it is clear from the graph that there is a big impact between the focused and unfocused light sources (cyan and pink lines) on the performance of the solar cell. To be specific, the halogen spotlight at 320mm distance (cyan line) produce about 25% more voltage in the solar cell than the halogen desk lamp at the same distance (pink line).

To conclude, this characterization experiment suggests that there are four factors one should consider when choosing the lighting system to power FLASH. The first is the type of light (i.e. Halogen or LED). The second is the geometry of the solar cell. The third is the distance of the light source from the cell and the last is the type of lenses most appropriate for a specific application (i.e. spotlight or coarse light). It was found that halogen spotlight is the most suited light source to power FLASH as it produces light in spectrums best absorbed by the solar cell and can be placed at a further distance than coarse halogen light without sacrificing the efficiency of the solar cell. Moreover, the light intensity of halogen light can be easily controlled by changing the voltage/current supply making it more flexible and adjustable in terms of light output and colour tone. This is important for remote powering as one can maintain the efficiency of the solar cell by adjusting the light intensity in accordance to the robot position with the light source. In addition, the colour tone can also be adjusted to activate smart light sensitive material for complex control.

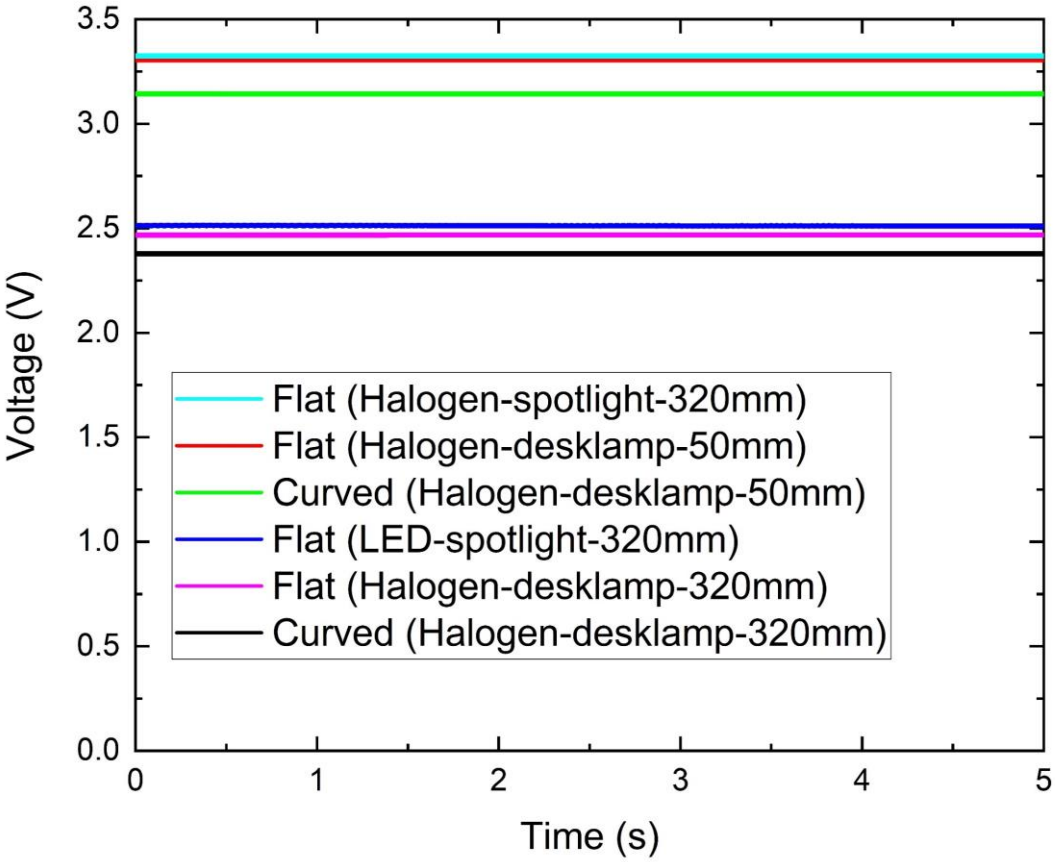

Figure A2: Solar panel performance characterisation against different geometries and light sources.

Appendix B

Average thrust generated at lower and higher energy inputs comparison

This section presents additional details related to the optimal geometry to maximum thrust generation (Chapter 4, section 4.1) which were omitted in the main text.

Table B.1: Average force responses at lower and higher energy inputs comparison across all tested samples.

Sample	**Lower Energy Inputs (J)**	**Average Force response at lower energy inputs (N)**	**Higher Energy Inputs (J)**	**Average Force response at Higher energy inputs (N)**
1 (6mm diameter)	88-220	4.682	313-421	5.738
2 (8mm diameter)	88-220	11.515	313-421	12.273
3 (10mm diameter)	88-220	17.703	313-421	17.492
4 (12mm diameter)	88-220	19.751	313-421	21.019
5 (14mm diameter)	88-220	23.709	313-421	25.273
6 (16mm diameter)	88-220	31.494	313-421	28.360
7 (18mm diameter)	88-220	30.842	313-421	31.019
8 (20mm diameter)	88-220	32.217	313-421	34.151
9 (22mm diameter)	88-220	34.305	313-421	37.188
10 (24mm diameter)	88-220	33.905	313-421	39.586
11 (26mm diameter)	88-220	34.623	313-421	40.275
Average all samples	**88-220**	**25.0**	**313-421**	**26.58**

Table B.1 shows the average force response at lower input energy is similar to that of higher input energy, 25 N and 26.5N respectively. This suggests that it will be more efficient and economical to operate FLASH at lower energy input with the given design. The largest average force response is 40N at higher input energy and with the largest nozzle. The table also shows that the amount of input energy has limited effect on the thrust generated as there is little difference in the amount of force generated at lower and higher energy in across all tested sample. The parameter has the most significant impact on thrust generation is orifice size. As can be seen from table B.1, there is a relatively linear relationship between orifice size and thrust generation.

Loadcell force response of oxyhydrogen combustion at different input energy for all samples

This section provides additional information related to the optimal geometry to maximum thrust generation (Chapter 4, section 4.1).

(i) Sample 1 – 6mm

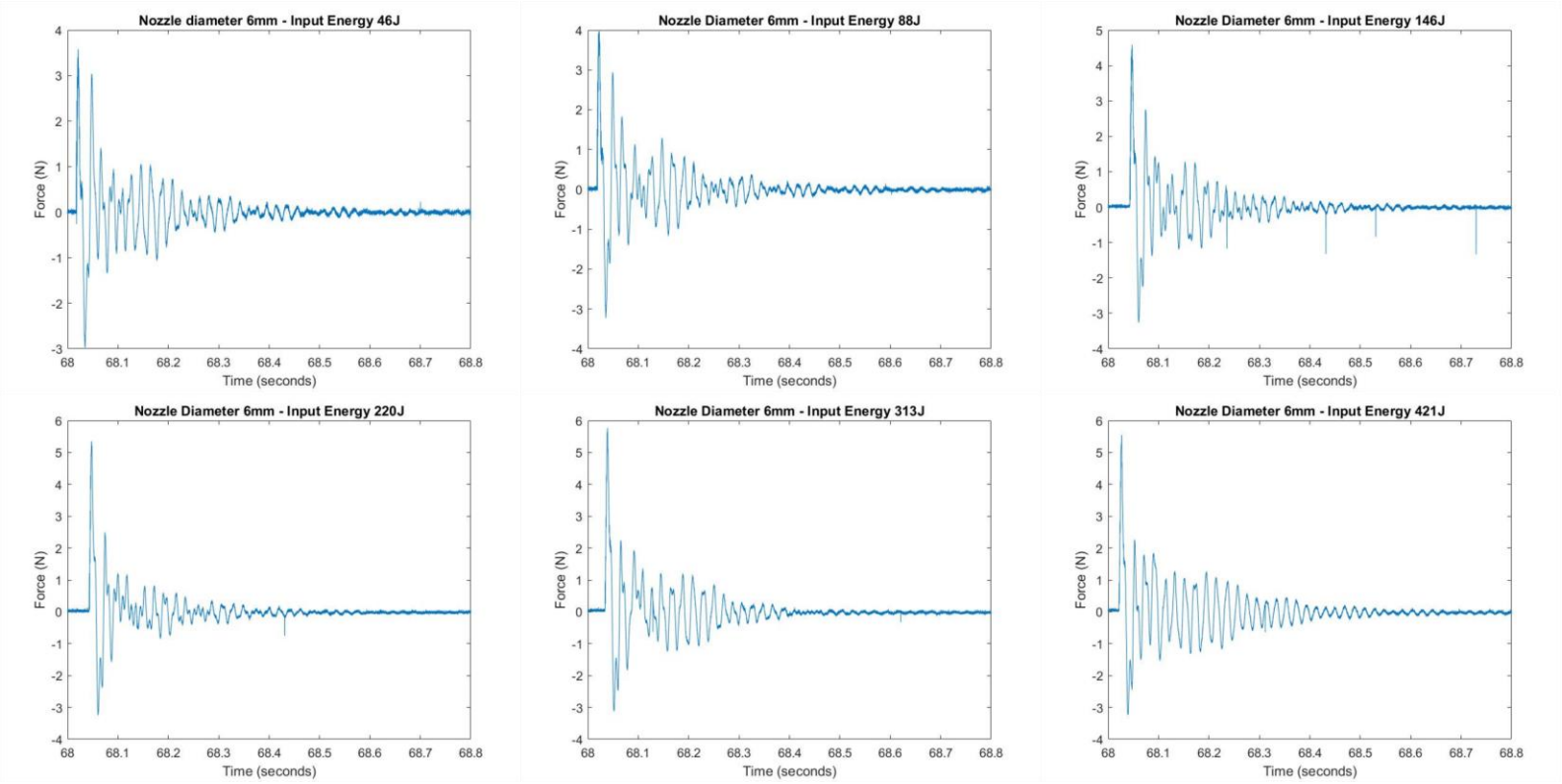

(ii) Sample 2 – 8mm

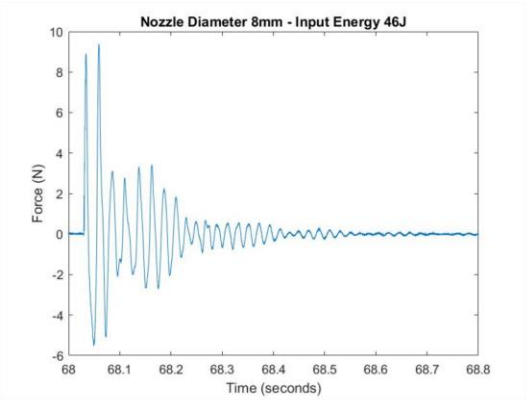

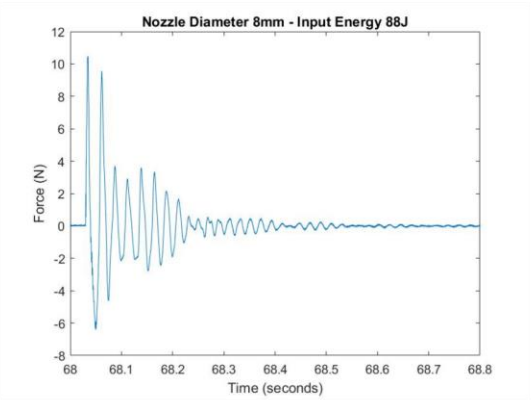

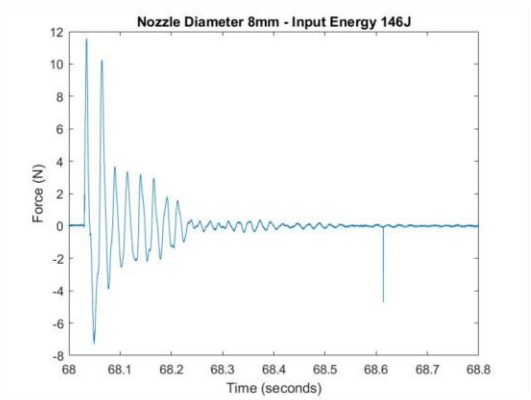

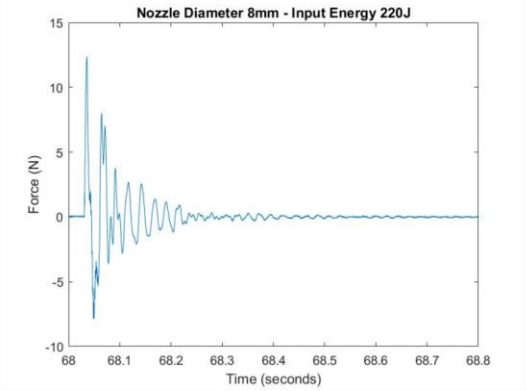

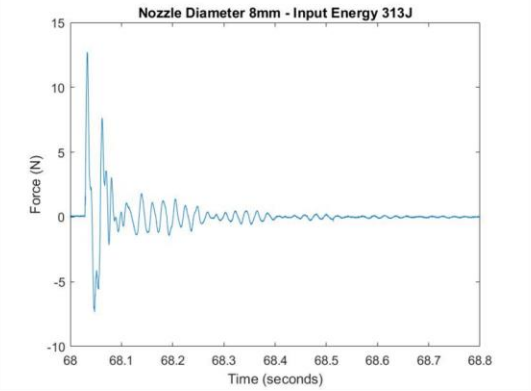

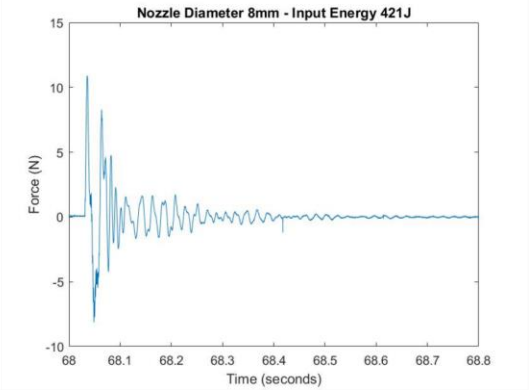

(iii) Sample 3 – 10mm

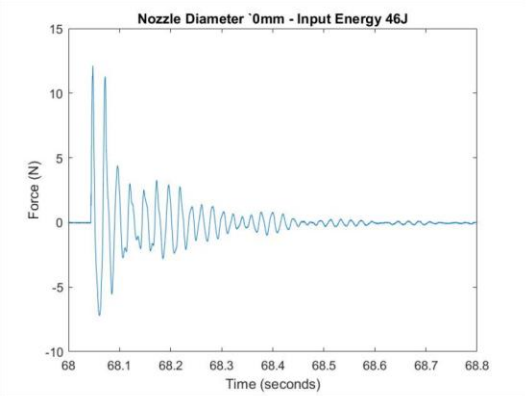

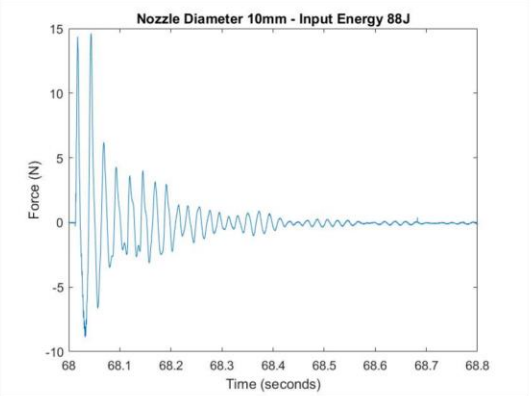

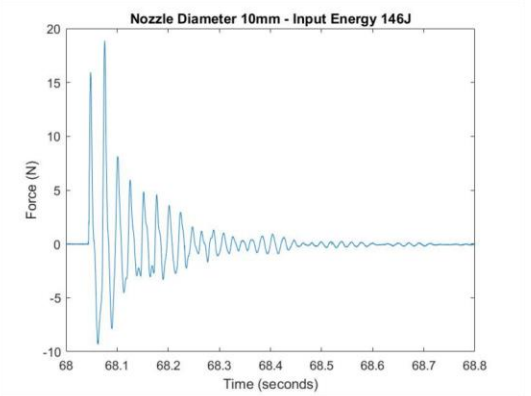

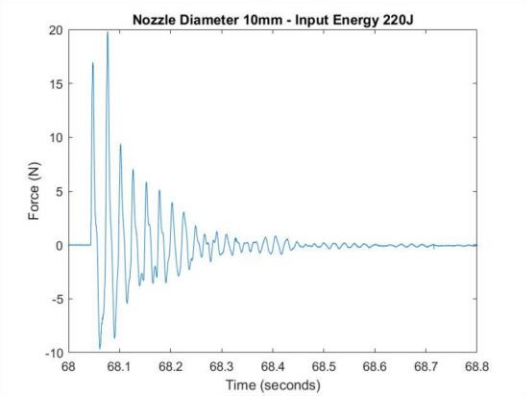

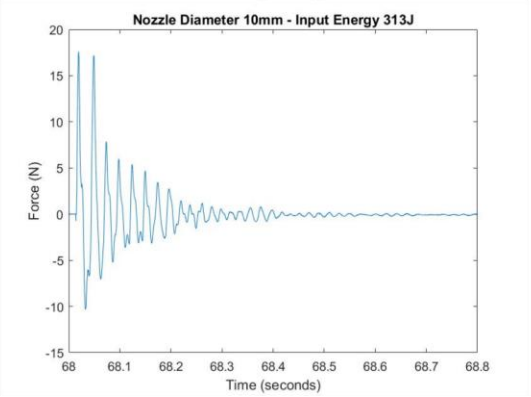

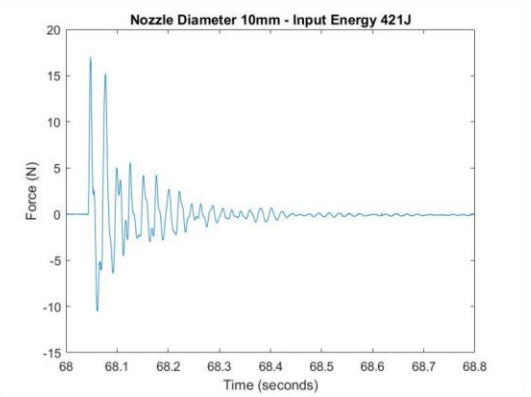

(iv) Sample 4 – 12mm

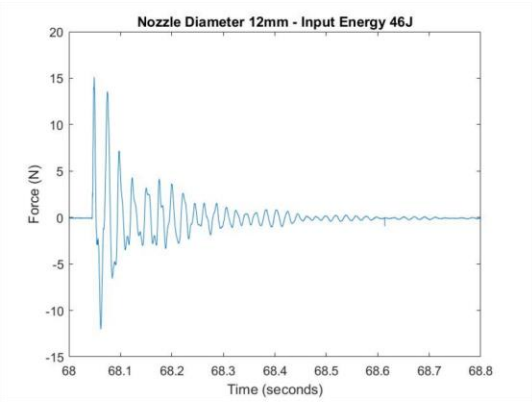

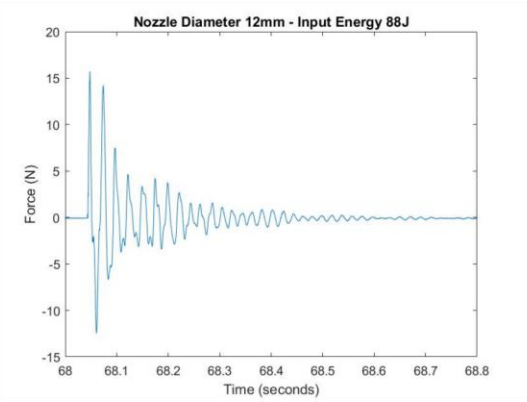

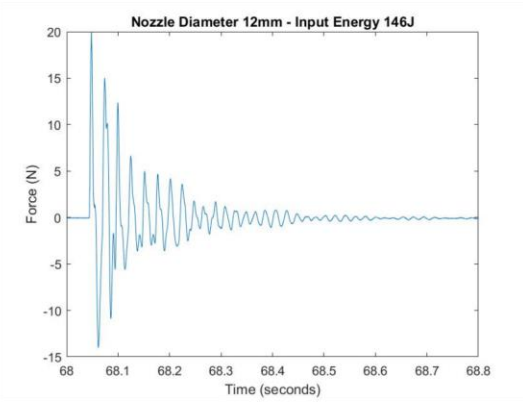

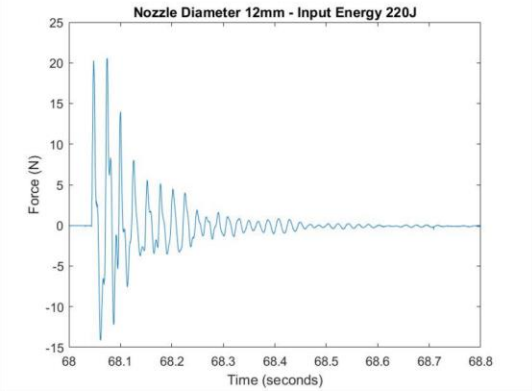

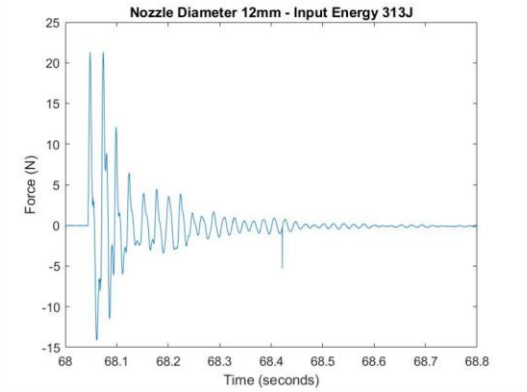

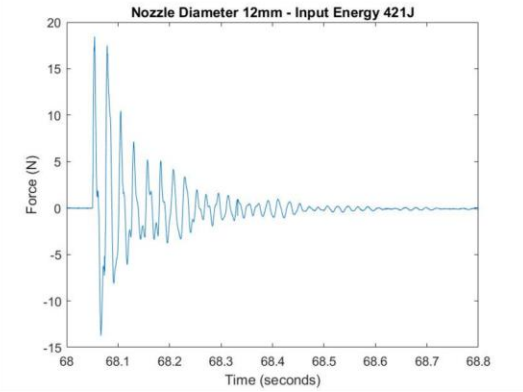

(v) Sample 5 – 14mm

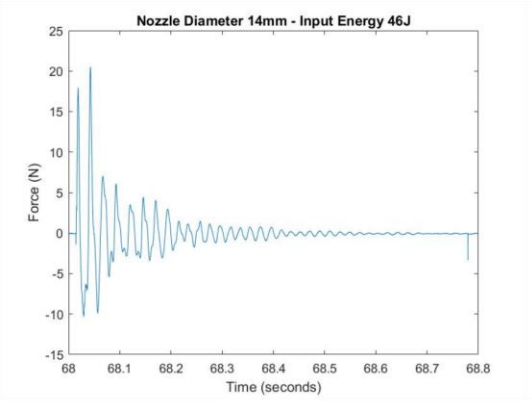

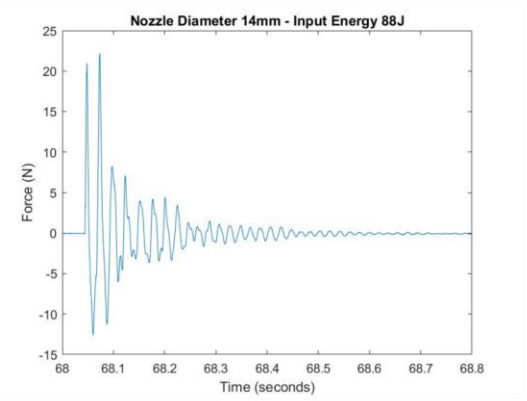

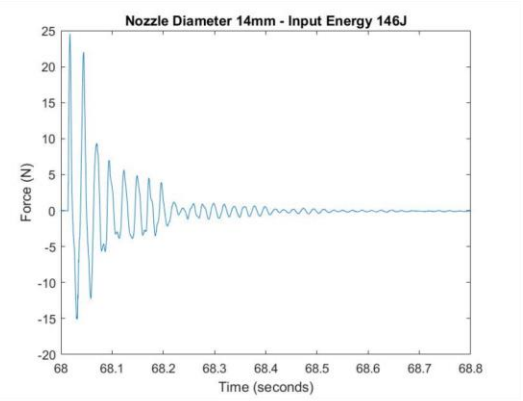

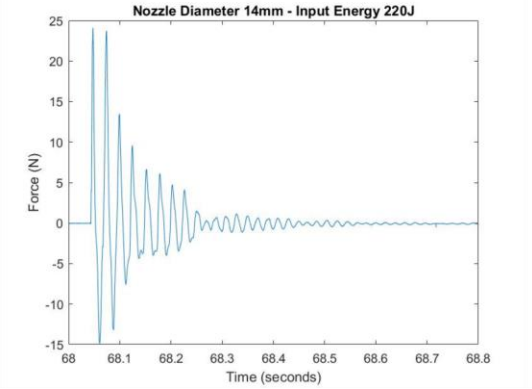

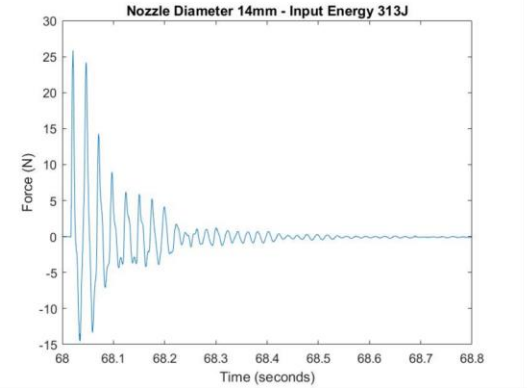

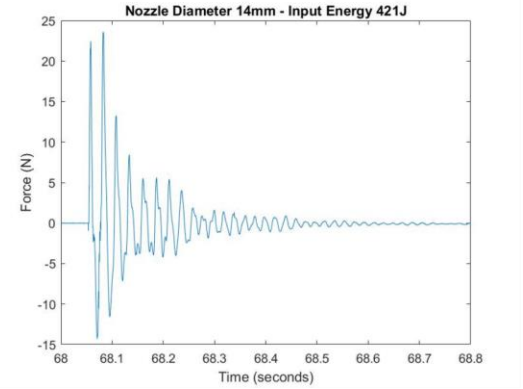

(vi) Sample 6 – 16mm

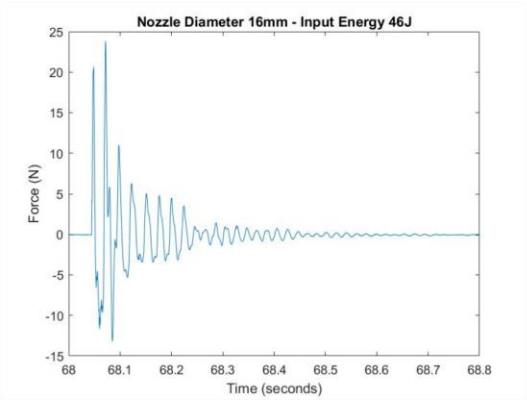

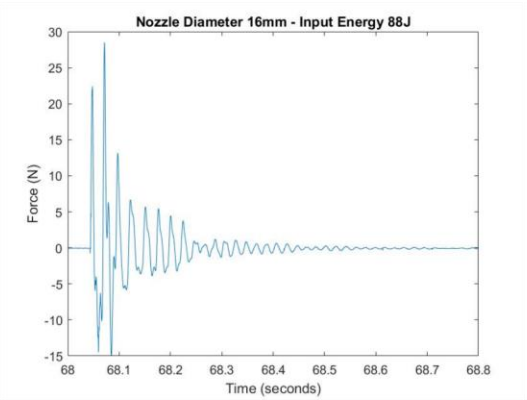

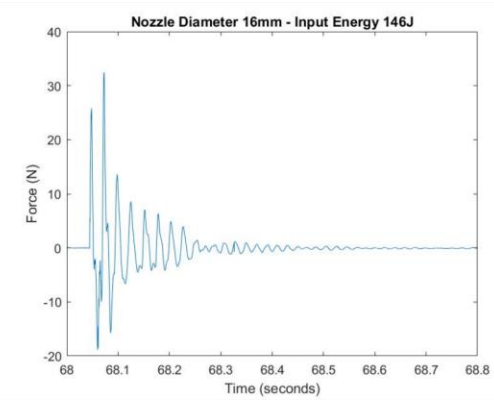

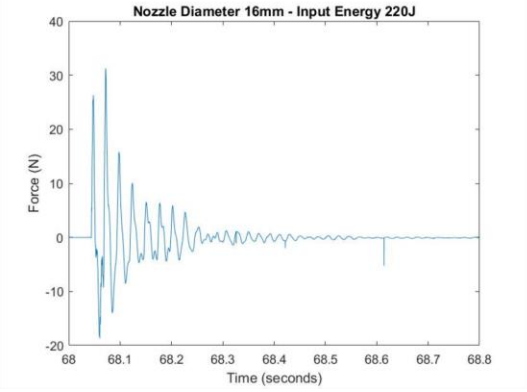

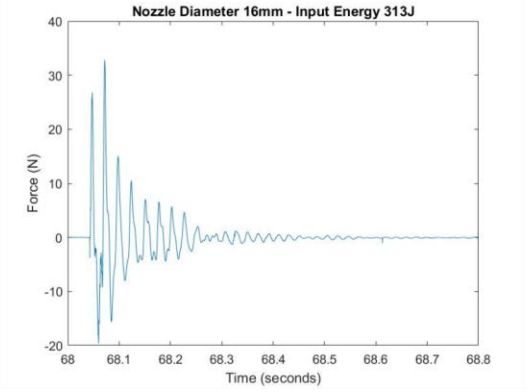

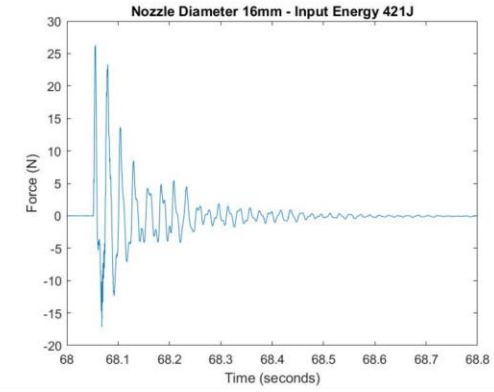

(vii) Sample 7 – 18mm

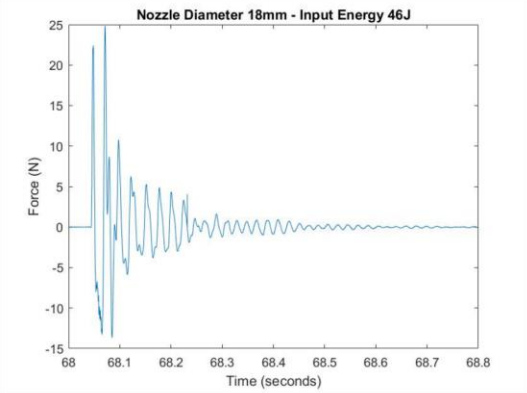

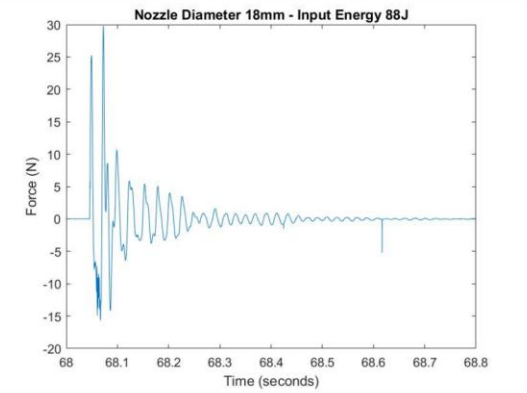

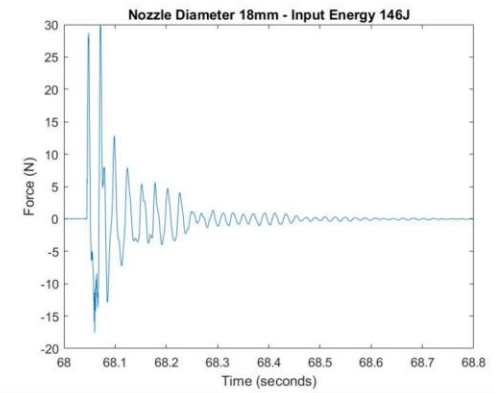

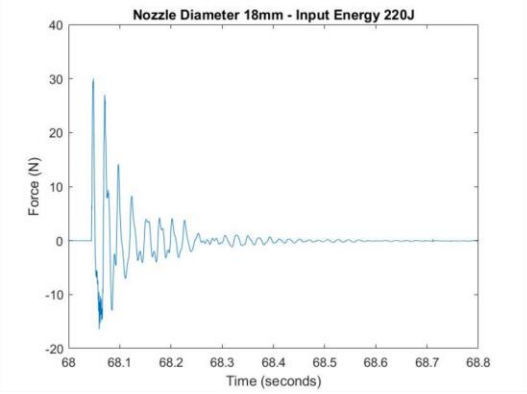

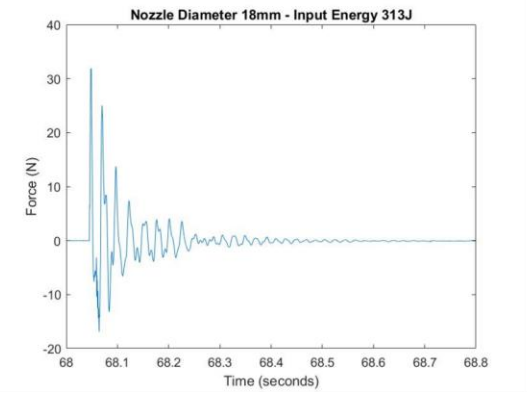

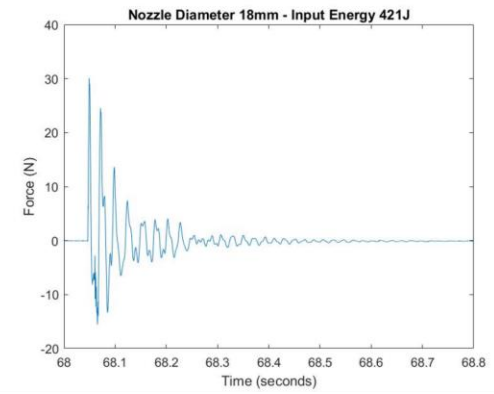

(viii) Sample 8 – 20mm

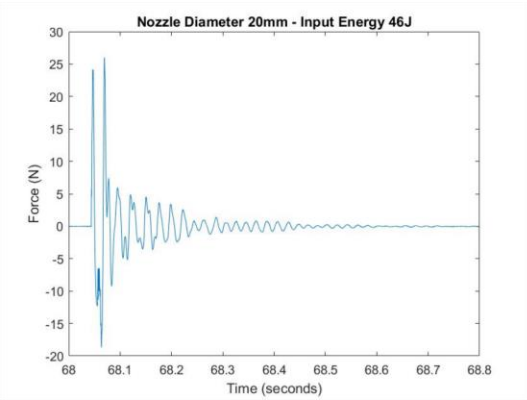

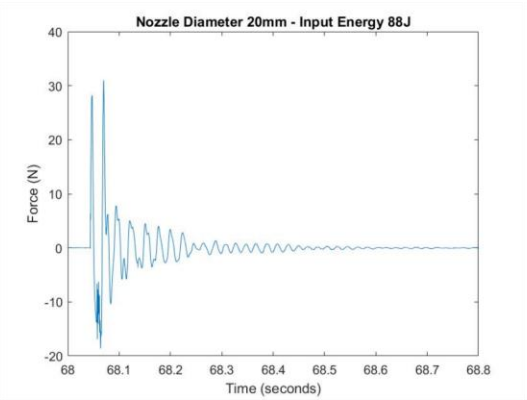

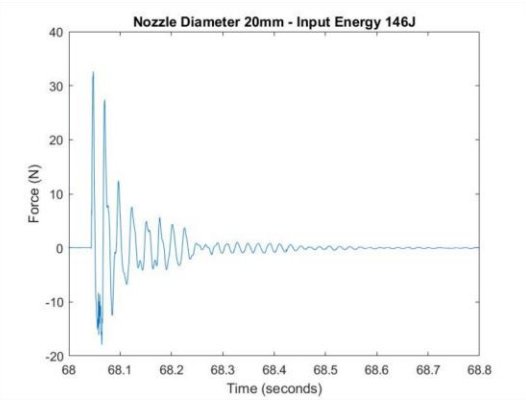

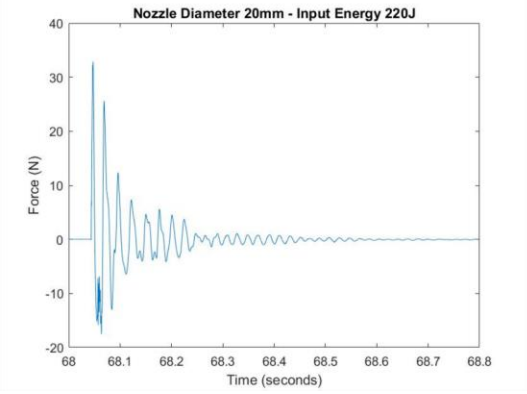

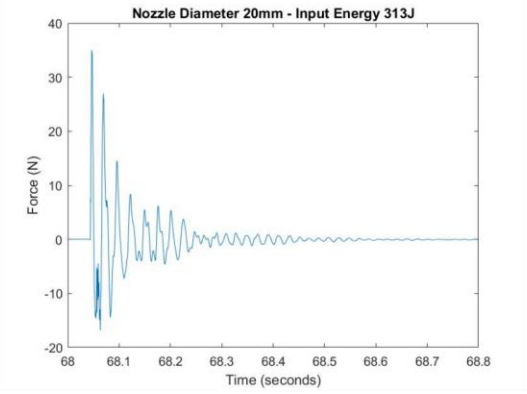

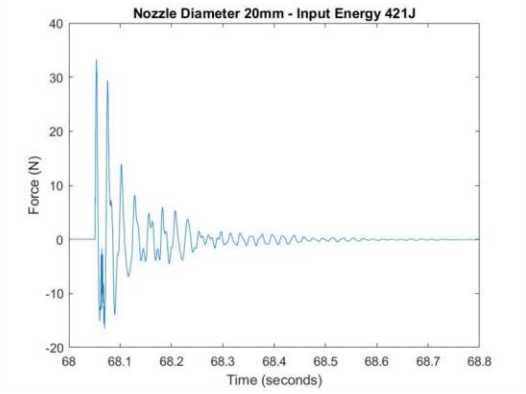

(ix) Sample 9 – 22mm

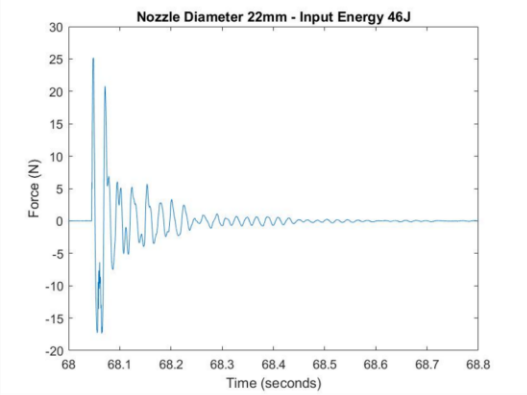

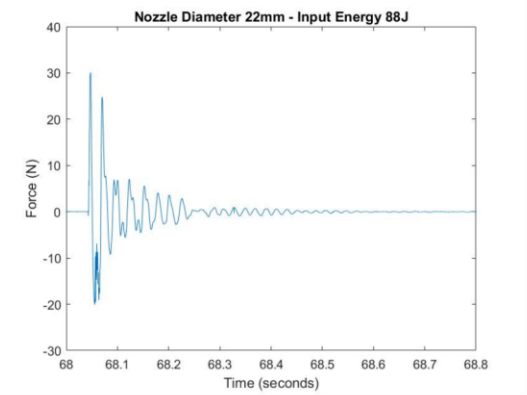

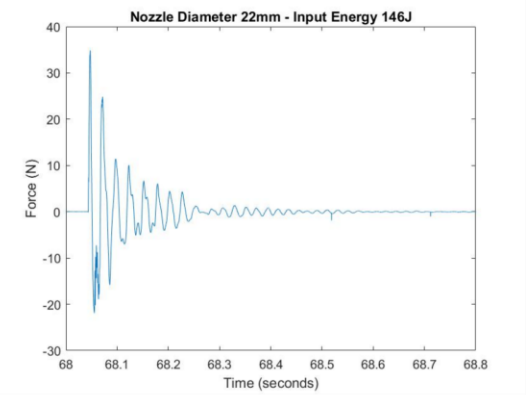

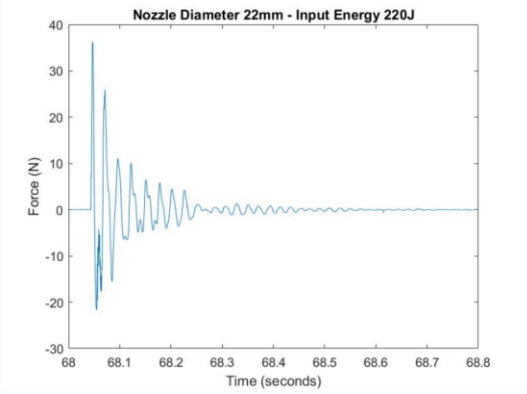

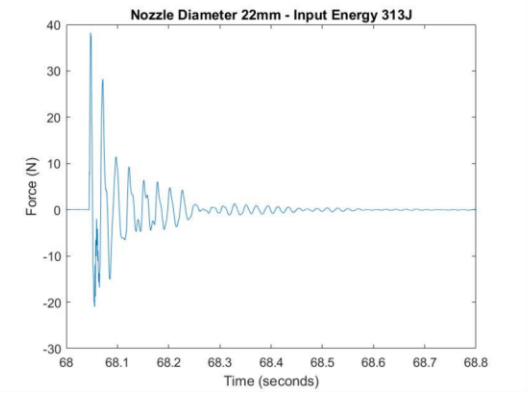

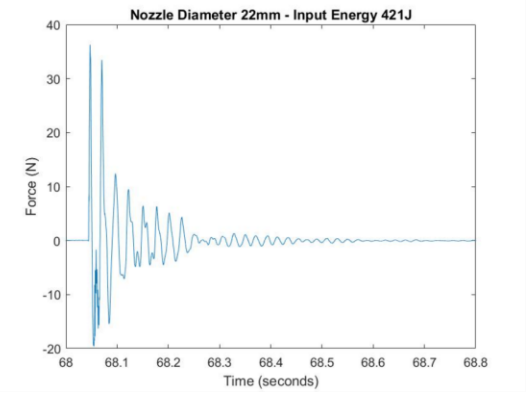

(x) Sample 10 – 24mm

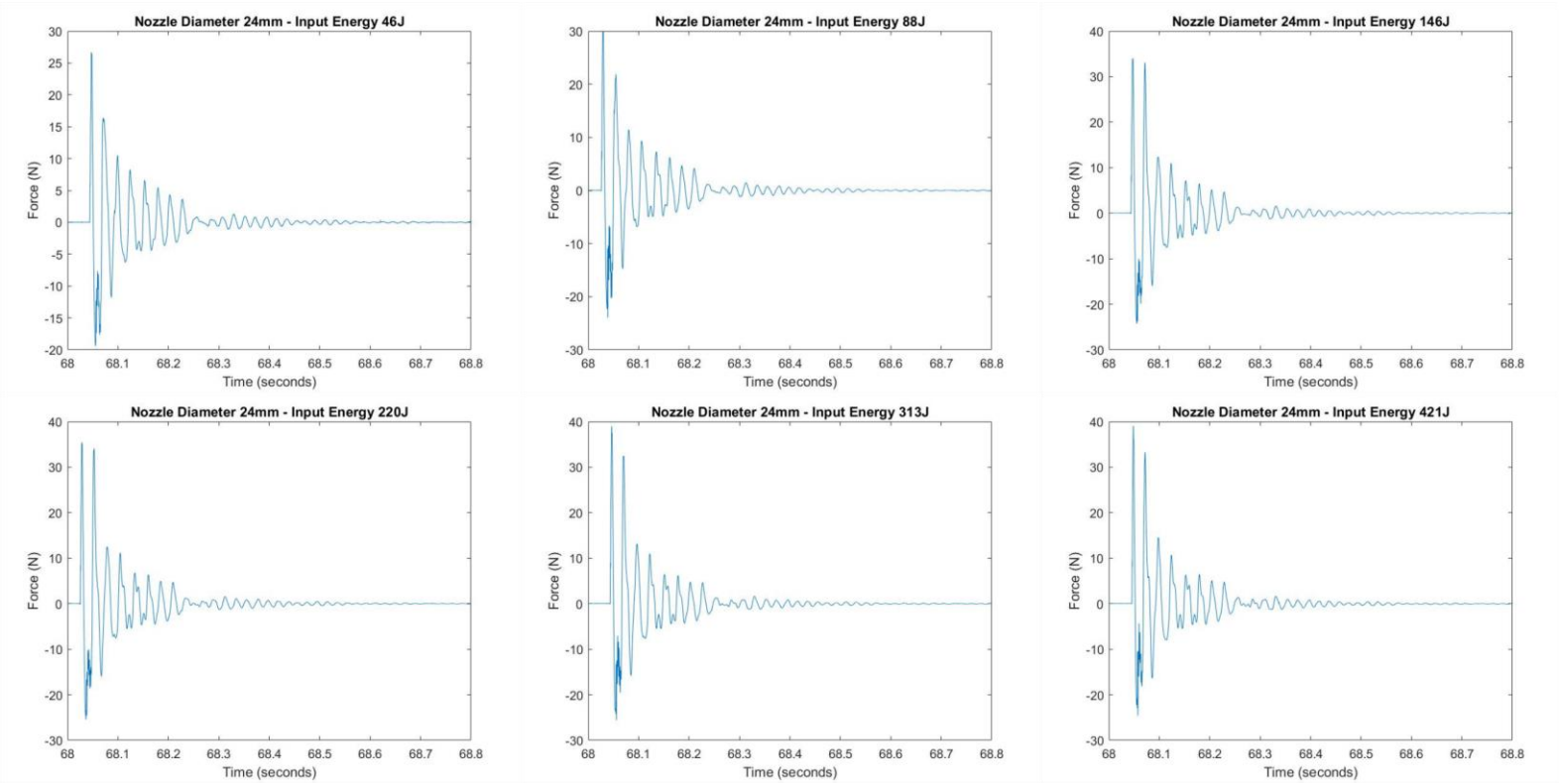

(xi) Sample 11 – 26mm

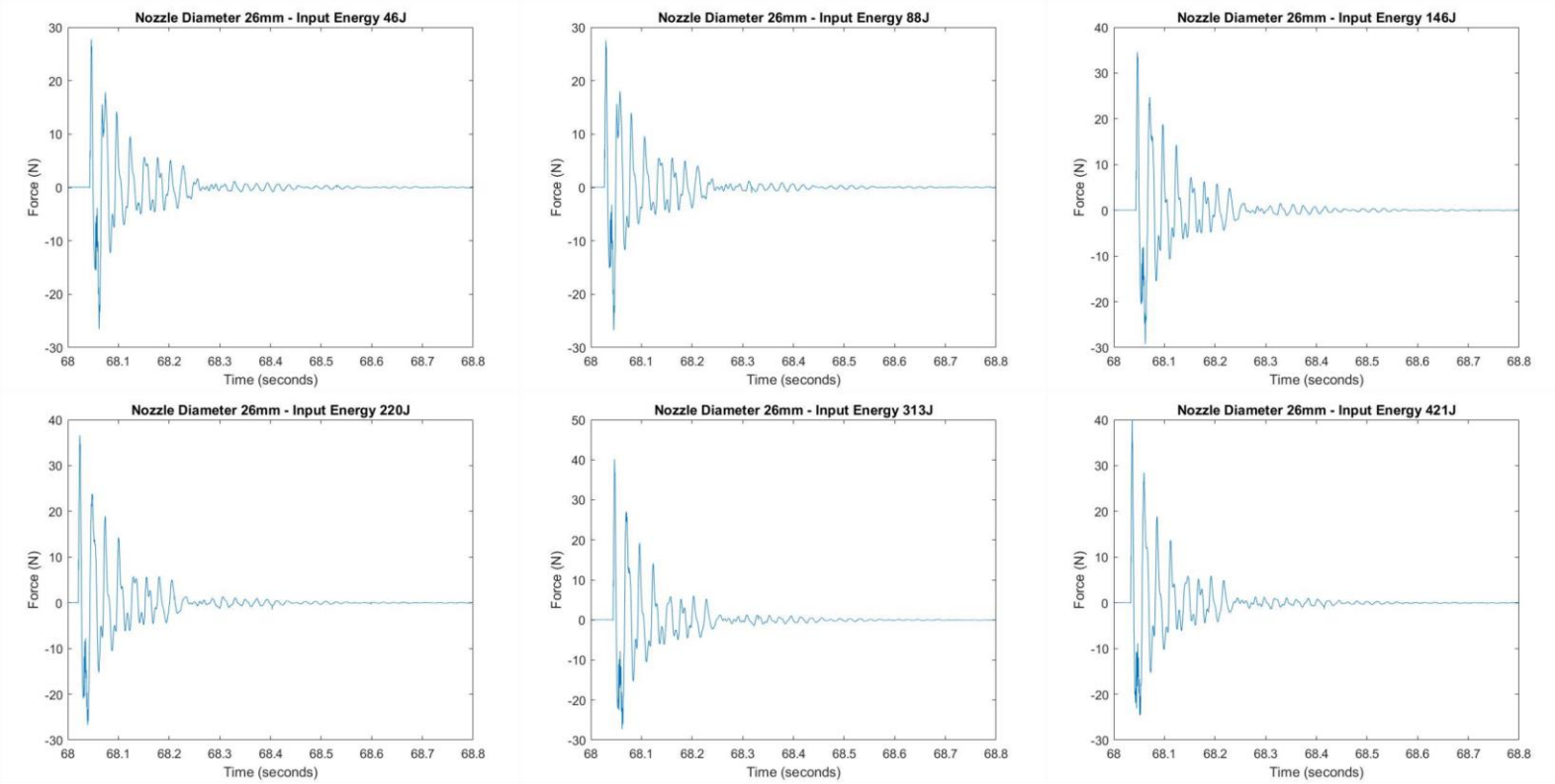

Figure B1: Oxyhydrogen combustion thrust generation at different geometries.

Appendix C

B:Ionic Glove: A Soft Smart Wearable Sensory Feedback Device for Upper Limb Robotic Prostheses

Based on work presented at the following peer reviewed venue. **Nguyen Hao Le is co author of this paper**.

M. F. Simons, K. M. Digumarti, **N. H. Le**, H. Chen, S. C. Carreira, N. S. S. Zaghloul, R. S. Diteesawat, M. Garrad, A. T. Conn, C. Kent, J. Rossiter., "B:Ionic Glove: A Soft Smart Wearable Sensory Feedback Device for Upper Limb Robotic Prostheses," in IEEE Robotics and Automation Letters, vol. 6, no. 2, pp. 3311-3316, April 2021, doi: 10.1109/LRA.2021.3064269.

Contribution statement: All the authors were involved in conceptualisation of design, planning of experiments and writing the final manuscript. M. F. Simons fabricated the structures. M. F. Simons and K. M. Digumarti and N. H. Le performed the experiments, analysed the data and wrote the first draft.

This section details the design, fabrication and experimental characterisation of the B:Ionic glove, wearable over a robotic hand which contains sensing, computation and actuation on board. It uses shape memory alloy (SMA) actuators integrated into an armband to gently squeeze the user's arm when pressure is sensed in novel electro-fluidic fingertip sensors and decoded through soft matter logic.

System design

The B:Ionic glove (Fig. C1 and C2) consists of three components: i) a glove worn on the prosthetic hand with a soft sensor pad underneath each fingertip connected to silicone channels and containing a conductive liquid, ii) an electro-fluidic controller (Soft Matter Computer), and iii) a tactile armband. When the pad is pressed, the volume change forces the conductive liquid through a network of silicone channels. This fluid then bridges the gap between pairs of electrodes along the channel, closing the electrical circuit. In its simplest form, each pad is connected to one coiled SMA actuator on the armband. Once the circuit has been closed, the corresponding SMA on the armband contracts as the current drawn from the battery heats the SMA actuator, generating skin-stretching and squeezing sensations on the skin.

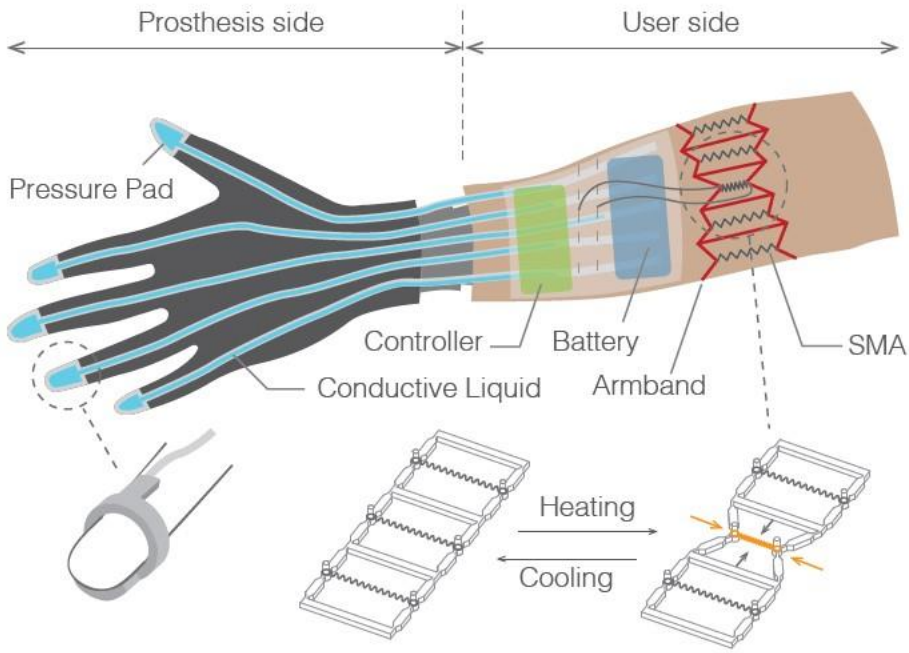

Figure C1: Illustration of the B:Ionic glove, consisting of pressure pads containing conductive fluid wrapped around the fingertip of a prosthesis, an electro-fluidic control unit including the battery, and an armband actuated by shape memory alloys (SMAs) by way of heating and cooling, generating axial, radial and circumferential forces on the user's arm.

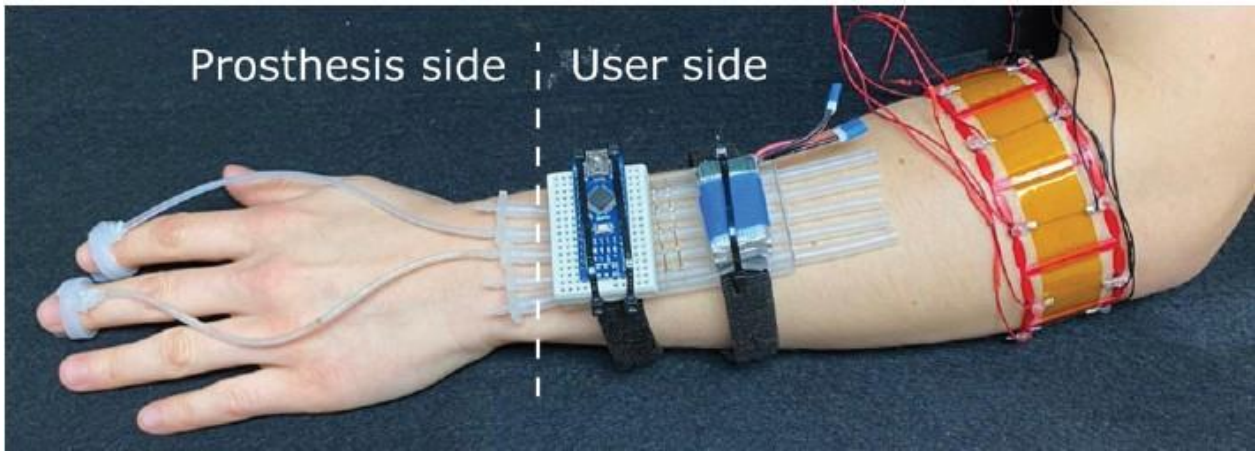

Figure C2: The B:Ionic glove prototype as demonstrated on a non-amputee, where the components on the left hand side are to be mounted on the upper limb prosthetic device and the components on the right hand side are to be worn on the residual limb of the user.

Pressure Pad Tactile Sensors

The pads are fabricated using silicone elastomer (Dragonskin 10, Smooth-On). They are cast in two parts using 3D printed moulds. After curing, the two silicone parts are joined using Sil-Poxy adhesive (Smooth-On) to form an enclosed cavity as illustrated in Fig. C3. The pads have an outlet channel that wraps around the finger so that the silicone tube inserted into this channel runs along the dorsal side of the hand to reduce possible interference. This tube acts as the physical connection between the pads and the Soft Matter Computer and carries the fluid that is used for communicating touch. The relation between the force applied to the fluidic pad and the displacement of

fluid in the channels was characterised as follows. A single pad with an outlet channel was affixed to a linear stage. The pad was filled with a coloured fluid and the initial position of the meniscus in the channel was marked. As the linear stage moved, a probe pressed down onto the pad. The force applied on the pad was detected by a force transducer placed underneath it. Simultaneously, the displacement of the fluid meniscus in the channel was recorded on camera. Pads with three different cross sections and the same internal volume were tested: rectangle, square and circle. A graph of the relationship between force and displacement of the fluid is shown in Fig. C4 with the mean and standard deviation of three trials for each shape. The circular pressure pad proved most sensitive, showing the least amount of force for the same fluid displacement. This may be due to the corners of the square and rectangular designs increasing the tension across the surface of the pad as it is pushed, making it harder to displace the liquid compared with the circular design. A displacement of 25mm required a force of 2.5N (σ=0.7N), 2.1N (σ=0.4N), and 1.4N (σ=0.9N) for the rectangle, square and circle geometries respectively. Positional deviation of the probe across trials and complex local interactions at the fluid-wall interface might influence the variance. The circular pad design was chosen for the following experiments and in the glove prototype.

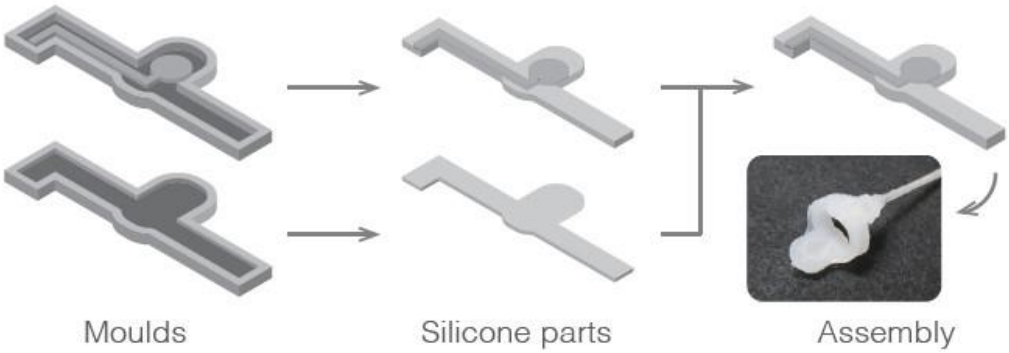

Figure C3: Three-step fabrication process of the pressure pads. The top and bottom parts of the pads are cast separately from silicone in 3D printed moulds. They are then joined together to form an enclosed cavity. The pad is then rolled up to create a fingertip collar.

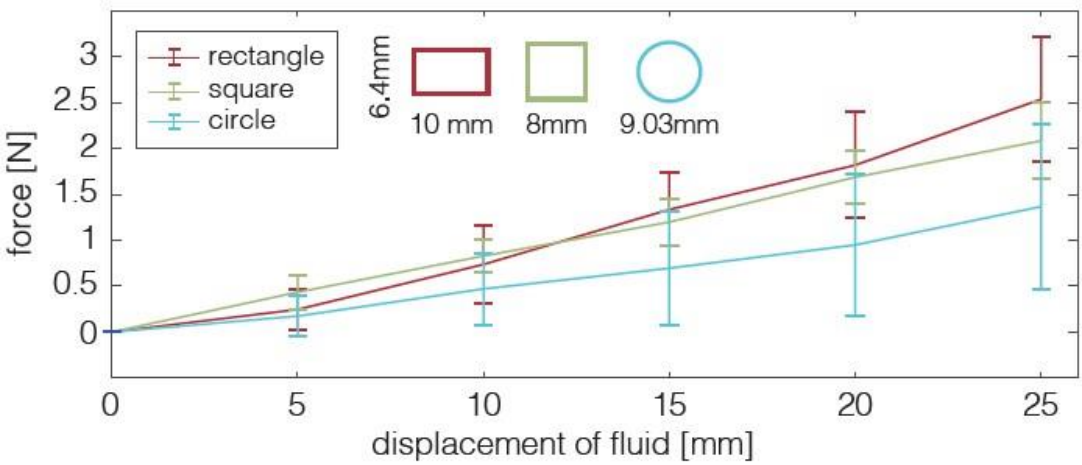

Figure C4: Characterisation of the sensitivity of pressure pads with three different cavity shapes (rectangle, square and circle). The plot shows the displacement of conductive liquid along a connecting channel under different forces exerting on the pressure pads.

Electro-Fluidic Control

The control unit is based on the Soft Matter Computer (SMC) developed by Garrad et al. [295]. For this device, the SMC was made out of silicone (PDMS, Sylgard 184, Dow Corning) cast into a 3D printed mould. Salt water was used as the ionic-conductive fluid. It has the benefit of being low-cost and non-toxic in case of leakage. The SMC contains five channels for silicone tubes to slot in to. Each channel has two holes separated by 10mm into which gold plated copper electrodes can be inserted and then sealed with silicone adhesive (Sil-Poxy, Smooth-On). Wires are soldered to each electrode and connected to a DC battery which is turned into an AC current via an H-bridge circuit. AC is required to prevent electrolysis of the salt water. To demonstrate the potential SMC control of the device, we developed a system that would allow for more complex tactile information processing and feedback (Fig. C5). Two pressure pads, A and B (representing two fingers), were set up with an OR gate followed by an AND gate along the tubing. The channels were filled with saturated salt water (40g NaCl per 100ml water) to the level such that pressing either of the pads activates the OR gate, and pressing both pads activates the AND gate. The SMA actuators were substituted for LEDs to visualise the moment the fluid made an electrical connection, which was recorded on camera. A gap of 30mm between the OR and AND gates ensured a clear separation between the two different signals. The working system is demonstrated in the Supplementary Video.

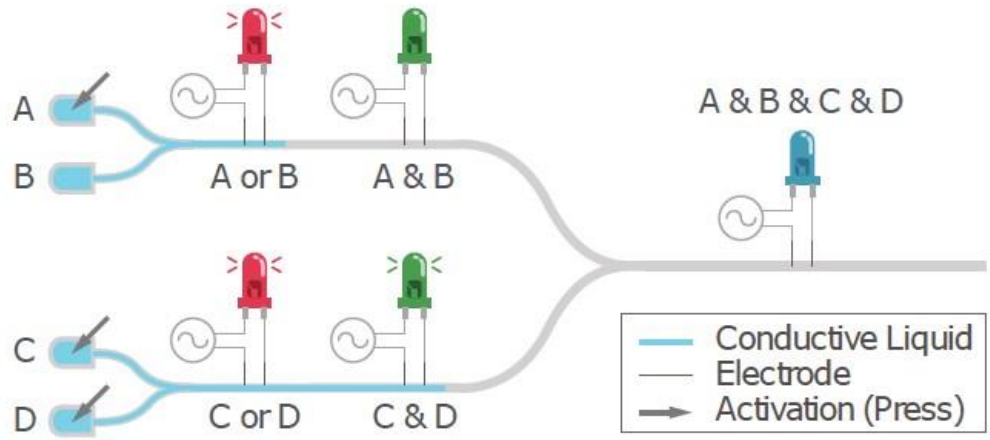

Figure C5: Model of control setup, including OR and AND gates so that the user may be able to determine when two of the fingers are in contact with an object. The LEDs replace the SMA actuators of the armband for this test setup to visualise connectivity.

Tactile Armband

To provide mechanotactile stimulation to the user's upper limb, we designed a wearable haptic interface (Fig. C6). The design of the tactile armband was based on the Squeeze armband presented in [296] , but further developed and optimised for this study. The armband consists of five re-entrant hexagon auxetic units arranged end-to-end, with the addition of hinges along the beams allowing for strong contraction of each unit. It was 3D printed

(Wanhao Duplicator i3) with flexible filament (TPU, RigidInk). Coiled SMA wires (BioMetal Helix, BMX series 150) were connected across the centre of the units and secured with glue. When in its relaxed state, the auxetic units are open and in a square shape. When the SMAs are activated, they contract, squeezing the skin in an axial direction. Small PLA printed circles were also adhered to the underside of the armband to increase the sensations felt at these contact points on the skin. Due to the auxetic nature of the armband, contracting one auxetic unit will also result in a shortening or contraction of the armband, generating additional circumferential and radial forces on the user's arm (Fig. C1).

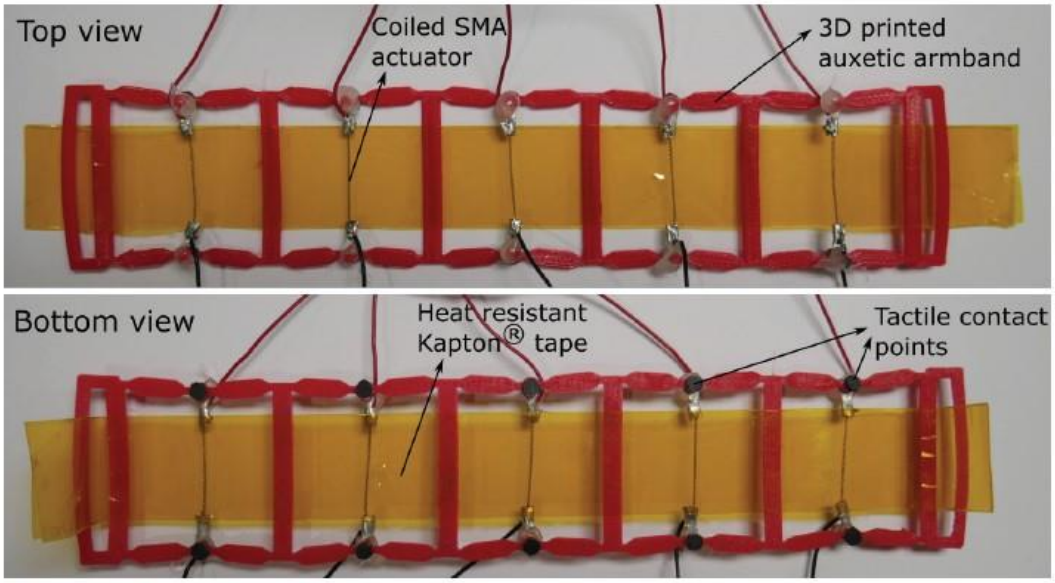

Figure C6: 3D printed tactile armband consisting of five re-entrant hexagon units. Coiled SMA wires provide contraction of the device, while the Kapton tape provides a heat resistant layer between these wires and the skin. The tactile points on the bottom of the armband aims to increase the sensations felt on the skin at these points of movement.

USER STUDY

We investigated subjective responses to the sensations generated by the armband on 20 healthy and non-amputee volunteers (8 female; 12 male; age range 20-50yrs). The armband was tested in isolation to ensure that the responses provided by the participant were directly related to the armband only. The armband was placed on the participant's arm and activated by an external power supply, with a minimum of 5s between each stimulation to allow the SMA actuators to return to their initial state. Participants were visually isolated to prevent them from seeing any actuation which may interfere with their responses. The user study comprised two parts: determining sensitivity threshold and identifying pressure and position.

Sensitivity Threshold

The first part of the user study aimed to determine the sensitivity threshold of the participants' skin; the lowest value of power supplied to the SMA actuator that creates a noticeable sensation on the participant's skin. Two sites for the armband were used: the lower-part of the upper arm and the upperpart of the lower arm, approximately 3cm from the elbow joint either side (Fig. C7). We used Psychophysics Toolbox Version 3 (PTB-3) on Matlab (2019b) to run the QUEST adaptive algorithm as described by [297]. One SMA of the armband was stimulated (central location) with an initial random estimated threshold of μ=0.1386W (σ=0.03465W), correlating to 200±100mA through 3.465Ω. Depending on the response of the participants, the algorithm would provide a greater or lesser current for each subsequent stimulation, converging on the user's sensitivity threshold. The sensitivity threshold of the two sites are similar, with a mean of 0.149W (σ=0.046) for the lower arm and 0.165W (σ=0.045) of the upper arm. A paired-samples t-test confirmed that there was no reliable difference between the lower and upper arm in terms of sensitivity, $t(19)=1.39$, $p=0.182$, $d=0.31$.

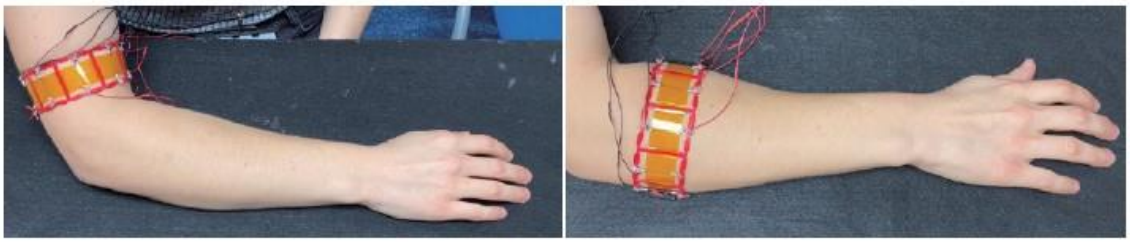

Figure C7: Location of armband placement on upper arm (left) and lower arm (right) for the user study.

Strength and Location Mapping

The second part of the user study aimed to determine the ability of the participants to distinguish between different strengths and different locations of activation. First, one SMA (central location) was activated randomly at three different powers relative to the participant's threshold value: 1.1, 1.5, and 1.9 times the threshold value. As P = I2R (P=Power; I=Current; R=Resistance), where R is assumed to be constant, this correlates to 1.05, 1.22 and 1.38 times the current at threshold. The participants were asked to rate the strength of the sensations on a scale of 0-3 (0 = did not feel, 3 = strongest). Secondly, all SMAs were activated individually in a random order at 1.5 times the power of the participant's threshold value. The participants were asked which SMA was activated.

Participants found it difficult to distinguish between different powers of actuation of the armband (Fig. C8, left), with only 66% correct responses. The three levels of power used for differentiation were chosen to ensure a range within the capabilities of the SMA wires (150-400mA) which was tailored to their skin sensitivity. A lower power would result in the SMA contracting more slowly and with a lower contraction than a higher power. Higher powers also require a longer period for cooling and participants noted that it was sometimes the relaxation that they felt as opposed to the initial squeezing. In general, people with a lower skin threshold found it easier to differentiate

the lowest strength from the highest two, whereas people with a higher threshold found it easiest to distinguish the highest strength from the lowest two. This may be because when the sensitivity is high, the highest strength is close to the maximum capability of the SMA and some people recorded they could feel a slight heat from the SMA wires. In comparison, participants found it easier to detect the different locations of tactile stimulation with 81% correct responses. However, where users incorrectly guessed a position, they almost exclusively selected the position next to the correct one (Fig. C8, right). Some participants found the outer two locations of the armband (i.e. correlating to the thumb and little finger) the hardest to distinguish. This may be due to the thicker velcro strap at the end of the armbands making it stiffer. Most participants could distinguish between three particular regions of stimulations: region containing location 1 and 2, region containing location 3, and region containing location 4 and 5. As location 3 was used throughout the previous part of the user study, participants may have become familiarised with the location of this stimulation.

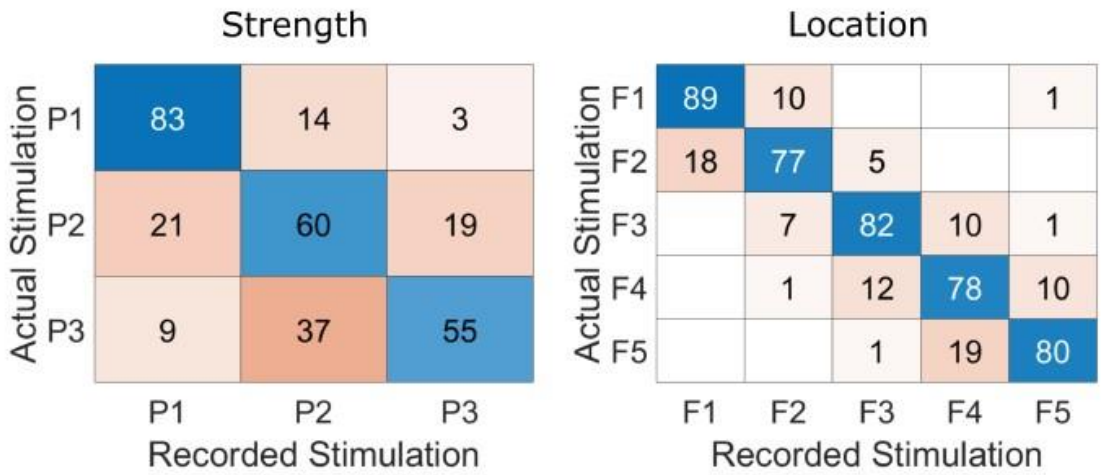

Figure C8: Confusion matrices in percentages of (left) the three different powers where P1 = 1.1, P2 = 1.5, and P3 = 1.9 times the threshold power, and (right) the five different locations; F1 = thumb, F2 = index, F3 = middle, F4 = ring, and F5 = little finger.

PROOF-OF-CONCEPT

To demonstrate how the device could be used in a realworld scenario, we set up a two fingered robotic gripper controlled by a user wearing the armband (Fig. C9). A fluidic sensor pad was attached to each finger of the gripper and connected using the OR/AND gate logic as described above (Fig. C5). A screen was placed between the participant and the robotic gripper to hinder visual cues and force the participant to rely solely on the tactile feedback provided by the B:Ionic glove. The objective of the task was to grip a Rubik's cube placed between the fingers of the grippers with sufficient force to allow it to be picked up. This test highlights how the glove could offer a sense of touch for upper-limb amputees who currently can only rely on their vision to grasp objects [298]. In addition, the glove could assist them in better handling of delicate objects. Both gripper fingers were controlled

independently by separate servo motors connected to switches with 3 modes: closing, stop, and opening. The user attempted to close the gripper until both pressure pads were in contact with the object. If only one of the pads is in touch with the object, only the SMA connected to the OR gate contracts. When both pads contact the object with sufficient force, the SMA connected to the AND gate also contracts, allowing the user to identify when the object is safely gripped. The OR/AND gate logic operates as a discretised version of pressure sensing. We have successfully demonstrated grasping of a Rubik's cube using the B:Ionic glove sensor system using only tactile feedback from contraction of the SMA actuators (Supplementary Video). We also showcase how a possible control architecture could be achieved with simple OR/AND gate logic. Although only one user participated in this proof-of-concept study and only grasping of a Rubik's cube was tested, we aim to expand this to a full-scale user study in future work to investigate the effectiveness of the glove and the tactile response of the system on various objects. The successful demonstration of working OR/AND gate logic, though simple in this first demonstration, opens up the possibility to perform complex computations in more elaborate tasks [295].

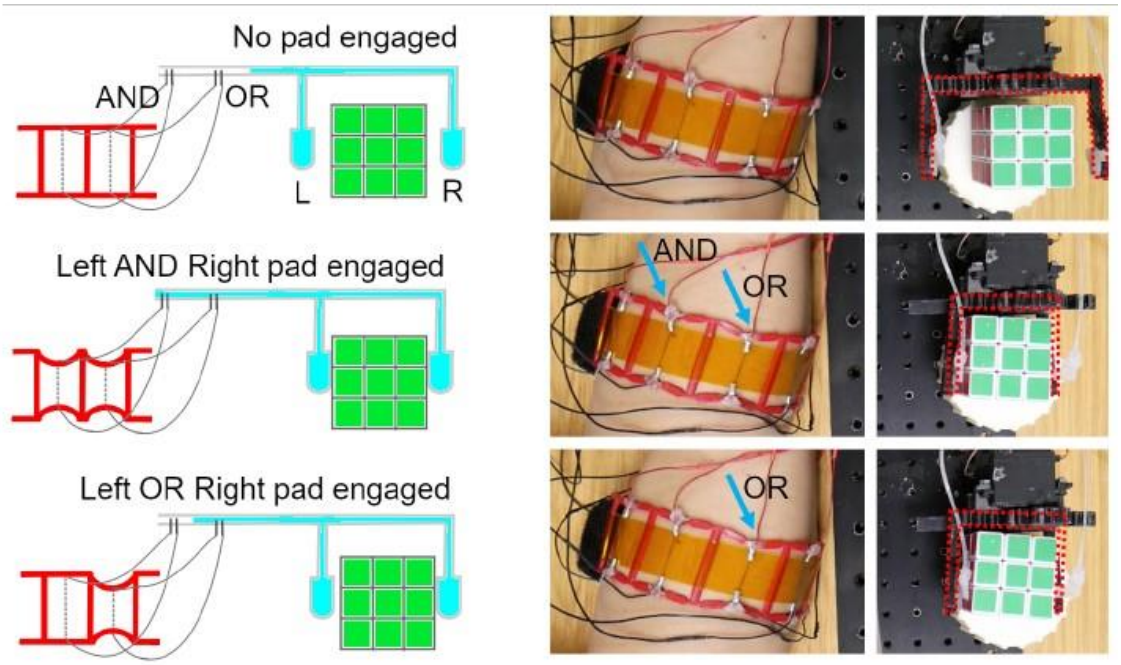

Figure C9: Illustration and video frames of the proof-of-concept demonstration. The user wears the armband and controls a two fingered gripper (outlined with a red dashed line) bearing pressure pads to grasp a Rubik's cube using the sensory feedback encoded by the control unit (OR/AND gates).

Discussion

This paper presents the B:Ionic glove, a wearable tactile feedback device for use with upper limb prosthetic devices. Experiments were conducted to test the ability of the device to bridge the sensory gap between a prosthesis and the skin. The various components were characterised separately and a prototype of the whole device is shown in Fig C2. The geometry of the pressure pad affects the sensitivity of the device (Fig. C4), however

sensitivity can also be adjusted by the level of fluid in the channels, where more fluid will require less force to close the electrical circuit. This can be fine-tuned by the user for specific tasks and will be addressed in future work.

The SMC controller has scope for further control and computation, such as integral memory. For example, fluid could move from one sensor channel (e.g. A) to another (e.g. B) after a grasp, self-adjusting sensitivity ready for the next grasp. Further factors that could affect the control, especially in terms of the time delay in the system, include volume and viscosity of conductive fluid, diameter of the channels, space between the gates, and space between pairs of electrodes. The lower and upper arm did not have significantly different sensitivity thresholds. The data presented in [299] shows that the two-point discrimination distance is greater on the upper arm than the lower arm. This suggests that there are more sensory nerve endings present on the forearm and therefore we would expect the sensory threshold for the forearm to be lower. More trials of experiments are needed to study this. Forces exerted on the user's skin by the armband were not measured directly, however previous work on a tactile device actuated by the same coiled SMA actuators shows a force of approximately 1.25N when actuated at 2.5V for 2s [300]. The participants found the location differentiation test to be intuitive. The normal pressure distributed across the arm generated by the auxetic nature of the armband did not interfere with the participants' ability to distinguish between actuation sites. The two-point discrimination threshold as stated by [299] for the forearm is approximately 38mm. The distance between the SMA actuators on the B:Ionic armband is 32mm, so increasing this distance may also improve user's ability to distinguish between different sites of stimulation. We are currently extending the preliminary user studies in this work to optimise the number, placement, and strength of the wristband actuators and to widen the scope of the user group in order to increase the repeatability of the results. Efforts were made to ensure all SMA actuators were of the same length but variation in resistance from 3.31-3.70 was found. Lower resistance instilled a stronger SMA response. Further work would need to characterise this. The armband was not moved after measuring the participant's sensitivity threshold, as a slight change in location on the skin, or tightness of the strap, could potentially change sensitivity. Care was taken to ensure the armband was placed in the same position for all participants with the middle actuator in line with the participant's middle finger when resting their arm on the table in front of them. We know from literature that skin sensitivity varies not only from proximal to distal areas of the arm, but also circumferentially around the arm with more sensitive skin on the medial and posterior forearm for women and men respectively [301]. We allowed enough time between stimulations for the SMAs to return to their relaxed state. However, repeated stimulation of the same area of skin could lead to saturation of the mechanoreceptors and therefore a lower sensitivity. In general, people tended to find the device pleasant and stated the sensations as "tingling", "twitching", "something crawling", or "muscle activity".

To continue the development of the B:Ionic glove, we are currently performing further user evaluations. While the evaluation in this paper focused on assessing the performance of the individual glove components, these further experiments will measure the performance of the entire system on a range of every day tasks including grasping a range of commonly used objects. We are also planning a series of experiments involving users of prosthetic limbs. This will allow us to measure task performance in a realistic scenario, while also gathering qualitative feedback about ease of use and device comfort. For the B:Ionic glove to operate in the real world, it must be capable of operating untethered, with power consumption low enough to enable long-term use. The SMA actuators used in the wristband require an operating voltage of 1.5-3V, meaning they can be powered by a small lithium polymer battery. By using an electro-fluidic control scheme, we eliminate the need to power pressure sensors or a micro-controller. While the electro-fluidic control scheme currently requires additional electronics to generate an AC signal, we are currently investigating alternative conductive fluids to overcome this limitation.

Summary

This paper presents the proof-of-concept of the B:Ionic glove which has the potential to be used as a sensory feedback device with upper limb robotic prostheses. The device is completely soft and wearable with on-board computation. We have shown that the device can be used to relay different strengths and locations of pressure from prosthetic fingertips to the user's skin, with scope for more complex computation. In future work, we will test the device on upper limb amputees to assess the device in real applications. With this device, they may be able to grasp objects more naturally and intuitively without relying solely on visual feedback. This could reduce phantom limb pain and increase embodiment, consequently increasing acceptance of the prosthetic device and reducing the current high rejection rates.

Appendix D

Towards self-healing stimuli-responsive soft robots for environmental interaction

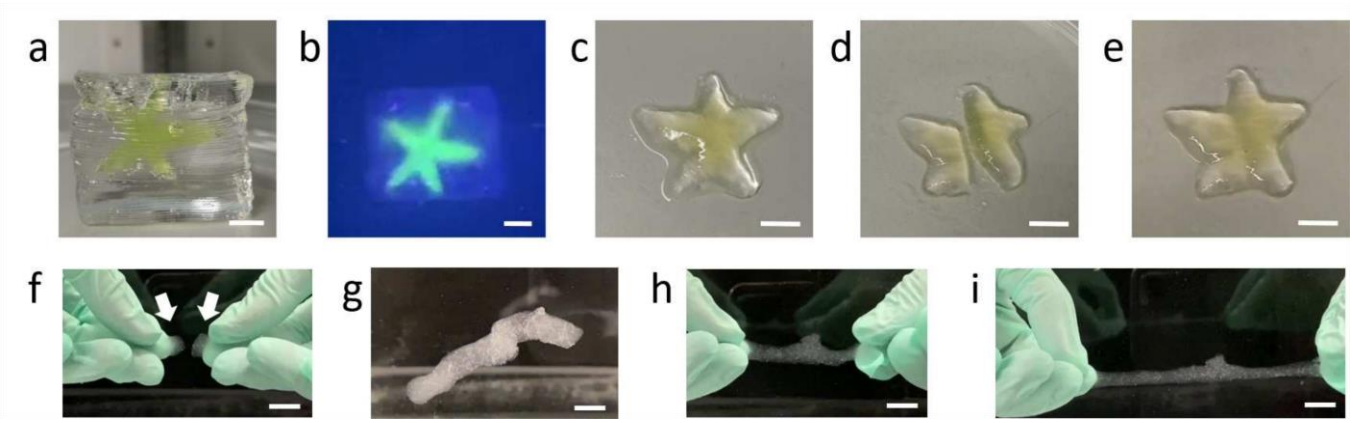

Figure 6.1: Demonstration of printing and self-healing with KGM-Borax ink. (a) A 3D printed upright star shape with KGM-Borax ink and Ultrez support. The ink has been mixed with a fluorescent dye for visualisation. (b) Washing the printed structure in salt water. The star is clearly visible in the presence of UV light. (c) The star after the support structure has been washed away. (d) A cut is made to split the star into two parts. (e) When the cut surfaces are brought together, the material heals and the star shape is regained. (f - i) Demonstration of healing under water. (f) Two separated KGM-Borax samples, indicated by arrows, submerged under water prior to healing. (g) The healed sample after 5 minutes of contact. (h) Healed sample at rest, prior to stretching. (i) Healed sample as it is being stretched. Scale bar = 1cm.

Soft materials are inspiring the next generation of light driven intelligent and versatile devices [302]. This has been highlighted in the photo-responsive mechanical materials and light driven robots of the future in chapter 2. These soft robots are able to adapt and react to challenges in their operating environments. For instance, a robust soft stimuli responsive material could form FLASH's body which is suitable for various applications, exploration in confined spaces or locomotion on uneven terrain [303]. Silicone elastomers, urethanes and foams are typically used in the construction of soft robots. However, these materials are generally not responsive to environmental stimuli or environmentally friendly. As such, hydrogels have been proposed as promising alternative materials [304] due to their attractive properties. They are capable of maintaining their structure while holding or expelling large quantities of water, many times the mass of the substance itself [305]. They are capable of physically and chemically reacting to external stimuli such as heat, electric fields, magnetic fields, pH, ionic concentration and light intensity, and in some cases, combinations of the above [306]. Depending on the composition, hydrogels are also biocompatible and can degrade benignly at the end of their life. There is also the possibility of fabricating edible robots [307] [308].

Polysaccharides are one class of hydrogels with great potential as a material for soft robots. These are commonly derived from biological sources - from animals (chitin, chitosan), from plants (pectin, galactomannan, glucomannan), from algae (alginate, carrageenan, agarose), or from microbes (xanthan, gellan) [309]. Consequently they are typically biodegradable, and are considered to be non-toxic and biocompatible [310]. Gels of this type have been studied for a wide variety of applications: as bio-materials in tissue engineering [311] [312], for the transport and controlled release of drugs [313] [314], as rheology modifiers in cosmetics, and as food additives.

Konjac glucomannan (KGM), a polysaccharide, is derived from the corms of *Amorphophallus konjac* and consists of β-1-4 linked D-glucose and D-mannose in a molar ratio of 1:1.6 [315] [316]. Like many polysaccharides, konjac has a history of use as a foodstuff, in particular in the Levant (using an analogue derived from the salep orchard [317]) or as konnyaku noodles or jelly in East Asian cuisine. The customary method of preparation of konjac gel is to induce gelation through heating an aqueous KGM solution in the presence of an alkali. Glucomannan chains contain randomly scattered acetyl groups which are removed on addition of the alkali. Heating causes aggregation of the chains due to hydrogen bonding and hydrophobic interactions [318] [319] [320]. Unlike other gels held together by hydrogen bonding (such as gelatine), these chains will not disentangle upon reheating, and so the gellation of KGM prepared in this manner is thermo-irreversible. This makes the freeform fabrication and 3D printing of alkali-based KGM challenging, since the gel cannot be shaped once it is set.

An alternative means of gellation of konjac is through the addition of the crosslinking agent sodium tetraborate (borax) [321]. This is the basis for the ink presented in this paper. Borax, in aqueous solution, exists as equal parts of boric acid and tetrahydroxyborate ion (see equation 1).

$$B_4O_7^{2-} + 7H_2O \rightleftharpoons 2H_3BO_3 + 2B(OH)_4^- \qquad \textit{Eq. 1}$$

The tetrahedral borate ion interacts with the cis-hydroxy groups on mannose to form a crosslink (figure 6.2). This manner of crosslinking gives the KGM-Borax gel unique properties. Firstly, the equilibrium represented in equation 1 can be altered by the addition of an acid or an alkali [322]. Consequently, the crosslinked KGM-Borax gel is responsive to changes in pH, with alkaline conditions producing a mechanically stronger gel.

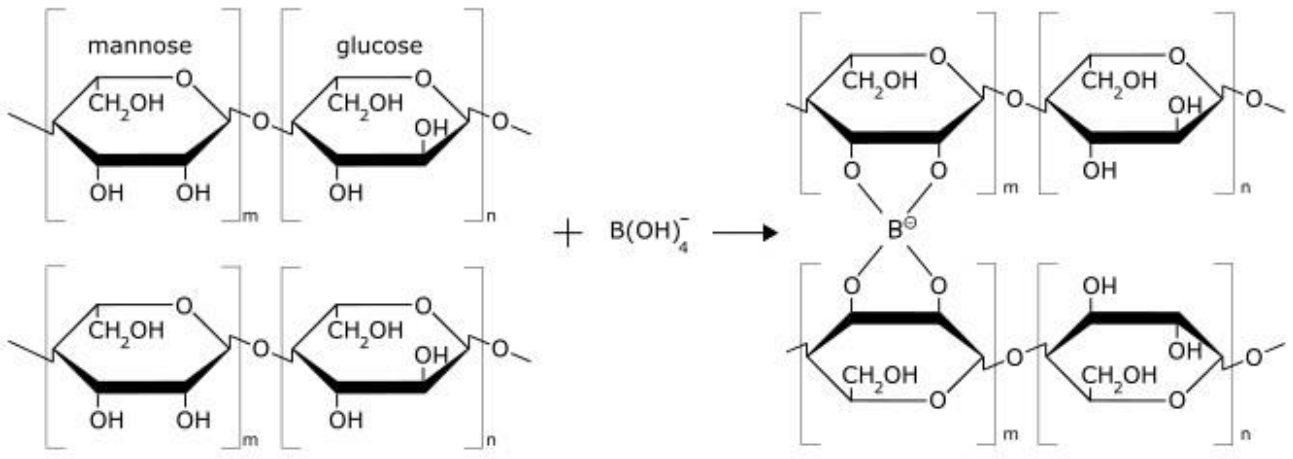

Figure 6.2: Konjac glucomannan chains crosslinking. (Left) A pair of Konjac glucomannan chains, each with D-mannose and D-glucose linked through a β-1-4 glycosidic bond. (Right) KGM chains cross-linked through the borate ion.

Second, in the presence of free borate ions, the KGM-Borax gel also exhibits self-healing, while remaining stiff enough to maintain its form [322]. Several approaches have been proposed to realise polymers that repair themselves, popular among which are dynamic covalent bonds [323] [324] and reversible chemical reactions [325] [326]. The latter has been employed in the context of soft robotics. The advantage of the KGM-Borax gel is that the healing is autonomous, requiring no external stimulus, and the participating ions are intrinsic to the gel. Sensitivity to pH and the ability to self-heal make this a particularly important material for future gel-based robots. A common method to fabricate soft robots is by casting a soft material into a carefully designed mould. This manner of fabrication is low cost, well characterised, and offers a low barrier to entry. As such, many biocompatible, high tensile strength hydrogels reported in literature use casting as a main fabrication method to form shapes [327] [328] [329] [330]. However, moulding can be challenging when it comes to manufacturing complex internal structures as parts can be easily damaged during the removal process. Although this could be mitigated through the self-healing process, it often requires external stimulus and could impact the mechanical properties of the materials. In addition, it would add a layer of complexity into the fabrication process. In contrast, three dimensional free-form fabrication of soft robots has the potential to unlock many new opportunities [331]. Using additive manufacturing, it is possible to fabricate complex geometries that incorporate multiple functions such as sensing and actuation into the mechanical structure [332]. Unfortunately, most of the high tensile strength hydrogels mentioned above are not compatible with 3D printing due to their high viscosity and low shear thinning properties [330].

Hydrogels are commonly used as inks in printing scaffolds for cell culture [333]. However, printing large 3D structures with these gels is challenging due to their inability to support their own weight. To overcome this, a

support gel can be used [334]. Yet, other challenges, such as precise control of temperature in the case of gelatine-based gels, remain unaddressed. In this context, the KGM-Borax gel presented in this paper is an attractive choice for 3D printing because the entire fabrication process takes place at room temperature. While aqueous KGM solutions have recently been deposited by bio-printing [335], borax crosslinked KGM has only been used in casting. The ability to print with the gel allows the fabrication of intricate geometries not realisable with other forms of fabrication. Furthermore, since the KGM-Borax gel is responsive to an external stimulus, the geometry and function of a printed part can be altered to suit a desired function after it has been fabricated, enabling 4D printing [336].

In this paper, we show a novel method of printing with borax-crosslinked KGM gels. Our work is the first demonstration of printing and curing using a KGM-Borax gel. We also provide a rheological characterisation of the printable ink and the resultant crosslinked gel. We also determine the most appropriate printing parameters. Additionally, we investigated the self-healing property of KGM-Borax gels, which occurs without requiring an external stimulus. We present results of tensile testing to demonstrate the robustness of the gel after it has been damaged and repaired. We present the entire process of preparing a printable ink, fabricating free form structures using additive manufacturing, curing the printed structure, washing the support material to extract the part, and self-healing of the structure upon infliction of damage. We also demonstrate a novel feature of the KGM-Borax gel which is the self-healing of the gel when it is completely submerged in water. This behaviour is demonstrated, for the first time, in this paper.

Material and methods

Ink preparations

Konjac glucomannan was purchased as konjac gum powder from Special Ingredients Ltd., Chesterfield, UK. Borax (sodium tetraborate decahydrate ACS reagent>99.5%, S9640) was purchased from Sigma Aldrich. 500mg of KGM powder was gradually dissolved in 50mL of deionised water at room temperature. The mixture was continuously agitated using an overhead stirrer (Cole Parmer, 50006-03) at 1000rpm for 30 minutes. The mixture was then allowed to rest for 16 hours to ensure thorough wetting of solute particles. Borax was dissolved in deionised water to make 11.8mM solutions. Prior to printing, 3ml of 11.8mM borax solution was added to the prepared KGM solution. The addition of borax partially crosslinked the KGM. It was then mixed in a dual axis planetary mixer (Thinky, ARE250) for 5 minutes at 2000rpm. This partially crosslinked gel was used as the ink for 3D printing as soon as it was prepared.

Support gel preparations

To print complex three-dimensional shapes with overhangs, a support structure is required. This was realised by using a support gel made of high molecular weight polyacrylic acid. Carbopol Ultrez 10 NF was obtained in powder form from Lubrizol. Sodium hydroxide was purchased from Fisher Scientific (15678110). 4g of Ultrez was dispersed in 400mL deionised water by stirring to form a solution. 8M sodium hydroxide was added to neutralise the pH, which immediately resulted in the formation of a gel. This gel was prepared in bulk and stored in air-tight containers at room temperature. Just before printing, the gel was transferred to a smaller container of 30mL volume, and spun in a planetary mixer at 2000rpm for 10 seconds to remove air bubbles.

Printing protocol

A bioprinter, (Bio-X, Cellink), was used to print the ink. Partially crosslinked KGM-Borax ink, prepared as described in section 6.1.1, was loaded into 3mL syringes. A regulated positive pressure was used to drive the ink through a nozzle. A secondary syringe was loaded in a similar manner with Ultrez (prepared as in section 6.1.2) and used to deposit the support gel.

Printing was carried out at ambient temperature (20°C) with the syringes and the print-bed maintained at this temperature. Glass was used as substrate for printing. After printing, a two-step process was followed to produce a crosslinked structure free of support material:

1. The print (including support material) was removed from the substrate and immersed in a vat of 94mM borax solution. The excess of borate ions ensured thorough crosslinking of the KGM chains and cured the ink.
2. The support structure was removed by gently agitating the print in a 3wt% aqueous solution of sodium chloride (obtained as a powder from Honeywell Fluka, 71382). Ultrez disassociates in the presence of the salt and was easily washed off, leaving the finished KGM print.

Print parameter characterisation

The controllable parameters for a KGM-Borax gel print are the pressure applied, the speed at which the print-head moves, and the diameter of the nozzle. With the aim of achieving a detailed print, the minimum workable nozzle diameter was first established. A syringe nozzle of diameter 0.41mm (22 gauge) and length 32mm was the smallest size through which the ink could consistently flow. To determine the optimum printer parameters for this nozzle, a series of tests was performed by printing zig-zag lines on a glass substrate with varying values of pressure and speed. In each case, the width of the printed line was measured prior to curing at 5 positions under a microscope (Hirox KH-7700, Japan). The distance between the tip of the nozzle and the print-bed, i.e. the layer height, was maintained at 0.4mm.

Rheological characterisation

Rheological characterisation of our KGM-Borax printable gel material was carried out using a rotational rheometer (TA Instruments Discovery HR-30). Two materials were studied: the ink used for printing and the crosslinked gel. For the ink, the mixture was prepared as described in section 2.1. As the ink was a medium viscosity liquid, a cone-plate geometry was used, with a cone angle of 4° and plate diameter of 40mm. Ink was loaded onto the plate using a syringe, the was cone lowered to its truncation gap and excess ink was removed.

For the crosslinked gel, samples were printed without support as 40mm diameter, 1mm thick discs using the prepared ink with a nozzle of 0.4mm diameter and a rectilinear infill of 100% density. The discs were cured after printing with a 94mM borax solution. They were used within 24 hours of their preparation. As the crosslinked gel is a soft solid, samples were tested using a 40mm diameter Peltier plate with parallel geometry. The samples were carefully placed onto the surface of the lower plate, and the upper flat plate was lowered until a force was detected. For both materials, the linear viscoelastic (LVE) region was first determined using an amplitude sweep of the rotational strain at a frequency of 63 rad/s with deformation ranging from 0.5 to 500%. Frequency sweeps were then performed on fresh samples within the LVE with a fixed oscillation strain of 1% and frequency ranging between 0.4 and 100 rad/s.

In all cases, the temperature was controlled at 20°C. Before testing, samples were left for 1 minute to reach mechanical and thermal equilibrium. Each study was repeated with a new material sample three times.

Tensile test

Tensile testing was performed to characterise the self-healing ability of the fully cured gel. Test specimens for measuring the peak load and elongation at break were prepared in a manner similar to that followed in making the ink for printing (section 6.1.1) up to the addition of borax. A higher-concentration solution of 94mM borax was then used to crosslink the gel. 3mL of borax solution was used for every 50mL of ink. On mixing of the borax, the gel was immediately cast into cylindrical containers (diameter 5mm, length 65mm) and left to set for 24 hours to ensure complete crosslinking had occurred.
Tensile tests were performed using a universal testing machine (Instron 3343 with 1kN load cell). A gauge length of 35mm and a test speed of 100mm/min were used. The samples had an initial diameter of 5mm. Samples were loaded by hand between parallel grips, the faces of which were tightened until the gel was held firm. The test configuration is shown in figure 6.5.

Samples for self-healing experiments were prepared identically to the ones above. They were cut in half and the exposed surfaces placed next to each other with no external load. Points were marked on either side of the join

to show its position. Samples were left to heal for 5min, 30min or 60min respectively. During this resting time, no external force was applied to the ends. After resting, these samples were tested under tension as described above. The tensile test results were post processed using MATLAB 2018a and moving median technique to filter out undesirable noise.

Results

Rheological properties of Kojac Hydrogel

The result of the rheological examination can be seen in figure 6.3. It can be seen from figure 6.3b that with increasing frequency, the storage modulus (G') and the loss modulus (G'') gradually increase. Since G' is higher than G'' across the full frequency range, the elastic behaviour of the materials predominates over its viscous behavior. In addition, with increasing frequency, i.e. low relaxation time, sample flexibility is diminished and they become increasingly rigid. The error of the test method was less than 8%.

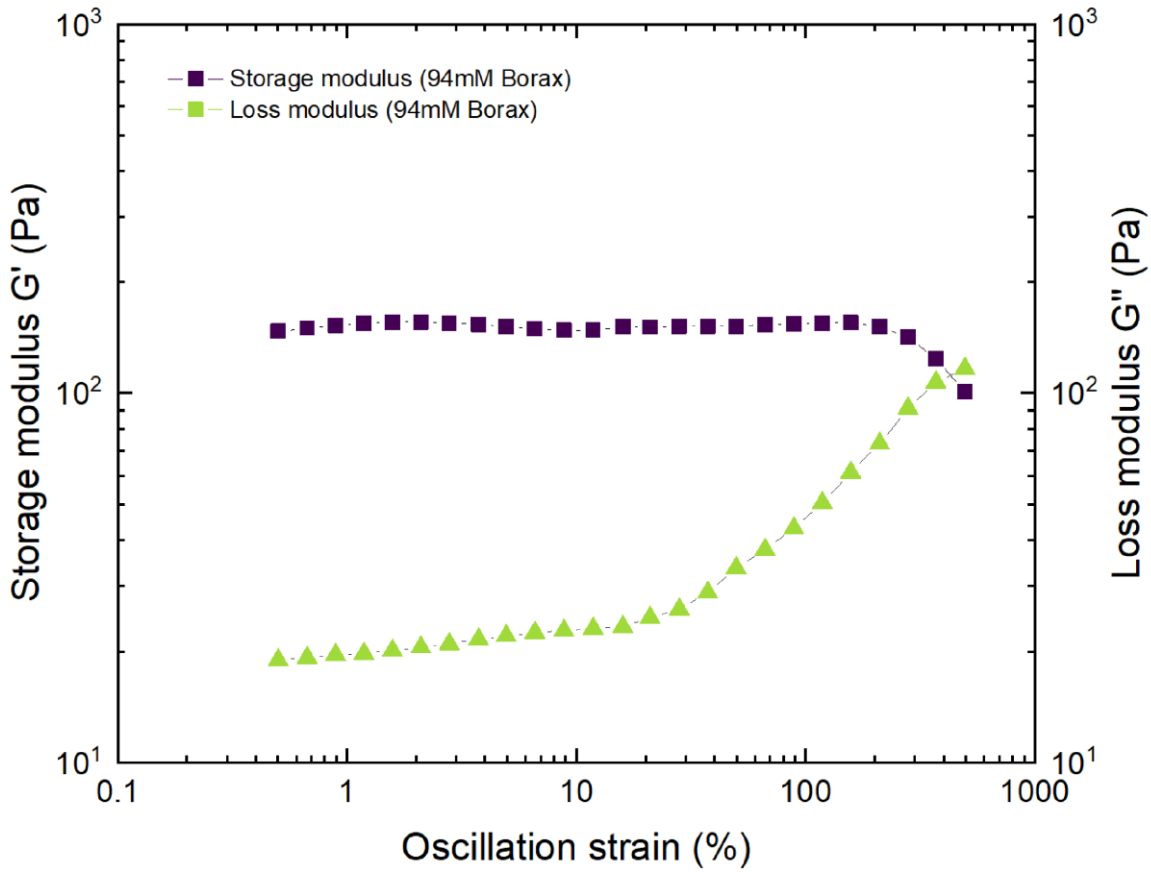

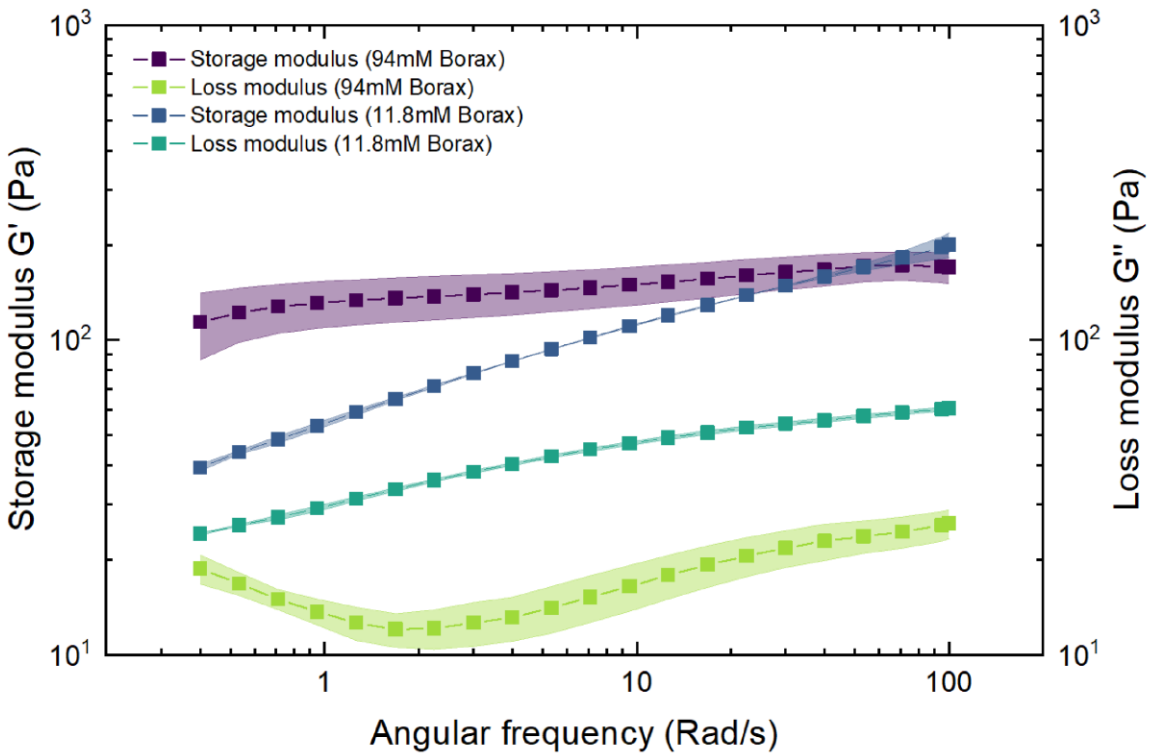

Figure 6.3: Rheology test results. (a) Storage and loss moduli of the KGM-Borax ink as a function of amplitude of the rotational strain at a frequency of 63rad/s. (b) Storage and loss moduli of the KGM-Borax ink (11mM Borax) and fully cured KGM gel (94mM Borax) as a function of frequency, with a fixed oscillation strain of 1% and within the linear viscoelastic region.

Printing of Kojac Hydrogel

The results of experiments to determine print quality for various printing parameters are shown in figure 6.4. The width of the printed track varies as a function of print speed and extrusion pressure for a given nozzle size. For instance, the minimum line width of 650µm was achieved at 40kPa and 60mm/s and the maximum line width of 5700µm was measured at 100kPa and 10mm/s. At constant pressure, a decrease in width was observed on increasing print speed. At a set print speed, higher pressures resulted in wider print tracks. The mean standard deviation in width across all pressures was measured to be 4, 5 and 6.5% of the average track width at 40, 50 and 60mm/s speeds respectively. This provides important information for 3D fabrication.

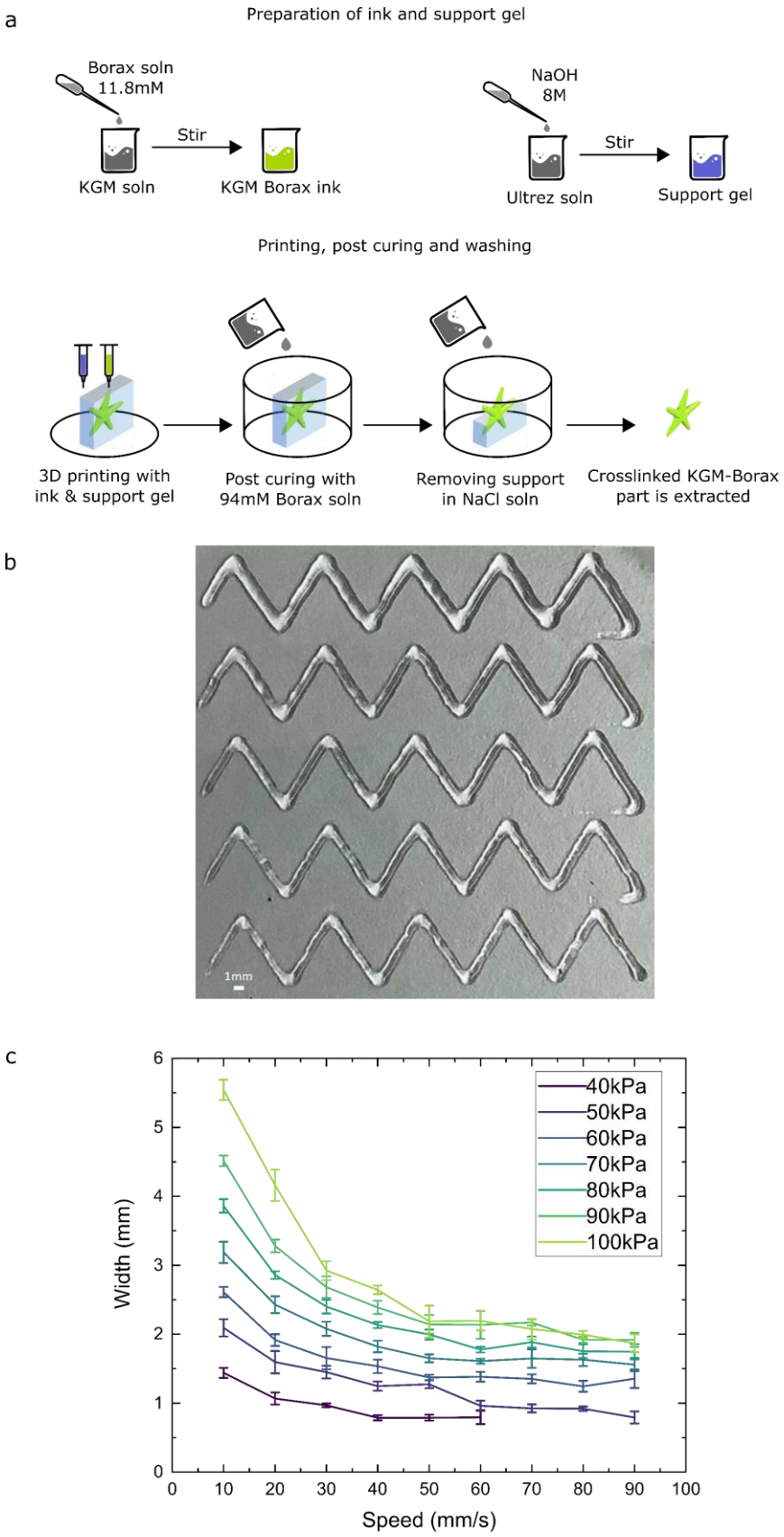

Figure 6.4: 3D printing results. (a) A schematic showing the preparation of the KGM-Borax ink, printing with it, post curing and washing away the support. (b) Optimisation of printing parameters by printing zig-zag lines with various parameters. One of the samples at 40kPa pressure and speeds of 10-50mm/s. Scale bar = 1mm. (c) Mean and standard deviation of print width measured at 5 locations for various printing parameters.

Tensile properties of Kojac Hydrogel

Results from the tensile testing can be seen in figure 6.5. To characterise the self-healing capability of the gel, an approach similar to that of López-Díaz *et al.*[337] was followed. Two parameters are considered: maximum load before failure (LF) of the gel, and the load at 50% extension ($LF_{50\%}$). The healing efficiency (η) for each of these parameters is the ratio of the value measured for the healed gel versus that of the virgin gel. Therefore, for the load at failure, healing efficiency,

$$\eta_{LF} = \frac{LF_{Healed}}{LF_{Virgin}} \qquad \textit{Eq. 2}$$

The mean value of LF_{Healed} was 39.5mN and the mean value of $LF_{Virgin}$was 188.2mN, giving η_{LF} = 21%. This can be seen in figure 6.5a. The load at failure of the virgin specimens is roughly five times that of the healed specimens.

In a similar manner, for the load at 50% extension, healing efficiency,

$$\eta_{LE} = \frac{LE_{50\%,Healed}}{LE_{50\%,Virgin}} \qquad \textit{Eq. 3}$$

The mean value of $LE_{50\%,Healed}$ was 20.6mN and the mean value of $LE_{50\%,Virgin}$ was 21mN, giving η_{LE} = 98%, a high healing efficiency (see inset, figure 6.5).

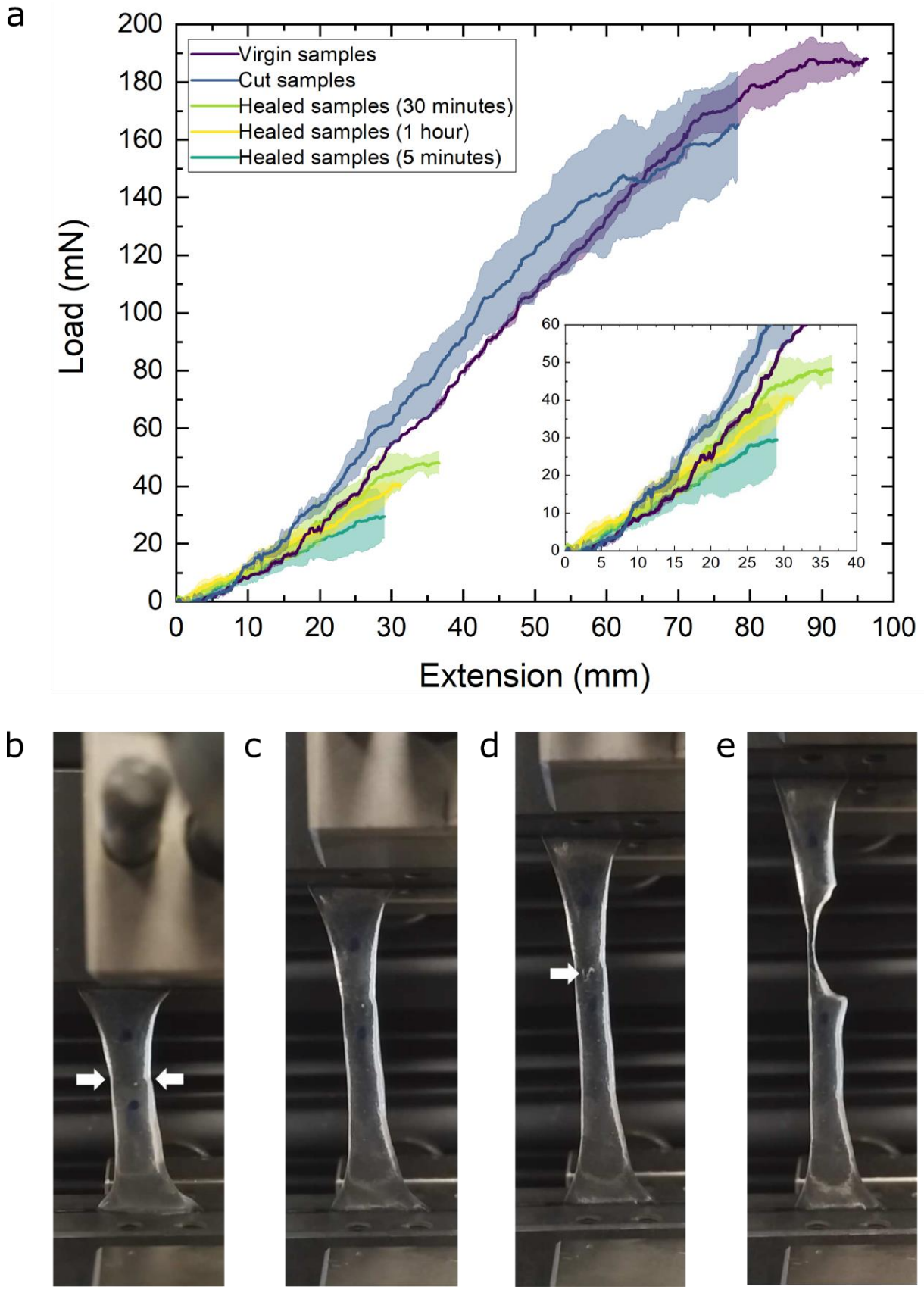

Figure 6.5: Tensile test results. (a) Load-extension profiles of crosslinked KGM-borax samples as prepared and after healing. (b – e) A self-healed sample being stretched to break. (b) Sample before test, at rest length of 35mm. Arrows indicate the position of the seam where the sample was cut and healed. (c) Sample at an intermediate extension. (d) A crack appears in the material at the location indicated by the arrow. (e) Snapshot of the sample prior to breaking.

Discussion

Evaluation of print quality showed that the KGM-Borax ink remains printable at pressures as low as 40kPa and speeds from 10mm/s up to 90mm/s. At higher speeds and lower pressures, the print fails. This was due to insufficient flow of the material and poor adhesion of the extrudate to the print bed. At higher pressures and lower speeds, the width of the track was more than 13 times larger than the diameter of the nozzle. The smallest average printed gel track width was 0.78mm and was attained at a speed of 40mm/s and pressure of 40kPa. Extrapolating from the optimisation study presented for alginate-gelatine gels in [338], the KGM-Borax ink prints at a finer resolution (0.78mm vs. 1.13mm) even with a larger nozzle (0.41mm vs. 0.26mm) while requiring less extrusion pressure (40kPa vs. 100kPa).

The KGM-Borax was designed to be of a low enough viscosity to extrude through small nozzles. This was achieved by partial crosslinking. Printed structures therefore required further curing with a solution of higher borax concentration to stabilize the structure. The abundance of borate ions in the curing solution facilitates high crosslinking of the polysaccharide chains, resulting in more rigid structures. The high concentration of the borax solution and the long (24 hour) curing time ensure that the low-volume (<10ml) samples cure fully, and therefore the degree and rate of curing were not considered for this investigation. For larger samples it is expected that accounting for these will be necessary, as KGM at the core of the sample will remain uncured until the borax diffuses to it, and there will be a stiffness gradient corresponding to the degree of curing. The temperature of the sample while curing may also have an effect. It is anticipated that temperatures above room temperature will reduce curing time, but at the cost of lowering the quality of the print due to the decreased viscosity of both the support gel and KGM ink.

The gel presented here is soft and can autonomously self-heal. Other biocompatible gels in the literature offer higher tensile strengths [327] but do not self-heal autonomously. Previous work [339] suggests that modification of the gel by addition of microfibrillated cellulose can improve gel strength whilst retaining the other properties. Alternative nanofillers, in particular nanoclay, have also been shown to improve the tensile strength of KGM gels, although these were not crosslinked with borax [340].

There is also potential for improving the characteristics of the gel through blending with other polysaccharides. Intermixing with xanthan has been shown to significantly increase the strength of thermally gelled KGM [341], and experimentation with KGM-Guar-Borax blends within our lab has shown initial results of qualitatively stronger gels which retain the autonomous self-healing and pH responsivity of KGM-Borax.

A range of 3D KGM-borax structures were printed. A polyacrylic acid-based support ink was used to maintain the 3D structure of the KGM-Borax ink while printing. This support material showed no noticeable change in properties in the presence of the borax curing agent and is easily removed by NaCl solution. The support material was extruded from a second nozzle at the same time as the ink. Figure 6.1a-e shows a three-dimensional star as printed in its upright position with support material. The support gel holds the structure intact until it is subsequently cured in a concentrated borax solution. When cut and placed next to each other without additional force, the samples were able to repair the damage (figure 6.1e). The 3D printed parts retain the ability to mechanically heal and regain mechanical strength.

An alternative approach to achieving complex 3D structures is to print the ink directly into a container filled with polyacrylic acid support material [334] [342]. However, this method requires long preparation time as air bubbles need to be removed from the gel to ensure high quality printing. Another problem is that the support gel inhibits the permeation of borax solution at the post curing stage. This leads to the printed parts being incompletely crosslinked and easily damaged during the extraction process. The last drawback is that the maximum height of the printed structures is limited to the length of the nozzle. In contrast, printing support gel simultaneously with the KGM-Borax ink requires significantly less preparation time and quantity of support material. We also observed that this method allowed the borax solution to permeate through the support material during post-curing. This ensures the printed parts are fully cross-linked. Another advantage is that it allows the printing of taller structures while using nozzles of shorter length.

The Carbopol Ultrez support as currently used is neutral in pH and has no effect upon the surface of the KGM-Borax print. However, it retains the gelation and shear-thinning properties which make it an effective support material even when excess sodium hydroxide is added. There is therefore potential for stiffening of the KGM-Borax gel due to an increased pH if an alkali support was used.

The KGM-Borax gel presented here is made with readily available materials and does not require a carefully controlled temperature profile to manufacture. Since it only requires mixing of the reagents at ambient temperatures, it is easier to manufacture, in contrast to other polysaccharide gels, which, for example, require thermal gelling with an alkali.

The KGM-Borax gel is a pH responsive material. This is due to the shifting of the borate ion equilibrium described in equation 1. A decrease in pH favours the dissociation of ions from the polysaccharide chains and results in a weakening of the gel. An increase in pH has the opposite effect, stabilising the tetrahedral structure of the borate ions and strengthening the gel. Song *et al.* [322] consider the rheological properties of a similar KGM-Borax gel at both pH 2 and pH 10. They demonstrate an increase in shear storage modulus within the LVE region on the order

of 15x when transitioning from acidic to alkali conditions. This property can be exploited to design programmable, task specific, responsive soft robots that react to environmental changes.

Self-healing polymers have been used in the context of soft robotics [325] [326]. Typically, polymer networks are crosslinked with a thermoreversible Diels-Alder reaction. A recent study investigated 3D printing with these gels [343]. An external stimulus, in the form of heat, is required to trigger the process of healing. In contrast, the printable KGM-Borax gel presented here does not require an external stimulus to initiate healing. The borate ion, which contributes to the healing, is intrinsic to the gel. Another intrinsic and autonomous self-healing material has been presented where polyborosiloxane was used to repair damage [344]. Dynamic bonds between boron and oxygen in the polyborosiloxane networks contribute towards healing. Polyborosiloxane is not prone to deterioration such as evaporation of the solvent, which is common in the case of hydrogels. However, natural degradation of the gel may be a desirable property in applications including environmental monitoring and remediation that employ large numbers of micro or nano robots. A timed, benign decay of the gel would eliminate post-operative cleanup and additional pollution of the environment. Further study is required to quantify the biodegradability of the KGM-Borax gel.

A further feature of the printable KGM gel is its ability to heal under water (figure 6.1 j-m). Cylindrical samples, made in a manner similar to those used in the tensile tests, were cut in half and brought together when completely submerged in water. The samples healed within 5 minutes. Under tension, they were able to withstand stretching in excess of twice the initial length (figure 6.1m). This is the first demonstration of underwater healing in KGM-Borax gels. This ability is highly desirable in robots operating in aquatic settings. The healing efficiency under water will be further studied in future work.

3D printable polysaccharide gels are a potential route towards self-healing stimuli-responsive light driven soft robots. The hydrogel could replace the current solid body of FLASH and make it more compliant. For instance, due to the inherent softness and the strong underwater self-healing capability, FLASH can easily navigate through different obstacles and repair damage cause by collisions. It also enables safer environmental interaction due to its biodegradability. The edibility of KGM gels depends on the crosslinker used. While KGM itself is edible, the presence of borax makes it unsafe for ingestion in large quantities. While not toxic in minute quantities, any potentially detrimental effects of borax on humans and the environment can be avoided by using alternative crosslinkers or incorporating KGM into other gels such as Xanthan gum and Carrageenan [345]. This could open up many interesting research avenues. For example, a light driven smart robot becomes food for the animals in the environment at the end of its life cycle.